THE UNIVERSITY OF
SYDNEY

Reliable Measurement of Slip Using Colloid Probe Atomic Force Microscopy

Submitted in accordance with the requirements of the degree of Doctor of Philosophy at The University of Sydney

Liwen Zhu

The University of Sydney

School of Chemistry

August 2012

Declaration

The work presented in this Thesis was carried out by the author during March 2009 to August 2012 in the School of Chemistry, The University of Sydney, as a part of the requirements for the degree of Doctor of Philosophy in Science. No part of this Thesis has been submitted for any other degree to this or any other institution. When collaboration has been necessary, the collaborators have been named and the extent of the collaboration made clear. Results from other authors are referenced in the usual manner throughout the Thesis.

Liwen Zhu Date

Acknowledgements

Through the three and half years of my PhD, I have had the help and support from numerous people. First and foremost, I would like to thank my supervisor, Dr Chiara Neto, for taking me as a student, guiding me, continuing to inspire me to work on this project and for always being patient with me. Words are never enough to thank you for your encouragement, support and guidance.

I would like to express my deep appreciation to my co-supervisor, A/Prof. Phil Attard, for his useful advice and great ideas to improve my work through my PhD. Thanks for being so flexible with your hours and never getting tired of answering my questions.

I would also like to thank my colleague Tom Lee who took time to discuss my work and gave me useful feedback.

Sincere thanks to my parents in China for their love and support in completing this project, and to my friends in Sydney who shared great moments with me in the past three and half years.

Finally, I acknowledge the support from the University of Sydney and the Australian Research Council.

Without the help mentioned above, I would have faced many difficulties doing this project. A sincere thanks to all of you again.

Abstract

Recent research has shown that Newtonian liquids can slip at solid surfaces in confined geometries, which contradicts the classical no-slip boundary condition in which the liquid is stationary at the solid surface. The study of liquid boundary conditions that provides a fundamental understanding of the physics of liquid flow in confined geometries, such as in porous media, and also could benefit various commercial applications, such as micro and nanofluidic applications. The aim of our work was to build a reliable experimental and theoretical framework to investigate liquids slip on solid surfaces by colloid probe atomic force microscopy (AFM).

Colloid probe AFM provides an accurate way to study slip at a solid surface by measuring the hydrodynamic drainage force between a colloid probe and a solid substrate as the two surfaces approach to contact. In our studies, we have investigated the slip of a one-component viscous liquid (di-*n*-octylphthalate) on bare silicon substrates and hydrophobised silicon substrates. In order to obtain reliable slip results, we solved experimental problems in previously published experiments and improved the theoretical modeling which affects the reliability and accuracy of the measured slip lengths. In the new improved experimental protocol we used a closed loop scanner to produce a constant driving velocity, minimised the virtual deflection due to top-scan AFM by removing a constant slope in the force curve, and clarified the true compliance and zero separation in the force curve. The need for tight control over experimental conditions in slip measurements was highlighted, such as extremely careful surface cleaning, the use of a one-component liquid, continuous monitoring of the liquid temperature, and repeat measurements in different locations of the substrate. By performing slip measurements in symmetric and asymmetric systems, a new method was developed to self-assess the accuracy and reproducibility of the slip force measurements.

A new mathematical algorithm was built to predict the hydrodynamic drainage force independently of experimental data. This new mathematical algorithm reduced the noise greatly in the theoretical forces over that in the previous treatments; it was demonstrated by blind test that this new calculation method provides reproducible and reliable slip length values and spring constant values with the uncertainty within 3%. The new mathematical algorithm can be easily applied to simulate slip lengths and hydrodynamic forces in

different experimental conditions, such as the presence of nanoparticle contamination on the substrate surface and the flattening of the colloid probe, which were both demonstrated to affect the measured slip lengths. The exact variable drag force on soft cantilevers was calculated for the first time and applied to fit the experimental force. This calculation revealed that the dependence of slip on the driving velocity and the cantilever shape found in literature could be a spurious effect due to the assumption that the drag force on the cantilever is constant during force measurements.

In our studies, it was also shown that the measured slip length actually decreases with increasing shear rate, rather than being a constant value as commonly assumed. A new shear dependent model for slip fitted well experimental hydrodynamic forces for all separations down to a few nanometres. A possible molecular explanation was proposed for the mechanism of shear rate dependent slip in our experiments.

Publications arising from this work

1. L. Zhu; P Attard; C Neto; Reconciling Slip Measurements in Symmetric and Asymmetric Systems, *Langmuir*, 2012, **28**, 7768-7774.

2. L Zhu; P Attard; C Neto; Reliable Measurements of Interfacial Slip by Colloid Probe Atomic Force Microscopy. III Shear rate dependent slip, *Langmuir*, 2012, **28**, 3465-3473.

3. L Zhu; P Attard; C Neto; Reliable measurements of interfacial slip by colloid probe atomic force microscopy: I. Mathematical Modelling, *Langmuir*, 2011, **27**, 6712-6719.

4. L Zhu; P Attard; C Neto; Reliable measurements of interfacial slip by colloid probe atomic force microscopy: II hydrodynamic force measurements, *Langmuir*, 2011, **27**, 6701-6711.

Presentations arising from this work

1. 86th ACS Colloid and Surface Science Symposium, Maryland (U.S.), Oral presentation, 2012.

2. Australian Colloid and Surface Science Student Conference, Newcastle (Australia), Oral presentation, 2012.

3. Australian Colloid and Interface Symposium, Hobart (Australia), Oral presentation, 2011.

4. DRSPOC, The University of Sydney, Oral presentation, 2010.

5. Australian Colloid and Surface Science Student Conference, Adelaide (Australia) Poster presentation, 2010.

Table of Contents

Chapter 1 Introduction and Background

1.1 Preamble

Fluid mechanics is one of the oldest topics in physical science. For hundreds of years the no-slip boundary condition based on empirical evidence has provided a convenient approximation to model flows in many macroscopic conditions.[1] However, no-slip is not the only available boundary condition. In 1823, Navier[2] first pointed out that a fluid might slip on a solid surface. (A schematic of the two different boundary conditions is illustrated in Figure 1.1.) After that, the validity of a no-slip boundary condition was widely debated throughout the 19th and early 20th centuries by many great scientists, as reviewed by S. Goldstein.[3] In the late 20th and 21st centuries, the rapid development in nanotechnology enabled further studies into the fluid mechanics near fluid-solid interfaces by more accurate detection and more effective molecular simulations.

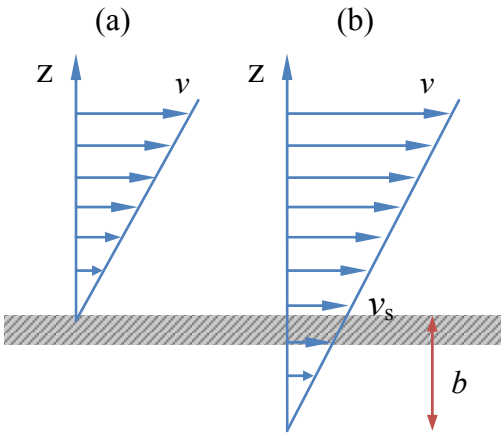

Figure 1.1 Schematic illustration of two boundary conditions. (a) No-slip boundary condition: the velocity of the liquid relative to the solid decreases to zero at the solid surface. (b) Slip boundary condition: the velocity of the liquid v_s decreases gradually toward the solid, but it is non-zero at the solid surface. The slip length b is the extrapolated distance beyond the solid surface where the liquid velocity is equal to zero.

In general, the flow boundary condition is a fundamental element to describe the liquid flowing on solid surfaces, and it provides a measurement of molecular momentum

transport at fluid-solid interfaces and of the nature of the fluid in the vicinity of the surface. This is the primary reason for the strong interest in the understanding of the flow at the fluid-solid interface. Another reason lies in its potential applications in many areas of industrial and technological processes, such as micro- and nanofluidics, flow in porous media, particle aggregation, sedimentation, extrusion, friction and lubrication, and biological fluids. All these processes deal with small size systems which suffer the difficulties of the driving and mixing of fluids in such confined geometries. Therefore understanding liquid behaviour at interfaces in confined geometries, especially the liquid boundary conditions and the factors they depend on, is fundamental to solve microfluidic problems.

During the past decade, the substantial scientific research invested in the slip phenomenon has shown a clearer picture of flow at the boundary. Most evidence indicates that liquids can slip on hydrophobic solid surfaces.[4-10] The measured slip length varies from nanometre to micrometre scale by different techniques. Slip lengths above tens of nanometres are mostly believed to be "apparent slip" due to experimental artifacts such as gas layers at hydrophobic or superhydrophobic surfaces[5, 11-13], contamination in experimental systems, shape of cantilevers used, misinterpretation of experimental data and limitations in techniques used. The latter four effects are discussed in Chapters 3 and 4, and in Section 1.4. Therefore the accuracy of the measurement technique needs to be improved and the possibility of artifacts needs to be investigated and eliminated to reduce this wide variation in the reported slip lengths for nominally similar surfaces.

Colloid probe atomic force microscopy (AFM) is a sophisticated technique, especially when used for measuring nanometre sized slip lengths. This technique has been widely used in the investigation of boundary conditions on liquid-solid interfaces. The measured slip length can be accurate at the nanoscale. However, experimental artifacts and the issue of interpreting data are considered possibly to affect the accuracy of slip measurements by colloid probe AFM method. Therefore this thesis focuses on these issues on both experimental force measurements and the theoretical modeling to build a reliable colloid probe AFM protocol for liquid slip measurements on solid surfaces.

1.2 Outline of the Thesis

In the remainder of Chapter 1 a brief background of the research undertaken is presented. Firstly the basic interaction forces at interfaces are introduced. Then the different methods of probing slip in liquids are explored, followed by summarising the slip results that are in the literature in the form of tables. Finally the parameters upon which slip has been found to depend are discussed.

In Chapter 2 the main experimental techniques and methodologies used in this thesis are specified.

Chapter 3 describes an improved theoretical modeling for fitting the experimental force curves to obtain a reliable slip length result. Several possible artifacts are modeled: the effects on slip from the exact drag force on the cantilever, particle contamination on solid surfaces, the flattening of the colloid probe surface, and the discrepancy between the approximate solution of the Taylor equation and the exact Brenner force at small separations. This work was published in 2011.[14]

Chapter 4 illustrates direct measurements of hydrodynamic forces acting on a sphere in a viscous Newtonian liquid by a reliable colloid probe AFM experimental protocol. The Taylor equation with derived correction for slip boundary by Vinogradova is used to fit the force curves. In this Chapter, the issues of the virtual deflection, effect of friction on compliance in force curve analysis, and possible particle contamination in the system are addressed to build a reliable experimental protocol, which has been summarised in a published paper in 2011.[15]

In Chapter 5 a new slip model including a shear rate dependent slip length is introduced, both theoretically and experimentally. The drag effect on the slip measured using soft cantilevers is demonstrated experimentally. This work was published in 2012.[16]

Chapter 6 discusses slip measurements performed on symmetric and asymmetric systems, in order to reconcile the measured slip results on different systems. This work was published in 2012.[17]

In Chapter 7, a conclusion based on significant results is presented along with a brief perspective of this field.

1.3 Surface Forces

Surface forces are important in fundamental physics to determine the behaviour and properties of colloids, including biological molecules, micelles and membranes.[18] Many methods have been used to measure surface forces, including devices with molecular resolution such as the surface force apparatus and AFM, which is used in our experiments. In this section, we introduce van der Waals forces, electrostatic double forces, hydrophobic, and hydrodynamic forces, all of which normally occur in slip measurements by colloid probe AFM.

1.3.1 Van der Waals forces

In physical chemistry, the *van der Waals forces*, named after Dutch theoretical physicist Johannes Diderik van der Waals, are the sum of the attractive or repulsive forces between molecules. They are not as strong as covalent bonds, Coulomb or hydrogen bonding forces, but they are omnipresent.

1.3.1.1 Total intermolecular pair potential, Mie and Lennard-Jones potential

In the early 20th century, a few semi-empirical relations were proposed for the intermolecular interaction energy. In 1903, Mie[19] proposed a semi-empirical interaction pair potential by summing the attractive and repulsive potentials in the form

$$w_{\text{total}}(r) = w_{\text{attractive}}(r) + w_{\text{repulsive}}(r) = -\frac{A}{r^n} + \frac{B}{r^m} \tag{1.1}$$

where A, B, n and m are constants, and $m > n$.[20] Mie's potential applies to two non-polar, spherically symmetrical molecules, which are completely isolated in free space.

Another interaction potential was proposed by Lennard-Jones (1925), which can be considered as a special case of the interaction potential proposed by Mie. Eq. 1.2 with n =

6 and m = 12 is also known as L-J potential or 6-12 potential. This equation was developed based on the hypothesis that the pair of interacting molecules is subject to attractive forces at the long range and repulsive forces at the short range. The attraction part (negative) is due to the van der Waals interaction potential. The short-range repulsion term (positive) is due to the overlap of the molecular orbitals (known as Pauli repulsion or Born repulsion).[21] The Lennard-Jones potential is expressed as

$$w_{\text{total}}(r) = -\frac{A}{r^6} + \frac{B}{r^{12}} \tag{1.2}$$

where n = 6 is taken from the well-known inverse sixth power dependence of the separation distance in van der Waals interactions, and m = 12 is used for repulsive interactions.

The long-range van der Waals forces between pairs of molecules are constituted by the London dispersion force, along with the Keesom force and the Debye force. In condensed matter, the intermolecular interactions are summed over all the molecules. They are often called long-range forces because they can have measurable effects up to ~ 10 nm. Within the long-range van der Waals forces, the dispersion force is probably the most important force and is present for all materials. It plays very important roles in adhesion, adsorption, wetting, physical properties of gases and liquids, thin films, coagulation of colloids, coalescence of drops and bubbles and many other phenomena.[18]

In the early 20th century, Keesom and Debye proposed theories of van der Waals attractive forces as arising from orientation and induction effects, respectively. Their theories can explain the interaction between two polar molecules or one polar molecule and one non-polar/symmetric molecule. The interaction between two permanent dipoles (permanent dipoles are polar molecules) is known as the Keesom orientation force. In the polar molecules of some materials, although electrically neutral overall, due to the fixed distortion in the distribution of electrical charge in the structure of these molecules, one side of the molecules is always slightly positive and the opposite side slightly negative. This distribution of electrical charge causes the molecules to attract and align with each other, resulting in a net attractive force. The interaction between a permanent dipole and a

temporary dipole is known as the Debye induction force. This kind of interaction can be expected between any polar molecule and a non-polar/symmetric molecule. In such case, a non-polar molecule experiences a temporary dipole as one side of its electrons are attracted or repelled by a neighbouring polar molecule. This induction force is far weaker than Keesom force, but stronger than the London dispersion force. However neither of these two above interactions can explain interactions of non-polar molecules. After the establishment of quantum mechanics, a German-American physicist, Fritz London, first suggested how an attractive force between non-polar molecules arises from an instantaneous dipole inducing another complementary dipole in an adjacent molecule. These interactions are known as London dispersion forces. This theory is based on the fact that the electrons are mobile. At any one instant, electrons move towards one end of the molecule, which causes that end to be slightly negative (δ^-) while the other end will be temporarily short of electrons, and so become slightly positive (δ^+). This can also happen in monatomic molecules such as the noble gas helium. In this case, this temporary polarised molecule will attract an adjacent and non-polar molecule by inducing a temporary dipole in this attracted molecule. A net attractive force is given arising from the oppositely charged ends between two molecules, and this is called dispersion or London force.

1.3.1.2 Van der Waals interactions between macroscopic bodies

In the previous section, the van der Waals attraction was discussed at the atomic or molecular level. However, at the microscopic or macroscopic level, such as in colloid and surface science, the calculation of the van der Waals interaction between two bodies is particularly interesting. This was first caculated by H. C. Hamaker [22] in 1937 by summing the van der Waals attractive interaction energies between all pairs of molecules in the two bodies. In order to perform integrations in a simple way, Hamaker used several assumptions[20] and introduced the concept of a Hamaker constant (A) which fundamentally scales the magnitude of the van der Waals interactions between particles of various shapes with intervening media. Hamaker constants are usually inserted in expressions for the potential energy of interaction between particles and surfaces. The van der Waals interaction energy and force expressions in different geometries have been derived.[18, 20]

Here, we only introduce two geometries which are relevant to our experiments. One is the sphere-surface geometry (Figure 1.2a) which is the same as that in a typical colloid probe AFM experiment in this Thesis. Another is a two-crossed-cylinders geometry (Figure 1.2b) which is typically used in the surface force apparatus.

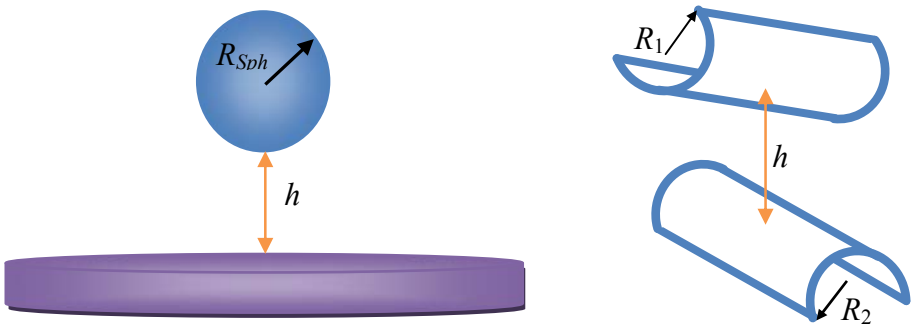

Figure 1.2 Geometries of two bodies with surfaces h apart: (a) a sphere near a flat surface (b) two crossed cylinders.

For a spherical particle (with radius R_{Sph}) and a planar surface at a distance h ($R_{Sph} >> h$), the van der Waals attractive interaction energy between them is expressed as below by applying the Derjaguin approximation,[20]

$$w(h)_{\text{Sphere–Surface}} = -\frac{AR_{Sph}}{6h}. \tag{1.3}$$

The corresponding attractive dispersion force per unit area between sphere and surface is directly derived from Eq. 1.3 by differentiation, as follows[20]

$$F(h)_{\text{Sphere–Surface}} = -\frac{AR_{\text{Sph}}}{6h^2}. \tag{1.4}$$

For two parallel cylinder-shaped materials which cross each other, by invoking the Derjaguin approximation, the van der Waals attractive interaction energy is[20]

$$w(h)_{\text{Crossed–Cylinders}} = -\frac{A\sqrt{R_1R_2}}{6h}. \tag{1.5}$$

As a result of differentiation from Eq. 1.5, the attractive dispersion force per unit area between two crossed cylindrical surfaces is[20]

$$F(h)_{\text{Crossed-Cylinders}} = -\frac{A\sqrt{R_1 R_2}}{6h^2}. \quad (1.6)$$

In the initial Hamaker constant calculation, the additivity of simple pair-potentials is assumed and the influence of neighbouring atoms on the interaction between any pair of atoms is ignored. In real condensed systems (such as liquids and solids) where two atoms are not isolated, the effective polarisability of an atom changes when surrounding atoms are present. Therefore a theory is needed to avoid this weakness in the initial Hamaker approach. In 1956, E.M. Lifshiz introduced a powerful way to deal with the interaction of macroscopic bodies, by expressing the Hamaker constant as an integral over frequency of a function of the materials' dielectric constants. The calculation of Hamaker constant based on the Lifshitz theory can be found in Israelachvili's book.[18] In practice, Hamaker constants are more commonly obtained from direct measurements of van der Waals forces rather than by a Lifshitz calculation.

1.3.2 Electrostatic Double Layer Forces

The electrostatic double layer refers to a region across a liquid-solid or liquid-liquid interface where an equal and opposite charge is carried by two separate phases, such as a layer of negative ions adsorbed on colloidal particles that attracts a layer of positive ions in the surrounding electrolyte solution. Several mechanisms contribute to the charging of a surface in a liquid[18]. The most common mechanism of development of charge on a surface is the absorption of ions (such as simple electrolyte ions, ionic surfactants or polyelectrolytes) from solution onto an initially uncharged surface. Another possible mechanism is the ionization or dissociation of a surface group, e.g. the dissociation of protons from carboxylic groups present on the solid surface by the mechanism R-COOH $\rightarrow$ R-COO$^-$ + H$^+$, which leaves a negatively charged surface.

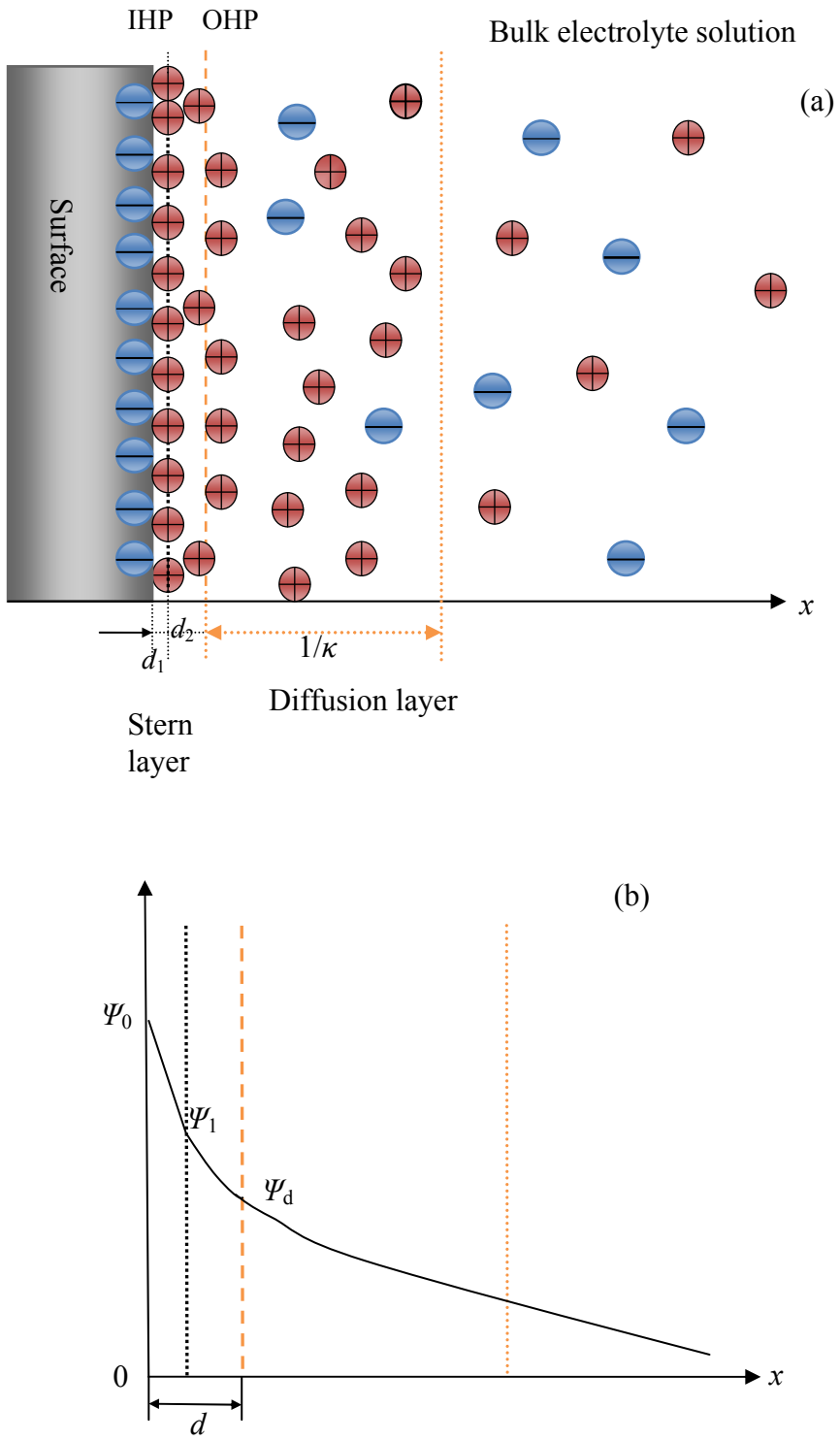

Figure 1.3 (a) Schematic illustration of Stern layer and diffusion layer of electrostatic double layers. (b) Corresponding variation of potential as a function of distance away from the charged surface. Adapted from Erbil.[20]

By the above charging mechanisms, the final surface charge is balanced by an equal but oppositely charged region of counterions next to the surface. The region containing

counterions can be divided into two parts: the Stern layer and the diffuse layer (see Figure 1.3). The compact layer of bounding conterions onto the surface is known as Stern layer in honour of Otto Stern (1924) who proposed the existence of this layer. The inner part of the Stern layer is known as the inner Helmholtz plane (IHP), in which the counterions are specifically adsorbed on the surface. The potential across this layer drops sharply. The outer Helmholtz plane (OHP) is located on the centre between IHP and next layer. The next layer is known as the diffuse layer which forms an atmosphere of ions in rapid thermal motion close to the surface. The 'thickness' of the diffuse layer is known as the Debye length (represented by $1/\kappa$). The Debye length for monovalent ions is inversely proportional to the concentration of electrolyte in the solution. The extent of the double layer decreases with increases in electrolyte concentration due to the shielding of charge at the liquid-solid interface. The ions of higher valence are more effective in screening the charge.

Electrostatic double layer Repulsion between two surfaces

When two similarly charged surfaces approach each other closely, the repulsive force between the surfaces begins to develop due to the overlapping of the double layers on their surfaces. This repulsive force plays an important role in the stabilisation of emulsions, foams and colloids.

Firstly, one fundamental equation for describing the electrostatic interactions between ion molecules in solutions has to be proposed, i.e. Poisson – Boltzmann (PB) equation,

$$\frac{d^2\psi}{dx^2} = -\frac{ze\rho_0}{\varepsilon\varepsilon_0} e^{-ze\psi/kT} \tag{1.7}$$

where ε_0 is the permittivity of free space; ε is the dielectric constant of the solvent; k is the Boltzmann constant; e is the elementary electron charge; z is the ion valency; ψ is the electrostatic potential; electrical field; ρ_0 is counterion density in the midpoint between the two surfaces, i.e. at the point $x = 0$; T is the temperature.

In the following, by solving PB equation we present some approximation expression for the electrostatic double layer interaction between charged surfaces in electrolyte. At low surface potential, below 25mV, the repulsive pressure between two planar surfaces can be approximately written as

$$P \approx 2\varepsilon\varepsilon_0\kappa^2\psi_0^2 e^{-\kappa D} = 2\sigma^2 e^{-\kappa D}/\varepsilon\varepsilon_0 \text{ N/m}^2, \quad (1.8)$$

while for two spheres of radius *R*,

$$F \approx 2\pi R\varepsilon\varepsilon_0\kappa\psi_0^2 e^{-\kappa D} = 2\pi R\sigma^2 e^{-\kappa D}/\kappa\varepsilon\varepsilon_0 \text{ N} \quad (1.9)$$

In the above σ is surface charge density $\sigma = \varepsilon\varepsilon_0\kappa\psi_0$ only valid for low potential (< 25 mV); *D* is the distance between two surfaces. These two above equations are often applied for all electrolytes whether 1:1, 2:1, 2:2, 3:1 or even mixtures, as long as the appropriate Debye length κ is used, although they have limited accuracy at higher ionic strengths.

For two surfaces of different charge densities or potentials, the interaction energy can have a maximum or minimum at some finite distance, usually below 1/ κ. Approximate equations for the interactions of two surfaces of unequal charge but constant potentials or for constant charge but unequal potentials have been reviewed in Israelachvili's book.[18]

The DLVO theory

The DLVO theory was proposed in 1940s by Soviet and Dutch scientists independently as a starting point to understand the stability and phase behaviour of colloidal dispersions. It combines the effects of the van der Waals attraction, which dominates at short range, and the electrostatic double layer repulsion, which dominates at long range. This theory suggested that an energy barrier arising from the electrostatic repulsive force prevents two particles approaching each other and coagulating together, resulting in a stable colloidal system. If this energy barrier is overcome, the van der Waals attractive force between particles becomes stronger and causes them to aggregate irreversibly, and coagulation will take place.

1.3.3 Hydrophobic Interactions

Hydrophobic interactions refer to the unusually strong attractions between hydrophobic molecules and surfaces in aqueous solutions. This interaction has been extensively studied due to its importance in a wide range of areas, from protein folding and biological interactions to separation of hydrophobic particles in froth flotation. This attraction can act over up to several hundred nanometres between hydrophobic surfaces, so it is also called a long-range attraction.[23] However the origin of hydrophobic interactions was unclear for a long time. In Israelachvili's book[18] three possible mechanisms are suggested for the hydrophobic interactions: 1) an attractive solvation force due to water structure 2) an attractive electrostatic van der Waals like force between correlated charges or dipoles at the surfaces 3) a capillary force due to bridging of nanobubbles. According to several recent review papers,[23, 24] nanobubbles are the most likely explanation for long-range attractive hydrophobic forces, and there is experimental and theoretical evidence against other possible mechanisms. In a recent paper,[25] hydrophobic forces were divided into two types: a short range reproducible force, typically < 20 nm and stronger than the van der Waals force; a long range variable force. The short range force is argued to be the result of a depleted fluid density between the hydrophobic surfaces. The long-range force is considered to be due to bridging nanobubbles on the surfaces. Nanobubbles existing on hydrophobic surfaces have been detected in many experiments. [26-29]

1.3.4 Hydrodynamic Theory

Hydrodynamics is the study of the motion of liquids. The basic equations for hydrodynamic flow are the Navier-Stokes equations which describe the changes of momentum per volume of the liquid according to the forces, pressure force, body force and viscous force, applied to a unit volume of the liquid.[1]

For an incompressible and Newtonian fluid (viscosity η constant), the Navier-Stokes equations can be written as

$$\rho\left(\frac{\partial \mathbf{u}}{\partial t}+\mathbf{u}\cdot\nabla\mathbf{u}\right)=F-\nabla p+\eta\nabla^2\mathbf{u} \tag{1.10}$$

where **u** is the velocity vector in the fluid, p is the pressure, ρ is the density of the fluid, μ is the viscosity of the fluid, F is the body force per unit volume.

The simplest case in which the Navier-Stokes equation can be solved is for a spherical particle of radius R moving with velocity v in a viscous fluid having viscosity η under the no-slip boundary condition. In this case, the Navier-Stokes equation allows one to predict the hydrodynamic drag force to which the particle is subjected. For very low Reynolds' number (Re <<1), the Stokes drag force on a spherical particle is given by

$$F_d = -6\pi\eta R v \tag{1.11}$$

This expression is usually known as Stokes' law for the resistance to a moving and rigid solid sphere. This expression assumes no slip boundary conditions. However for the motion of other spheres, such as droplets or gas bubbles in an immiscible fluid, the slip boundary condition is traditionally considered to apply. The ratio of inner (η_i) and outer (η) fluid viscosities λ is introduced, $\lambda = \eta_i / \eta$. The drag force acting on such a sphere is then[30]

$$F_d = -2\pi\eta R v \frac{2+3\lambda}{1+\lambda} \tag{1.12}$$

The above equation reduces to Stokes' law (1.17) in the limiting case of a rigid sphere because λ approaches zero (the inner fluid has an infinite viscosity). For another limiting case, a gas bubble exists in the fluid, the viscosity of gas tends to zero, and the expression becomes[30]

$$F_d = -4\pi\eta R v \tag{1.13}$$

For the case of a solid sphere of radius R moving with constant velocity $\dot{h}$ perpendicularly towards a plane solid surface (Figure 1.4), the Navier-Stokes equation was solved by Brenner[31] and Taylor (see note 38 in the reference[32]) to describe the hydrodynamic drainage force between the moving sphere and the plane surface. The approximate expression for the hydrodynamic drainage force is expressed by Taylor as,

$$F_h = \frac{-6\pi\eta R^2 \dot{h}}{h} \quad (h << R) \tag{1.14}$$

where h is the separation, which is the distance of closest approach of the sphere to the substrate surface, and $\dot{h}$ is the velocity of the microsphere relative and perpendicular to the substrate, ($\dot{h}$<0 corresponds to decreasing separation and $\dot{h}$>0 corresponds to increasing separation). This equation is an approximation that is valid when the separation between the two surfaces h is smaller than the radius of the microsphere R. $h << R$ this condition is referred to as the lubrication approximation.

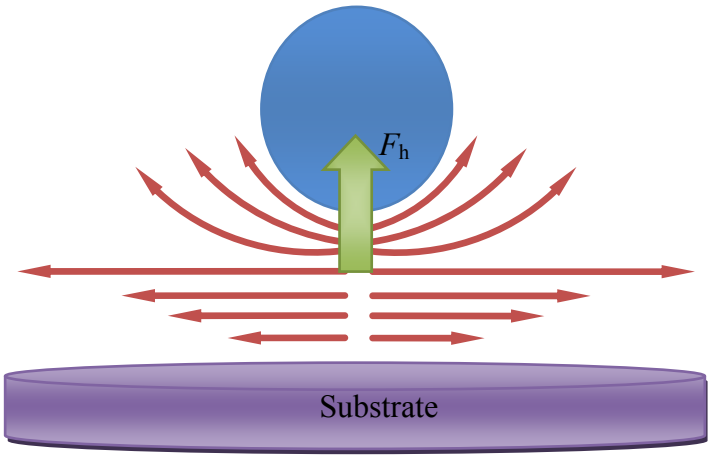

Figure 1.4 Schematic of hydrodynamic drainage forces on a sphere approaching a solid substrate.

In 1961, Brenner[31] derived the exact solution for the sphere-flat geometry at arbitrary distances on the hypothesis of no relative motion at the fluid solid interface (i.e. no-slip boundary condition). However Brenner's expression includes Stokes drag, and indeed it becomes the Stokes drag at large separations, whereas the Taylor's expression is the pure hydrodynamic drainage force that goes to zero at large separations. Details of the Brenner equation and differences compared to the Taylor equation are discussed in Chapter 3.

In 1995, Vinogradova[33] found that the classic hydrodynamic drainage equations (the Taylor equation and the Brenner equation) based on the Reynolds' lubrication theory cannot be applied for the satisfactory description of the drainage of a liquid between two surfaces if at least one of them is hydrophobic. She considered that there may be some distinct deviation from the Reynolds theory due to interfacial slip of the liquid over the

hydrophobic surface. She presented a correction for slip f^* in the Reynolds theory. The hydrodynamic drainage force in the slip boundary condition becomes

$$F_h = \frac{-6\pi\eta R^2 \dot{h}}{h} f^* \quad (h << R). \tag{1.15}$$

In an asymmetric system, which is discussed in Vinogradova's solution, two approaching surfaces may differ in their slip behaviour, so the slip length on one surface is defined to be $b_2 = b$, while for the other surface, it is $b_1 = b\,(1+k)$. The factor f^* indicates the occurrence of slip. Under a no-slip boundary condition, $f^* = 1$. A general expression for the f^* factor is

$$f^* = -\frac{2Ah}{BC} - \frac{2h}{C-B}\left[\frac{(B+h)(B-A)}{B^2}\ln\left(1+\frac{B}{h}\right) - \frac{(C+h)(C-A)}{C^2}\ln\left(1+\frac{C}{h}\right)\right] \tag{1.16}$$

$$A = b(2+k) \tag{1.17}$$

$$B = 3b(2+k+\sqrt{1+k+k^2}) \tag{1.18}$$

$$C = 3b(2+k-\sqrt{1+k+k^2}) \tag{1.19}$$

For three limiting cases, three corresponding f^* factors are provided by Vinogradova.

If one of the two surfaces has a no-slip boundary condition, then $k \to -1$ and Eq. 1.16 becomes

$$f^* = \frac{1}{4}\left(1+\frac{3h}{2b}\left[\left(1+\frac{h}{4b}\right)\ln\left(1+\frac{4b}{h}\right)-1\right]\right) \tag{1.20}$$

If the slip behaviour is equal at two surfaces (this system is defined as symmetric), then $k \to 0$, $b_1 = b_2 = b$ and

$$f^* = \frac{h}{3b}\left[\left(1+\frac{h}{6b}\right)\ln\left(1+\frac{6b}{h}\right)-1\right] \tag{1.21}$$

If one surface has an infinite slip length and the other has a finite slip length b, $k \to \infty$ and

$$f^* = \frac{h}{6b}\left[\left(1+\frac{h}{3b}\right)\ln\left(1+\frac{3b}{h}\right)-1\right] \tag{1.22}$$

In order to simplify the experiment and fitting procedures, in Chapters 4 and 5 we use the symmetric Eq.1.21 to fit an average slip length, *b*, over two different surfaces when measuring hydrodynamic drainage forces at asymmetric systems. The actual slip length on the investigated surface using the general symmetric equation (Eq. 1.16) and the reason for using asymmetric systems to investigate slip are discussed in Chapter 6.

1.4 Techniques for the Investigation of Boundary Conditions

Many experimental and simulation methods have been used to investigate interfacial slip in the last two decades. The surface force technique and velocimetry are the two main categories of experimental methods which are most commonly used in liquid slip measurements, as indicated in slip literature. The surface force technique includes surface force apparatus and AFM, which are believed to be the accurate methods for investigating interfacial slip in the current slip measurements. However, this first category is an "indirect" method because the slip length has to be deduced by comparison of experimental results with theory. In order to investigate liquid slip directly, the velocimetry technique is applied, which can calculate the liquid velocity at the liquid/solid interface. However, this technique suffers from a low resolution. Recently, some attention has been paid to improving this technique, ranging from the classical particle image velocimetry (PIV), to the more accurate μ-PIV, and further high resolution methods which combine with high resolution optical spectrometry, such as total internal reflection fluorescence PIV, fluorescence correlation spectroscopy (FCS), double-focus fluorescence cross-correlation spectroscopy (DF-FCCS) total internal reflection fluorescence cross-correlation spectroscopy (TIR-FCCS). Other experimental methods have been used to study liquid /solid boundary conditions, including using quartz crystal microbalance by resonating,[34, 35] a torsional ultrasonic oscillator,[36] rheometer system (Cone-and plant torque),[12] and flow metering system[37]. In addition, molecular dynamic simulations and Lattice Boltzmann simulations are complementary methods for studying liquid slip theoretically.

1.4.1 Surface Force Measurements

The principle of the force measurement for the investigation of hydrodynamic boundary conditions is to measure the hydrodynamic drainage force at small separations between two surfaces moving perpendicularly to each other, either by a steady motion or an oscillatory motion. A force – separation relationship is determined as the two surfaces approach each other until they reach contact. Comparing the experimental force–separation relationship with that from a theoretical calculation of the fluid motion in the gap, and assuming either no–slip or slip boundary conditions, the best fit to the boundary condition and the slip length, if any, can be found.

Two similar experimental apparatus have been used to measure hydrodynamic drainage forces, the surface force apparatus (SFA) and the atomic force microscope (AFM). In SFA, two crossed cylindrical surfaces are arranged perpendicularly and immersed in a liquid. The separation distance between the two surfaces is usually measured by interferometry. The instantaneous hydrodynamic drainage force arising from the normal approach or oscillatory motion is measured by a spring system of known properties attached to the moving surface. In AFM, the hydrodynamic drainage force arises from the motion of approach between a microsphere and a solid surface in a liquid, either at a fixed velocity or a certain frequency. The deflection of the flexible cantilever beam attached to the microsphere is recorded, and then used to deduce the instantaneous hydrodynamic drainage force on the microsphere. Recent experimental results on the investigations of liquid slip by SFA and AFM are summarised in Table 1 and Table 2. Most of the slip length results measured by SFA and AFM are less than tens of nanometres.

Table 1 Recent slip results measured by atomic force microscopy

AFM	**Probe**	**Surface**	**Liquid**	**Slip length (nm)**
Maali *et al.*[38]	Soda lime glass (θ = 20.3±1.5º)	Mica (θ = 0º)	water	<2 (below resolution)
Maali *et al.*[39] (Dynamic AFM)	Silicon	Graphite (θ = 74º)	water	8 ± 2
Stark *et al.*[40]	Silica	PDMS (θ_A< 2°)	5.9 kD PDMS	70
			8.4 kD PDMS	0
			18.8 kD PDMS	0
		PI (θ_A<20°)	2.5 kD PI	5 – 10
			4.8 kD PI	30 – 100
			10.2 kD PI	30 – 80
Sun *et al.*[41]	Silica	Mica	1-propanol	10 – 14
Bhushan *et al.*[42] (Dynamic AFM)	Soda lime glass	Mica (θ_A =0°)	water	0
		Self-assembly of alkane n-hexatriacontane (θ_A = 91°)		43
		Lotus wax (nonacosane-10,12-diol and nonocosane-10-ol) (θ_A = 167°)		236
Bonaccurso *et al.*[43]	Silica (θ_R = 0 º)	Mica (θ_R = 0 º)	water	8 – 9
McBride and Law[44]	Silane SAM (θ =5 ~ 40 º)	Silane SAM (θ = 5 ~ 40 º)	n-alkanes	10 – 14
Guriyanova *et al.*[45]	Silica (θ_A <5 º)	Silica (θ_A <5 º)	KCl or KNO_3 solution	6

AFM	**Probe**	**Surface**	**Liquid**	**Slip length (nm)**
Bowles *et al.*[46]	Silane SAM (θ_A = 11 º)	Silane SAM (θ_A = 11 º)	n-pentane / n-hexane	5 – 20
			n- hexadecane	0
Craig *et al.*[47]	Thiol SAM * (55 º)	Thiol SAM * (55 º)	sucrose solution	0 – 20
Cottin-Bizonne *et al.*[48]	Pyrex	OTS SAM	n-dodecane	20
Honig *et al.*[11]	Silica	Hydroxyl-glass (<5º), methyl-glass (78º), and graphite (30º) *	Sucrose solution	< 2 (below resolution)
Honig *et al.*[49]	Silica	Hydroxyl-glass (<11 º), methyl-glass (<12 º), and graphite (<11 º) *	Silicon oil	0 – 30

The symbols used in this table are: PDMS: Plydimethylsiloxane, θ_A: Advancing contact angle; θ_R: receding contact angle; θ: equilibrium liquid contact angle PI: Polyisoprene; OTS: octadecyltrichlorosilane; SAM: self-assembled monolayer. *Advancing and receding contact angles were reported in the cited papers, the values listed here are the average of the two.

Table 2 Recent slip results measured by SFA

SFA	**Surface1**	**Surface2**	**Liquid**	**Slip length(nm)**
Horn *et al.*[50]	Silica (θ = =45º)	Silica(θ = 45º)	NaCl aqueous solution	0
Zhu *et al.*[51]	OTE(θ= 110º)	OTE(θ = 110º)	water	0 – 2500
	OTE (θ =44º)	OTE (θ = 44º)	Tetradecane	0 – 1500
	Mica (θ = 12º)	Mica (θ = 12º)	Tetradecane(contain 0.2% hexadecylamine)	0 – 1000
Zhu *et al.*[52]	HDA SAM (θ = 12º)	HDA SAM (θ = 12º)	Tetradecane	0 – 14
	HDA SAM	HDA SAM	dodecanene	0 – 8
	HDA SAM	HDA SAM	octane	0 – 2
Cottin-Bizonne *et al.*[48]	Pyrex	OTS SAM	*n*-dodecane	20
Cottin-Bizonne *et al*.[53]	Pyrex (θ_A < 3º)	Phospholipid SAM (θ_A = 95 º) and OTS SAM (θ_A = 105º)	Water	8 – 20
	Pyrex(θ_A <3º)	Pyrex (θ_A <3º)	Water	<2 (below resolution)
	Pyrex (θ_A < 3 º)	OTS SAM (θ_A = 28º)	*n*-dodecane	<2 (below resolution)

Some symbols used in this table has been specified in Table 1 with additional symbols as: OTE:Octadecyltriethoxysilane; HDA: Hexadecylamine.

1.4.2 Velocimetry

Velocimetry has drawn great interest since it is employed in liquid slip measurements.[6, 54-56] Although it currently suffers from a low resolution, as an important "direct" method as opposed to the surface force methods, the potential applications in

liquid slip are great and lots of work has been done to improve this method. In this section, we specify the basic principle of the different velocimetry techniques, and discuss their advantages and disadvantages in slip measurements, followed by a summary of slip length results obtained by several techniques in the literatures.

Velocimetry is the direct measurement of the velocity of fluids or flow profile, as often used to solve fluid dynamics problems. It takes advantage of various optical methods to monitor fluorescent tracer particles flowing with the liquids. The advantage of this technique is that it is non-intrusive, because it does not require the placement of any type of probes in the medium (apart from the tracer particles), which could affect the overall flow. This technique can also return information about the flow in the entire surface, instead of only probing a limiting region of the surface as in the AFM. However, the accuracy of this technique is normally much lower than that of force methods due to relatively low optical resolution, system noise arising from polydispersity of tracers, the need to extrapolate the measured profile to the surface, and difficulties in decoupling flow from diffusion. Therefore, it is normally expected that a slip length of the order of a few tens of nanometres cannot be detected by the velocimetry technique. In the following, the velocimetry technique is discussed in two categories.

1.4.2.1 Particle image velocimetry

Particle Image Velocimetry (PIV) is a technique for imaging the velocity of fluorescent particles in the fluid flow (Figure 1.5). The determination of the particle motion arising from the fluid allows a mapping of the flow motion. The idea of PIV is to use small particles as passive tracers in the flow, and then illuminated periodically by a laser. The movement of the particles is recorded by successive digital images from charged coupled device (CCD) cameras. These images can be analysed by a computer to determine the velocities of the tracer particles and provide the flow profile next to the solid surface. The extrapolated velocities at the solid surface from the flow profile thus obtained give information on the boundary conditions. However, because of the low optical resolution, the distances of extrapolation are actually of the order of microns. Therefore, it is argued

that neither the information about the nature of the fluid next to the surface nor the actual velocity profile next to the surface can be provided by this method.

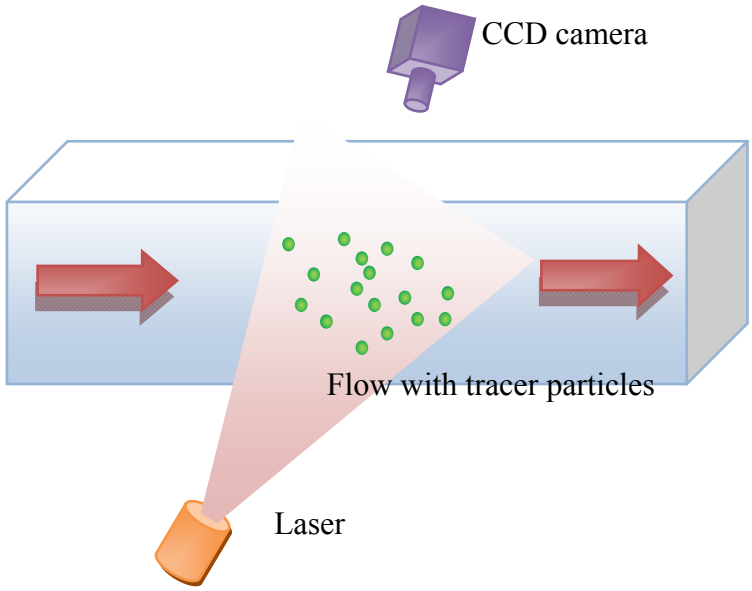

Figure 1.5 Schematic of particle image velocimetry setup

Micro-Particle Image Velocimetry (μ-PIV)

Classical particle image velocimetry has been combined with microchannels to investigate liquid slip. This micro-particle image velocimetry (μ-PIV) substantially reduces the flow dissipation in the microchannel along with decreasing Taylor dispersion (Taylor dispersion is an effect in fluid mechanics in which a shear flow can increase the effective diffusivity of a species), which is the problem in the classical particle velocimetry. However, slip results from Joseph *et al* [57] show that due to a fundamental optical limitation, this method is unable to discriminate slip effect for water flow on hydrophilic and smooth hydrophobic surfaces.

Total internal reflection fluorescence PIV

In the proximity of an interface the normal resolution can be significantly increased using total internal reflection microscopy (TIRM). In TIRM the effect of total internal reflection on the interface between two media with different refractive indices is used to create an evanescent wave that extends (and therefore can excite fluorescence) only in a tuneable region of less than ~ 200 nm from the interface. During the last few years TIRM

imaging was successfully applied for improving the resolution of particle tracking close to solid interfaces.[58-60]

The new method of total internal reflection fluorescence (TIRF)-PIV is particularly suitable for the investigation of slip occurring within submicrometre distance from the surface. The speed profiles can be directly analysed, rather than relying on any modeling of the behaviour of the fluid or the tracers in the vicinity of the surface. Moreover, this method can be applied to a variety of systems even with poorly characterised surfaces. Different fluids can also be investigated; the only limitation is the possible aggregation of tracers in non-aqueous solvent. The summary of slip results from μ-PIV and TIRF-PIV measurements are shown in Table 3.

Table 3 Slip results measured by μ-PIV and TIRF-PIV

	Surface	**Liquid**	**Wettability**	**Slip length(nm)**
Tretheway *et al.*[61]	Hydrophilic glass	water	*μ*-PIV	0
	OTS SAM (θ = 120°)			~1000
Tsai *et al.*[7]	Flat PDMS/glass (θ = 120°)	water	*μ*-PIV	200 ± 200
	Patterned PDVF/glass (θ = 127.4°±2.6°)			A few micrometres
Joseph *et al.*[57]	OTS SAM(θ = 95 º)	water	*μ*-PIV	-35 ± 100
	CDOS (θ = 95 º)			57 ± 100
	Hydrophilic glass			50 ± 50
Joseph *et al.*[62]	carbon nanotube forest (>165º)	water	*μ*-PIV	0 – 1500
Byun *et al.*[63]	glass	water	*μ*-PIV	No–slip
	PDMS (105º)			2000
	Superhydrophobic PDMS (θ = 136º~145º)			400 – 5400
Lasne *et al.*[58]	OTS (θ = 90 º)	water	TIRF-PIV	45 ± 15
		NaCl solution		50 ± 10
Huang *et al.*[59]	OTS	Water or NaCl aqueous solution	TIRF-PIV	~100 – 50
	glass	water	TIRF-PIV	~50
Bouzigues *et al.*[60]	Silica (θ = < 20 º)	water	TIRF-PIV	0 ± 10
	OTS (θ = 95 º)			38 ± 6

Some symbols used in this table have been specified in Table 1 and Table 2 with additional symbols: PDVF: Polyvinylidene fluoride; CDOS: Chlorodimethyloctylsine.

1.4.2.2 Fluorescence Correlation Spectroscopy (FCS)

Fluorescence Correlation Spectroscopy is a correlation analysis of fluctuations of the fluorescence intensity. It is based on a method that measures the fluctuations of the fluorescent light emitted by tracers passing through a confined geometry in the liquid. A proper analysis of these fluctuations allows evaluation of the tracer's diffusion. The measurable difference in the diffusion reflects the hydrodynamic boundary condition that applies on solid substrates, which allows one to deduce the corresponding surface slip. Compared with PIV methods, FCS has good statistics in the evaluated velocities, allows high tracer velocities to be measured, and even can use single molecules as tracers. However, it suffers from the limited resolution of optical microscopes.

Double-focus Fluorescence Cross-Correlation Spectroscopy (DF-FCCS)

Double-focus fluorescence cross-correlation spectroscopy extends the FCS procedure by introducing two similar laser foci instead of one. The tracer particles pass through two lasers separated by a short distance. Fluctuations of the detected fluorescence signal are due to the tracer particles entering and leaving the observation windows. The particle concentration and dynamics are determined from the autocorrelation of the time resolved fluorescence signal.

Total internal reflection fluorescence cross-correlation spectroscopy (TIR-FCCS)

Another high resolution technique couples FCS with the high normal resolution of the total internal reflection fluorescence (TIRF). It allows the measurements of the distance of tracers in the range of 0 – 200 nm from the wall through the exponential decay of a evanescent wave. It further improves the accuracy of the approach.

Table 4 Slip results measured by fluorescence correlation spectroscopy

	Solid surface	**liquid**	**Technique**	**Slip length**
Vinogradova *et al* [56]	Silica (θ_A < 5º)	Electrolyte solution	DF-FCCS	0
	Trimethylchlorosilane SAM (θ_A = 95 º)			80 – 100
Schmitz *et al.*[54]	Silica (θ_A < 5 º)	Phosphate buffer	TIR-FCCS	<10 (below resolution)
Joly *et al.* [64]	OTS SAM	10^{-5}M NaOH; and 10^{-3}M KCl aqueous solution(	FCS	18 ± 5 nm
Lumma *et al.*[65]	Glass/Mica	Water/NaCl	DF-FCCS	0.22 – 1.0μm

1.4.3 Computer Simulations of Interfacial Slip

Experimental measurements provide a great way to investigate slip in physical experiments. Computer simulations present a new way to explore slip by interactions in atom or molecules. The magnitude of slip length, *b*, in simulation literature is much smaller than the experimental results, typically of the order of the molecular length scale. One possible explanation for the discrepancy between experiments and simulations is the different shear rate conditions used, as discussed in Chapter 5. In this section, we introduce two popular computer simulations in the study of liquid slip, molecular dynamics simulation and Lattice Boltzmann simulation.

The Navier-Stokes equations, which are used for most problems in fluid dynamics, require the boundary conditions to be specified, either slip or no slip, and if slip, the value of the slip length. The influence of molecular interaction on the slip boundary condition is not known. Molecular dynamics (MD) simulations, which have been extensively used in the study of liquids flow, provide a good way to investigate the boundary conditions by simulating the fluid-solid interactions.

MD simulations provide a view of physical movements of atoms and molecules by calculating the interaction between atoms or molecules for a period of time. A Lennard-Jones interaction is normally used in most MD simulations to calculate the force on each molecule arising from all the other neighboring molecules. Then, solving Newton's equations of motion determines how the molecule moves in response to this force. The trajectories of all the molecules in the box are computed simultaneously and continuously in space and time. Different L-J parameters are varied to explore the effects on slip boundary conditions in MD simulations. Dammer *et al.*[66] used MD simulations to investigate the effect of gas and hydrophobicity on wall slip. By controlling the amount of dissolved gas, the hydrophobicity of the wall and the type of gas as parameters in the MD simulation, they found the velocity in the liquid film at the hydrophilic wall is not altered by the gas. On the other hand, at a hydrophobic wall, the gas significantly changes the velocity profiles, leading to corresponding slip lengths from 3.4 ~ 7.9 σ (σ = 0.34 nm) by gas enrichment at the liquid-hydrophobic wall interface. Chinappi *et al.* [67] described liquid water flowing over a self-assembled-monolayer of an OTS surface by a MD simulation. The slip length results are in the range of 0.3 – 0.6 nm. Ho *et al.*[68] used equilibrium and non-equilibrium MD simulations to study liquid water slip. They discovered that contact angles larger than 90º are not necessary to attain hydrodynamic slip. Instead, liquid slip is determined by the distribution of water molecules in contact with the solid and the strength of water-solid interactions. If favourable adsorption sites on solid surface exist, but are separated from each other by intrinsic subnanometre distances, no slip is observed. Conversely, if favourable adsorption sites are close to each other, liquid slip can occur, because this packed structure provides relatively weak water-solid interactions.

However, because of insufficiencies of the computer power today, MD simulations are usually limited in the number of particles (a few tens of thousands), length scale (a few nanometres), time scales (nanoseconds), and shear rates (orders of magnitude higher than in any experiment), which make the simulation conditions not easily achieved in experiments. In addition, a recent paper[69] found that the commonly used practice of thermostating fluids in the simulations can often cause artifacts in the simulated slip length, while removing the heat through the walls provides a more realistic answer.

Comparing small accessible time and length scales of MD simulations, mesoscopic simulation methods, such as Lattice Boltzmann (LB) simulations, offer a closer relation to experimentally relevant time and length scales. LB simulations are well applicable for the simulation of microflows and to study boundary slip. The LB method is a discrete computational method based on the Boltzmann kinetic equation on a lattice. The Boltzmann kinetic equation describes the evolution of the single particle probability density. At each time step, the fluid particles can collide with each other as they move along their corresponding directions, possibly under applied forces. Due to collisions between particles, their momentum change. By collision rules, the particles are re-distributed, but the particle number (mass), momentum and energy should be conserved before and after the collision. Through a Chapman Enskog analysis, one can recover the governing continuity and Navier-Stokes equations from the LB simulation algorithm. Jens *et al.*[70] reviewed recent efforts on investigations of the effect (apparent) boundary slip by utilizing Lattice Boltzmann simulations. By introducing a model for hydrophobic fluid-surface interactions and studying pressure driving flow in microchannel, they showed that an experimentally detected slip can have its origin in the hydrophobic interaction, but is constant with varied shear rates and decreases with increasing pressure.

1.5 Slip Dependence on Physical Parameters

Many experiments and simulations have been performed to investigate the factors which determine the occurrence of slip and affect its magnitude. The first factor is type of fluid and its properties such us fluid viscosity,[44] polarity,[71] or electric charge[60]; the second factor is the physical and chemical properties of the surface, such as surface wettability and roughness. The third factor is the flow shear rate. In the following, the emphasis is put on the effects of the surface roughness, wettability and shear rate on the slip behaviour, as they are much easier to control to modify slip in applications.

1.5.1 Surface roughness

The effect of surface roughness on interfacial slip is a controversial issue with contradicting experimental and simulation findings.[45, 64, 72-74] It is commonly accepted that

a change in surface roughness may cause an inevitable change in surface wettability. If correlating the effect of surface roughness on wettability, it has been suggested that roughness reduces slip if the liquid totally wets the surface; while roughness increases the slip if it partially wets the surface or does not wet the surface, due to the formation of trapped gases or a vapour phase at the cavities and crevices of the surface.[7] However, some literature on interfacial slip contradicts the existence of this correlation between roughness and wetting properties of surface. A typical example is demonstrated by Bonaccurso *et al*.[72] In their experiment, large roughness generated extremely large slip on hydrophilic surfaces. However, later literature showed that the uncertainty in determining the zero position on the rough surface could lead to misinterpret the slip results.[45, 73] Joly *et al*.[64] investigated the role of roughness on the slip length and found that the addition of moderate roughness of 3 nm RMS on a OTS – coated surface reduces slip to no slip compared to a smooth OTS – coated surface. Yang [74]used non-equilibrium MD simulations to investigate the effect of surface roughness and interface wettability on the boundary condition of simple fluids in a nanochannel. He observed that the presence of surface roughness always suppresses the fluid slip on both hydrophilic and hydrophobic surfaces in nanochannels, which he thinks is due to an increase of drag resistance at the solid –fluid interface. Guriyanova *et al*.[45] found that liquid slip is not only influenced by the overall surface roughness, but also by the different length scale of the surface nanostructures. Molecular dynamics simulations that varied the size and spacing of the atoms of the solid (molecular level roughness) showed that for Lennard-Jones solid and fluid, slip was maximum when the size and spacing disparity was very large or very small, and that slip was a minimum when the solid and fluid were commensurate.[75]

1.5.2 Wetting

In most experimental and simulation studies, slip is observed on hydrophobic surfaces.[42, 48, 53, 56, 58-61, 64, 67] This could be directly explained by the strength of liquid-solid interactions. Many MD simulations see an increase in slip when the strength of the interaction potential between the liquid and wall solid molecules is reduced. In the real world, this molecular interaction is qualified by the liquid-solid contact angle, i.e. the wettability of the solid surface. A high contact angle is indicative of a weak interaction

between liquid and solid, which can be more easily overcome, causing the fluid molecules to slide across the solid. Many experiments performed at hydrophobised surfaces support this concept of hydrophobic slip. However, most of experimentally observed slip lengths are of the order of tens to hundreds of nanometres, which is much larger than the MD simulation results. One explanation for the discrepancy between simulations and experiments is the presence of a "gas cushion",[13] owing to the large viscosity ratio between liquid and air, which induces a large apparent slip length. Another reason could be the large discrepancy of shear rate used between experiments and MD simulations.[16] Even though liquid slip on hydrophobic surfaces is now widely accepted, there is no broad agreement of no-slip on hydrophilic surfaces,[15, 16, 41, 43-45, 47, 68] because in addition to wettability, many other delicate factors (as previously discussed) are involved and strongly connected in liquid slip on solid surfaces. On the other hand, it may be unjustifiable to extend conclusion from static measurements directly to dynamic flow conditions. It is possible that dynamic interactions could introduce subtle factors that alter the relation between wettability and slip, a factor which could explain the contradicting slip experimental reports in hydrophilic system. For example in the recent MD simulation, Ho *et al*.[68] suggested that if a hydrophilic surface can be manufactured with high density of adsorption sites close to each other, this would allows water molecules to easily migrate from one to the next, and liquid could slip on such hydrophilic surface. In this case, the dynamic contact angle hysteresis should be used instead of static contact angle to determine the hydrophobic VS hydrophilic character of the surface.

1.5.3 Slip Depends on Shear Rate

In the original Taylor model and the Vinogradova model, the slip length does not depend explicitly on shear rate. Some investigations agree with the constant slip length model. However, many measurements and simulations are in contrast with this idea; these results show that the slip length either increases or decreases with shear rate increasing. In Chapter 5, the shear rate dependence of the slip will be discussed in detail and experimental evidence and the numerical model will be provided to understand this slip behaviour.

References

1. Batchelor, G. K., *An Introduction to Fluid Dynamics*. Cambridge: UK, 1970.

2. Navier, C. L. M. H. Mémoire sur les lois du mouvement des fluides. *Mem. Acad. Sci. Inst. Fr.* **1823**, *6*, 389-416, 432-436.

3. Goldstein, S., Note on the condition at the surface of contact of a fluid with a solid body. In *Modern Developments in Fluid Dynamics*, Goldstein, S., Ed. The Clarendon press: Oxford, 1938; Vol. 2, pp 678-680.

4. Neto, C.; Evans, D. R.; Bonaccurso, E.; Butt, H. J.; Craig, V. S. J. Boundary slip in Newtonian liquids: a review of experimental studies. *Rep. Prog. Phys.* **2005**, *68*, 2859-2897.

5. Lauga, E.; Brenner, M. P.; Stone, H. A., Microfluidics: The No-slip Boundary Condition. In *Handbook of Experimental Fluid Dynamics*, Foss, J.; Tropea, C.; Yarin, A., Eds. Springer: New York, 2005; p Chapter 15.

6. Cao, B. Y.; Sun, J.; Chen, M.; Guo, Z. Y. Molecular momentum transport at fluid-solid interfaces in MEMS/NEMS: a review. *Int. J. Mol. Sci.* **2009**, *10*, 4638-4706.

7. Tsai, P.; Peters, A. M.; Pirat, C.; Wessling, M.; Lammertink, R. G. H.; Lohse, D. Quantifying effective slip length over micropatterned hydrophobic surfaces. *Phys. Fluids* **2009**, *21*, 112002.

8. Voronov, R. S.; Papavassiliou, D. V.; Lee, L. L. Review of fluid slip over superhydrophobic surfaces and its dependence on the contact angle. *Ind. Eng. Chem. Res.* **2008**, *47*, 2455-2477.

9. Bocquet, L.; Charlaix, E. Nanofluidics, from bulk to interfaces. *Chem. Soc. Rev.* **2010**, *39*, 1073-1095.

10. Tabeling, P. A brief introduction to slippage, droplets and mixing in microfluidic systems. *Lab Chip* **2009**, *9*, 2428-2436.

11. Honig, C. D. F.; Ducker, W. A. Thin film lubrication for large colloidal particles: experimental test of the no-slip boundary condition. *J. Phys. Chem. C* **2007**, *111*, 16300-16312.

12. Choi, C.-H.; Kim, C.-J. Large slip of aqueous liquid flow over a nanoengineered superhydrophobic surface. *Phys. Rev. Lett.* **2006**, *96*, 066001.

13. Vinogradova, O. I.; Belyaev, A. V. Wetting, roughness and flow boundary conditions. *Journal of Physics-Condensed Matter* **2011**, *23*, 184104.

14. Zhu, L. W.; Attard, P.; Neto, C. Reliable measurements of interfacial slip by colloid probe atomic force microscopy. I. Mathematical modeling. *Langmuir* **2011**, *27*, 6701-6711.

15. Zhu, L. W.; Attard, P.; Neto, C. Reliable measurements of interfacial slip by colloid probe atomic force microscopy. II. Hydrodynamic force measurements. *Langmuir* **2011**, *27*, 6712-6719.

16. Zhu, L. W.; Attard, P.; Neto, C. Reliable measurements of interfacial slip by colloid probe atomic force microscopy. III. Shear rate dependent slip *Langmuir* **2012**, *28*, 3465–3473.

17. Zhu, L.; Attard, P.; Neto, C. Reconciling slip Measurements in symmetric and asymmetric systems. *Langmuir* **2012**, *28*, 7768-7774.

18. Israelachvili, J. N., *Intermolecular and Surface Forces*. 3rd ed.; Acadamic Press: Waltham, MA, 2011.

19. Mie, G. Zur kinetischen Theorie der einatomigen Körper. *Annalen der Physik* **1903**, *11*, 657-697.

20. Erbil, H. Y., Surface chemistry of solid and liquid interfaces. In Blackwell Pub.: Oxford, UK, 2006.

21. Pashley, R. M.; Karaman, M. E., *Applied Colloid and Surface Chemistry*. Wiley: England, 2004.

22. Hamaker, H. C. The London–van der Waals attraction between spherical particles. *Physica* **1937**, *4*, 1058-1072.

23. Attard, P. Nanobubbles and the hydrophobic attraction. *Adv. Colloid Interface Sci.* **2003**, *104*, 75-91.

24. Christenson, H. K.; Claesson, P. M. Direct measurements of the force between hydrophobic surfaces in water. *Adv. Colloid Interface Sci.* **2001**, *91*, 391-436.

25. Hampton, M. A.; Donose, B. C.; Nguyen, A. V. Effect of alcohol-water exchange and surface scanning on nanobubbles and the attraction between hydrophobic surfaces. *J. Colloid Interface Sci.* **2008**, *325*, 267-274.

26. Attard, P.; Tyrrell, J. W. G. Atomic force microscope images of nanobubbles on a hydrophobic surface and corresponding force-separation data. *Langmuir* **2002**, *18*, 160-167.

27. Zhang, X. H.; Maeda, N.; Craig, V. S. J. Physical properties of nanobubbles on hydrophobic surfaces in water and aqueous solutions. *Langmuir* **2006**, *22*, 5025-5035.

28. Zhang, X. H.; Li, G.; Maeda, N.; Hu, J. Removal of induced nanobubbles from water/graphite interfaces by partial degassing. *Langmuir* **2006**, *22*, 9238-9243.

29. Zhang, X. H.; Quinn, A.; Ducker, W. A. Nanobubbles at the interface between water and a hydrophobic solid. *Langmuir* **2008**, *24*, 4756-4764.

30. Guyon, E.; Hulin, J.-P.; Petit, L.; Mitescu, C. D., *Physical Hydrodynamics*. Oxford University Press, : New York, 2001.

31. Brenner, H. The Slow Motion of a Sphere through a Viscous Fluid Towards a Plane Surface. *Chem. Eng. Sci.* **1961**, *16*, 242-251.

32. Horn, R. G.; Vinogradova, O. I.; Mackay, M. E.; Phan-Thien, N. Hydrodynamic slippage inferred from thin film drainage measurements in a solution of nonadsorbing polymer. *J. Chem. Phys.* **2000**, *112*, 6424-6433.

33. Vinogradova, O. I. Drainage of a thin liquid-film confined between hydrophobic surfaces. *Langmuir* **1995**, *11*, 2213-2220.

34. McHale, G.; Newton, M. I. Surface roughness and interfacial slip boundary condition for quartz crystal microbalances. *J. Appl. Phys.* **2004**, *95*, 373-380.

35. Ellis, J. S.; Hayward, G. L. Interfacial slip on a transverse-shear mode acoustic wave device. *J. Appl. Phys.* **2003**, *94*, 7856-7867.

36. Willmott, G. R.; Tallon, J. L. Measurement of Newtonian fluid slip using a torsional ultrasonic oscillator. *Phys. Rev. E* **2007**, *76*, 066306.

37. Choi, C. H.; Westin, K. J. A.; Breuer, K. S. Apparent slip flows in hydrophilic and hydrophobic microchannels. *Phys. Fluids* **2003**, *15*, 2897-2902.

38. Maali, A.; Wang, Y. L.; Bhushan, B. Evidence of the No-Slip Boundary Condition of Water Flow between Hydrophilic Surfaces Using Atomic Force Microscopy. *Langmuir* **2009**, *25*, 12002-12005.

39. Maali, A.; Cohen-Bouhacina, T.; Kellay, H. Measurement of the slip length of water flow on graphite surface. *Appl. Phys. Lett.* **2008**, *92*, 053101.

40. Stark, R.; Bonaccurso, E.; Kappl, M.; Butt, H. J. Quasi-static and hydrodynamic interaction between solid surfaces in polyisoprene studied by atomic force microscopy. *Polymer* **2006**, *47*, 7259-7270.

41. Sun, G. X.; Bonaccurso, E.; Franz, V.; Butt, H. J. Confined liquid: simultaneous observation of a molecularly layered structure and hydrodynamic slip. *J. Chem. Phys.* **2002**, *117*, 10311-10314.

42. Bhushan, B.; Wang, Y.; Maali, A. Boundary slip study on hydrophilic, hydrophobic, and superhydrophobic surfaces with dynamic atomic force microscopy. *Langmuir* **2009**, *25*, 8117-8121.

43. Bonaccurso, E.; Kappl, M.; Butt, H. J. Hydrodynamic force measurements: boundary slip of water on hydrophilic surfaces and electrokinetic effects. *Phys. Rev. Lett.* **2002**, *88*, 076103.

44. McBride, S. P.; Law, B. M. Viscosity-dependent liquid slip at molecularly smooth hydrophobic surfaces. *Phys. Rev. E* **2009**, *80*, 060601.

45. Guriyanova, S.; Semin, B.; Rodrigues, T. S.; Butt, H. J.; Bonaccurso, E. Hydrodynamic drainage force in a highly confined geometry: role of surface roughness on different length scales. *Microfluid. Nanofluid.* **2010**, *8*, 653-663.

46. Bowles, A. P.; Honig, C. D. F.; Ducker, W. A. No-slip boundary condition for weak solid-liquid interactions. *J. Phys. Chem. C* **2011**, *115*, 8613-8621.

47. Craig, V. S. J.; Neto, C.; Williams, D. R. M. Shear-dependent boundary slip in an aqueous Newtonian liquid. *Phys. Rev. Lett.* **2001**, *87*, 054504.

48. Cottin-Bizonne, C.; Cross, B.; Steinberger, A.; Charlaix, E. Boundary slip on smooth hydrophobic surfaces: Intrinsic effects and possible artifacts. *Phys. Rev. Lett.* **2005**, *94*, 056102.

49. Honig, C. D. F.; Ducker, W. A. Squeeze film lubrication in silicone oil: experimental test of the no-slip boundary condition at solid-liquid interfaces. *J. Phys. Chem. C* **2008**, *112*, 17324-17330.

50. Horn, R. G.; Smith, D. T.; Haller, W. Surface forces and viscosity of water measured between silica sheets. *Chem. Phys. Lett.* **1989**, *162*, 404-408.

51. Zhu, Y. X.; Granick, S. Rate-dependent slip of Newtonian liquid at smooth surfaces. *Phys. Rev. Lett.* **2001**, *87*, 096105.

52. Zhu, Y.; Granick, S. No-slip boundary condition switches to partial slip when fluid contains surfactant. *Langmuir* **2002**, *18*, 10058-10063.

53. Cottin-Bizonne, C.; Steinberger, A.; Cross, B.; Raccurt, O.; Charlaix, E. Nanohydrodynamics: The intrinsic flow boundary condition on smooth surfaces. *Langmuir* **2008**, *24*, 1165-1172.

54. Schmitz, R.; Yordanov, S.; Butt, H. J.; Koynov, K.; Dünweg, B. Studying flow close to an interface by total internal reflection fluorescence cross-correlation spectroscopy: Quantitative data analysis. *Phys. Rev. E* **2011**, *84*, 066306.

55. Yordanov, S.; Best, A.; Butt, H.-J.; Koynov, K. Direct studies of liquid flows near solid surfaces by total internal reflection fluorescence cross-correlation spectroscopy. *Optics Express* **2009**, *17*, 21149-21158.

56. Vinogradova, O. I.; Koynov, K.; Best, A.; Feuillebois, F. Direct measurements of hydrophobic slippage using double-focus fluorescence cross-correlation. *Phys. Rev. Lett.* **2009**, *102*, 118302.

57. Joseph, P.; Tabeling, P. Direct measurement of the apparent slip length. *Phys. Rev. E* **2005**, *71*, 035303.

58. Lasne, D.; Maali, A.; Amarouchene, Y.; Cognet, L.; Lounis, B.; Kellay, H. Velocity profiles of water flowing past solid glass surfaces using fluorescent nanoparticles and molecules as velocity probes. *Phys. Rev. Lett.* **2008**, *100*, 214502.

59. Huang, P.; Breuer, K., S. Direct measurement of slip length in electrolyte solutions. *Phys. Fluids* **2007**, *19*, 028104.

60. Bouzigues, C. I.; Tabeling, P.; Bocquet, L. Nanofluidics in the debye layer at hydrophilic and hydrophobic surfaces. *Phys. Rev. Lett.* **2008**, *101*, 114503.

61. Tretheway, D. C.; Meinhart, C. D. Apparent fluid slip at hydrophobic microchannel walls. *Phys. Fluids* **2002**, *14*, L9-L12.

62. Joseph, P.; Cottin-Bizonne, C.; Benoit, J. M.; Ybert, C.; Journet, C.; Tabeling, P.; Bocquet, L. Slippage of water past superhydrophobic carbon nanotube forests in microchannels. *Phys. Rev. Lett.* **2006**, *97*, 156104.

63. Byun, D.; Kim, J.; Ko, H. S.; Park, H. C. Direct measurement of slip flows in superhydrophobic microchannels with transverse grooves. *Phys. Fluids* **2008**, *20*.

64. Joly, L.; Ybert, C.; Bocquet, L. Probing the nanohydrodynamics at liquid-solid interfaces using thermal motion. *Phys. Rev. Lett.* **2006**, *96*, 46101.

65. Lumma, D.; Best, A.; Gansen, A.; Feuillebois, F.; Rädler, J. O.; Vinogradova, O. I. Flow profile near a wall measured by double-focus fluorescence cross-correlation. *Phys. Rev. E* **2003**, *67*, 056313.

66. Dammer, S. M.; Lohse, D. Gas enrichment at liquid-wall interfaces. *Phys. Rev. Lett.* **2006**, *96*, 206101.

67. Chinappi, M.; Casciola, C. M. Intrinsic slip on hydrophobic self-assembled monolayer coatings. *Phys. Fluids* **2010**, *22*, 042003.

68. Ho, T. A.; Papavassiliou, D. V.; Lee, L. L.; Striolo, A. Liquid water can slip on a hydrophilic surface. *Proc. Natl. Acad. Sci. U. S. A.* **2011**, *108*, 16170-16175.

69. Pahlavan, A. A.; Freund, J. B. Effect of solid properties on slip at a fluid-solid interface. *Phys. Rev. E* **2011**, *83*, 021602.

70. Harting, J.; Kunert, C.; Hyvaluoma, J. Lattice Boltzmann simulations in microfluidics: probing the no-slip boundary condition in hydrophobic, rough, and surface nanobubble laden microchannels. *Microfluidics and Nanofluidics* **2010**, *8*, 1-10.

71. Cho, J. H. J.; Law, B. M.; Rieutord, F. Dipole-dependent slip of Newtonian liquids at smooth solid hydrophobic surfaces. *Phys. Rev. Lett.* **2004**, *92*, 166102.

72. Bonaccurso, E.; Butt, H. J.; Craig, V. S. J. Surface roughness and hydrodynamic boundary slip of a Newtonian fluid in a completely wetting system. *Phys. Rev. Lett.* **2003**, *90*, 144501.

73. Vinogradova, O. I.; Yakubov, G. E. Surface roughness and hydrodynamic boundary conditions. *Phys. Rev. E* **2006**, *73*, 045302.

74. Yang, S. C. Effects of surface roughness and interface wettability on nanoscale flow in a nanochannel. *Microfluidics and Nanofluidics* **2006**, *2*, 501-511.

75. Galea, T. M.; Attard, P. Molecular dynamics study of the effect of atomic roughness on the slip length at the fluid-solid boundary during shear flow. *Langmuir* **2004**, *20*, 3477-3482.

Chapter 2 Experimental Methods

2.1 Atomic Force Microscopy

In this Thesis AFM was the main technique employed for both measurements of hydrodynamic forces and the imaging of the surface topography. In this Chapter we introduce the basic principles of force mode and imaging mode in AFM and briefly provide the most relevant experimental parameters and methods used in the following Chapters

2.1.1 Imaging mode

Atomic force microscopy (AFM) is a type of scanning probe microscopy, with high resolution of topographic analysis which can reach a subnanometre scale.[1] The basic principle of AFM is simple (A schematic representation of the technique is shown in Figure 2.1): a sharp tip reveals information on the surface, such as topography by scanning over it and interacting with the surface at short distances (<10 nm). The typical cantilevers used for scanning are made of silicon or silicon nitride, and have a tip with a radius in the order of nanometres at the end of the cantilever. A cantilever with a sharp tip is mounted on a piezoelectric crystal that can move the tip towards and away from the sample in the z direction above the sample surface, while the sample is mounted on another piezoelectric crystal moving in the *x*, *y* directions. This design is usually used in the top scanning AFM, such as Asylum AFM MFP-3D used in this Thesis. An alternative design is the bottom scanning AFM, such as Bruker (Veeco) AFM Multimode. In the bottom scanning design, a scanner piezo tube underneath the sample stage combines three piezoelectric crystals which move the sample in the *x*, *y* and *z* directions. When the tip is driven into the proximity of a sample surface, the interaction between the tip and the sample leads to a deflection of the cantilever which is sensed through a laser spot reflected off the back of the cantilever and monitored by a photodiode. Usually, a feedback loop is employed, which maintains the cantilever deflection constant by adjusting the cantilever up and down

using the *z* piezoelectric crystal as the sample is scanned in the *x*-*y* directions. The movements of the piezoelectric crystals in the *x*, *y* and *z* directions allow one to map the topography of the sample surface.

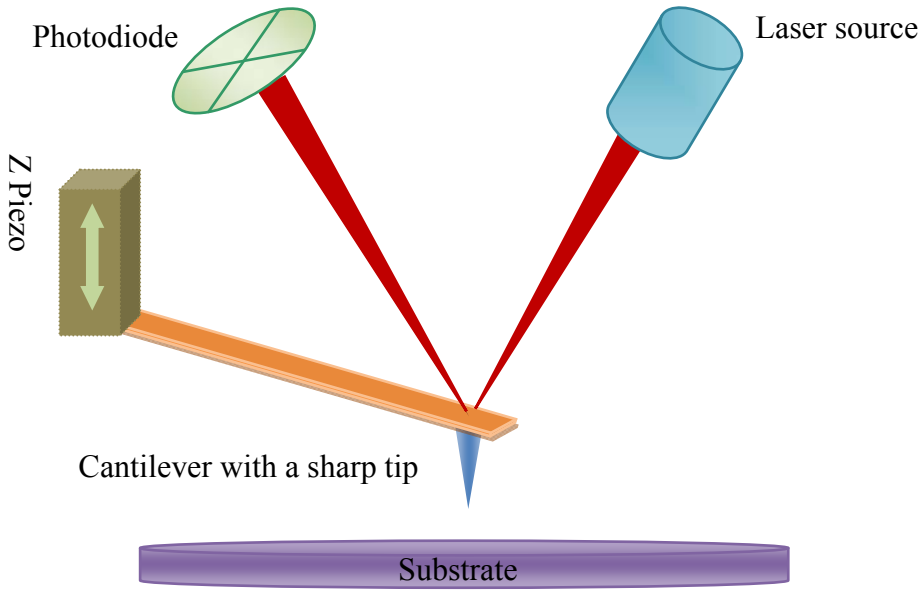

Figure 2.1 Schematic of a typical top scanning AFM setup. A piezoelectric crystal supports a cantilever, and drives the cantilever up and down according to the interaction between the cantilever tip and the sample surface. The deflection of the cantilever because of the interaction is amplified by the movement of a reflected laser spot on the photodiode.

For imaging applications, contact mode and tapping mode are the primary modes in the operation of AFM. In contact mode, the tip and sample surface are in contact, and the overall interaction force is repulsive. In tapping mode, the cantilever is driven to oscillate up and down at near its resonance frequency by a small piezoelectric crystal. The feedback loop adjusts the cantilever height to maintain a constant cantilever amplitude while the tip scans over the sample.

Due to the non-linear movement of the piezoelectric crystal, a sensor is applied to detect the deviation from an ideal piezo movement and corresponding corrections are made to the piezo driving signal. This design is known as a closed loop AFM, which ensures a constant piezo drive velocity, whereas the non-sensored piezo AFM is referred as an open

loop AFM. For hydrodynamic force measurements, the use of a closed loop AFM is particularly important to ensure that the piezo drive velocity is known and reproducible.

2.1.2 Force Mode

Besides operating in imaging mode, another major application of AFM is force spectroscopy, which directly measures interaction forces between the tip and the sample surface as a function of the separation between them. As in imaging mode, these interactions cause the cantilever to bend and the reflected laser moves up or down on the photodiode amplifying the deflection on the cantilever. In a typical force measurement, the cantilever with the tip is driven towards the surface at a certain velocity until it comes into contact, and then the cantilever is made to retract back from the surface to its starting position. A force measurement can be performed in either a static or dynamic mode. In the dynamic mode, the cantilever is oscillated by the piezoelectric crystal at a particular frequency during the whole force measurement. This dynamic mode was not used in our AFM hydrodynamic force measurements, but sometimes it is employed in the surface force apparatus. AFM force measurements have been applied to investigating both equilibrium surface forces, such as van der Waals, electric double layers, and hydrophobic force in liquids, and hydrodynamic forces. Equilibrium forces are typically measured at a very low drive velocity. Hydrodynamic forces depend explicitly on the driving velocity, and are often investigated at high velocities.

In this Thesis, the colloid probe technique[2, 3] was employed to measure hydrodynamic forces using an Asylum MFP-3D AFM at the static force mode. A colloid probe is a tipless cantilever with an attached silica microsphere and is typically used in hydrodynamic force measurements by AFM. Both colloid probe and investigated solid substrate are placed in the AFM liquid cell filled with a viscous liquid. During an experiment, the liquid is squeezed out of the gap between the microsphere and the solid surface when the colloid probe moves perpendicularly towards the flat solid substrate from a certain distance until the two surfaces are in contact (extension), and then the liquid fills back the gap when the colloid probe retracts away from the solid surface (retraction). At each extension and retraction, hydrodynamic forces acting on the microsphere causes

deflections of the cantilever. A series of piezoelectric driving velocities in the range of 10 – 80 μm/s were employed to investigate hydrodynamic forces. At each driving velocity, several (~10) repeat force measurements were completed. Raw cantilever deflection (signal in Volts) as a function of piezoelectric crystal displacement would be converted to hydrodynamic force versus separation distance between the microsphere and the flat surface, using a spreadsheet developed in this Thesis (the details of the raw data conversion are presented in Appendix 2). Important improvements to this conversion procedure are discussed in Chapter 4, Section 4.3.

Slip measurements by AFM are a delicate procedure severely influenced by contamination in the system. Therefore sample cleaning, as described in Section 2.4.1, is a critical step before any force measurements are taken. The fitting of the experimental hydrodynamic drainage force to derive a slip length requires accurate values of the microsphere radius R, the spring constant k, and the viscosity of liquid η. Usually these three parameters are obtained from independent measurements. The microsphere radius R can be indirectly calibrated by the AFM inverse imaging method or directly measured from scanning electron microscopy (SEM) images, as discussed in Section 2.2.2. The spring constant k can be calculated from the hydrodynamic drainage force method, the Sader method,[4, 5] or the thermal method,[6] all of which is explained in Section 2.2.3. The calibration of the viscosity of di-*n*-octylphthalate liquid is presented in Section 2.3.

2.2 Colloid Probes

The physical properties of the colloid probe are very important in AFM hydrodynamic drainage force measurements. The topography of the microsphere surface affects the behaviour of the measured force. The value of the spring constant of the colloid probe used for the force conversation determines the accuracy and reliability of the final force results. Therefore, the calibration of the colloid probe, including the spring constant and the topography of the microsphere, is necessary. In this section, the colloid probe preparation is described, and several methods of deriving the spring constant of the colloid probe and the topography of the microsphere are introduced.

2.2.1 The Preparation of the Colloid Probe

The cantilever used in the colloid probe technique is a tipless rectangular cantilever (NSC12/CSC12 series) from MikroMasch with 6 different cantilever arms, 3 tipless cantilevers (A, B, C) on one side of the chip, and the other 3 tipless cantilevers (D, E, F) on the other side. The silica microsphere (Duke Scientific, Palo Alto, CA) has a radius ~10 μm. The microsphere is picked up by a clean capillary under a microscope and carefully glued using a micromanipulator (Newport, 462-XYZ-M) at the end of the tipless cantilever. A scanning electron microscopy (SEM) micrograph of a typical colloid probe is shown in Figure 2.2a). A small amount of Araldite glue (epoxy adhesive) is put at the cantilever end prior to putting on the microsphere. The setup is schematically illustrated in Figure 2.2b.

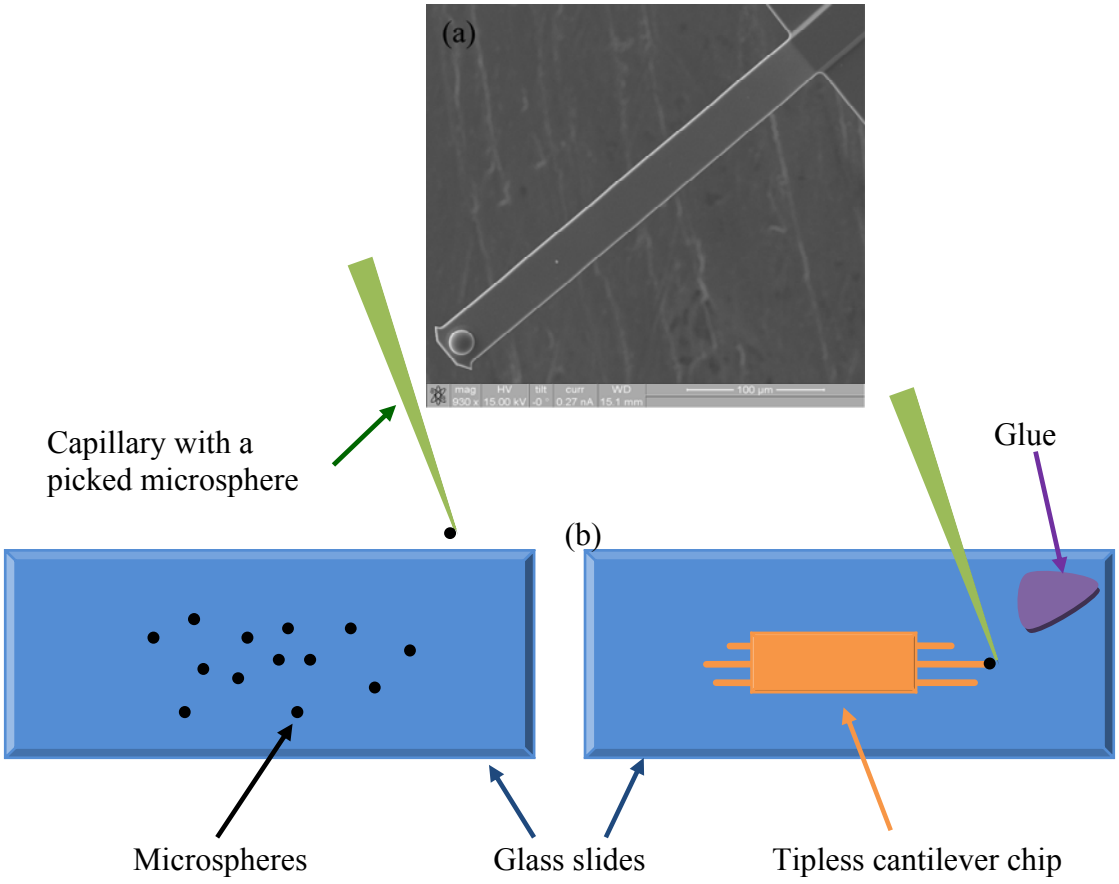

Figure 2.2 (a) A SEM image of a colloid probe (b) Schematic of a setup for preparing a colloid probe. Left: A clean capillary is picking up a microsphere from a glass side under a microscope (not to scale). Right: A microsphere is attached at a preferred cantilever end by glue (not to scale).

2.2.2 Characterisation of Colloid Probes

The radius of the microsphere R is an important parameter used in theoretical hydrodynamic drainage force calculations. The roughness of the microsphere surface can affect the measured hydrodynamic drainage forces and introduce an error in the actual slip length, due to an uncertainty in the determination of the separation between the rough microsphere surface and the flat surface (this issue is discussed in Chapter 4). Two calibration methods for colloid probes were employed in this Thesis to obtain information on the microsphere: an inverse AFM imaging method and SEM.

Inverse AFM Imaging of Colloid Probes

In the inverse AFM imaging method, a colloid probe (silica microsphere attached to the end of an AFM tipless cantilever) is made to scan a silicon calibration grating, TGT01(NT-MDT, Moscow), containing an array of sharp tips which are much sharper than the microsphere.[7] This scanning produces an AFM image that consists of arrays of spherical caps, shown in Figure 2.3. Each spherical cap in the image is an independent image of the same part of the microsphere made against the different sharp tips in the TGT01 grating. The imaged part of the microsphere will participate in the force measurement and interact with the flat substrate surface.

To obtain a reproducible force measurement, the colloid probe needs to be clean and smooth, so the imaged spherical cap must not present any asperity or “baby spheres”, as shown in Figure 2.3a. Any colloid probe that presented debris or defects on the top surface of the microsphere, as shown in Figure 2.3b, was rejected as unsuitable for use in force measurements. The average radius of the microsphere can be derived from the profile of the imaged microsphere by a cross section analysis shown in Figure 2.3c, either calculated from the measured width and height of each sphere cap in the profile image by an equation,[7] or obtained by fitting a circle for each microsphere cap.

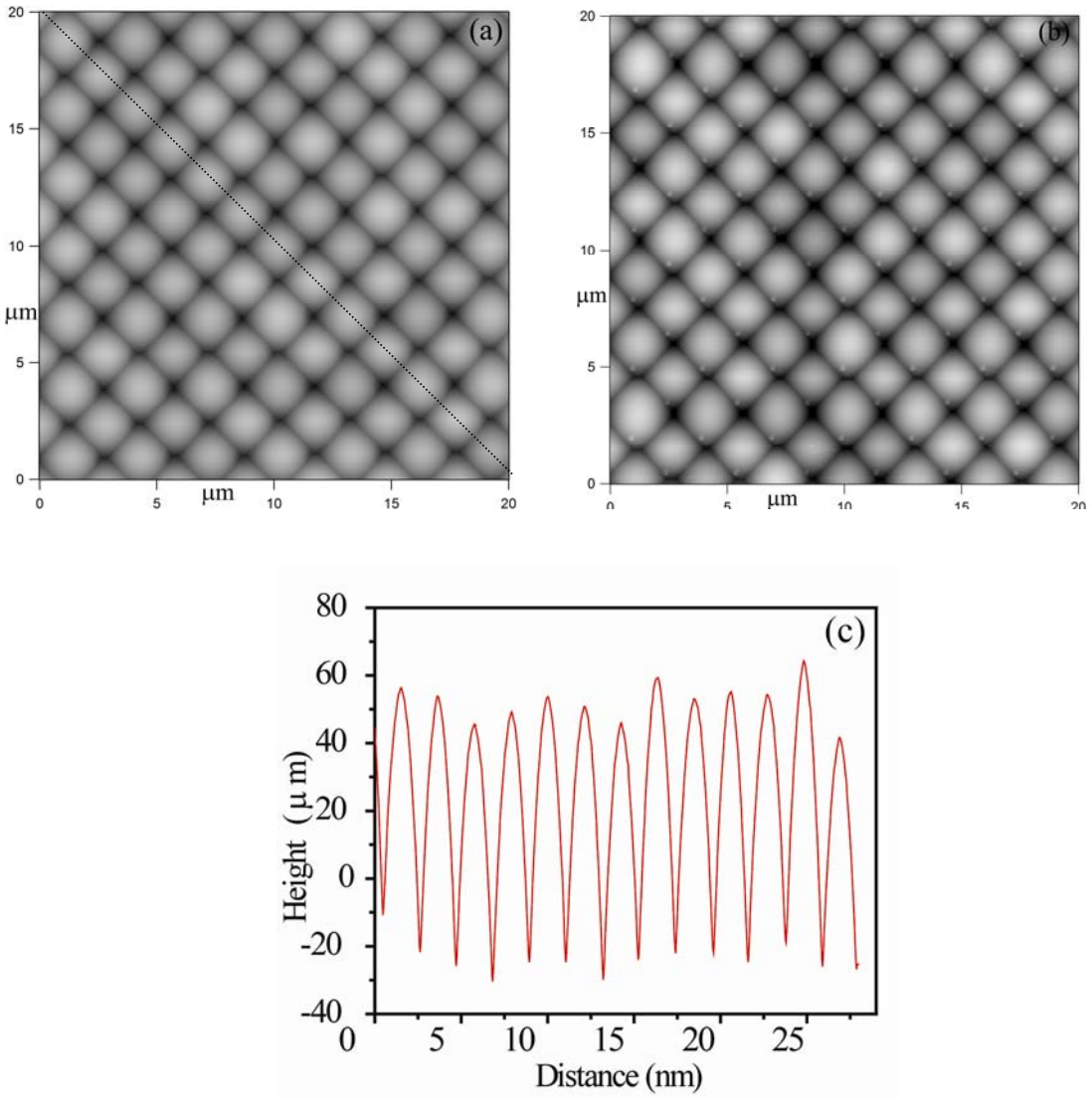

Figure 2.3 (a) AFM inverse image of a clean and smooth colloid probe, suitable for slip measurements. (b) A contaminated colloid probe, presenting a nanoparticle close to the apex of the microsphere. The height of the nanoparticle is about 20 nm. (c) Cross section profile of the imaged microsphere through the line drawn in (a). The scan parameters used for inverse imaging of the microsphere are: scan size 20 µm; set point 0.1 V; scan rate 1 Hz; integral gain 10.0; proportional gain 0.

SEM Imaging of Colloid Probes

An alternative method for the calibration of colloid probes is to use scanning electron microscopy (SEM). In conventional SEM, a focused electron beam scans across the sample surface in a series of parallel tracks. These high energy electrons interact with atoms at or near the sample surface to produce various types of signals including secondary electrons,

back-scattered electrons, X-rays and other luminescence. Corresponding detectors collect different signals and convert them into imaging signals, displayed on a screen.[8]

Secondary electrons come from the surface and very near the surface of the sample, thus the secondary electron image represents mostly topographic information. The surface features of the microsphere can be directly imaged by SEM using the secondary electron detector. Due to vacuum conditions and the usage of electrons in conventional SEM, all water must be removed from the samples. For conventional SEM sample surfaces have to be electrically conductive. Nonconductive samples tend to charge when hit by the electron beam, which causes scanning faults and other image artifacts, especially using the secondary electron mode. Therefore nonconductive sample surfaces are usually coated with a thin layer of conductive material by a sputter coater before scanning. By this way, colloid probes have to be calibrated after force measurements because a conductive coating is required to avoid charging. Microspheres are made of silica and cantilevers are made of silicon, but there is a native oxide layer on a silicon surface, which makes colloid probes nonconductive.

Since the invention of Environmental SEM (ESEM), the viewing of nonconductive or wet samples has become possible. Therefore, uncoated colloid probes can be imaged before force measurements by ESEM.[9] The instrument used in our experiments is a FEI Quantan 200 SEM, which is performed in ESEM mode with a gaseous secondary electron detector (GSED). The ESEM image of an uncoated probe is shown in Figure 2.4.

The geometry of a colloid probe, including the microsphere radius, the length and width of the cantilever and the cleanness of the microsphere, can be directly measured from SEM or ESEM images.

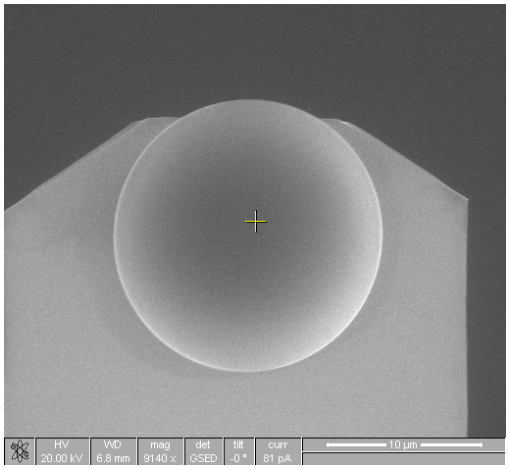

Figure 2.4 ESEM image of a silica microsphere attached to a tipless cantilever.

2.2.3 Calibration of the Cantilever Spring Constant

In an AFM force measurement, the force acting on the microsphere causes the deflection of the cantilever, which is amplified by the photodiode. The force F (nN) and the cantilever deflection x (nm) are related by Hooke's law $F = -kx$. In the equation the spring constant k (N/m) must be known accurately to obtain a reliable force. There are three independent ways to calibrate the spring constant of the cantilever (colloid probe), the thermal noise method,[6] the Sader method[4, 5] and the hydrodynamic method.[10]

Thermal noise method

The principle of the thermal noise method is to link the spring constant of the cantilever and its thermal motion to its thermal energy via the equipartition theorem,[6]

$$\frac{1}{2}k_B T = \frac{1}{2}k\left\langle \Delta z^2 \right\rangle \tag{2.1}$$

where k is the spring constant of the cantilever, Δz^2 is the mean-square deflection of fluctuations of the cantilever at its tip (cantilever vertical deflection signal), k_B is the Boltzmann constant, and T is the absolute temperature.

The traditional thermal noise method eliminates all vibrational modes, except the fundamental mode. This fundamental mode in the thermal noise power spectrum is fitted by the power response function $S(f)$ of a simple harmonic oscillator (SHO).[11] (Sometimes a

Lorentzian model is used, which gives a very similar result as the simple harmonic oscillator model). However the SHO model is only valid to describe the motion of the first vibrational mode of the cantilever, i.e. fundamental mode.

$$S(f) \cong P_{white} + \frac{P_{dc} f^4{}_R}{\left(f^2 - f^2{}_R\right) + \left(\frac{f\, f_R}{Q}\right)^2} \tag{2.2}$$

where P_{white}, P_{dc}, f_R and Q are fitting parameters.[12] f is the frequency in Hz, f_R is the resonance frequency in Hz, Q is the quality factor, P_{white} is a white-noise floor (V^2 Hz^{-1}), and P_{dc} is the dc power response (V^2 Hz^{-1}) of the cantilever measured from the photodetector[13]. The mean square deflection Δz^2 is measured by integrating the second term in Eq. 2.2 over all frequencies, i.e. integrating the fundamental resonance peak only (here the fundamental resonance peak normally refers to the first large thermal peak in the thermal spectrum). Incorporating this integration and the definition of the inverse optical lever sensitivity (*InvOLS*), the following result can be obtained[11]

$$\Delta z^2 = \frac{\pi}{2} InvOLS^2 f_R P_{dc} Q \tag{2.3}$$

InvOLS is the ratio of the cantilever deflection change Δz in nanometre (equal to the change of Z piezo position) to the measured photodiode signal change in voltage due to cantilever deflections ΔV ($InvOLS = \frac{\Delta z}{\Delta V}$) in the regime where the colloid probe and sample surface are in contact. This region is called the contact region. At this region, the deflection of the cantilever directly corresponds to the movement of the Z piezo. The value of the *InvOLS* can be derived from the inverse *slope* of the linear contact part of the raw force curve, and this force slop is also termed the "*compliance*", because the cantilever is the most compliant component of the system. This sensitivity is used to convert photodiode voltage signals (V) into cantilever deflections of nanometres (nm) before the colloid probe and the sample surface coming into contact which is called the non-contact region. Substituting Eq. 2.3 to Eq. 2.1, then gives the result:

$$k = \frac{2k_B T}{(InvOLS)^2 \pi f_R P_{dc} Q} \tag{2.4}$$

However, it is claimed by Proksch *et al*, that the values of the inverse OLS (*InvOLS*) are different depending on the cantilever has the force only acting at the end ($InvOLS_{\text{end}}$) or it vibrates freely in thermal motion ($InvOLS_{\text{free}}$).[14] A factor $\chi = InvOLS_{free} / InvOLS_{end} = 1.09$ is introduced to relate the two sensitivities.[15] The $InvOLS_{\text{end}}$ is from the slope of the contact region of the force curve obtained experimentally with an Asylum AFM MFP-3D. The calculated free $InvOLS_{\text{free}}$ is used for the spring constant calibration in Eq. 2.3 and Eq.2.4. However, it has been pointed out by Attard *et al.*[16] that there are several serious errors in the work of Walters *et al.*, who assumed a factor of χ = 1.09, which are repeated in the inbuilt software in the Asylum AFM, and which cause the deduced spring constant to be inaccurate. Attard *et al.*[16] presented measured data that showed that only the corrected thermal expression gives spring constants that were consistent in air and in water and that were in agreement with those obtained by other methods.

Sader method

The Sader method[4, 5] determines the spring constant of cantilevers by measuring the cantilever fundamental mode resonant frequency f_R and the quality factor of the cantilever Q in fluid (normally in air) and knowing its plan-view geometry (the length and width of the cantilever). This technique is restricted to a long rectangular cantilever with an idealised geometry in which the length of the cantilever greatly exceeds its width, and the width greatly exceeds its thickness. The calibration equation derived by Sader *et al*. is [5]

$$k = 0.1906 \rho_f w^2 L Q \Gamma_i(\text{Re})(2\pi f_R)^2 \tag{2.5}$$

where f_R *is* the fundamental mode resonant frequency in Hertz which is the same as in Eq. 2.4 in the thermal noise method (note that Sader used the radial frequency in his original formulas), Q is the quality factor in fluid which is also the same value used in Eq. 2.4, ρ_{f} is the density of the fluid in which the rectangular cantilever is immersed, w and L are the width and the length of the cantilever respectively. Γ_{i} is the imaginary part of the

hydrodynamic function depending on Reynolds number (Re) which is given by $\mathrm{Re} = 2\pi\rho_f f_R w^2/(4\eta_f)$, where η_f is the viscosity of the surrounding fluid (often air). The Sader method has been made available on a website where the calculation is performed by a Java applet and the downloadable Mathematica code is also provided. The hydrodynamic function calculation is automatically calculated by the Java program, and the details of its analytical expression can be found in Sader's paper.[5]

Hydrodynamic force method

The hydrodynamic force method involves obtaining the spring constant by fitting the experimental hydrodynamic drainage force at large separations with the theoretical hydrodynamic drainage no-slip force.[10] From the Vinogradova *f** equation, it can be shown explicitly that the influence of the slip length is negligible at large separations ($h >> b$), so the measured hydrodynamic drainage forces can be considered as no-slip forces. A satisfactory spring constant gives a good agreement between the theoretical no-slip hydrodynamic drainage force (from Taylor equation) and the measured experimental hydrodynamic drainage force at large separations. In this Thesis, the hydrodynamic method is the main method for calibrating the spring constant of the cantilever. The details of fitting the spring constant using this method are specified in Appendix 2.

2.3 Measurement of Viscosity

In earlier work,[17, 18] two-component solutions, such as a sucrose aqueous solution, were used as a viscous liquid to measure hydrodynamic forces. These liquids are agued to be not ideal, because segregation and adsorption of the sucrose on the surface might cause a viscosity discrepancy between the surface region and the bulk. This could be the cause of the apparent slip length. Here a one-component liquid with high viscosity (di-*n*-octylphthalate, Aldrich, 98% pure, distilled before use) was used to measure hydrodynamic forces, which avoids the risk inhomogeneity in the viscosity at the solid surface.

As liquid viscosity varies with temperature, and liquid viscosity is an important parameter in calculating the theoretical hydrodynamic force. The temperature of the liquid

was monitored throughout the AFM experiment *in situ* to get accurate viscosity values. Because of the heating of electronic components during AFM force measurements, the liquid temperature in the liquid cell slightly increased over the course of an experiment. An example of how the liquid temperature varied with time during one experiment is shown in Figure 2.5. The viscosity changed slightly during measurements depending on the temperature in the liquid cell, which was affected by the room temperature, the temperature of the AFM head and the bottom scanner. The change in temperature of the liquid ranged from 1.5 – 3°C during a typical experiment. In order to obtain the accurate viscosity of the liquid (di-*n*-octylphthalate), a thermocouple (Mineral insulated thermocouple, 1.5 mm diameter × 150 mm long, with type T miniature plug, from TC Direct Australia) connected to a thermometer (YC-717, from TC Direct Australia) was placed through one of the ports of the liquid cell to record the temperature continuously during the measurements, as shown in Figure 2.6.

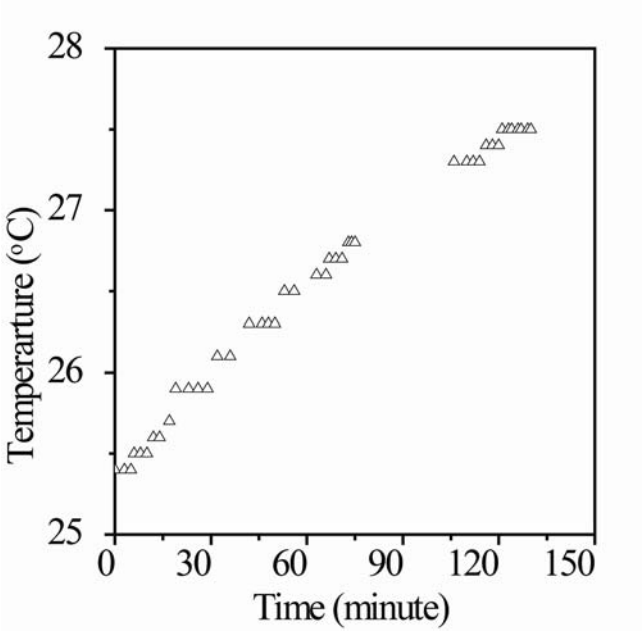

Figure 2.5 Typical example of the liquid (di-*n*-octylpthalate) temperature in the liquid cell during force measurements in one experiment

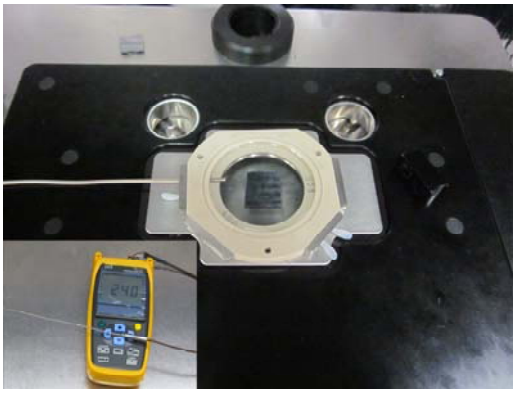

Figure 2.6 Asylum AFM liquid cell with an inserted thermocouple to measure the temperature of the liquid in the cell. Inset: Thermocouple with thermometer.

In this work, a U-tube viscometer (Ubbelohde viscometer, Koehler, Size 2) was used to measure *ex situ* the liquid viscosity as a function of temperature, see Figure 2.7. This viscometer consists of a big lower reservoir bulb in one arm, an upper measuring reservoir bulb with a thin capillary in another arm and a third arm extending from the end of the capillary and open to the atmosphere.

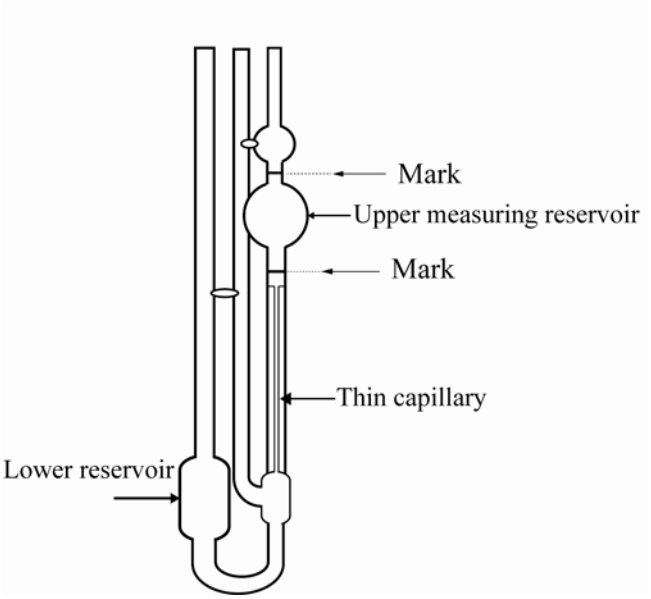

Figure 2.7 Schematic of an Ubbelohde viscometer. The liquid is sucked from the lower reservoir to the upper reservoir by a pipette bulb. Then the liquid flows back from the upper reservoir through the thin capillary to the lower reservoir. The time taken for the liquid to pass through the two marks on the upper reservoir is measured.

The viscometer was placed inside a constant temperature bath to equilibrate the liquid temperature in the lower reservoir. The liquid was drawn up from the lower reservoir through the capillary into the upper reservoir using suction and then allowed to flow down through the capillary back to the lower reservoir. The time taken for the liquid to fall back down between the two calibrated marks on the upper reservoir was measured. The dynamic viscosity was calculated by

$$\eta = K\rho t \tag{2.6}$$

where K was a constant for the particular viscometer, which depends on its geometry. K is 0.0979 for the viscometer used in our work. ρ is the density of the liquid, and t is the measured time.

The dependence of the viscosity of di-*n*-octylpthalate on temperature was calibrated by the Ubbelohde viscometer, as presented by filled squares in Figure 2.8. The relationship between the viscosity (η in Pas) of di-*n*-octylphthalate and the temperature (T in Kelvin) (in the temperature range of 19 ~ 27^{o}C) could be fitted using a linear regression by the equation

$$\mathrm{Ln}\,\eta = -20.66 + 5302/T \tag{2.7}$$

Alvarez *et al*, fitted the relationship between the temperature and the viscosity of di-*n*-octylphthalate by the equation[19]

$$\mathrm{Ln}\,\eta = -21.17 + 5450/T. \tag{2.8}$$

The literature values calculated by Eq. 2.8 in the same experimental temperature range are plotted in Figure 2.8 as empty circles and compared to our experimental obtained values. It is shown that our experimental values are closely related to the literature values.

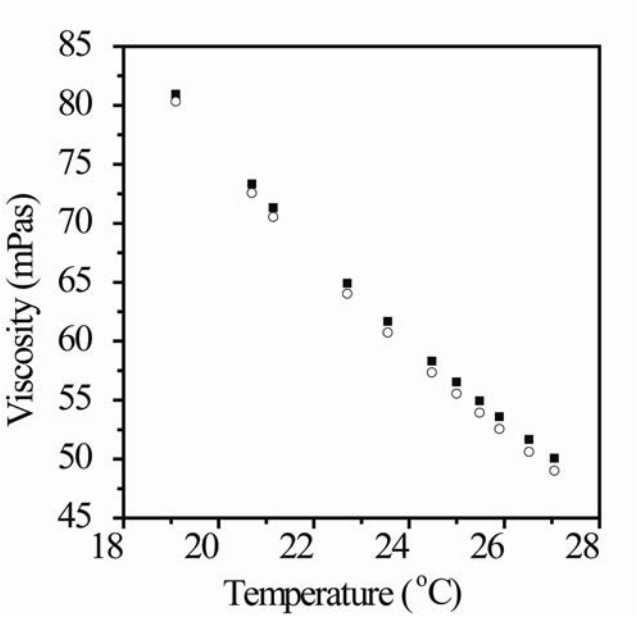

Figure 2.8 Viscosity – temperature relationship for di-*n*-octylpthalate. Filled squares represent experimentally measured viscosities. Empty circles represent the predicted viscosities with the equation by Alvarez *et al*.[19]

2.4 Sample Preparation and Characterisation

Two different types of solid surfaces, hydrophilic and hydrophobic in nature, were involved in the investigation of liquid slip on the solid surface in this Thesis. In this section, the sample preparation including the cleaning procedure, and the silanisation of the sample surface are discussed, as well as the characterisation of the sample surface, which includes the measurement of surface wettability by goniometry and the thickness of the silane layer on the solid surface by ellipsometry.

2.4.1 Cleaning Procedure

The cleaning procedure for force measurements is very important. In order to get reproducible results, we strictly followed the cleaning procedure discussed below before force measurements for all samples, colloid probes and the liquid cell used in the AFM force measurement. Most steps of the cleaning procedure were completed on a laminar flow bench to reduce particle contamination. Before cleaning, all tweezers used were sonicated in distilled acetone and blow dried using high purity nitrogen. Plain silicon

wafers and self-assembled monolayers (SAM)-coated silicon wafers (octadecyltrichlorosilane (OTS) SAM and dichlorodimethylsilane (DCDMS) SAM) were the main surfaces used in the hydrodynamic force measurements. These surfaces were sonicated in the distilled ethanol and acetone for 1 minute each, and blown dried with nitrogen, followed by CO_2 snow-jet cleaning. (The details of the CO_2 treatment and the principle are presented in Appendix 1) All plain silicon wafers were also exposed to a radio-frequency generated, low-temperature air plasma (PDC-32G-2 Harrick Plasma) as the last step, but not the silanised samples. Plasma treatment removed residues of organic contamination by oxidizing the surface of the material.[20] All colloid probes were only cleaned by plasma treatment before use, except silanised ones. The AFM liquid cell and tubing were cleaned by sonication in distilled ethanol and dried by nitrogen. Because of the poor chemical resistance of the O-ring (Viton) on the bottom side of liquid cell and the membranes (Viton), use of acetone was not recommended. The glass disk in the liquid cell was subjected to the same procedure as the plain silicon wafers.

2.4.2 Silanisation of Silicon Wafers and Colloid Probes from Vapour Phase

Organosilanes are commonly used for surface coatings and modification. During the silanisation process, smooth self-assembled monolayers (SAMs) can be grown on surfaces that have mineral components such as mica, glass, silicon, and metal oxide surfaces, in liquid phase or vapour phase. The most commonly used silanes are chlorosilane-based, such as octadecyltrichlorosilane (OTS) and dichlorodimethylsilane (DCDMS), which were used in our experiments. However, silanisation is problematic due to the ready formation of oligomers, so well-controlled conditions are necessary for obtaining homogenous SAMs.[21-24] In this section we discuss the preparation of DCDMS coatings on silicon surfaces by vapour phase silanisation process. The preparation of OTS coating was performed by C. Neto according to a published protocol.[22]

Plain silicon wafers and colloid probes were cleaned by the cleaning procedure presented above and then placed a Teflon base inside a 50ml glass container (Figure 2.9). The container was flushed with nitrogen gas for 5 minutes to remove oxygen and humidity,

and then droplets of a volatile silane (DCDMS typically 300 µl) were injected into the bottom of container without touching colloid probes and silicon wafers. The sealed container was kept at room temperature for 2-3 hours, allowing silane vapours to react with the surface of the silicon wafer and silica colloid probe surfaces.

After silanisation, the lid was left open in the fume hood for 1 hour to eliminate residues of silane. Then silicon wafers and colloid probes were removed from the glass container and immersed in hexane to remove unbound silane. Silanised silicon wafers can be further sonicated in hexane or acetone for a more aggressive rinsing. Finally, silanised silicon wafers and colloid probes were dried with nitrogen and stored for future use. The uniformity of the coating and the cleanliness of the surfaces were inspected by AFM imaging in Tapping mode, as shown in Figure 2.10.

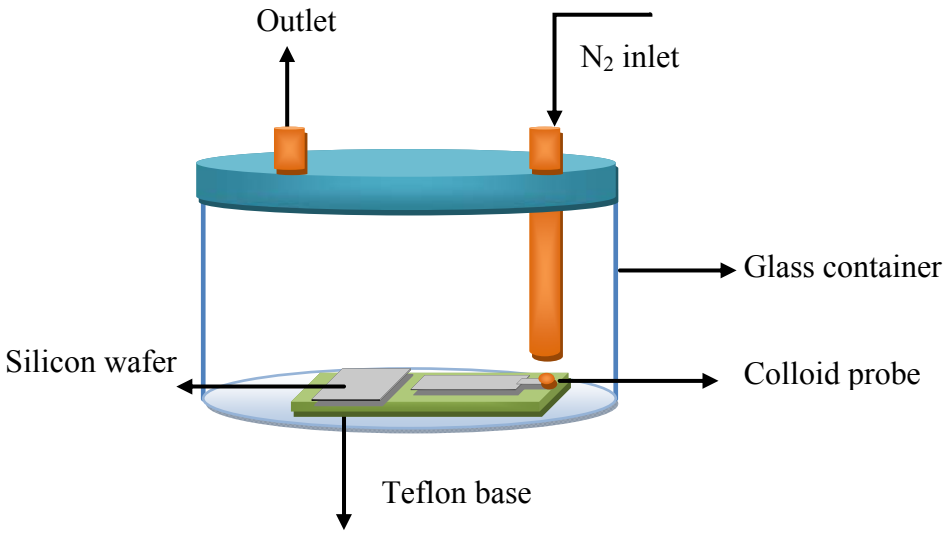

Figure 2.9 Sketch of the 50 ml glass container used for silanisation of silicon wafer and colloid probes by silane vapour. Silicon wafers and colloid probes are placed on the bottom of container. N_2 is flushed through the cell to remove O_2 and humidity. The silane agent is introduced through the outlet and placed on the bottom of the container after 5 minutes N_2 blow. The container is sealed for 2-3 hours for silanisation.

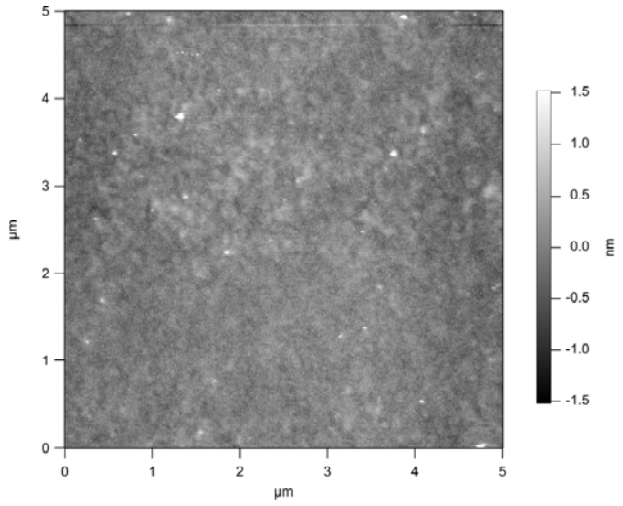

Figure 2.10 AFM image of a DCDMS-coated silicon wafer prepared in vapour phase. The coating surface was cleaned by the sonication of hexane, ethanol and acetone respectively, dried by pure N_2 and followed by CO2 snow-jet clean procedure at the final step before imaging. The RMS roughness value is 229 pm (5 µm × 5 µm).

2.5 Characterisation of Surface Wettability

A silane self-assembled monolayer on a silicon surface creates a new interface with low surface energy, which shows low wettability. Wettability refers to how a liquid placed on a solid substrate spreads out.[25] The wettability of a solid by a liquid can be quantitatively measured in terms of the contact angle of the liquid on the solid surface. If a contact angle is less than 90°, the liquid is said to wet the solid surface, and such a surface is said to be solvophilic (or hydrophilic surface if the solvent is water). If the contact angle of the liquid is greater than 90°, the liquid is said to not wet the surface as the liquid prefers to minimise the contact area with the surface and form a liquid hemispherical droplet. Such a surface is called solvophobic (or hydrophobic surface if the solvent is water). If the contact angle is greater than 150°, such a surface is defined as super-solvophobic (or superhydrophobic surface if the solvent is water). A schematic of the contact angle of a liquid on different surfaces is shown in Figure 2.11a. Contact angle can be measured on static and dynamic droplets. A static contact angle is measured on a constant volume droplet; a dynamic contact angle is found by increasing or decreasing the volume of the droplet, and measuring the maximum (*advancing contact angle* θ_A) and minimum (*receding contact angle* θ_R), respectively (Figure 2.11b). The advancing contact angle θ_A is

determined at the moment just before the three-phase contact line of the droplet on the solid surface moves outward as the volume of the droplet is increased. The receding contact angle θ_R is determined at the moment just before the three-phase contact line moves inward as the volume of the droplet is decreased. The advancing contact angle is always larger than or equal to the receding contact angle ($\theta_A > \theta_R$). The difference between the advancing and receding contact angles is termed contact angle hysteresis, and can be used to characterise surface heterogeneity and roughness.

The static contact angle, advancing and receding contact angles of any liquid droplet on a solid surface can be measured by a contact angle goniometer and characterised by fitting the Young-Laplace equation to the shape of the droplet.

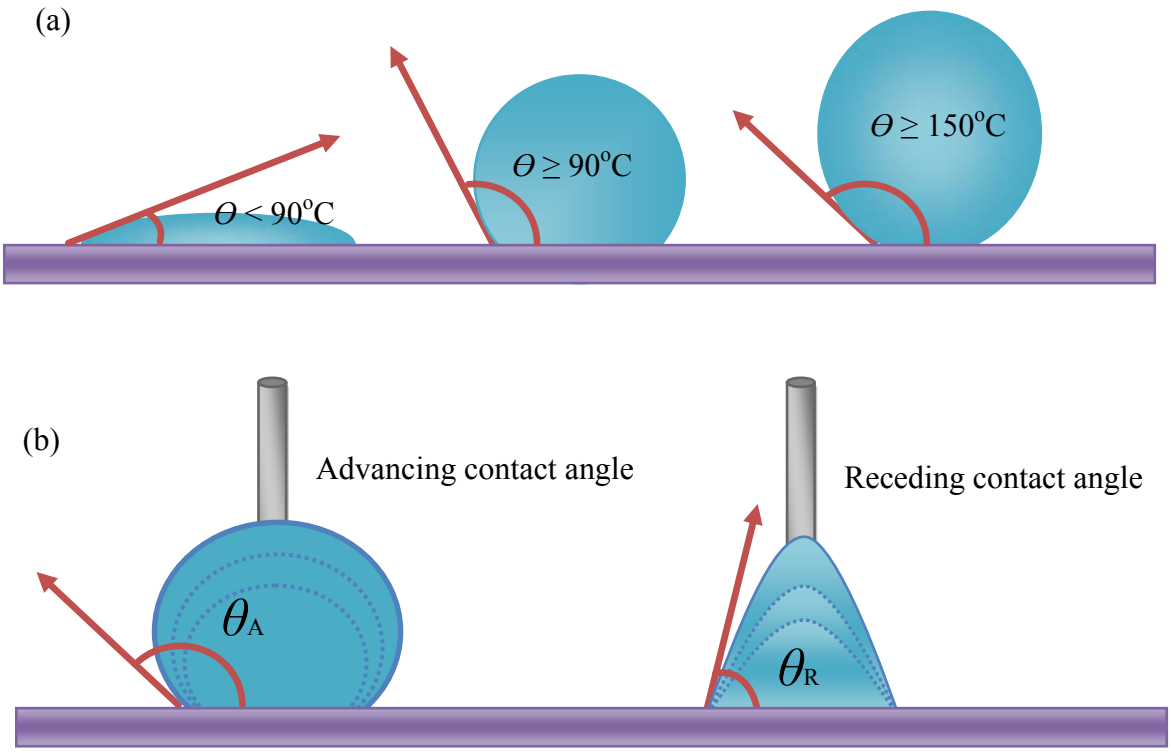

Figure 2.11 (a) Schematic of contact angles of a liquid on surfaces with different wettability. Solvophilic surface: θ < 90°C; solvophobic surface: $\theta \geq$ 90°C; super-solvophobic $\theta \geq$ 150°C. (b) Schematic of the advancing contact angle and the receding contact angle

Plain silicon wafer, OTS-coated and DCDMS-coated silicon wafers were used in the experiments. The advancing and receding water contact angles on OTS and DCDMS-

coated silicon wafers were measured by goniometry. The static contact angle of di-*n*-octyphthalate (D-*n*-OP) on the plain silicon wafer and OTS and DCDMS-coated silicon wafers were also measured by goniometry. The results are shown in Table 2.1. Dynamic contact angles of di-*n*-octylphthalate on the silanised surfaces were difficult and are not reported, due to the high viscosity of this solvent. For a correct measurement of advancing contact angle, a large enough drop is required to reduce the effect of the adhesion on the needle. Therefore in practice, a 5 μl droplet is first formed on the solid surface while the syringe needle remains in the droplet and then the droplet volume is increased at 0.2 μl/s by another 5 μl to measure the advancing contact angle. For a receding contact angle measurement, 5 μl of liquid is sucked through the need at 0.2 μl/s from a 10 μl droplet.

Table 2.1 Contact angles results on the three solid surfaces

	Advancing θ_A (water)	**Receding θ_R (water)**	**Static θ (D-*n*-OP)**
Plain silicon	<5º	<5º	21º ± 2º
OTS–coated silicon	113º	108º	45º± 1º
DCDMS–coated silicon	109 º	102 º	48º ± 1º

2.6 Ellipsometric Measurement of the Thickness of Self-assembled Monolayers (SAM)

Ellipsometry is a non-destructive optical technique, which is primarily used to determine thin film thickness and sample optical constants (refractive index and extinction coefficient). It is also applied to characterise chemical composition, crystallinity, surface roughness, and other material properties associated with a change in optical response.[26]

The principle of ellipsometry is to measure the change in the polarisation state of light upon its reflection from (or transmission through) a material structure. The ellipsometer model M-2000V from J.A.Woollam Co. Inc. used in our lab has a rotating

analyser ellipsometer design, shown in Figure 2.12 Unpolarised light produced by a light source becomes linearly polarised light after passing through a polariser. The linearly polarized light reflects off the sample surface as polarized light, and then enters a continuously rotating analyser. The detector converts the captured light to an electronic voltage signal to determine the polarisation state of the reflected light. The change in polarization caused by the sample reflection is determined by comparing the known input of linearly polarized light before hitting the sample to the output after reflection. The polarization change is represented as an amplitude ratio ψ, and a phase difference, Δ. A layer model can be constructed to describe the sample by predicting the measured quantities (ψ and Δ) in terms of the optical constants, the thickness of each layer and the polarizer and analyzer azimuthal angle. The thickness of silicon oxide layer on the silicon was determined previously to be 0.33 nm by ellipsometry. The thicknesses of OTS and DCDMS SAM layers on the silicon oxide surfaces were characterised by ellipsometry in the range of 370–1000 nm wavelength, at an incident angle of 75°. The schematic of ellipsometry is shown in Figure 2.12 and the measured results are shown in Table 2.2.

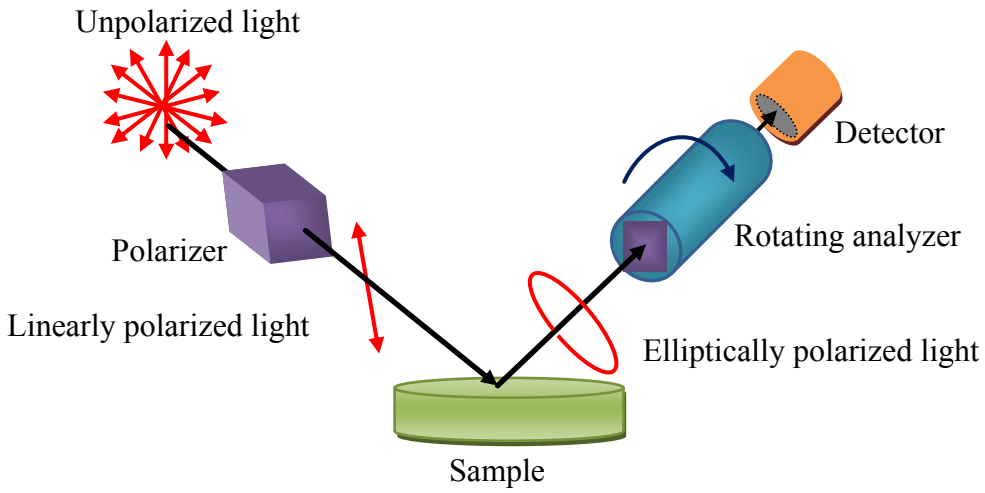

Figure 2.12 Schematic setup of an ellipsometry experiment. A linearly polarized light generated by a polarizer is incident on a sample. The light is reflected off the sample surface with different state of polarization through a rotating analyzer and finally converted into the information of the investigated surface by a detector. This Schematic is adapted from http://www.jawoollam.com/.

Table 2.2 Thickness and refractive index of the OTS and DCDMS SAM on silicon wafers

Silane	Thickness of SAM layers	Refractive Index
Silicon oxide layer	1.0 nm	1.458
OTS	2.7 ± 0.1 nm	1.440
DCDMS	2.4 ± 0.01 nm	1.485

References

1. Binnig, G.; Quate, C. F.; Gerber, C. Atomic force microscope. *Phys. Rev. Lett.* **1986**, *56*, 930-933.

2. Butt, H. J. Electrostatic interaction in atomic force microscopy. *Biophys. J.* **1991**, *60*, 777-785.

3. Ducker, W. A.; Senden, T. J.; Pashley, R. M. Direct measurement of colloidal forces using an atomic force microscope. *Nature* **1991**, *353*, 239-241.

4. Sader, J. E.; Larson, I.; Mulvaney, P.; White, L. R. Method for the calibration of atomic force microscope cantilevers. *Rev. Sci. Instrum.* **1995**, *66*, 3789-3798.

5. Sader, J. E.; Chon, J. W. M.; Mulvaney, P. Calibration of rectangular atomic force microscope cantilevers. *Rev. Sci. Instrum.* **1999**, *70*, 3967-3969.

6. Hutter, J. L.; Bechhoefer, J. Calibration of atomic-force microscope tips. *Rev. Sci. Instrum.* **1993**, *64*, 1868-1873.

7. Neto, C.; Craig, V. S. J. Colloid probe characterization: radius and roughness determination. *Langmuir* **2001**, *17*, 2097-2099.

8. Joseph Goldstein, D. E. N., David C. Joy , Charles E. Lyman , Patrick Echlin , Eric Lifshin , Linda Sawyer , Joseph R. Michael, *Scanning Electron Microscopy and X-ray Microanalysis*. 3rd ed.; Kluwer Academic/Plenum Publishers: New York, 2003.

9. Stokes, D. J., *Principles and Practice of Variable Pressure: Environmental Scanning Electron Microscopy (VP-ESEM)*. Wiley: UK, 2008.

10. Craig, V. S. J.; Neto, C. In situ calibration of colloid probe cantilevers in force microscopy: hydrodynamic drag on a sphere approaching a wall. *Langmuir* **2001**, *17*, 6018-6022.

11. Higgins, M. J.; Proksch, R.; Sader, J. E.; Polcik, M.; Mc Endoo, S.; Cleveland, J. P.; Jarvis, S. P. Noninvasive determination of optical lever sensitivity in atomic force microscopy. *Rev. Sci. Instrum.* **2006**, *77*, 013701.

12. Somasundaran, P., *Encyclopedian of Surface And Collid Science*. 2 ed.; CRC Press: New York, 2006; p 852-853.

13. P_{dc}, i.e. DC Power Response, cannot be found in the Asylum AFM Force Panel. Only the Thermal DC can be found in the Force Panel. Thermal DC =SQRT(DC Power Response)×AmpInvOLS.

14. Proksch, R.; Schaffer, T. E.; Cleveland, J. P.; Callahan, R. C.; Viani, M. B. Finite optical spot size and position corrections in thermal spring constant calibration. *Nanotechnology* **2004**, *15*, 1344-1350.

15. Walters, D. A.; Cleveland, J. P.; Thomson, N. H.; Hansma, P. K.; Wendman, M. A.; Gurley, G.; Elings, V. Short cantilevers for atomic force microscopy. *Rev. Sci. Instrum.* **1996**, *67*, 3583-3590.

16. Attard, P.; Pettersson, T.; Rutland, M. W. Thermal calibration of photodiode sensitivity for atomic force microscopy. *Rev. Sci. Instrum.* **2006**, *77*, 116110.

17. Craig, V. S. J.; Neto, C.; Williams, D. R. M. Shear-dependent boundary slip in an aqueous Newtonian liquid. *Phys. Rev. Lett.* **2001**, *87*, 054504.

18. Bonaccurso, E.; Butt, H. J.; Craig, V. S. J. Surface roughness and hydrodynamic boundary slip of a Newtonian fluid in a completely wetting system. *Phys. Rev. Lett.* **2003**, *90*, 144501.

19. Alvarez, G. A.; Lodge, A. S.; Cantow, H. J. Inertial contributions to the pressure in the truncated-cone-and-plate apparatus with application to dilute polymer-solutions. *Rheol. Acta* **1985**, *24*, 377-384.

20. Liston, E. M.; Martinu, L.; Wertheimer, M. R. Plasma surface modification of polymers for improved adhesion: a critical review. *J. Adhes. Sci. Technol.* **1993**, *7*, 1091-1127.

21. Wasserman, S. R.; Tao, Y.-T.; Whitesides, G. M. Structure and reactivity of alkylsiloxane monolayers formed by reaction of alkyltrichlorosilanes on silicon substrates. *Langmuir* **1989**, *5*, 1074-1087.

22. Brzoska, J. B.; Ben Azouz, I.; Rondelez, F. Silanization of solid substrates: a step towards reproducibility. *Langmuir* **1994**, *10*, 4367-4373.

23. Fadeev, A. Y.; McCarthy, T. J. Self-assembly is not the only reaction possible between alkyltrichlorosilanes and surfaces: monomolecular and oligomeric covalently attached layers of dichloro- and trichloroalkylsilanes on silicon. *Langmuir* **2000**, *16*, 7268-7274.

24. Zhuang, Y. X.; Hansen, O.; Knieling, T.; Wang, C.; Rombach, P.; Lang, W.; Benecke, W.; Kehlenbeck, M.; Koblitz, J. Vapor-phase self-assembled monolayers for anti-stiction applications in MEMS. *J Microelectromech S* **2007**, *16*, 1451-1460.

25. de Gennes, P.-G.; Brochard-Wyart, F.; Quéré, D., *Capillarity and Wetting Phenomena: Drops, Bubbles, Pearls, Waves*. Springer: New York, 2004.

26. Fujiwara, H., *Spectroscopic Ellipsometry: Principles and Applications*. Wiley: Chichester, 2007.

Chapter 3 Mathematical Modeling of Hydrodynamic Forces

3.1. Introduction

Colloid probe AFM can be used to measure the hydrodynamic drainage force when a liquid is squeezed out of the space between a colloid probe and a flat solid surface (Figure 3.1).[1] The slip length is deduced from the fit of the experimentally derived force with the slip and no-slip theoretical hydrodynamic drainage forces. An exact calculation of the hydrodynamic drainage force acting on a microsphere in a Newtonian liquid under the no-slip boundary condition was provided by Brenner.[2] A simple approximate equation attributed to Taylor describes this force when the microsphere is approaching a flat wall perpendicularly,[3]

$$F_{\mathrm{h}} = \frac{-6\pi\eta R^2 \dot{h}}{h} (h << R), \tag{3.1}$$

where η is the viscosity of the fluid, R is the radius of the microsphere, h is the separation, which is the distance of closest approach of the sphere to the substrate surface, and $\dot{h}$ is the velocity of the microsphere relative and perpendicular to the substrate, ($\dot{h}$ <0 corresponds to decreasing separation and $\dot{h}$ >0 corresponds to increasing separation). This equation is an approximation that is valid when the separation between the two surfaces h is smaller than the radius of the microsphere R.

Under a slip boundary condition, Vinogradova[4] introduced a correction factor f^* that depends upon the slip length b. In symmetric systems, the correction is:

$$F_h = \frac{-6\pi\eta R^2 \dot{h}}{h} f^* \ (h << R) \tag{3.2}$$

with $f^* = \frac{h}{3b}\left[\left(1+\frac{h}{6b}\right)\ln\left(1+\frac{6b}{h}\right)-1\right]$. (3.3)

For a no-slip boundary condition $f^*=1$ and for a slip boundary condition $f^*<1$.

The large majority of publications investigating liquid flow in confined geometries in the past decade have measured some degree of slip in partially wetting or non-wetting systems, with a slip length typically around tens of nanometres.[3, 5-9] However, there are discrepancies in the magnitude of the published slip length, with some well-cited cases maintaining that the no-slip boundary condition is generally applicable.[10, 11]

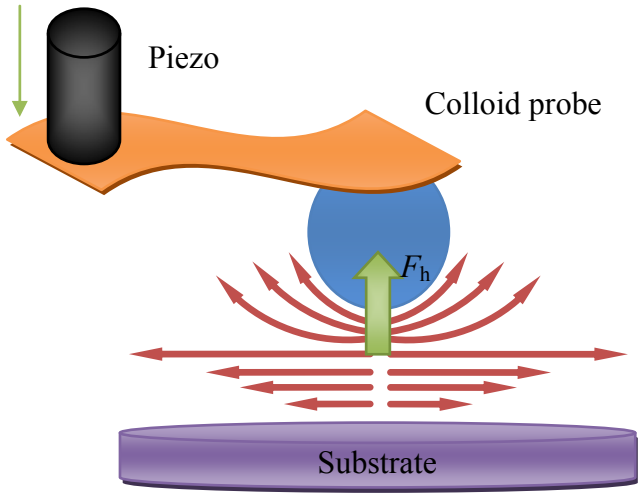

Figure 3.1 Schematic of a hydrodynamic force measurement by colloid probe AFM.

In the case of AFM experiments, it has been suggested that there may be limitations in the experimental procedure, for example, nonlinearity in the piezo-drive speed and position,[12] variations in the liquid viscosity in liquid mixtures, particle contamination on the substrate surface,[11] and restrictions in the force analysis and theoretical fitting, such as excessive approximation in estimating the drag component on the cantilever,[13] the presence of virtual deflection,[11, 14, 15] and increased noise from using experimental velocities in the fitting.[1, 16] Recent observations that the measured slip length depends on the cantilever geometry[16] and spring constant[17] further question the reliability of AFM slip measurements.

In this Chapter, a mathematical algorithm is presented, which more reliably fits the hydrodynamic drainage forces measured by AFM. This new algorithm was calculated independently of the experimental data, and significantly reduces the noise due to the

experimental cantilever velocity and separation used in the previous theoretical force calculation. This algorithm numerically solves differential equations by a simple stabilised single-step method that is a variant of the Leap frog or Verlet integration algorithm for solving differential equations, and is more stable than the Euler method.[18] This algorithm is suitable for use in a spreadsheet, and is much easier and convenient for fitting experimental data compared to other methods which have used mathematical software and multistep processes.[13, 17, 19] We calculated the mathematical algorithm for the exact drag force varying with the movement of cantilever in a force measurement; we investigated how using the commonly used approximate drag force and our new exact drag force affects the measured slip length as a function of the cantilever type. We also simulated other factors that might possibly cause artificial slip lengths using our new mathematical algorithm, such as the flattening of the microsphere due to wear and the presence of particulate contaminants on the substrate surface. The extent to which these factors influence the fitting of the slip length to the experimental results is demonstrated in this Chapter. In Chapter 4 we employed this new mathematical algorithm to fit new colloid probe AFM experiments and investigate interfacial slip.

3.2 Theoretical Modeling of the Hydrodynamic Force

In many published AFM papers,[1, 10, 11, 15, 16, 20-23] in order to derive the slip length, the colloid probe velocity $\dot{h}$ deduced from the difference in successive experimentally measured separations is used either in the theory[1, 16] or in scaling the experimental data,[10, 11, 15, 20-23] which introduces large errors and shows noise. (See Figure 3.2a for the noise introduced into theoretical curves.) In this way, an accurate value of the slip length is not easy to determine because of noise in the modeling or in the scaled experimental data. To increase the accuracy of the fitting procedure, a theoretical hydrodynamic force that is independent of actual experimental data is obtained by the method described below. In this method, the velocity $\dot{h}$ is predicted by calculating the tip motion of the AFM cantilever at each time step due to the influence of the drainage force.

The mathematical calculations presented in Sections 3.2.1, 3.4 and 3.6, including the FORTRAN code in Appendix 2, were originally derived by A/Prof. Phil Attard, and tested and modified by Ms Liwen Zhu.

3.2.1 Mathematical Calculations for the Algorithm for Hydrodynamic Forces

I. Basic Force Balance

In a typical measurement of hydrodynamic forces by colloid probe AFM, four basic forces are measured: the hydrodynamic drainage force F_h acting on the microsphere, the drag force F_d acting on the cantilever, the van der Waals force F_v at small sphere–surface separations, and the restoring force of the cantilever F_k. (In our one-component Newtonian liquid system, di-*n*-octylphthalate, there is no electric-double-layer force). The force acting on the microsphere when the colloid probe moves in a Newtonian liquid in a quasi-steady state can be described at any time t by

$$F_v(t) + F_d(t) + F_h(t) + F_k(t) = 0. \tag{3.4}$$

van der Waals Force

The van der Waals force for a sphere–flat geometry is[24]

$$F_v = \frac{-RA}{6h^2}\left(1 - \frac{S^6}{4h^6}\right). \tag{3.5}$$

where, A is the Hamaker constant, typically 10^{-22}~10^{-19} J, and S, which comes from a Lennard-Jones intermolecular potential, sets the range of the repulsion between the two solid surfaces and avoids producing a divergent force.[25] In the present modeling, this was fixed at $S = 0.5$ nm.[24]

Drag force on the cantilever

The Stokes drag force acting on the cantilever is given by

$$F_d = -6\pi\eta L_e \dot{z}, \tag{3.6}$$

Here, the cantilever velocity is taken to be constant and equal to the piezo-crystal driving velocity $\dot{z}$. L_e is the effective drag length of the cantilever, and its value depends on the shape and the dimension of the cantilever. In our experiments performed with rectangular cantilevers, the effective drag length is less than the physical length of the cantilever because the actual drag force is distributed over the entire cantilever, and using an effective drag length is a way of treating the force as if it were concentrated at the tip like the other force. The drag length can be determined experimentally from each measurement, together with the spring constant, by fitting the experimental force curve with the no-slip theoretical force at large separations (typically around 4 to 5 μm from contact).[26] The effective drag length should be independent of the drive speed, and we have confirmed experimentally that this is the case, which provides an additional check of the correct fitting procedure. The Stokes drag force mentioned here is a constant force. In Section 3.6, the exact variable drag force acting on the cantilever will be discussed.

Hydrodynamic Drainage Force between two surfaces

The drainage force acting on the sphere approaching the flat surface is[4]

$$F_h = \frac{-6\pi\eta R^2 \dot{h}}{h} f^* \tag{3.7}$$

As mentioned in Eqs 3.2 and 3.3, $f^* = 1$ for the no-slip boundary condition and $f^* < 1$ for the slip boundary condition.

Restoring Force of the Cantilever

Hooke's law describes the restoring force of the cantilever as Eq. 3.8

$$F_k = -kx \tag{3.8}$$

Here x is the deflection of the cantilever at any time t and k is the spring constant of the cantilever.

After substituting Eqs 3.5, 3.6, 3.7 and 3.8 into Eq. 3.4, the restoring force of the cantilever in a quasi-steady state is given by

$$F_k = -kx = \frac{6\pi\eta R^2 \dot{h}}{h} f^*(h/b) + 6\pi\eta L_e \dot{z} + \frac{RA}{6h^2}\left(1 - \frac{S^6}{4h^6}\right) . \quad (3.9)$$

II. Theoretical Deflection

According to the equation of uniformly accelerated linear motion, the deflection of the cantilever *x'* at a time (t+Δt) can be described by

$$x' = x + \dot{x}\Delta t + \frac{\ddot{x}\Delta t^2}{2} \approx x + \dot{x}\Delta t . \quad (3.10)$$

Here, x and $\dot{x}$ are the deflection and deflection velocity of the cantilever at time t respectively, and both are assumed to be known. $\ddot{x}$ is the acceleration of the cantilever, and Δt is the time step, which is discussed in detail later. The acceleration term is negligible for a small enough time step.

III. Theoretical Deflection Velocity

At each time step, the velocity needs to be updated. If the velocity of the cantilever $\dot{x}'$ at the time step (t+Δt) was known, then a more accurate estimation of the position would be

$$x' = x + \frac{1}{2}\Delta t\left[\dot{x} + \dot{x}'\right]. \quad (3.11)$$

This expression is obtained by writing the acceleration above as $\ddot{x} = (\dot{x}' - \dot{x})/\Delta t$. This equation is the key to the stability of the algorithm now given. This deflection would also satisfy the force balance condition (i.e. Eq. 3.9). Therefore, the deflection of the cantilever at the time step (t+Δt) can be expressed by

$$x' = -\frac{6\pi\eta R^2 \dot{h}'}{k\,h'} f^*(h'/b) - \frac{6\pi\eta L_e \dot{z}}{k} - \frac{RA}{6k h'^2}\left(1 - \frac{S^6}{4h'^6}\right) \quad (3.12)$$

We solve the equations of motion by simple time stepping. At time *t,* the microsphere–surface separation is $h(t) = x(t) + z(t)$, and the rate of change of separation (or relative microsphere velocity) is $\dot{h}(t) = \dot{x}(t) + \dot{z}(t)$. The drive position of the piezo-crystal $z(t)$ is specified in advance. Normally, $\dot{z}(t)$ has a fixed velocity that can be taken

from experiment. One has $\dot{z}(t) < 0$ for the extension and $\dot{z}(t) > 0$ for the retraction, Eq.3.12 then becomes:

$$x' = -\frac{6\pi\eta R^2(\dot{z}+\dot{x}')}{k(x'+z')} f^*(h'/b) - \frac{6\pi\eta L_e \dot{z}}{k} - \frac{RA}{6k(x'+z')^2}\left(1 - \frac{S^6}{4(x'+z')^6}\right), \tag{3.13}$$

where for the no-slip boundary condition f^*=1, and for the slip boundary condition f^* is a function of *h'* and slip length. The next deflection velocity can be obtained by rearranging Eqs 3.11 and 3.13,

$$\dot{x}' = -\frac{-x - \frac{\Delta t}{2}\dot{x} - \frac{6\pi\eta R^2 \dot{z}}{k(x'+z')} f^*(h'/b) - \frac{6\pi\eta L_e \dot{z}}{k} - \frac{RA}{6k(x'+z')^2}\left(1 - \frac{S^6}{4(x'+z')^6}\right)}{\frac{\Delta t}{2} + \frac{6\pi\eta R^2}{k(x'+z')} f^*(h'/b)}. \tag{3.14}$$

This completes the new deflection x' (obtained from Eq. 3.10) and new deflection velocity $\dot{x}'$ (obtained from Eq. 3.14) in the new time step, and the algorithm is ready for the next time, $t''= t+2\Delta t$.

IV. Initial Conditions for No-slip and Slip Boundaries

As discussed above, all calculations are based on assuming that the initial conditions (i.e. deflection x_0 and $\dot{x}_0$) are known. For a complete AFM force measurement, the piezo-crystal always approaches the surface (extension) first and then retracts back from contact to the initial starting separation (retraction). At large separations, the effect of slip on the hydrodynamic drainage force is negligible (f^*=1), so at the start time step, the initial conditions for no-slip and slip are the same. In the present modeling, the algorithm commences with the extension from large separations. At the initial time, the cantilever deflection velocity is very small, close to zero $\dot{x}_0 \to 0$. The initial microsphere velocity $\dot{h}_0$ can be taken to be approximately equal to the piezo-crystal driving velocity $\dot{z}$. The initial separation h_0 is approximately equal to the starting piezo-position z_0 ($h_0 \approx z_0$, initial deflection x_0 is negligible). Here, the initial separation h_0 can be set to any reasonable value similar to the experimental starting separation. Therefore, the initial deflection x_0 can be obtained from Eq. 3.13 by

$$x_0 = -\frac{6\pi\eta R^2 \dot{z}}{k h_0} - \frac{6\pi\eta L_e \dot{z}}{k} - \frac{RA}{6k h_0^{\,2}}\left(1 - \frac{S^6}{4h_0^{\,6}}\right). \tag{3.15}$$

For the retraction process, the calculations of the deflection and deflection velocity are the same as those for extension. The initial deflection x_{0r} and deflection velocity $\dot{x}_{0r}$ for retraction are set equal to the final deflection and deflection velocity values at the end of the extension.

V. Choice of Time Step

The choice of time step is vital to the stability of the modeling. It depends on the separation and the piezo-crystal driving velocity. A variable time step is used in the algorithm. For small separation or a large driving velocity, the change in cantilever deflection is very fast and a small time step is needed for accurate results. At large separation, a larger time step should be used. In the present modeling, the time step ranged between about 10^{-4} and 10^{-6} s.

For N time steps, with the piezo-crystal initial position z_0 and the piezo-crystal final position z_N, the total time for one extension trip is determined by the piezo-crystal driving distance (z_0-z_N) and velocity $\dot{z}$, and is

$$T = \frac{z_0 - z_N}{\dot{z}}. \tag{3.16}$$

As mentioned above, when the cantilever contacts the surface, the separation is $h(t) = z(t)+x(t) = 0$, $z(t) = -x(t) <0$. Therefore, the piezo-crystal final position z_N should be set a negative value (in our present simulations z_N is set –20 to –200 nm).

The first time step is Δt_1, the number of data points is N (N= 5991 in our modeling), the initial time is $t_0 = 0$. Each new time step is decreased from the previous time step by a constant factor of $\Delta t_{n+1} = (1 - f)\,\Delta t_n$. A value of $f = 0.001 – 0.0005$ was found to give stable results. Hence, the nth time step is

$$\Delta t_n = \Delta t_1 (1 - f)^{n-1} \quad (1 \le n \le N) \tag{3.17}$$

The total time is then:

$$T = t_0 + \Delta t_1 + \Delta t_2 + \cdots + \Delta t_n = \frac{\Delta t_1 [1-(1-f)^{N-1}]}{f} \tag{3.18}$$

Eqs 3.16 and 3.18 can be rearranged to give the first time step

$$\Delta t_1 = \frac{(z_0 - z_N) f}{\dot{z}\,(1-(1-f)^{N-1})}. \tag{3.19}$$

The first time step is included in Eq. 3.17 to give any time step. For the retraction, the time steps are used in the reverse order of those for the extension. The time steps are always positive for both extension and retraction. The reason for formulating the time step algorithm in this fashion is that it enables a stable numerical procedure, because in the large separation and the slow velocity regime, a large time step is needed, and in the small separation and fast velocity regime, a small time step is better, whereas the simplest form of time stepping (i.e. the constant time step) is unstable.

3.2.2 Comparison between the Previous and the New Algorithm

As we mentioned above, using the experimental velocity $\dot{h}$ introduces noise into the theoretical modeling, as shown in Figure 3.2a. If the force is normalised by velocity to eliminate noise from the theory, then the noise is transferred to the experimental data.[16] The improved theoretical modeling with the predicted velocity $\dot{h}$ is illustrated in Figure 3.2b. Hydrodynamic drainage forces under the no-slip and slip boundary conditions are presented by dashed and solid lines, respectively, in Figure 3.2b. The results show that the improved theoretical curves are much smoother than the previous one, especially at small separations, which is the important range for determining the slip length.

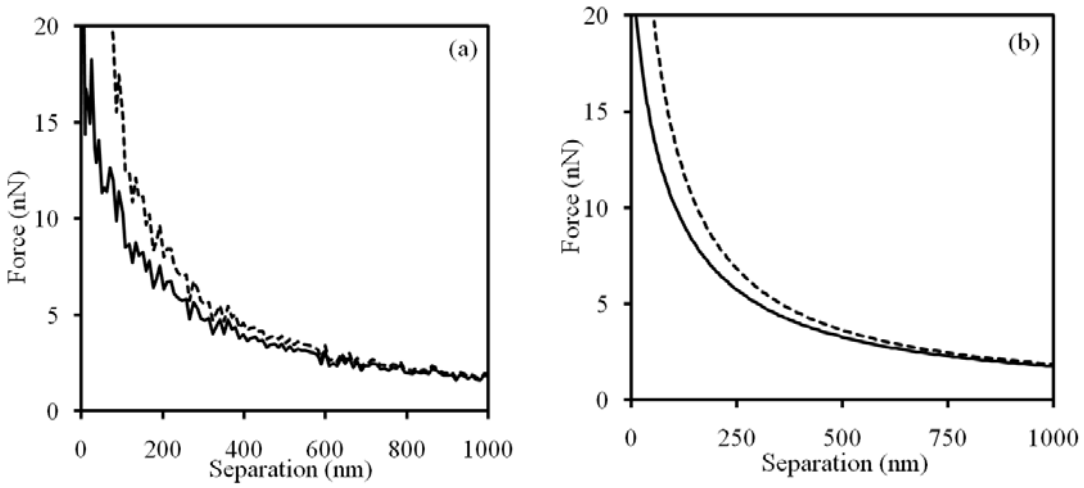

Figure 3.2 (a) Theoretical modeling of the hydrodynamic drainage force acting on a sphere approaching a flat surface calculated using the experimentally measured finite velocity $\dot{h}'$. The theory is affected by noise. (b) Theoretical modeling of the hydrodynamic drainage force calculated by the new mathematical algorithm. The dashed line represents the no-slip hydrodynamic drainage force. The solid line represents the slip hydrodynamic drainage force. In both models, the spring constant is 0.25 N/m, the viscosity is 61.7 mPa s, the piezo-crystal driving velocity is 15.2 μm/s; the slip length in a and *b* is 30 nm.

3.2.3 Blind Test on Our New Mathematical Algorithm

In colloid probe AFM force measurements, the spring constant can be obtained by fitting the experimental force with the theoretical hydrodynamic drainage modeling at large separation regimes.[26] We have been able to estimate the accuracy of the fitting procedure for the slip length and the spring constant with our model by using a blind test. In the blind test, a theoretical hydrodynamic drainage force was generated with added noise (the same as or larger than the experimental noise) and was treated as an experimental force to be fitted by our algorithm. This generated experimental curve was analysed by someone who was not privy to the improved theoretical parameters. The fitted slip length and spring constant were compared to the actual slip length and spring constant used to generate the theoretical force. In Figure 3.3, six different cases of blind test results are shown. The noise applied to the generated force curves is 0.5 nm in deflection, which is the same as the noise in the experimental deflection except in the circled case, where the noise was twice as large (1 nm). The error in the spring constant was estimated in the blind

test as a standard deviation of three fits performed over different separation regimes, typically at 5000 – 4000 nm, 5000 – 3000 nm and 5000 – 2000 nm. The error in the slip length is a standard deviation of slip lengths obtained as a consequence of the choice of the spring constant. By this blind test, we estimated that our modeling determines the fitted slip length with an average error of 2 nm and the fitted spring constant with a 3% error. This error is the sum of systematic error resulting from the visual fitting and statistical error due to the experimental noise. It can be seen in Figure 3.3 that the errors estimated by the blind fitter (the error bars) are quite close to the actual errors in the fitted slip length and spring constant.

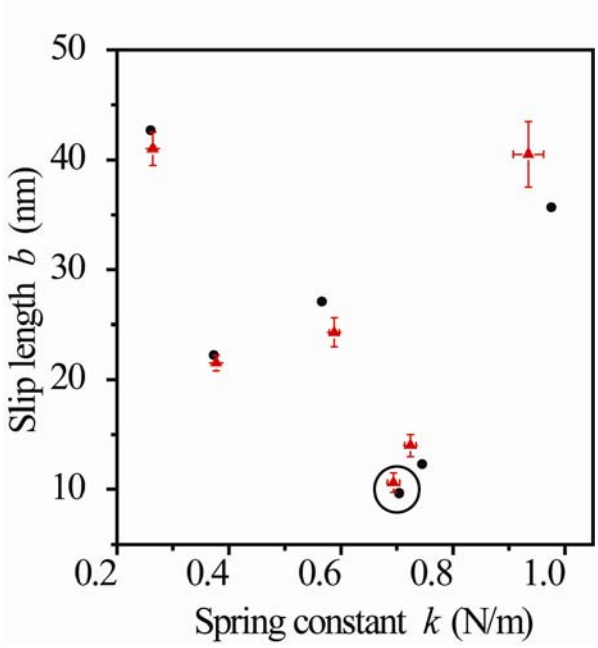

Figure 3.3 Results of the blind test for the estimation of the spring constant and slip length in six different cases. The filled red triangles are the fitted spring constants and slip lengths with corresponding errors. The filled black circles are the actual spring constants and slip lengths used to generate the theoretical curves. In the circled case, the noise in the generated force is 1 nm for deflection. In the remaining cases, the noise in the generated force is 0.5 nm for deflection, which is the same as in the experiments. The error bars are discussed in the text.

3.3 Comparison of Brenner and Taylor Hydrodynamic Drainage Force Equations

In the force measurement, the drag force on the cantilever and the spring constant k of the cantilever can be obtained from the region of the force curve at large separations, where the slip hydrodynamic drainage force can be neglected, using a modification of the hydrodynamic method described previously.[26] The larger the separation, the more negligible the slip, and consequently the more accurate the drag force and the spring constant that are obtained. The fitted slip length is dependent upon the accuracy of the drag force and the spring constant, which suggests using a large z-piezo driving distance and large separations (in AFM experiments, larger than 4 μm). However, the Taylor equation (Eq. 3.1) is considered to be accurate when the separation h is much smaller than the radius of the microsphere. (The microsphere radius is typically around 10 μm.) These are contradictory requirements for the separation that can be used. In literature[16] as well as in our own experiments, in order to obtain a more accurate drag force and spring constant, the maximum driving distance is chosen to be close to the microsphere radius or half of the radius. The validity of the Taylor solution is questionable in such a case. In the following, the approximate Taylor solution and the exact Brenner[2] solution (valid for any separation h) are compared to determine the discrepancies between them at such large separations.

Brenner[2] has derived an exact hydrodynamic force equation in Newtonian fluids under the no-slip boundary condition:

$$F = -6\pi\eta R\dot{h}\lambda . \tag{3.20}$$

λ is an infinite series:

$$\lambda = \frac{4}{3}\sinh\alpha\sum_{n=1}^{\infty}\left(\frac{n(n+1)}{(2n-1)(2n+3)}\left[\frac{2\sinh(2n+1)\alpha+(2n+1)\sinh 2\alpha}{4\sinh 2(n+1/2)\alpha-(2n+1)2\sinh 2\alpha}-1\right]\right).$$

Here, $\alpha = \cosh^{-1}(d/R)$, where d is the distance from the centre of the microsphere to the flat surface ($d = h + R$). For the separation with h tending to infinity, λ tends to 1 and the Brenner equation (Eq. 3.20) simply reduces to the Stokes equation, $F = -6\pi\eta R\dot{h}$, which shows that the Brenner equation (Eq. 3.20) is the sum of the hydrodynamic drainage

force and the drag force on the microsphere. However, the Taylor equation (Eq. 3.1) gives the pure hydrodynamic drainage force. To compare the Brenner and Taylor models, we must remove the drag force from the Brenner model, and our plot of the Brenner hydrodynamic drainage force is $F_h = -6\pi\eta R\dot{h}(\lambda - 1)$. The theoretical hydrodynamic drainage forces calculated by the Brenner and Taylor equations in the separation range of 0 to 10 μm (the microsphere radius is 9.5 μm) are shown in Figure 3.4a. It can be seen that at large separations the Taylor force is slightly smaller than the Brenner force. However, at small separations the Taylor force (solid line) is generally close to the Brenner force (dashed line). The relative error in the two forces is plotted in Figure 3.4b: the error decreases with decreasing separation. The relative error at a separation of 10 μm is about 11%, and at a separation of 5 μm it is about 9.5%. However, the absolute error between the two force curves in Figure 3.4a is approximately 0.1 nm over the separation range of 5–10 μm, which is much smaller than the deflection noise (about 0.5 nm) obtained from the actual force measurements using the same cantilever spring constant of 0.562 N/m. Hence, it can be concluded that the Taylor equation is able to predict the hydrodynamic drainage force in this separation range with an acceptable error, and it is not necessary to use the exact expression of the Brenner equation. A similar comparison was done previously by Craig and Neto,[26] but in their paper the drag force was not subtracted from the Brenner equation, so the error they found in comparison is much larger than we found. From our work, we conclude that the effective drag length and the spring constant obtained by fitting the Taylor force are still accurate at much large separations ($h \approx R$).

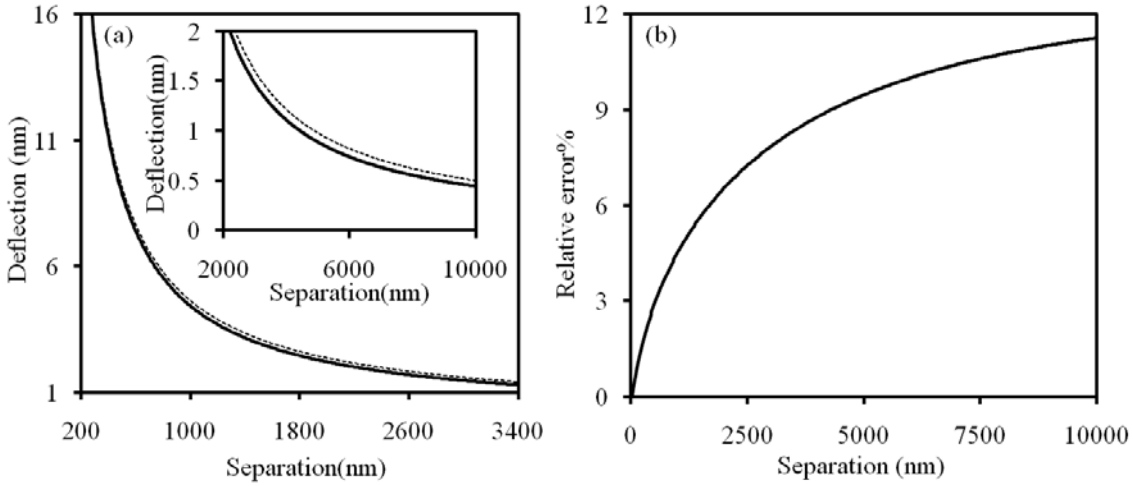

Figure 3.4 (a) Drainage component of Brenner's solution (---) and Taylor's solution (—) for the hydrodynamic drainage force in sphere–flat geometry. (Inset) An enlargement of the two solutions at large separations. The parameters used in the calculation of these forces are those typical of a colloid probe AFM experiment: a sphere radius of 9.5 μm, a solution viscosity of 47.71 mPa s, an approach velocity of 30.7 μm/s and spring constant of 0.562 N/m. (b) Relative error between the Taylor and Brenner equations in the range of 0 to 10 μm separation. The relative error % = (Taylor force–Brenner force)/Brenner force×100%.

3.4 Flattened Contact Areas of Microspheres

A. Calculation of Hydrodynamic Drainage Force on a Flattened Microsphere

The Vinogradova expression for the hydrodynamic drainage force (Eqs 3.2 and 3.3) is valid in the case of a sphere and flat surface system. However, the microsphere glued to the tip of the AFM cantilever could become flattened in the contact region because of irreversible wear from rubbing on the substrate or a manufacturing defect. In such case, as shown in Figure 3.5, the measured hydrodynamic drainage force would be different compared to the perfect sphere–flat geometry, which could change the slip length result. Neglecting this flattening as in the current Vinogradova expression may preclude an accurate value of the slip length. In the following, we derive the hydrodynamic drainage force in this special flattened sphere–flat geometry case and compare it with the sphere–flat geometry case.

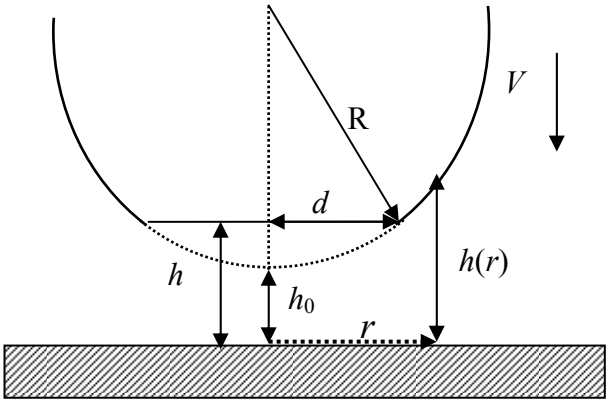

Figure 3.5 Microsphere with a flattened contact area approaching a plane substrate with a velocity V. The radius of the microsphere is R, the radius of the flat disk on the microsphere is d, the distance from the flat disk surface to the substrate surface is h, and the distance of closest approach of the perfect microsphere to the substrate surface is h_o. r is the lateral radius of the cylindrical coordinate system. $h(r)$ is the distance between a point on the microsphere beyond the flat disk and the substrate surface.

The net hydrodynamic drainage force on a microsphere can be obtained by integrating the hydrodynamic pressure $P(r)$ on the microsphere surface. The integration is divided into two parts: a flattened part and the remainder. Hence, the net hydrodynamic drainage force is given by

$$F = \int_0^d 2\pi r\left(P(r) - P_0\right)dr + \int_d^{R'} 2\pi r\left(P(r) - P_0\right)dr$$

$$= \int_0^d 2\pi r\left(P(r) - P(d) + P(d) - P_0\right)dr + \int_d^{R'} 2\pi r\left(P(r) - P_0\right)dr \tag{3.21a}$$

$$F = \int_0^d 2\pi r\left(P(r) - P(d)\right)dr + \pi d^2\left[P(d) - P_0\right] + \int_d^{R'} 2\pi r\left(P(r) - P_0\right)dr \tag{3.21b}$$

In Eq. 3.21, r is the lateral radius in the cylindrical coordinate system and P_0 is the atmospheric pressure away from the microsphere.

For the first term in Eq. 3.21a, when $r < d$, (i.e., in the flattened range), h is not a function of r. Following Bikerman,[27] using the standard hydrodynamic equations, it can be shown that the derivative of pressure is given by

$$P'(r) = \frac{6\eta r\dot{h}}{h^3 + 6bh^2} \quad (r < d) \tag{3.22}$$

Integrating the pressure is give by

$$P(r) = \frac{3\eta\dot{h}}{h^3 + 6bh^2} r^2 \quad (r < d) \tag{3.23}$$

so the first term in Eq. 3.21b, at $r < d$ region, can be expressed by

$$\int_0^d 2\pi r\left(P(r) - P(d)\right)dr = \frac{6\pi\eta\dot{h}}{h^3 + 6bh^2}\left(-\frac{d^4}{4}\right) \tag{3.24}$$

For the second term in Eq. 3.21a, when $r \geq d$, out of the flattened range, h is a function of r, $h(r)$

$$h(r) = h_0 + r^2/2R \ \ (r \geq d) \tag{3.25}$$

The derivative of pressure can be given by

$$P'(r) = \frac{6\eta r\dot{h}}{h(r)^3 + 6bh(r)^2}\frac{dh(r)}{dr} = \frac{6\eta R\dot{h}}{36b^2}\left[\frac{6b}{h^2(r)} - \frac{b}{h(r)} + \frac{1}{h(r)+6b}\right]\frac{dh(r)}{dr}. \tag{3.26}$$

Here, $r = R\,dh(r)/dr$, which is from the derivative of Eq. 3.25.

By integrating $P'(r)$ (Eq. 3.26) from R' to r and assuming that $P(R') = P_0$, (R' here is a specified distance in the direction of the cylindrical coordinate, which is much larger than d and R) we can write

$$P(r) - P_0 = \frac{6\eta R\dot{h}}{36b^2}\left[\frac{-6b}{h(r)} + \frac{6b}{h(R')} - \ln\frac{h(r)\left(h(R')+6b\right)}{\left(h(r)+6b\right)h(R')}\right] (\mathrm{r} \geq \mathrm{d}) \tag{3.27}$$

Following Eq. 3.25, if $R' = 2R$ $h(R') = h_0 + 2R$; if $r = d$, then $h(d) = h_0 + d^2/2r$.

Therefore, $h(R') = h(d) - \frac{d^2}{2R} + 2R$.

We set $H = h(R')$ so

$$P(d) - P_0 = \frac{6\eta R\dot{h}}{36b^2}\left[\frac{-6b}{h(d)} + \frac{6b}{h(R')} - \ln\frac{h(r)\left(h(R')+6b\right)}{\left(h(r)+6b\right)h(R')}\right]$$

$$= \frac{6\eta R\dot{h}}{36b^2}\left[\frac{-6b}{h} + \frac{6b}{H} - \ln\frac{h(H+6)}{H(h+6b)}\right] \tag{3.28}$$

If $r > d$, then by integrating Eq, 3.27 and substituting in $r = R\,dh(r)/dr$, the third term in Eq. 3.21 can be expressed as

$$\int_d^{R'} 2\pi r\,(P(r) - P_0)\,dr = \frac{6\pi\eta R\dot{h}}{h} f^* \tag{3.29}$$

$f^* = \frac{h}{3b}\left[\left(1+\frac{h}{6b}\right)\ln\left(1+\frac{6b}{h}\right) - 1\right]$, here f^* is the Vinogradova correction factor.

By substituting Eqs 3.24, 3.28 and 3.29 into Eq. 3.21, the hydrodynamic drainage force in the flattened microsphere case can be given by

$$F = -\frac{6\pi\eta d^2\dot{h}}{h} f^{\#} - \frac{6\pi\eta R^2\dot{h}}{h} f^* \tag{3.30}$$

We define $f^{\#}$ as another correction factor for slip in the flat–flat geometry case,

$$f^{\#} = \frac{R}{6b}\left(1 - \frac{h}{H} + \frac{h}{6b}\ln\frac{h(H+6)}{H(h+6b)}\right) + \frac{d^2}{4h(h+6b)}.$$

B. Results of Hydrodynamic Drainage Force on a Flattened Microsphere

The typical radius of the flat disk on the microsphere is in the range between 100 and 300 nm, as obtained from our inverse AFM microsphere images (Figure 3.6). (For details on the inverse AFM microsphere technique, see Section 2.2) With the radii of the flattened areas taken to be 100 and 300 nm, the corresponding theoretical hydrodynamic drainage forces as calculated by Eq. 3.30 are shown in Figure 3.7. This data illustrates that when the disk radius is 100 nm the corresponding hydrodynamic drainage force (…) is almost identical to the normal hydrodynamic drainage force (—) under the assumption of a perfect microsphere. If the radius of the flat disk is assumed to be 300 nm, the associated hydrodynamic drainage force (—) increases gradually at small separations. This indicates that there is a larger force on the flattened sphere than that on the perfect sphere. The larger the flattened area, the larger the force. All three forces have been calculated assuming a slip length of 35 nm. The discrepancy between the green curve (—) and the black curve (—) is shown in the inset in Figure 3.7, and the discrepancy increases from 0.25 to 2.96 nN

in the separation range of 0–150 nm. The blue dashed curve (---) in Figure 3.7 is the force produced by the perfect microsphere modeling, which partially fits the green curve (—) and has a slip length of 30 nm. This result suggests that the effect on the hydrodynamic drainage force due to a flat area on the microsphere might not be neglected if the radius of the flattened area of the attached microsphere is equal to or larger than 300 nm. It also indicates that if we use the perfect microsphere modeling to fit the force on the flattened microsphere, the slip length would be underestimated.

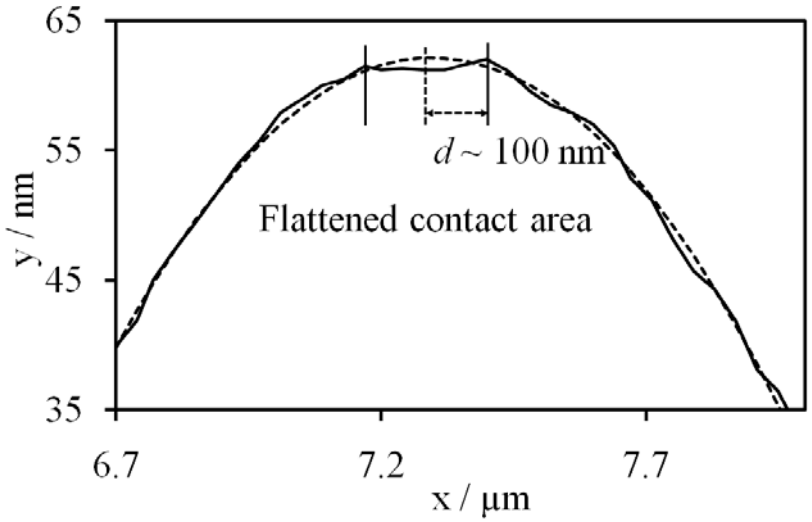

Figure 3.6 Cross-section of the apex of a colloid probe obtained from the inverse AFM imaging of the microsphere (—). The dotted line is the circle of best fit for the microsphere that is used to determine the radius of the microsphere. The radius of the flattened contact area on the apex of the microsphere is $d \sim 100$ nm.

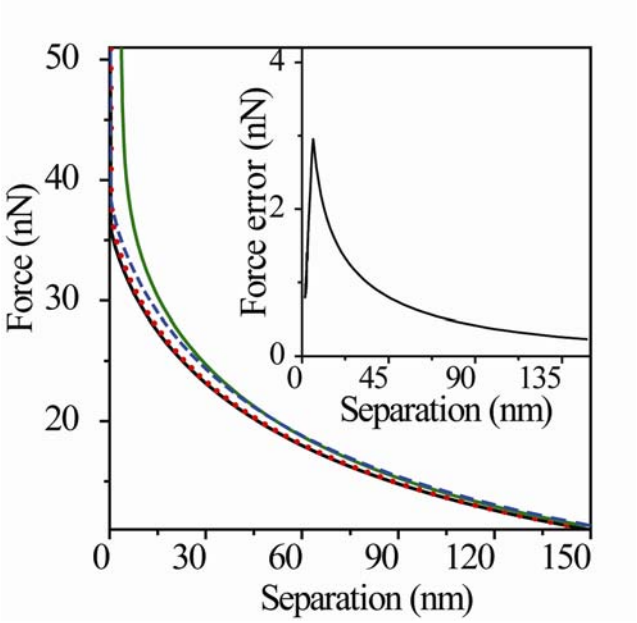

Figure 3.7 Theoretical hydrodynamic drainage forces calculated for a perfectly round microsphere and for flattened microspheres. The black curve and the blue dashed line represent the hydrodynamic drainage force on the perfect microsphere with slip length of 35 nm and 30 nm respectively. The red dotted line and the green curve are the hydrodynamic drainage forces on flattened microspheres both with a slip length of 35 nm, calculated by assuming that the radii of the flat disk on the microsphere is 100 nm (…) and 300 nm (—). The colloid probe used in these four situations is the same. It has a spring constant of 0.56 N/m and a microsphere of 9.5 μm radius. The inset is the absolute force error between the square curve and the solid line in the separation range of 0–150 nm.

3.5 Contamination of the Substrate with Nanoparticles

For accurate force measurements, extremely clean experimental conditions are essential but they can also be difficult to obtain. Particle contamination in force measurements is one of the most common sources of contamination. Nanoparticles might be expected to affect the results similarly to nanoasperities. Guriyanova *et al.*[28] have discussed the influence of nanoasperities on the surface of the AFM colloid probe. Their experimental results showed that the experimentally determined slip length values when surface asperities were present were higher than those when a smooth sphere was in full contact with the substrate surface. Fan *et al.*[29] have mathematically simulated hydrodynamic forces on slippery microspheres with a nanoasperity, which showed reduced hydrodynamic forces compared to those on smooth microsphere surfaces. Similarly, in the

following section, our modeling demonstrates that particles on the substrate surface can cause large apparent slip lengths. Assuming that there is a nanosized particle contaminant of radius r on the substrate surface under the colloid probe of radius R, as shown in Figure 3.8, the hydrodynamic drainage force expression can be given by

$$F = -\frac{6\pi\eta R^2 \dot{H}}{H+2r} - \frac{6\pi\eta r^2 \dot{H}}{H}. \tag{3.31}$$

Here, H is the separation between the colloid probe and the topmost surface of the nanoparticle, and r is the radius of the nanoparticle. At large separations ($r << H$), the force is dominated by the hydrodynamic drainage force due to the colloid probe and the flat surface. At small separations ($r > H$), the force caused by the small particle becomes dominant.

In Figure 3.9, the theoretical hydrodynamic drainage forces with particle contamination and without are predicted by Eq. 3.31. In these two systems, the other conditions are exactly the same. In the particle contamination case, the particle size r is assumed to be 65 nm and the force curve (●) is partially fitted by Vinogradova's slip hydrodynamic model (---, calculated from Eqs. 3.2 and 3.3) and provides an apparent slip length of 70 nm. In the clean system without particle contamination, the fitted slip length of the force curve (▲) is 23 nm. It is clearly shown that in the nanoparticle contamination case, the slip length is higher, which can be due to the unreliable determination of zero separation. In the present of the particle on the surface, the measured separation H is not the separation h from the substrate surface but from the nanoparticle surface. To obtain the exact zero separation in the particle contamination case, the position of hard contact should be shifted from the particle surface to the substrate surface by the particle size. The contaminated force curve (●) was shifted way from contact by 65 nm (particle size). The shifted force (×) agrees with the force curve (▲) in the no-particle case, and we obtain the same slip length of 23 nm, shown in Figure 3.9. Therefore, it can be concluded that the particle contamination can cause an apparently large slip length, and the true slip length can be obtained by shifting the force curve to its real separation. In Chapter 4, we demonstrate the nanoparticle contamination in our force curves experimentally and

describe a practical method to reduce the possibility of the occurrence of nanoparticles; however, their presence is hard to exclude a priori, and substrates and microspheres should always be imaged to check for cleanliness.

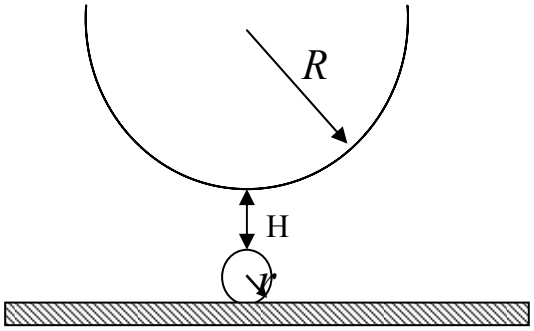

Figure 3.8 Sketch of a nanoparticle of radius *r* on the substrate surface directly under the microsphere. *H* is the distance between the microsphere and the particle contaminant. *R* is the radius of the microsphere.

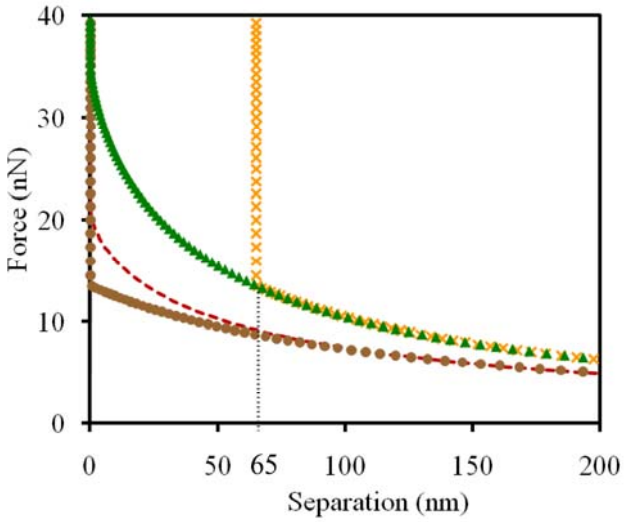

Figure 3.9 Hydrodynamic drainage force on a colloid probe calculated both in the presence and absence of nanoparticle contaminants. In the case without nanoparticle contamination, the slip length is 23 nm (▲). In the case with nanoparticle contamination, the slip length is 70 nm (●). The dashed line is the theoretical slip force, which partially fits the force with a particle contaminant to get an apparent slip length of 70 nm. The crosses (×) indicate the force obtained with a particle contaminant (●) shifted away from contact by 65 nm which is equal to the particle size.

3.6 Drag Force on the Cantilever

In most drag force calculations,[13, 29-36] the drag force on the cantilever is treated as a constant force during the approach of the colloid probe to the surface, as expressed by Eq. 3.6. However, as the base of the cantilever approaches the surface with a constant velocity that is imposed by the AFM piezo-crystal over the entire separation, the free tip of the cantilever with the attached microsphere deflects away from the flat surface. As a result, the velocity of the cantilever varies along the length of the cantilever and decreases at the tip with decreasing separation. This suggests that the drag force on the cantilever is not constant during the approach to the surface at a particular drive speed. If we consider that the drag force is constant and subtract it from the experimental force, then the hydrodynamic drainage force that remains would be underestimated, which may consequently cause an overestimate of the actual slip length. Recently, there have been reports that the fitted slip length depends on the shape and/or the spring constant of the cantilever.[16, 17] One possible reason, we suggest, might be due to neglecting this variation in drag force, because this is the only force that depends upon the shape and/or spring constant of the cantilever. (Shape includes the geometry, for example, rectangular versus triangular, and also the aspect ratio.) Here, we formulate the exact drag force expression for a rectangular cantilever to quantify this effect on the fitted slip length.

Two research groups have attempted to calculate a variable drag force.[15, 28, 37] Butt's group[28,37] used an empirical parameter α to predict the variation of the drag force during the approach. With this approximation, the authors[28] found that a value of α between 0.8 and 0.9 provided the best fit to their experimental data. Honig and Ducker[15] integrated the drag force at each small increment over the whole cantilever. However, this method approximates the colloid probe cantilever as being evenly loaded, which is not the case because of the hydrodynamic drainage force on the tip of the cantilever and a distributed drag force that varies over the entire cantilever. This assumption could lead to significant inaccuracies in their calculation. In this section, we illustrate the exact and constant drag forces and compare the difference between these two.

A. Exact Drag Force Calculation

In this section, we calculated the variable drag force acting on the AFM cantilever exactly, as the cantilever moves through the liquid and bends. The total angular bending of the cantilever is the sum of the bending due to the distributed drag force on a bare cantilever plus the bending due to a point force from drainage on the end of the cantilever (between the colloid and the surface). The drainage force determines the rate of change of bending of the cantilever, and this in turn determines the local drag force at each position along the cantilever.

The mathematical details are as follows. To obtain the exact drag force that is measured in the AFM, three effects need to be accounted for. First, the drag force is distributed along the length of the cantilever, y, where $y = 0$ is the base and $y = L$ is the tip of the cantilever. Second, the local drag force per unit length, $f(y)$, is proportional to the local velocity $\dot{x}(y)+\dot{z}$ of the cantilever, $f(y) = -c\left(\dot{x}(y)+\dot{z}\right)$. Here, c is a drag constant that is independent of y for the rectangular cantilever modeled here and that can be obtained from the experimental data at large separations (see below). Third, the photodiode of the AFM measures the angle of the cantilever at the tip, $\mathrm{d}x(L)/\mathrm{d}y$, rather than the deflection $x(L)$ itself. The linear relationship between the deflection and the deflection angle has a different proportionality constant with respect to the photodiode signal if the force is a point force concentrated at the tip, than if it is a distributed, nonuniform force, or if it is a combination of the two, as here for the drainage force plus the drag force. In AFM modeling, it is important that the actual photodiode signal be calculated. These three effects mean that the shape of the cantilever as a function of position and time, $x(y, t)$, under the influence of the drainage force at the tip and the drag force along its length needs to be obtained self-consistently during the simulation of the AFM force measurement. The rate change of the local deflection is obtained at each time step from a finite difference approach, $\dot{x}(y,t) = \left[x(y,t) - x(y,t-\Delta t)\right]/\Delta t$. Because $x(y, t)$ itself depends upon the local velocity along the whole cantilever, this and the shape equation below are iterated several times at each time step until convergence is reached. The y coordinate was discretised into about 100 nodes, and the integrals below were evaluated by Simpson's rule. The relation between the bending moment due to the elastic response of a cantilever and its curvature is described as[38]

$$EI\frac{d^2x}{dy^2} = M(y) \tag{3.32}$$

where E is Young's modulus, I is the moment of inertia, $M(y)$ is the bending moment, x is the deflection, and y is the distance along the cantilever ($y = 0$ is the base, $y = L$ is the tip). Following Attard *et al.*,[39, 40] here and below, the elastic parameter is $B = E\,I$, and for a cantilever of length L, the spring constant is

$$k = 3B / L^3 \tag{3.33}$$

The total force over the entire cantilever in the quasi steady state (i.e. zero acceleration) must vanish

$$F_0 + F_L + \int_0^L dy' f(y') = 0 \tag{3.34}$$

where F_0 is the restoring force at the fixed base of the cantilever, F_L is the hydrodynamic drainage force on the microsphere at the free end of the cantilever, (the same force as F_h in Section 3.2.1), and $f(y)$ is the force due to drag at y.

The bending moment or torque over the entire cantilever must also vanish in the quasi steady state:

$$M_0 + F_L L + \int_0^L dy' f(y') y' = 0 \tag{3.35}$$

At a position y on the cantilever, an internal force $F(y)$ can be balanced at equilibrium:

$$F(y) + F_0 + \int_0^y dy' f(y') = 0 \tag{3.36}$$

Its corresponding bending moment can be expressed by

$$M(y) + M_0 - F_0 y - \int_0^L dy' f(y')(y - y') = 0 \tag{3.37}$$

Hence, by combining Eqs 3.34 and 3.35 with 3.37, one obtains

$$M(y) = (L - y)F_L + \int_y^L dy' f(y')(y' - y) \tag{3.38}$$

Inserting this into Eq. 3.32 allows the shape of the cantilever to be calculated at each time step.

At large separations, one can neglect the hydrodynamic drainage force F_L=0, and take the drag force to be a uniform force i.e. $f(y') = f$. In this case, Eq. 3.38 is

$$M(y) = f\int_y^L dy'(y' - y) = \frac{1}{2} f \cdot (L - y)^2 \tag{3.39}$$

from which it follows that the shape is

$$x(y) = B^{-1}\int_0^y \int_0^y M(y)dy = B^{-1} f \cdot \left(\frac{1}{4}L^2 y^2 - \frac{1}{6}Ly^3 - \frac{1}{24}y^4\right) \tag{3.40}$$

Hence, the cantilever deflection at the free end is

$$x(L) = \frac{3}{8}k^{-1} f\, L \tag{3.41}$$

In this situation, the deflection of the tip is due to a uniform distributed drag force on the cantilever. The drag force deflection can also be expressed by

$$x(L) = \frac{F_{\mathrm{d}}}{k} = \frac{-6\pi\eta \dot{z} L_{\mathrm{e}}}{k} \tag{3.42}$$

By combing Eqs 3.41 and 3.42, the uniform force per unit length f is

$$f = \frac{-16\pi\eta\dot{z}L_{\mathrm{e}}}{L} \equiv -c\dot{z} \tag{3.43}$$

It can be shown that $L_{\mathrm{e}} = 9\widetilde{L}_{\mathrm{e}}/8$, where $\widetilde{L}_e$ is the apparent effective drag length determined from the experimentally measured force at large separation. This apparent effective drag length used here is the same as the experimentally measured effective drag length used in Eq. 3.6. This determines the constant c from the experimentally measured force at large separations. If f is a uniform value and the drainage force is nonzero, then $F_{\mathrm{L}} \neq 0$, Eq. 3.38 can be rearranged as

$$M(y) = (L - y)F_L + f\left(\frac{1}{2}L^2 + \frac{1}{2}y^2 - yL\right) \tag{3.44}$$

$$\theta = \frac{dx}{dy} = B^{-1}\left(\frac{1}{2}L^2 F_L + \frac{1}{6}L^3 f\right) \tag{3.45}$$

Therefore, the deflection at the free end of cantilever is

$$x(L) = \int_0^L dy \frac{dx}{dy} = \frac{L^3}{B}\left(\frac{1}{3}F_L + \frac{1}{8}f\right) \tag{3.46}$$

The photodiode in the AFM does not measure the cantilever deflection *per se* but rather measures the change in the angle of the cantilever $\Delta\theta$ that is proportional to the change in the photodiode voltage ΔV:

$$\beta = \Delta V / \Delta\theta \,. \tag{3.47}$$

This equation is always valid for either the point force or the distributed force. β is a constant.

In the actual experimental force analysis, constant compliance is required to convert the measured photodiode voltage to the cantilever deflection. The compliance is based on the fact that when the colloid probe and the surface are in contact, the change in the deflection of the cantilever Δx is proportional to the change in the photodiode voltage ΔV:

$$\alpha = \left(\Delta V / \Delta x\right)_{\text{point}} \tag{3.48}$$

Here, α is the constant compliance slope obtained in contact. This equation is true only when the force is a point force. In this case of a point force, the change in the deflection is also proportional to the change in the angle of the cantilever tip, and the relationship between the two constants is[39, 40]

$$\beta = \frac{2}{3}\alpha L \tag{3.49}$$

This relationship holds everywhere. However, if there is a distributed force, then the cantilever deflection has a different proportionality constant for the voltage, and this varies with separation as the distributed force varies. Hence the constant compliance slope α does not give the correct deflection $x(L)$ when a distributed force is present.

In the theory, the deflection angle $dx(L)/dy$ and the tip deflection $x(L)$ can be calculated at any time step. From the calculated deflection angle $dx(L)/dy$ and the experimental constant compliance slope, the voltage signal V can be predicted (using Eqs 3.47 and 3.49). The voltage can be predicted for any point force or distributed force. This voltage is then converted to an apparent deflection (and apparent separation) using the experimentally measured constant compliance slope in order to compare with the usual experimentally determined apparent deflection and separation. Finally, the spring constant is used to convert the apparent deflection to the apparent force to compare with experimental data.

B. Comparison of the Two Drag Forces

An exact drag force was calculated with the method above using the FORTRAN code presented in Appendix 3. The comparison of the effect of the exact and constant drag forces on the force curves is shown in Figure 3.10. The force curves shown here are a combination of the hydrodynamic drainage force, drag force, and van der Waals force. In each part of the Figure 3.10, the dashed and solid force curves include exactly the same hydrodynamic drainage force and van der Waals force but different drag forces. The dashed curve represents the force including the exact drag force and the solid curve represents the force including the constant drag force. Figure 3.10a and b show two different cases using a soft cantilever (k = 0.095N/m) and a stiff cantilever (k = 0.56N/m), respectively. The results show that there is a discrepancy between the dashed and solid curves at small separations in both cases. These discrepancies are clarified in Figure 3.10c. It can be seen that the errors between the two force curves are close to zero in both cases at large separations but increase sharply at small separations (< 800 nm). In the soft cantilever case (○), the force error increases significantly faster and is larger than that in the stiffer cantilever case (▲). In the case of the soft cantilever (inset of Figure 3.10a), in order to fit the exact force (---) with the constant drag model (—) a higher fitted slip length of 26 nm needs to be used, compared to the exact slip length of 20 nm. This means that when a soft cantilever is used (such as with the spring constant 0.095 N/m used here) the slip length can be overestimated by 6 nm or more if using the constant drag model. However, for a stiffer cantilever shown in the inset of Figure 3.10b, fitting the exact force with the constant drag model overestimates the slip length by only about 2 nm. Figure 3.10d shows the effect of changing the aspect ratio of the cantilever (greater length) while keeping the same spring constant as in the soft cantilever case. Here again the constant drag force (—) cannot fit the exact drag force (---) with the same slip length of 20 nm. A higher slip length of 33 nm needs to be used in the constant drag model to fit the exact force (---) (inset of Figure 3.10d), which means that the effect of a different shape of the cantilever can be similar and even stronger than the effect of the spring constant alone. Hence, it can be concluded that the effects of the variability of the drag force on soft cantilevers are much more significant than on stiff cantilevers and that the shape of the

cantilever also has a significant effect on the soft cantilevers, but not significant for the stiff cantilevers. The drag force can be treated as a constant force only for relatively stiff cantilevers (k > 0.2 N/m, for the system given in Table 6.2 in Chapter 6) in AFM force measurements.

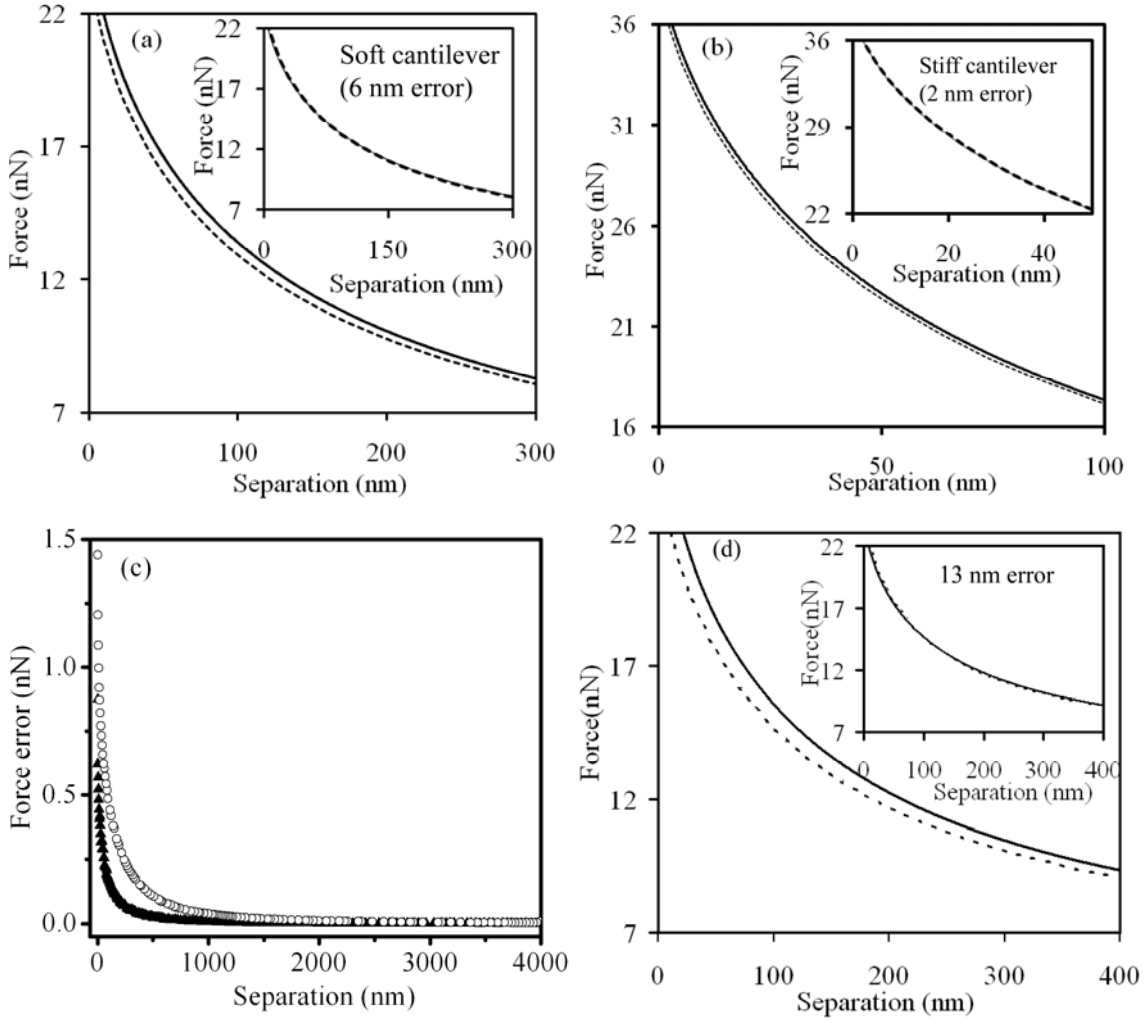

Figure 3.10 Hydrodynamic force acting on a colloid probe calculated by including the exact drag force on the cantilever (---) and the constant drag force (—). Each curve contains the hydrodynamic drainage force, drag force, and van der Waals force. (a) Calculation for a soft cantilever, k=0.095N/m, the rectangular cantilever length is 283 μm and the effective drag length is 86.5 μm. The parameters used in the calculation of these forces are those typical for a colloid probe AFM experiment: a sphere radius of 8.6 μm, a solution viscosity of 52.6 mPas and an approach velocity of 30.0 μm/s, and for both curves, an actual slip length of 20 nm. Inset: the constant drag (—) fits the exact force (---, slip length 20 nm) with a slip length of 26 nm. (b) Calculation for a stiff cantilever k=0.56N/m, the rectangular cantilever length is 246 μm and the effective drag length is

81.4 μm. The parameters used in the calculation of these forces are those typical of a colloid probe AFM experiment: a sphere radius of 9.5 μm, a solution viscosity of 53.54 mPa s and an approach velocity of 31.4 μm/s; for both, the fitted slip length is 45 nm. Inset: the constant drag (—) fits the exact force (---, slip length 45 nm) with a slip length of 47 nm. (c) Force errors (force with constant drag minus force with exact drag) for a soft cantilever (○) and a stiff cantilever (▲). (d) The parameters used in the calculation of these forces are the same as those in part a, but here the length of the cantilever is greater, 350 μm, and the effective drag length is also greater, 160 μm, whereas the spring constant is the same, 0.095 N/m. The slip length is 20 nm for the solid line (constant drag, the same as the solid line in part a), and 20 nm for the dashed line (exact drag). Inset: the constant drag (—) fits the exact force (---, slip length of 20 nm) with a slip length of 33 nm. All the effective drag lengths in this caption were experimentally measured values, and are the same mean as the one in Eq. 3.6 and the one ($\widetilde{L}_e$)in Section 3.6.

The corresponding experimental results of the drag force effect on soft cantilevers are specified in Chapter 5. We find that some of our measured slip lengths increase with driving velocities, as observed previously in the literature.[1] This dependence of slip on driving velocity only occurs in the experiments where soft cantilevers are employed, and this dependence could be removed if the exact drag forces are applied.

3.7 Conclusions

In this chapter, the force due to the drainage of Newtonian liquids in confined geometries was accurately predicted by a mathematical algorithm that is independent of experimental data. This helps reduce the noise in the theoretical forces over that in previous treatments. This mathematical algorithm is able to provide a reliable estimate of the fitting error in the determination of both slip length and spring constant, as shown by the blind test. The effect of a flattened microsphere, the effect of particle contamination, and the effect of the exact distributed, nonuniform, separation-varying drag force are all examined by our simulation to check the effects on the force curve and the slip length. The results show that the approximate Taylor equation is accurate enough even in the extremely large separation limit (the maximum separation is close to the radius of the microsphere) and can be used to predict the hydrodynamic drainage force instead of the

exact Brenner equation. This justifies using the large separation regime to fit the spring constant and the drag force. The constant drag force equation is appropriate for calculating the drag force on the cantilever within an acceptable error range for a relatively stiff cantilever (k > 0.2N/m) but not for a relatively soft one, where it can significantly overestimate the slip length. The same effect can occur from a change in shape (different aspect ratio for a rectangular cantilever or using a triangular cantilever). This may explain previous reports that the fitted slip length depends upon the shape and spring constant of the cantilever used to perform the measurements.[16, 17] It was found that flattened microspheres used in force measurements could underestimate the slip length if the area of the flattened surface is relatively large (radius larger than 300 nm). Nanocontaminants present on the substrate were found to give a large slip length in the fitted force curve that was of the same order as the size of the contaminant. Particle contamination could be one of the reasons for the extremely large slip lengths reported in some experimental systems. In Chapter 4, this new algorithm is employed to fit new AFM experiments of interfacial slip reliably and reproducibly. The drag force effect on soft cantilevers is experimentally demonstrated to be one of the possible reasons for the dependence of the measured slip length on the driving velocity, as discussed in Chapter 5.

References

1. Craig, V. S. J.; Neto, C.; Williams, D. R. M. Shear-dependent boundary slip in an aqueous Newtonian liquid. *Phys. Rev. Lett.* **2001**, *87*, 054504.

2. Brenner, H. The Slow Motion of a Sphere through a Viscous Fluid Towards a Plane Surface. *Chem. Eng. Sci.* **1961**, *16*, 242-251.

3. Neto, C.; Evans, D. R.; Bonaccurso, E.; Butt, H. J.; Craig, V. S. J. Boundary slip in Newtonian liquids: a review of experimental studies. *Rep. Prog. Phys.* **2005**, *68*, 2859-2897.

4. Vinogradova, O. I. Drainage of a thin liquid-film confined between hydrophobic surfaces. *Langmuir* **1995**, *11*, 2213-2220.

5. Lauga, E.; Brenner, M. P.; Stone, H. A., Microfluidics: The No-slip Boundary Condition. In *Handbook of Experimental Fluid Dynamics*, Foss, J.; Tropea, C.; Yarin, A., Eds. Springer: New York, 2005; Chapter 15.

6. Voronov, R. S.; Papavassiliou, D. V.; Lee, L. L. Review of fluid slip over superhydrophobic surfaces and its dependence on the contact angle. *Ind. Eng. Chem. Res.* **2008**, *47*, 2455-2477.

7. Tabeling, P. A brief introduction to slippage, droplets and mixing in microfluidic systems. *Lab Chip* **2009**, *9*, 2428-2436.

8. Cao, B. Y.; Sun, J.; Chen, M.; Guo, Z. Y. Molecular momentum transport at fluid-solid interfaces in MEMS/NEMS: a review. *Int. J. Mol. Sci.* **2009**, *10*, 4638-4706.

9. Bocquet, L.; Charlaix, E. Nanofluidics, from bulk to interfaces. *Chem. Soc. Rev.* **2010**, *39*, 1073-1095.

10. Honig, C. D. F.; Ducker, W. A. No-slip hydrodynamic boundary condition for hydrophilic particles. *Phys. Rev. Lett.* **2007**, *98*, 028305.

11. Honig, C. D. F.; Ducker, W. A. Squeeze film lubrication in silicone oil: experimental test of the no-slip boundary condition at solid-liquid interfaces. *J. Phys. Chem. C* **2008**, *112*, 17324-17330.

12. Semin, B.; Guriyanova, S.; Bonaccurso, E. Nonconstant piezo velocity in highly dynamic atomic force spectroscopy. *Rev. Sci. Instrum.* **2006**, *77*, 116107.

13. Vinogradova, O. I.; Butt, H. J.; Yakubov, G. E.; Feuillebois, F. Dynamic effects on force measurements. I. Viscous drag on the atomic force microscope cantilever. *Rev. Sci. Instrum.* **2001**, *72*, 2330-2339.

14. Zhu, L. W.; Attard, P.; Neto, C. Reliable measurements of interfacial slip by colloid probe atomic force microscopy. II. Hydrodynamic force measurements. *Langmuir* **2011**, *27*, 6712-6719.

15. Honig, C. D. F.; Ducker, W. A. Thin film lubrication for large colloidal particles: experimental test of the no-slip boundary condition. *J. Phys. Chem. C* **2007**, *111*, 16300-16312.

16. Henry, C. L.; Craig, V. S. J. Measurement of no-slip and slip boundary conditions in confined Newtonian fluids using atomic force microscopy. *Phys. Chem. Chem. Phys.* **2009**, *11*, 9514-9521.

17. Rodrigues, T. S.; Butt, H. J.; Bonaccurso, E. Influence of the spring constant of cantilevers on hydrodynamic force measurements by the colloidal probe technique. *Colloids & Surfaces A: Physicochem. Eng. Aspects* **2010**, *354*, 72-80.

18. Press, W. H., Teukolsky, S. A. , Vetterling, W. T. , and Flannery, B. P. , *Numerical Recipes: The Art of Scientific Computing*. 3rd ed.; Cambridge University Press: Cambridge, UK, 2007.

19. Chan, D. Y. C.; Horn, R. G. The Drainage of Thin Liquid-Films between Solid-Surfaces. *J. Chem. Phys.* **1985**, *83*, 5311-5324.

20. McBride, S. P.; Law, B. M. Viscosity-dependent liquid slip at molecularly smooth hydrophobic surfaces. *Phys. Rev. E* **2009**, *80*, 060601.

21. Bonaccurso, E.; Butt, H. J.; Craig, V. S. J. Surface roughness and hydrodynamic boundary slip of a Newtonian fluid in a completely wetting system. *Phys. Rev. Lett.* **2003**, *90*, 144501.

22. Cottin-Bizonne, C.; Steinberger, A.; Cross, B.; Raccurt, O.; Charlaix, E. Nanohydrodynamics: The intrinsic flow boundary condition on smooth surfaces. *Langmuir* **2008**, *24*, 1165-1172.

23. McBride, S. P.; Law, B. M. Improved in situ spring constant calibration for colloidal probe atomic force microscopy. *Rev. Sci. Instrum.* **2010**, *81*, 113703.

24. Attard, P.; Parker, J. L. Deformation and Adhesion of Elastic Bodies in Contact. *Phys. Rev. A* **1992**, *46*, 7959-7971.

25. Israelachvili, J. N., *Intermolecular and Surface Forces* 2nd ed.; Academic Press: London, 1991.

26. Craig, V. S. J.; Neto, C. In situ calibration of colloid probe cantilevers in force microscopy: hydrodynamic drag on a sphere approaching a wall. *Langmuir* **2001**, *17*, 6018-6022.

27. Bikerman, J. J. The fundamentals of tackiness and adhesion. *J. Colloid Sci.* **1947**, *2*, 163-175.

28. Guriyanova, S.; Semin, B.; Rodrigues, T. S.; Butt, H. J.; Bonaccurso, E. Hydrodynamic drainage force in a highly confined geometry: role of surface roughness on different length scales. *Microfluid. Nanofluid.* **2010**, *8*, 653-663.

29. Fan, T. H.; Vinogradova, O. I. Hydrodynamic resistance of close-approached slip surfaces with a nanoasperity or an entrapped nanobubble. *Phys. Rev. E* **2005**, *72*, 066306.

30. Vinogradova, O. I.; Yakubov, G. E. Dynamic effects on force measurements. 2. Lubrication and the atomic force microscope. *Langmuir* **2003**, *19*, 1227-1234.

31. Jana, A.; Raman, A.; Dhayal, B.; Tripp, S. L.; Reifenberger, R. G. Microcantilever mechanics in flowing viscous fluids. *Appl. Phys. Lett.* **2007**, *90*, 114110.

32. Ezkerra, A.; Wilson, P. A.; Mayora, K.; Ruano-Lopez, J. M. A mathematical model for the motion analysis of embedded straight microcantilevers under a pressure-driven flow. *J Micromech Microeng* **2008**, *18*, 095011.

33. Alcaraz, J.; Buscemi, L.; Puig-de-Morales, M.; Colchero, J.; Baro, A.; Navajas, D. Correction of microrheological measurements of soft samples with atomic force microscopy for the hydrodynamic drag on the cantilever. *Langmuir* **2002**, *18*, 716-721.

34. Liu, R. C.; Roman, M.; Yang, G. L. Correction of the viscous drag induced errors in macromolecular manipulation experiments using atomic force microscope. *Rev. Sci. Instrum.* **2010**, *81*, 063703.

35. Jones, R. E.; Hart, D. P. Force interactions between substrates and SPM cantilevers immersed in fluids. *Tribol Int* **2005**, *38*, 355-361.

36. Janovjak, H.; Struckmeier, J.; Muller, D. J. Hydrodynamic effects in fast AFM single-molecule force measurements. *Eur Biophys J Biophy* **2005**, *34*, 91-96.

37. Stark, R.; Bonaccurso, E.; Kappl, M.; Butt, H. J. Quasi-static and hydrodynamic interaction between solid surfaces in polyisoprene studied by atomic force microscopy. *Polymer* **2006**, *47*, 7259-7270.

38. Southwell, R. V., *An Introduction to the Theory of Elasticity for Engineers and Physicists*. The Clarendon Press: Oxford, England, 1936.

39. Attard, P.; Schulz, J. C.; Rutland, M. W. Dynamic surface force measurement. I. van der Waals collisions. *Rev. Sci. Instrum.* **1998**, *69*, 3852-3866.

40. Attard, P.; Carambassis, A.; Rutland, M. W. Dynamic surface force measurement. 2. Friction and the atomic force microscope. *Langmuir* **1999**, *15*, 553-563.

Chapter 4: Hydrodynamic Force Measurements by Colloid Probe AFM

4.1 Introduction

In recent years, the topic of the flow of Newtonian liquids in confined geometries has attracted new interest, and numerous research articles have cast doubts on the universality of the no-slip boundary condition, showing that under certain circumstances liquid slip might occur at the solid boundary. Some early experiments indicating slip, mostly involving the flow of liquids through thin lyophobic capillaries,[1] have received revived interest. A number of new experiments performed with more modern techniques have also shown evidence of boundary slip,[2, 3] although there are discrepancies in the magnitude of the measured slip length and the factors that affect liquid slip. These new experimental techniques include optical methods,[4-6] image velocimetry,[7-12] rheometry,[13, 14] quartz crystal microbalance,[15, 16] capillary flows,[17-19] and force measurements.[20, 21] (A more complete review of slip experiments is provided in Chapter 1).

Colloid probe atomic force microscopy (AFM) is one of the most accurate methods for measuring liquids slip on solid surfaces.[22-32] The probe can be driven at high approach rates, and large hydrodynamic forces can be measured at high resolution in distance Z (0.1 nm) with high force resolution. The measured slip length is derived from the comparison of the experimentally measured force by colloid probe AFM with the theoretical hydrodynamic drainage forces under the slip and no-slip boundary conditions. As described in Section 3.1, Taylor[33] provided an approximate equation to describe the hydrodynamic drainage force on a sphere approaching a flat surface perpendicularly under the no-slip boundary condition, which is

$$F_h = \frac{-6\pi\eta R^2 \dot{h}}{h} \quad (h << R), \tag{4.1}$$

where η is the viscosity of the liquid, R is the radius of the microsphere, $\dot{h}$ is the velocity of the microsphere relative and perpendicular to the substrate ($\dot{h} < 0$ corresponds to decreasing separation, $\dot{h} > 0$ corresponds to increasing separation), and h is the separation, which is the distance of closest approach of the sphere surface to the substrate surface.

Under slip boundary conditions, the hydrodynamic drainage equation has been modified by Vinogradova:[34]

$$F_h = \frac{-6\pi\eta R^2 \dot{h}}{h} f^* \quad (h << R), \tag{4.2}$$

where f^* is the correction factor for slip at two surfaces with the same slip length b (i.e. a symmetric system):

$$f^* = \frac{h}{3b}\left[\left(1+\frac{h}{3b}\right)\ln\left(1+\frac{6b}{h}\right)-1\right]. \tag{4.3}$$

The acquisition of slip results by colloid probe AFM is potentially affected by experimental errors, and the method of analysis of the data most often employed is affected by theoretical limitations. In Chapter 3, a new mathematical algorithm for the drainage of Newtonian liquids under the no-slip and slip boundary conditions that is independent of experimental data was given. This new algorithm has been demonstrated to reduce the noise in the theoretical forces over that in previous treatments and is able to fit data to provide reliable slip length and spring constant.

In this Chapter, the experimental protocol is improved by solving some important experimental problems in colloid probe AFM that are likely to cause significant errors in the measurement of slip, such as the virtual deflection in the cantilever, the friction force when the colloid probe and the solid surface are in contact, the consistency of the piezo drive rate in each measurement, the presence of nanoparticles, and the ability to measure viscosity accurately. Using this improved experimental protocol and the new mathematical algorithm from Chapter 3, reproducible slip measurements is presented, and the possible origin of some of the reported discrepancies in previously published results is explained.

4.2 Materials and Methods

In this Chapter, the cantilevers employed in the experiments have spring constants in the range of 0.24–5.40 N/m. The cantilever spring constant was measured using a modification of the hydrodynamic method by Craig and Neto,[23] which is specified in Appendix 2. Our modification includes the fitting of a value for drag length, as well as for *k* and checking that both values remain constant in an experiment. On the basis of the blind test introduced in Chapter 3, the error in the fit of the spring constant by this method is estimated to be about 3%. Di-n-octylphthalate (Aldrich, 98% pure) was used as a viscous liquid after being filtered through a Teflon filter with a pore size of 200 nm. An octadecyltrichlorosilane (OTS) self-assembled monolayer was prepared on a silicon wafer using standard procedures,[35, 36] and the resulting surfaces were hydrophobic The advancing and receding contact angles of water on the OTS-coated silicon surface were about 113° ± 1º and 108°± 3º, respectively. The equilibrium contact angle of di-*n*-octylphthalate is 45 ± 1º on the OTS-coated silicon surface. The cleaning procedure for the OTS-coated substrates included mainly sonication in ethanol and acetone. Half-way through the experiment, an additional clean with CO_2 snow-jet was introduced to reduce particle contaminants. Initially, the OTS layer on the silicon substrate was believed to be damaged by CO_2 snow-jet. However, our later experiment showed that the OTS layer still remained intact after the CO_2 treatment, as demonstrated by the AFM image and contact angle measurements (Appendix 1 contains the details of this characterisation). The hydrodynamic force measurements were taken by ramping the surfaces together over a distance of 4000 nm at an approach rate of 10–80 μm/s. The average piezo driving velocity was calculated using the raw data on piezo position and time provided by the Asylum MFP-3D AFM software. The average value of the velocity was used, as it was observed that the change in the instantaneous rate over time was less than 1% using the closed-loop scanner.

4.3 Force Curve Analysis

The direct result of an AFM force experiment is the measurement of the photodiode voltage (V) versus the displacement of the piezo transducer (nm). These raw data are

usually converted to force (N) versus separation distance (nm) between the microsphere and the plane substrate surface following an established procedure.[37] The data plotting procedures for the hydrodynamic drainage force curve in our experiments are specified in Appendix 2. Here, we only describe two significant improvements to this conversion procedure, correcting for the virtual deflection in the cantilever and for the friction force when the colloid probe and the solid surface are in contact.

I. Virtual Deflection in the Force Curves

As mentioned by Honig *et al.,*[38, 39] the Asylum MFP-3D top scanning AFM introduces an artifact into the data, a small but significant virtual deflection signal, that is not due to a real deflection of the cantilever but to the relative motion between the laser, photodiode, and cantilever during piezo movements. It is believed that this effect is caused by the elastic deformation of the Z stage of the AFM due to the pressure applied by the piezo transducer in the center of the stage and by the Z-stage flexure at the edges (see Figure 4.1a). This bending is small and elastic; therefore, it is the same during both extension and retraction and causes a virtual deflection that has the same sign and magnitude at the same position in both extension and retraction curves. The sign of the deflection can be either positive or negative. This virtual deflection cannot be due to thermal drift in the apparatus because thermal drift would not remain constant over time and would not be a function of the piezo position. However, in our experiments, the measured virtual deflection is a function of the piezo position, and is constant over time. In fact, the virtual deflection is the same in extension and reaction at the same position, even though these occur at different times. It is also known that the virtual deflection cannot be due to a real hydrodynamic effect on the cantilever, firstly because a hydrodynamic force would show hysteresis between extension and retraction curves. Second, the virtual deflection obtained for different piezo velocities was identical within the experimental error in the same experiment.

The virtual deflection is more obvious in the noncontact part of the force curve in relatively low velocity measurements (Figure 4.1b). This problem had been identified before and experimentally minimised by rocking the dials that control the diode and laser

alignment,[38, 39] but not actually removed from the experimental data. This effect is likely to be present only in top scanning AFM instruments and not necessarily in all brands.

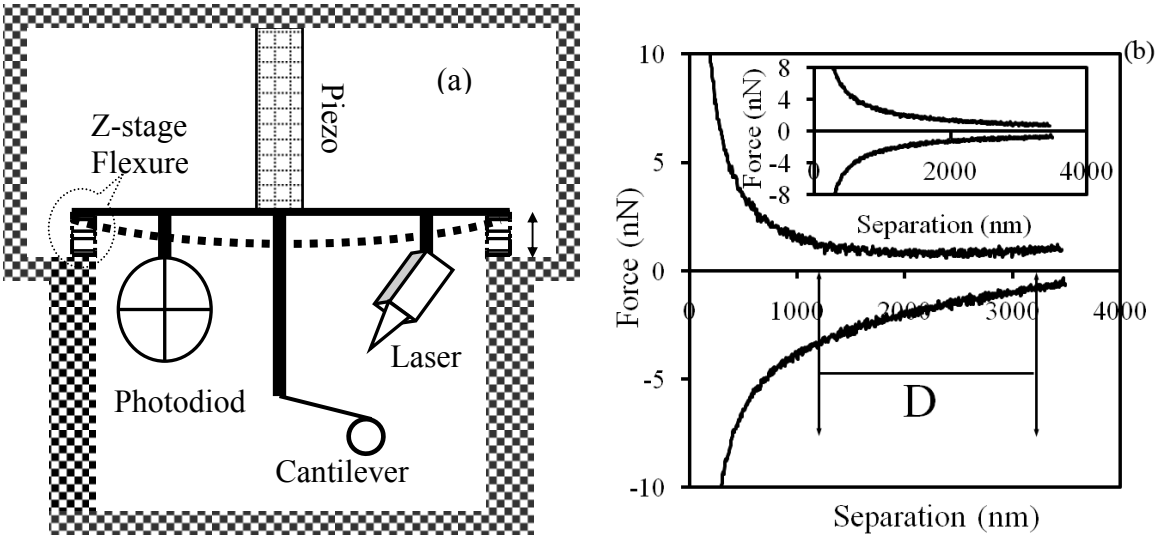

Figure 4.1 (a) Schematic of the motion of the photodiode, laser and cantilever in the Asylum MFP-3D AFM. When the piezo moves relative to the Z-stage flexure, pressure is applied to the Z stage that leads to a slight deformation, shown by the dotted line (the deformation is exaggerated in the schematic). (b) Typical hydrodynamic drainage force curve affected by the elastic stress, particularly visible in region D. The inset shows the force curve after the elastic stress correction. In this case, the piezo transducer driving velocity is 30.7 μm/s, the viscosity is 57.0 mPa s, and the spring constant is 0.94 N/m. The drag force has been subtracted.

In the following, the procedure to eliminate the virtual deflection from the experimental data is explained (more detailed provided in Appendix 2). At large separations, the deflection is caused by the drag force on the cantilever, the hydrodynamic drainage force on the colloid, and the elastic stress. Both drag and hydrodynamic deflections in extension (while the two surfaces are approaching each other) have the same magnitude but opposite signs to those in retraction (when the two surfaces are withdrawing from each other). We assume that the asymmetry introduced by the presence of the colloid probe on one side of the cantilever is negligible. However, the changing voltage (virtual deflection) due to the changing elastic stress has the same sign and slope for both the extension and the retraction. The relative slope is calculated in the separation interval *D* at large separations (Figure 4.1b). Hence, the effects due to drag and hydrodynamic drainage

forces can be removed by adding the extension and retraction force curve slopes; the remaining slope is twice the individual slope as a result of the elastic stress. Therefore, this effect can be eliminated by subtracting a straight line with the same slope from the extension and retraction curves. The corrected force curve is shown in the inset of Figure 4.1b. In all the data presented in this thesis, the virtual deflection was corrected using this method.

II. True Compliance and Zero of Separation

In a conventional AFM measurement, the slope measured in the region of the force curve close to zero separation, which is usually called the compliance region, is used to calibrate the measured vertical photodiode voltage and hence, with the measured spring constant, to quantify the measured force.[37] In this force conversion procedure, the angle of the cantilever with respect to the substrate and the torque due to the friction force as the probe slides over the substrate usually are not taken into account. Attard and co-workers[40-42] have exploited the compliance region to measure the friction coefficient in normal force measurements. They used the fact that the AFM cantilever sits at an angle of about 10º to the horizontal, and this angle causes the colloid probe to slide horizontally over the substrate as the force measurement is performed. The consequent friction force due to this sliding leads to a deflection in the cantilever in addition to that due to the normal force. The experimental data can be divided into the contact and noncontact regimes. In the noncontact regime, the separation is nonzero and the friction force is zero. In the contact regime, the separation is zero and the friction is nonzero. Because the colloid probe slides in opposite directions in extension and retraction at contact, as shown in Figure 4.2, the compliance takes on two slightly different values arising from the opposite sign of the friction force contribution in the two traces. The two different values of the compliance are a manifestation of friction at contact and can be calculated exactly when using a closed-loop instrument. Indeed in our experimental results the extension compliance is always smaller than the retraction compliance in the same run. The true calibration factor that converts the change in photodiode voltage (V) to the change in cantilever deflection (nm) in the absence of friction lies approximately halfway between the two slopes, as also shown by Honig *et al.*[38] Therefore, simply choosing one of the two values of compliance

will lead to errors in calculating the force in the noncontact regime where the drainage force must be measured and where there is no friction (details of this procedure are provided in Appendix 2). However, using the individual compliance values yields accurate values for the zero of separation, whereas using the average compliance makes it difficult to identify the location of first contact. Figure 4.3a shows an example of our measured photodiode signal as a function of piezo position. There is a slight difference between the slope on extension and retraction curves at contact, which is due to friction, as discussed above. Figure 4.3b and c shows the measured force converted using the average compliance and individual extension and retraction values of compliance, respectively. The data analysis protocol followed here is simplified on the basis of the fact that the contact region in the subsequent analysis of the drainage force can be ignored. In our analysis protocol, the individual value of the compliance is used first to find the zero of separation and then the average compliance value is used to calibrate the whole force curve.

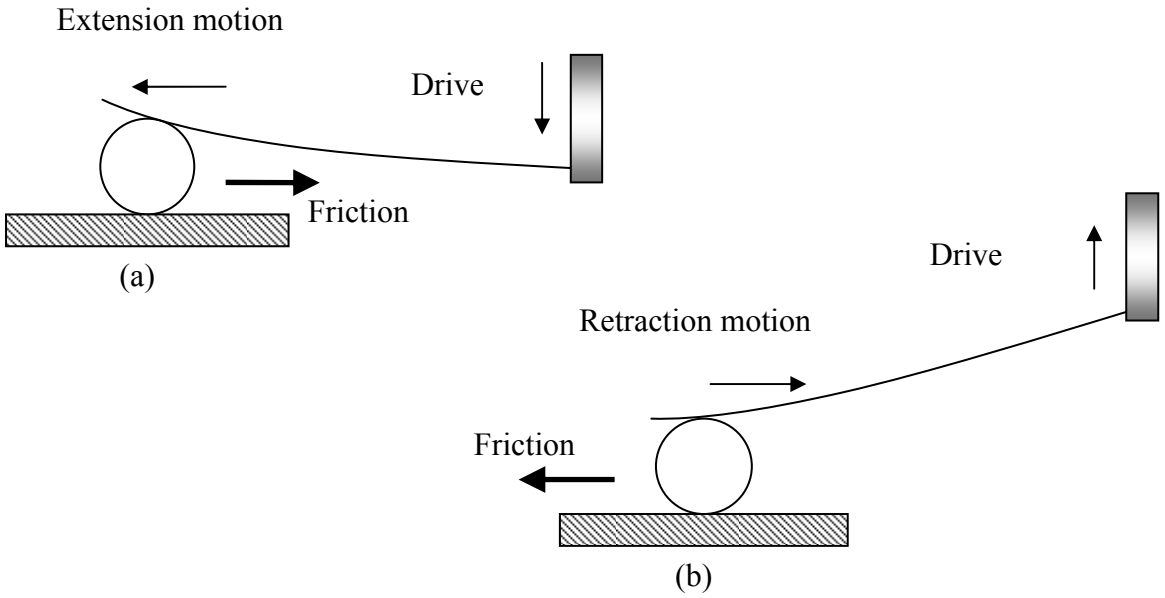

Figure 4.2 Schematic illustration of friction effects on cantilever deflection in contact. Friction on the colloid probe affects the cantilever deflection, causing an additional term in both extension (a) and retraction (b) parts of the force curve.

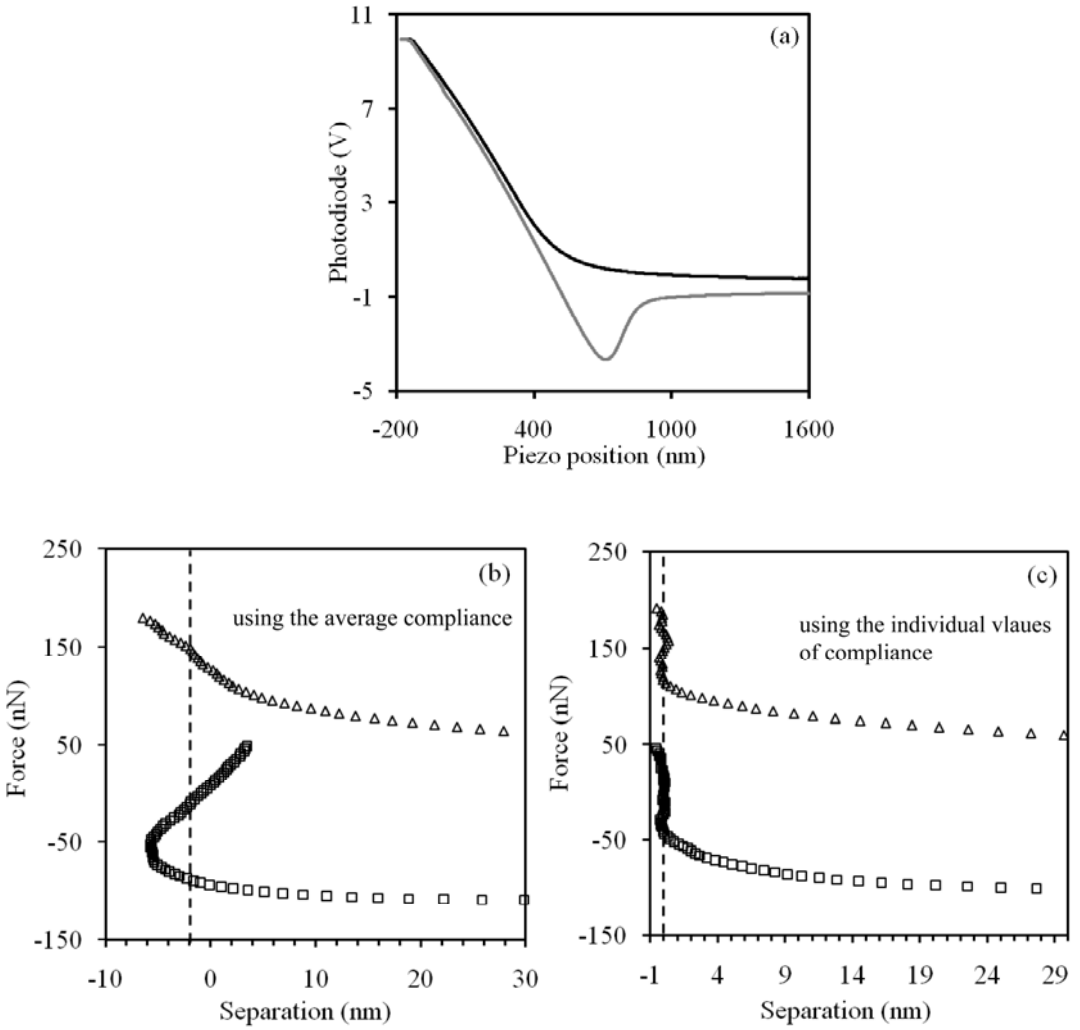

Figure 4.3 (a) Raw photodiode voltage as a function of piezo position. The black and gray lines represent extension and retraction traces, respectively. (b) Extension and retraction force curves calibrated using the average compliance. (c) Force curves calibrated by the individual extension and retraction compliances. Empty triangles and squares represent the extension force and retraction force, respectively. The spring constant is 0.61 N/m, the viscosity is 47.7 mPa s, and the driving velocity is 70.4 μm/s.

4.4 Results

Seven different experiments were performed using rectangular MikroMasch tipless cantilevers A–F with different spring constant (details shown in Table 4.1). For each experiment, force measurements were performed at one or more positions on the OTS-coated surface. At each position, a series of force curves were collected at piezo transducer driving velocities of 10, 15, 20, 30, 40, 50, 60, 70 and 80 μm/s. The collected force data

were analysed following the force analysis procedure in Appendix 2. All of the theoretical hydrodynamic forces were generated using the mathematical algorithm developed in Chapter 3. The slip length was obtained from the fit of the theoretical slip model (Eqs.4.2 and 4.3) to the experimental force.

Table 4.1 Average Slip Length Measured in Seven Experiments at Several Contact Positions[a]

Expt	Position Number	Cantilever type	Spring constant (N/m)	Average slip length *b* (nm)	Standard deviation of *b* (nm)
I	1	A	0.94	25.8	4.7
I	2	A	0.94	79.8	8.0
II	3	B	0.55	26.0	6.8
III	4	C	0.36	69.1	1.7
III	5	C	0.36	56.5	3.7
IV	6	D	0.24	25.2	1.3
IV	7	D	0.24	24.9	1.2
V	8	E	0.53	31.1	1.6
V	9	E	0.53	30.0	3.0
V	10	E	0.53	60.6	2.3
VI	11	F	0.61	26.1	2.5
VI	12	F	0.61	24.3	4.2
VI	13	F	0.61	23.9	5.4
VII*[b]	14	G	5.40	28.3	3.1
VII*[b]	15	G	5.40	25.7	1.0

[a] Each slip length reported is the average calculated over nine approach velocities.

*[b] In all experiments, the substrate surface was cleaned by sonication in ethanol and acetone. In experiment VII a final CO_2 snow-jet cleaning procedure was also added. The slip lengths at very low velocities (10 and 15 μm/s) are not considered because of the fact that this stiff cantilevers are not as sensitive as the softer ones and the measured forces cannot be fitted either by the slip or the no-slip force using the spring constant and slip length used at all other velocities.

A typical example of the force curve measured at a piezo driving velocity of about 30 μm/s is shown in

Figure 4.4. The Taylor expression (Eq. 4.1) is used as the theoretical hydrodynamic force under the no-slip boundary condition (---), and the Vinogradova expression (Eqs 4.2 and 4.3) is used as the theoretical hydrodynamic force under the slip boundary condition (—). Although our system is asymmetric, in order to simplify the calculation, the Vinogradova expression for a symmetric system is employed. This aspect of asymmetric and symmetric systems and the corresponding equations employed are addressed and resolved in Chapter 6. The experimental hydrodynamic force is consistently lower than that expected for a no-slip condition, and the data are best fit using the Vinogradova slip expression along the whole force curve down to separations of about 150 nm by varying the slip length *b*. The best fitted slip length *b* in this force curve is 32 nm. The algorithm used to calculate the theoretical curve is given in Chapter 3.

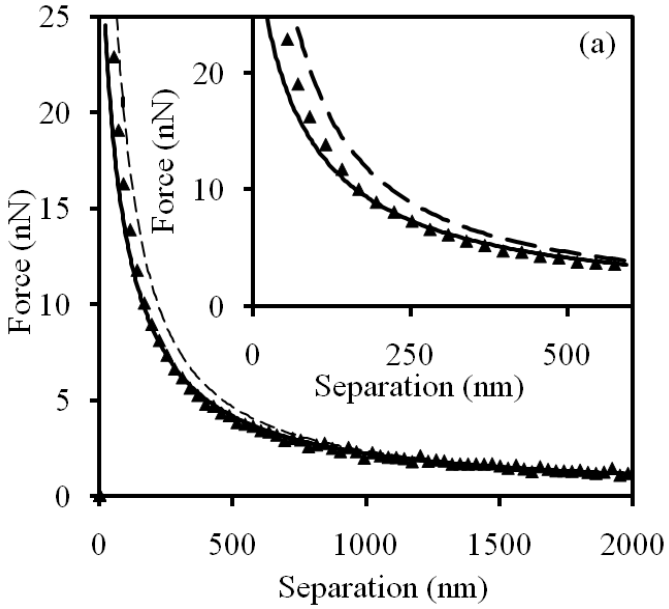

Figure 4.4 Experimental (▲) and theoretical (line) hydrodynamic forces acting on a silica microsphere approaching an OTS-coated silicon substrate in di-*n*-octylphthalate. The dashed line (---) is the theoretical no-slip force, and the solid line (—) is the slip hydrodynamic force. The spring constant is 0.53 N/m; the piezo-drive velocity is about 30 μm/s; the radius of the microsphere is 9.26 μm; the viscosity of liquid is 48.6 mPas in this measurement; and the fitted slip length is 32 nm.

The average values of slip length from the seven different experiments labeled with Roman numerals are presented in Table 4.1. In each experiment, force measurements were performed at several contact positions, which are identified by the position number in Table 4.1, column 2. The average values of slip length and the standard deviation were obtained from the slip length fitted to individual force curves measured at different velocities at the same position. Each slip length in the Table is the average of approximately nine drive velocities. At each velocity and position, one force curve was fitted and used for that average. In a few cases, several force curves were collected in the same position at the same velocity and then analysed to confirm the reproducibility of the measured hydrodynamic drainage force and slip length. In most experiments, the average slip lengths are in the range of 24–31 nm. However, in experiments I, III and V the measured slip lengths are initially the same value and then they suddenly increase in the same experiment when changing to a different position. This effect is clearly illustrated in Figure 4.5.

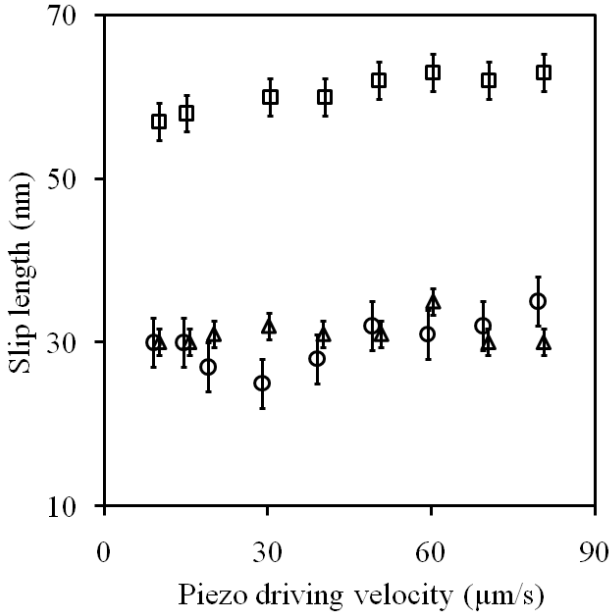

Figure 4.5 Measured slip length as a function of the piezo transducer driving velocity in experiment V. The empty triangles represent the slip lengths measured in the first position at different driving velocities, and the average slip length is 31.1 ± 1.6 nm. Empty circles represent the slip lengths measured in the second position, and its average slip length is 30.0 ± 3.0 nm. For this series, the values on the abscissa are all shifted to the left by 1μm/s

in order to avoid data overlap. Empty squares are the measured slip lengths in the third position, and the average slip length is 60.6 ± 2.3 nm.

Figure 4.5 shows the values of slip length against the piezo transducer driving velocity measured in experiment V. In this experiment, the hydrodynamic drainage forces were measured at three different positions on the same surface. At the first two positions (○ and Δ), the measured slip lengths were around 30 nm at all velocities. However, at the third position (□) the measured slip length increased to approximately 61 nm at all velocities.

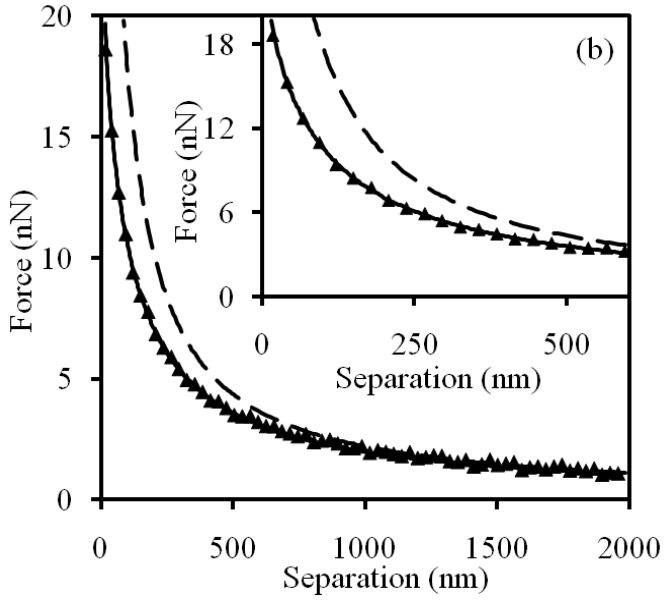

Figure 4.6 Experimental (▲) and theoretical (line) hydrodynamic forces acting on a silica microsphere approaching an OTS-coated silicon substrate in di-*n*-octylphthalate. The dashed line (---) is the theoretical no-slip force, and the solid line (—) is the slip hydrodynamic force. The force presented here was acquired in the same experiment as in Figure 4.4, but at different positions. All the experimental parameters are the same as in Figure 4.4, only the viscosity of the liquid is slight lower in this measurement, and it is 44.9 mPas. The best fitted slip length is 60 nm.

In these seemingly identical experiments (Experiments V8–V10), the fitted individual slip lengths are significantly different in Experiments V8 and V9 compared to Experiment V10. A typical force example from Experiment V8 is shown in Figure 4.4. It has a fitted slip length of 32 nm. Another typical force example from Experiment V10 and

measured at a similar piezo driving velocity (30 μm/s) as that in Figure 4.4 is shown in Figure 4.6. In this force curve, the best fitted slip length is 60 nm.

An alternative fit of these two typical force curves is shown in Figure 4.7. The force curve (▲) with the large slip length (b = 60 nm) was shifted to the right (i.e. to larger separations) by 56 nm. After this shift to the right, the shifted force curve (●) can be made to agree with the one with the small slip length (□) over all shifted separations greater than 56 nm and fitted with the same slip length (b = 32 nm).

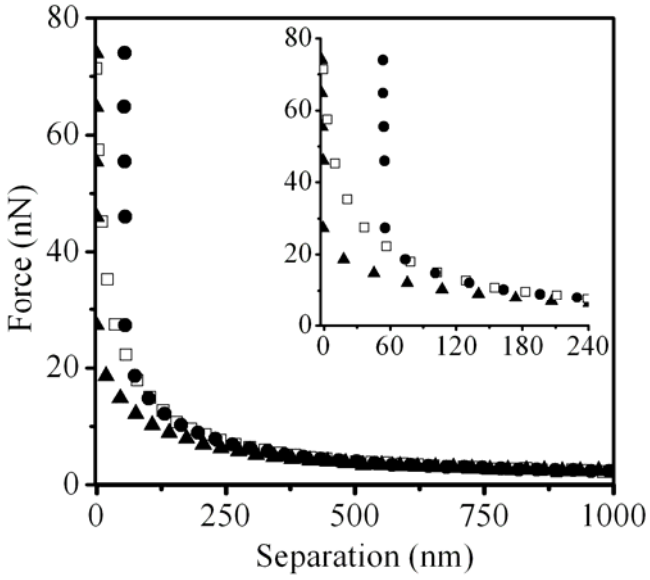

Figure 4.7 The same two experimental hydrodynamic force measurements shown in Figure 4.4 and Figure 4.6. Empty squares correspond to the experimental force shown in Figure 4.4 with a slip length b = 32 nm. Filled triangles correspond to the experimental force shown in Figure 4.6 with a slip length b = 60 nm. Filled circles are the force represented by filled triangles but shifted to the right by 56 nm. Inset: zoom in the small separation region of force curves.

One possible explanation for this behaviour comes from close inspection of the experimental conditions. Two AFM tapping-mode images of OTS-coated silicon wafer substrates are shown in Figure 4.8. The substrate in Figure 4.8a was cleaned only by sonication in distilled ethanol and acetone, and many nanoparticles, possibly contaminants, are visible here. The largest feature, highlighted by circle 1, is about 19 nm high and 78–176 nm wide. Feature 2 is approximately 3 nm high and 58–117 nm wide. The second

substrate in Figure 4.8b was cleaned by the same method plus an additional CO_2 snow-jet cleaning procedure[43] and has fewer nanoparticles.

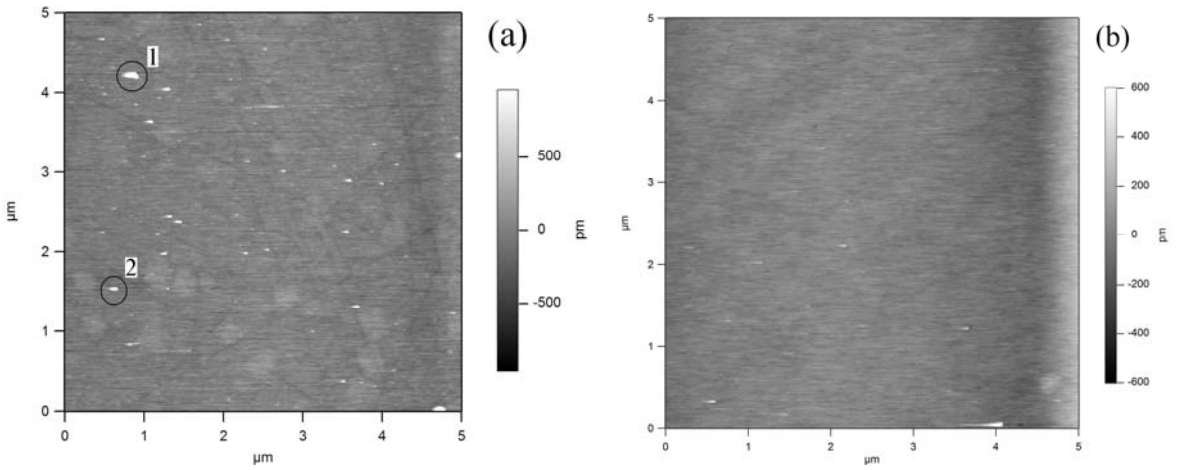

Figure 4.8 AFM images of OTS-coated silicon wafers cleaned by different methods. (a) This OTS-silicon wafer was cleaned by sonication in distilled ethanol and acetone and shows several contaminant nanoparticles. (b) This OTS-silicon wafer was cleaned by sonication in distilled ethanol and acetone, followed by CO_2 snow-jet cleaning.

4.5 Discussion

In this Chapter a best practice experimental protocol and data analysis for hydrodynamic force measurements were developed, which improve the reliability of the force measurements and eliminate some of the potential sources of error in colloid probe AFM based slip measurements. The key elements of our best practice protocol are the following:

(1) In our study, a one-component viscous liquid (di-*n*-octylphthalate) was used as opposed to the highly concentrated two-component aqueous solutions often used as viscous liquids in hydrodynamic measurements, such as sucrose solutions.[24, 27, 38, 44] This was done to avoid the possibility that the observed slip effect might be due to the depletion of one component of the solution at the solid surface, causing a local variation in the viscosity.[3]

(2) As in other published experiments, we used a closed-loop piezo transducer drive for all experiments because closed-loop operation provides a truly constant piezo

transducer driving velocity. In contrast, in an open-loop configuration, the piezo transducer driving velocity varies (by up to 50%) during each run because of the nonlinear response of the piezo transducer.[39, 45] In the theoretical hydrodynamic drainage force calculation, the piezo transducer driving velocity is assumed to be constant in each run, and the consequent rate of change of separation is calculated at each step.

(3) In our experiments, a thermocouple is placed in the liquid to record the temperature continuously and allow for the accurate calculation of the viscosity of the liquid in each run. The viscosity of the liquid is an important parameter in predicting the theoretical hydrodynamic force, see Eqs 4.1 and 4.2. During AFM force measurements, the electronic components heat up, which leads to an increase in the temperature of the liquid in the liquid cell. In a typical experiment, the liquid temperature was measured to increase by about 1.5–3ºC (see Chapter 2 Section 2.3), consequently changing the viscosity.

(4) In the force analysis, the improved theoretical calculation presented in Chapter 3 was used for the drainage force measured by colloid probe AFM. This theoretical calculation is independent of actual experimental data, which reduces noise in the model over that from previous treatments. The blind test shows that this theoretical calculation can provide a reliable, accurate fitting of the slip length, within an average error of about 2 nm, and of the spring constant within an error of about 3%. This is the first time the error in the fit of the data can be reliably predicted, and indeed it shows one of the lowest uncertainties in the spring constant yet reported.

(5) The hidden problems in the analysis protocol of force curves were corrected, which include eliminating the effects of artificial deflection of the cantilever due to friction in the contact area and changing elastic stress on the photodiode–laser assembly.

(6) In our experiments, each colloid probe was scanned using the inverse AFM imaging method[46] before each experiment to get the topography of the contact area of the microsphere. All of the microspheres used were checked to be smooth enough for experiments, as shown in Figure 2.3 and Figure 2.4 in Chapter 2. Therefore, asperities or large flattened areas on microspheres can be excluded as contributing to the slip length in our experiments, as suggested in the work of Guriyanova and co-workers.[26]

(7) By repeating experiments several times and at different locations on the substrate, an important possible source of error in AFM slip measurements was identified. In repeat experiments at different locations, reproducible slip lengths of 24–31 nm were measured, and at the same time in some force curves unusually large slip lengths were found, such as shown in experiments I, III, and V (Table 4.1). Figure 4.6, Figure 4.7 and Figure 4.8 show that there is a simple explanation for the unusually high slip length measured in some cases. By shifting the zero of separation of the force curve with the larger slip length, this force curve can be superimposed almost completely with the measured force fitted with a smaller slip length. This may indicate that there is an uncertainty in the measured zero of separation for the force curve with a large slip length, which is similar to the principle of large slip length due to asperities proposed by Guriyanova et al.[26] We believe that this uncertainty might be due to nanoparticle contamination on the substrate surface, as also hypothesized by other groups,[39, 47] with the shifted distance being the size of the nanoparticle contaminants. In Chapter 3, it was indeed proven that nanoparticle contamination can cause large slip length using our theoretical model. Figure 4.8a shows that nanoparticle contaminants exist on the typical substrate surface. Although these particular contaminants are very small and can be removed by CO_2 snow-jet cleaning, it is possible that contaminants are introduced into the system during the assembly and loading of the AFM liquid cell because of the uncontrolled ambient environment. It is suggested that the CO_2 snow-jet cleaning procedure should be used in all force work. Therefore, particle contamination on the surface may explain the large slip lengths measured in some of our experiments (I2, III4, III5 and V10 in Table 4.1) and in some published ones.

We believe that the results provide an important contribution to the recent debate on the existence of slip, its magnitude, and its dependence on various experimental parameters. Honig and Ducker[38,39] provided evidence that the measured hydrodynamic drainage forces were consistent with the no-slip boundary condition in a Newtonian, highly concentrated sucrose solution on both hydrophilic and hydrophobic solids and in silicon oil on the solvophilic surface. Although they did measure a constant slip length of up to 33 nm in some cases, they argued that these variations may have been due to the existence of a water layer. Henry and Craig[27] reported that the AFM cantilever shape affects the fitted

slip length, which could explain the difference between some published results.[38] They demonstrated that there was no evidence of boundary slip at a smooth hydrophilic surface if a rectangular cantilever was used, but an apparent slip length was measured using V-shaped cantilevers. In the paper by Rodrigues *et al*.,[44] the stiffness of the cantilever, the viscosity, and the scanning velocity were all shown to affect the boundary conditions to some degree simultaneously. They found that qualitatively the softer the cantilever, the larger the slip length. They also found that increasing the velocity of the colloid probe or using more viscous liquids also led to increased slip. In their studies, for piezo transducer driving velocities (around 40–55 μm/s) and very low solution viscosity (0.89 mPa s), the measured hydrodynamic force on hydrophilic surfaces was consistent with no-slip conditions unless the spring constant was under 0.06 N/m.

In our experiments (results summarised in Table 4.1), rectangular cantilevers with spring constant between 0.24–5.40 N/m and piezo transducer driving velocities of about 10–80 μm/s were used; the viscosity of the liquid studied was large, above 40 mPas with the exact viscosity depending on the temperature in each measurement. Our results show that in a partially wetting system the experimental hydrodynamic force is well fitted by a hydrodynamic theory with a slip boundary condition at the liquid–solid interface. It is found that the measured slip length is independent of the cantilever stiffness or length, and the drive velocity. One possible reason for Rodrigues' opposite conclusion (larger slip lengths with softer cantilever) could be the variation in the drag force with separation. This explanation is suggested because the drag force is the only force dependent upon the shape of the cantilever. In Chapter 3, it was demonstrated that the drag variation can be neglected for relatively stiff cantilevers but not for relatively soft cantilevers. If the variation in drag is neglected for a relatively soft cantilever, it will cause a significant overestimation of the slip length. Chapter 5 contains the explicit demonstration that the drag force on cantilevers causes artifacts in the measurement. In the work of Honig *et al*,[38, 39] a different way to fit the slip length was used. This method approximates the Vinogradova expression based on a linear expansion, which is valid for large separations, $6b/h << 1$.[30, 48] However, in the large separation regime, noise coming from resonance vibration, thermal noise in the cantilever, and electronic noise in the photodiode are magnified by plotting the inverse of

the measured force, which creates difficulties in determining the correct slip length. However, going to the small separation regime to minimise the noise makes the linear expansion invalid.

4.6 Conclusions

In this Chapter, a best practice experimental protocol to measure hydrodynamic forces with colloid probe AFM was established. This protocol highlights the need for tight control over experimental conditions in slip measurements, such as extremely careful surface cleaning, the use of one-component liquid, temperature monitoring, and repeat measurements in different locations. This protocol, in conjunction with our new theoretical calculations, leads to reproducible slip length values and to spring constant values with the lowest uncertainty yet reported. The evidence for this claim is the blind test results in Chapter 3, and it is also confirmed by measuring slip in two independent systems in Chapter 6 with consistent results. The developed experimental protocol could benefit measurements of slip with techniques other than AFM, such as SFA.

Our results are consistent with a slip boundary condition in Newtonian viscous liquid, di-*n*-octylphthalate, on partially wetted surfaces. We found that the measured slip length is independent of the spring constant and piezo transducer driving velocity. We showed that our best practice protocol, and in particular, the use of several repeated measurements, can detect the presence of nanoparticles, which is displayed by unusually large slip lengths in some measurements.

References

1. Vinogradova, O. I. Slippage of water over hydrophobic surfaces. *Int. J. Miner. Process*. **1999**, *56*, 31-60.

2. Lauga, E.; Brenner, M. P.; Stone, H. A., Microfluidics: The No-slip Boundary Condition. In *Handbook of Experimental Fluid Dynamics*, Foss, J.; Tropea, C.; Yarin, A., Eds. Springer: New York, 2005; Chapter 15.

3. Neto, C.; Evans, D. R.; Bonaccurso, E.; Butt, H. J.; Craig, V. S. J. Boundary slip in Newtonian liquids: a review of experimental studies. *Rep. Prog. Phys.* **2005**, *68*, 2859-2897.

4. Joly, L.; Ybert, C.; Bocquet, L. Probing the nanohydrodynamics at liquid-solid interfaces using thermal motion. *Phys. Rev. Lett.* **2006**, *96*, 46101.

5. Yordanov, S.; Best, A.; Butt, H.-J.; Koynov, K. Direct studies of liquid flows near solid surfaces by total internal reflection fluorescence cross-correlation spectroscopy. *Optics Express* **2009**, *17*, 21149-21158.

6. Vinogradova, O. I.; Koynov, K.; Best, A.; Feuillebois, F. Direct measurements of hydrophobic slippage using double-focus fluorescence cross-correlation. *Phys. Rev. Lett.* **2009**, *102*, 118302.

7. Bouzigues, C. I.; Tabeling, P.; Bocquet, L. Nanofluidics in the debye layer at hydrophilic and hydrophobic surfaces. *Phys. Rev. Lett.* **2008**, *101*, 114503.

8. Brigo, L.; Natali, M.; Pierno, M.; Mammano, F.; Sada, C.; Fois, G.; Pozzato, A.; Zilio, S. d.; Tormen, M.; Mistura, G. Water slip and friction at a solid surface. *J. Phys.: Condens. Matter* **2008**, *20*, 354016.

9. Huang, P.; Breuer, K., S. Direct measurement of slip length in electrolyte solutions. *Phys. Fluids* **2007**, *19*, 028104.

10. Lasne, D.; Maali, A.; Amarouchene, Y.; Cognet, L.; Lounis, B.; Kellay, H. Velocity profiles of water flowing past solid glass surfaces using fluorescent nanoparticles and molecules as velocity probes. *Phys. Rev. Lett.* **2008**, *100*, 214502.

11. Park, H. M.; Kim, T. W. Simultaneous estimation of zeta potential and slip coefficient in hydrophobic microchannels. *Anal. Chim. Acta* **2007**, *593*, 171-177.

12. Tsai, P.; Peters, A. M.; Pirat, C.; Wessling, M.; Lammertink, R. G. H.; Lohse, D. Quantifying effective slip length over micropatterned hydrophobic surfaces. *Phys. Fluids* **2009**, *21*, 112002.

13. Choi, C.-H.; Kim, C.-J. Large slip of aqueous liquid flow over a nanoengineered superhydrophobic surface. *Phys. Rev. Lett.* **2006**, *96*, 066001.

14. Lee, C.; Kim, C.-J. Maximizing the Giant Liquid Slip on Superhydrophobic Microstructures by Nanostructuring Their Sidewalls. *Langmuir* **2009**, *25*, 12812-12818.

15. Willmott, G. R.; Tallon, J. L. Measurement of Newtonian fluid slip using a torsional ultrasonic oscillator. *Phys. Rev. E* **2007**, *76*, 066306.

16. Zhuang, H.; Lu, P.; Lim, S. P.; Lee, H. P. Effects of interface slip and viscoelasticity on the dynamic response of droplet quartz crystal microbalances. *Anal. Chem.* **2008**, *80*, 7347-7353.

17. Hasegawa, T.; Ushida, A.; Narumi, T. Huge reduction in pressure drop of water, glycerol/water mixture, and aqueous solution of polyethylene oxide in high speed flows through micro-orifices. *Phys. Fluids* **2009**, *21*, 052002.

18. Joseph, P.; Cottin-Bizonne, C.; Benoit, J. M.; Ybert, C.; Journet, C.; Tabeling, P.; Bocquet, L. Slippage of water past superhydrophobic carbon nanotube forests in microchannels. *Phys. Rev. Lett.* **2006**, *97*, 156104.

19. Ulmanella, U.; Ho, C. M. Molecular effects on boundary condition in micro/nanoliquid flows. *Phys. Fluids* **2008**, *20*, 101512.

20. Cross, B.; Steinberg, S.; Cottin-Bizonne, C.; Rieu, J.-P.; Charlaix, E. Boundary flow of water on supported phospholipid films. *Europhys. Lett.* **2006**, *73*, 390-395.

21. Steinberger, A.; Cottin-Bizonne, C.; Kleimann, P.; Charlaix, E. High friction on a bubble mattress. *Nat. Mater.* **2007**, *6*, 665-668.

22. Bhushan, B.; Wang, Y.; Maali, A. Boundary slip study on hydrophilic, hydrophobic, and superhydrophobic surfaces with dynamic atomic force microscopy. *Langmuir* **2009**, *25*, 8117-8121.

23. Craig, V. S. J.; Neto, C. In situ calibration of colloid probe cantilevers in force microscopy: hydrodynamic drag on a sphere approaching a wall. *Langmuir* **2001**, *17*, 6018-6022.

24. Craig, V. S. J.; Neto, C.; Williams, D. R. M. Shear-dependent boundary slip in an aqueous Newtonian liquid. *Phys. Rev. Lett.* **2001**, *87*, 054504

25. Guriyanova, S.; Bonaccurso, E. Influence of wettability and surface charge on the interaction between an aqueous electrolyte solution and a solid surface. *Phys. Chem. Chem. Phys.* **2008**, *10*, 4871-4878.

26. Guriyanova, S.; Semin, B.; Rodrigues, T. S.; Butt, H. J.; Bonaccurso, E. Hydrodynamic drainage force in a highly confined geometry: role of surface roughness on different length scales. *Microfluid. Nanofluid.* **2010**, *8*, 653-663.

27. Henry, C. L.; Craig, V. S. J. Measurement of no-slip and slip boundary conditions in confined Newtonian fluids using atomic force microscopy. *Phys. Chem. Chem. Phys.* **2009**, *11*, 9514-9521.

28. Honig, C. D. F.; Ducker, W. A. No-slip hydrodynamic boundary condition for hydrophilic particles. *Phys. Rev. Lett.* **2007**, *98*, 028305.

29. Maali, A.; Cohen-Bouhacina, T.; Kellay, H. Measurement of the slip length of water flow on graphite surface. *Appl. Phys. Lett.* **2008**, *92*, 053101.

30. McBride, S. P.; Law, B. M. Viscosity-dependent liquid slip at molecularly smooth hydrophobic surfaces. *Phys. Rev. E* **2009**, *80*, 060601.

31. Neto, C.; Craig, V. S. J.; Williams, D. R. M. Evidence of shear-dependent boundary slip in Newtonian liquids. *Eur. Phys. J. E* **2003**, *12*, S71-S74.

32. Vinogradova, O. I.; Yakubov, G. E. Surface roughness and hydrodynamic boundary conditions. *Phys. Rev. E* **2006**, *73*, 045302.

33. Horn, R. G.; Vinogradova, O. I.; Mackay, M. E.; Phan-Thien, N. Hydrodynamic slippage inferred from thin film drainage measurements in a solution of nonadsorbing polymer. *J. Chem. Phys.* **2000**, *112*, 6424-6433.

34. Vinogradova, O. I. Drainage of a thin liquid-film confined between hydrophobic surfaces. *Langmuir* **1995**, *11*, 2213-2220.

35. Brzoska, J. B.; Ben Azouz, I.; Rondelez, F. Silanization of solid substrates: a step towards reproducibility. *Langmuir* **1994**, *10*, 4367-4373.

36. Wasserman, S. R.; Tao, Y.-T.; Whitesides, G. M. Structure and reactivity of alkylsiloxane monolayers formed by reaction of alkyltrichlorosilanes on silicon substrates. *Langmuir* **1989**, *5*, 1074-1087.

37. Ducker, W. A.; Senden, T. J.; Pashley, R. M. Direct measurement of colloidal forces using an atomic force microscope. *Nature* **1991**, *353*, 239-241.

38. Honig, C. D. F.; Ducker, W. A. Thin film lubrication for large colloidal particles: experimental test of the no-slip boundary condition. *J. Phys. Chem. C* **2007**, *111*, 16300-16312.

39. Honig, C. D. F.; Ducker, W. A. Squeeze film lubrication in silicone oil: experimental test of the no-slip boundary condition at solid-liquid interfaces. *J. Phys. Chem. C* **2008**, *112*, 17324-17330.

40. Stiernstedt, J.; Rutland, M. W.; Attard, P. A novel technique for the in situ calibration and measurement of friction with the atomic force microscope. *Rev. Sci. Instrum.* **2005**, *76*, 083710.

41. Attard, P.; Carambassis, A.; Rutland, M. W. Dynamic surface force measurement. 2. Friction and the atomic force microscope. *Langmuir* **1999**, *15*, 553-563.

42. Attard, P. Friction, adhesion, and deformation: dynamic measurements with the atomic force microscope. *J. Adhes. Sci. Technol.* **2002**, *16*, 753-791.

43. Sherman, R.; Hirt, D.; Vane, R. Surface cleaning with the carbon dioxide snow Jet. *J. Vac. Sci. Technol. A* **1994**, *12*, 1876-1881.

44. Rodrigues, T. S.; Butt, H. J.; Bonaccurso, E. Influence of the spring constant of cantilevers on hydrodynamic force measurements by the colloidal probe technique. *Colloids & Surfaces A: Physicochem. Eng. Aspects* **2010**, *354*, 72-80.

45. Vinogradova, O. I.; Yakubov, G. E. Dynamic effects on force measurements. 2. Lubrication and the atomic force microscope. *Langmuir* **2003**, *19*, 1227-1234.

46. Neto, C.; Craig, V. S. J. Colloid probe characterization: radius and roughness determination. *Langmuir* **2001**, *17*, 2097-2099.

47. Cottin-Bizonne, C.; Cross, B.; Steinberger, A.; Charlaix, E. Boundary slip on smooth hydrophobic surfaces: Intrinsic effects and possible artifacts. *Phys. Rev. Lett.* **2005**, *94*, 056102.

48. Cottin-Bizonne, C.; Steinberger, A.; Cross, B.; Raccurt, O.; Charlaix, E. Nanohydrodynamics: The intrinsic flow boundary condition on smooth surfaces. *Langmuir* **2008**, *24*, 1165-1172.

Chapter 5 Shear Rate Dependent Slip

5.1 Introduction

Despite the physical mechanisms that lead to slip being still unknown, the factors which determine the occurrence of slip and affect its magnitude have been receiving much attention in the past decade, such as fluid properties or surface properties (see section 1.5 in Chapter 1). Here, we focus on the effect of shear rate on interfacial slip.

Navier [1] introduced the "slip length", *b,* as the distance beyond the liquid/solid interface at which the liquid velocity extrapolates to zero. In this terminology, the velocity of the liquid at the interface with the solid, v_s, is related to the slip length by the condition

$$v_s = b\gamma, \tag{5.1}$$

where $\gamma = dv/dz$ is the local shear rate at the surface, and the direction z is perpendicular to the surface. It is usually assumed that the slip length b is a constant independent of shear rate, as in the Vinogradova expression[2] that is commonly used to fit hydrodynamic drainage force experiments. The hydrodynamic drainage force acting on a sphere approaching a flat surface in a viscous liquid as given by Vinogradova is:[2]

$$F_h = -6\pi\eta R^2 \dot{h} f^* / h_0, \tag{5.2}$$

where η is the viscosity of the liquid, R is the radius of the sphere, $\dot{h}$ is the rate of change of separation of the sphere perpendicular to the substrate, h_0 is the distance of closest approach of the sphere to the substrate, and f^* is the correction factor for symmetric slip at two surfaces: $f^* = h_0/3b[(1+h_0/6b)\ \ln(1+6b/h_0) - 1]$, where the constant slip length b appears (no-slip means $b = 0$ and $f^* = 1$).

In several studies, the constant slip length expression by Vinogradova has been used to fit drainage force measurements, and the slip length was seen to be independent of the

piezo velocity at which the two surfaces were driven toward each other. [3-9] There are three reasons why shear rate dependence may have overlooked in these cases. Firstly, these experiments only varied piezo velocity by about one order of magnitude. We instead focus on the actual shear rate, which changes by several orders of magnitude within the same force measurement, and which is a function of probe velocity, distance from the central axis, and surface separation. The AFM probes a much larger range of shear rates than other techniques. In velocimetry experiments, shear rate varies from 0–5000 s^{-1}.[10-12] In surface force apparatus (SFA) measurements, the typical shear rate are much lower.[3] For our AFM measurements, shear rate can vary from about 10^1 s^{-1} to 10^5 s^{-1} in the same experiment, due to the decreasing separation between the two surfaces. Therefore it is important to focus the slip fit on the small separation-high shear rate-regions of the force curves, where interesting phenomena related to shear rate could occur.

Secondly, some data analysis procedures commonly used to fit the slip length are intrinsically insensitive to the shear rate dependence.[3, 4, 9] In these cases, the extrapolated slip length is not affected by the high shear rate region at small separations. The details of this argument will be discussed later in the Chapter. Thirdly, the Vinogradova constant slip force expression (Eq. 5.2) is based on the slip length being constant with shear rate, so there is an intrinsic contradiction in trying to use this expression to draw a conclusion about shear rate dependent slip.

There are several instances in which slip has been observed to depend on driving rates (experiments) or shear rates (simulations). A few experiments performed with force measurements[13-17] and microchannels[18, 19] have suggested that slip in Newtonian liquids might increase with increasing driving rates or flow rates. A strong shear dependence of the slip length was measured with the surface force apparatus (SFA) by Zhu and Granick,[15] with slip lengths increasing from zero to micrometres with increasing flow rates. Craig *el al* observed that the slip length increased with increasing approach velocity in two different liquids by AFM.[13, 17] Choi *et al.*[19] found slip lengths varying approximately linearly with shear rates with values of approximately 30 nm at a shear rate of 10^5 s^{-1} using a high precision flow metering system. The observations of shear dependent slip have been explained in the literature[20] with a few mechanisms, such as contamination in the sample

preparation, shear-induced gas layers on the hydrophobic surface, and a flow induced reduction in viscosity. In this Chapter we discuss an alternative molecular mechanism which could explain the dependence of slip length on shear rate.

Molecular dynamics (MD) simulations also observed shear-dependent slip.[21-24] Thompson *et al.*[23] found that slip occurs above a critical (high) shear rate and it increases with shear rate as $Ls = L_s^0\left[1-\left(\dot{\gamma}/\dot{\gamma}_c\right)\right]^{-\alpha}$. Ho *et al.*[21] recently found that slip length decreases as the shear rate decreases in qualitative agreement with the results by Thompson.[23] However, the simulation by Pahlavan and Freund[22] provides an opposite nonlinear relationship of the slip length with the shear rate in the form of $Ls = L_s^0\left[1-\left(\dot{\gamma}/\dot{\gamma}_{no\,slip}\right)^{\alpha}\right]^{\beta}$ (with α = 1.25, β = 4 in their case). Importantly, so far the shear rates employed in nearly all MD simulations have been extremely high, $\gamma \sim 10^{11}$ s^{-1}. These values cannot be achieved experimentally, so it is possible that the slip regime observed in simulations in very different to that observed in experiments.

In Chapter 4, drainage force measurements were well-fitted with the Vinogradova constant slip expression (Eq. 5.2) at surface separations between 5000 nm and about 150 nm, but at lower separations the measured forces were consistently higher than the constant slip model (Figure 4.4).[8, 25] This higher than expected force suggests that the slip length is decreasing with increasing separation, which would occur if it were shear rate dependent, since the local shear rate increases with decreasing separation. In this Chapter, we present a new theoretical model for slip, which includes a shear-dependent component of the slip length, and we use it to fit drainage forces obtained in seven colloid probe atomic force microscopy (AFM) experiments, addressing in particular the short-separation region (< 150 nm). The experimental detail for the AFM force measurements presented here are the same as those presented in Chapter 4.

5.2 Theory on the Shear Dependence of Slip Flows

There is a sound physical reason to introduce a shear-dependent slip length. In colloid probe AFM drainage force measurements (Figure 5.1), the local shear rate $\gamma = dv/dz$ is an inverse function of separation, so the local shear rate goes to infinity as the

separation goes to zero. According to Eq. 5.1, a constant slip length would lead the slip velocity v_s to become infinite as the separation goes to zero. However, the slip velocity v_s cannot be infinite due to the finite friction force between the liquid and the solid. The only way to avoid the unphysical divergence in the slip velocity of the fluid at the surface is for the slip length in Eq. 5.1 to decrease with increasing shear rate.

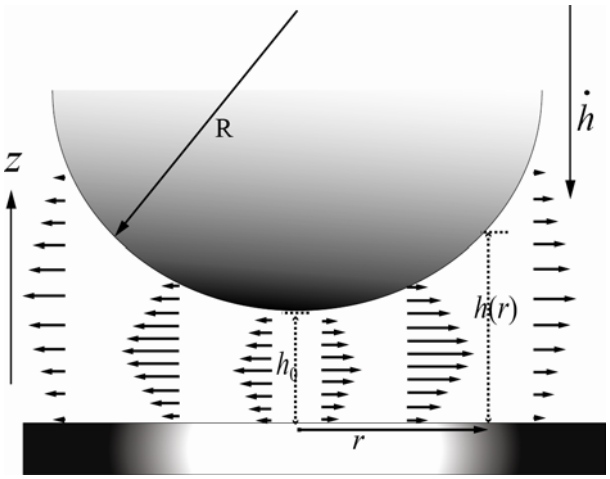

Figure 5.1 Drainage of a thin liquid film confined between a colloid probe of radius R approaching a flat surface. The distance of closest approach between the two surfaces is h_0. The distance between a point on the microsphere surface and the flat at the radial coordinate r is $h(r)$.

In force measurements the local shear rate γ varies drastically throughout the drainage regime, as shown in Figure 1, depending both on distance from the central axis (r) and on surface separation h. In particular the shear rate is approximately zero at large surface separations and large r, and very high at small surface separations and small r. Therefore we have good reason to investigate how the slip length varies with shear rate throughout a single experiment.

The shear-rate-dependent slip length proposed in the following cannot be simply inserted into the Vinogradova expression for the drainage force (Eq. 5.2), because the local shear rate γ varies throughout the drainage regime, as shown in Figure 5.1, and this changes the hydrodynamic pressure and flow fields that are used to derive the hydrodynamic force. Instead we have solved the hydrodynamic equations for arbitrary shear rate dependent slip in the colloid probe–flat surface geometry depicted in Figure 5.1,

and give the analytical expression for the drainage force. All the equations also apply for two convex bodies with arbitrary $h(r)$.

The mathematical calculations presented in Sections 5.2.1 to 5.2.4 were originally derived by A/Prof. Phil Attard, and tested and modified by Ms Liwen Zhu.

5.2.1 Derivation of Hydrodynamic Equations for Shear-Dependent Slip

On the basis of the classical lubrication theory,[26] the gradient of the pressure in creeping flow in a cylindrical coordinate system, (r, z), satisfies the condition:

$$\frac{\partial p(r,z)}{\partial r} = \eta \frac{\partial^2 v_r(r,z)}{\partial z^2}. \tag{5.3}$$

Here p is the pressure, v_r is the radial velocity, η is the viscosity. z is defined as in Figure 5.1 and $z = 0$ is defined in the middle between the two solid surfaces.

Integrating Eq. 5.3, we obtain $v_r(r,z) = \frac{p'(r)}{2\eta} z^2 + a\,z + c$.

Since $\frac{\partial v_r}{\partial z}$ must be equal to zero at $z = 0$ for a symmetrical system, $\left.\frac{\partial v_r}{\partial z}\right|_{z=0} = \frac{p'}{\eta} z \Big|_{z=0} + a = 0$, so a = 0.

The integration result shows $v_r(r,z) = \frac{p'(r)}{2\eta} z^2 + c$.

At the solid surfaces ($z = \pm h(r)/2$), for a slip boundary condition, the slip velocity is $v_s = v_r(r, \pm\frac{h}{2}) = \mp b \left.\frac{\partial v_r}{\partial z}\right|_{z=\pm\frac{h}{2}} = (\mp b)(\pm\gamma) = -b\gamma$.

By equating the above two equations, $-b\gamma = \frac{h^2}{8\eta} p'(r) + c$.

At the solid surfaces, the local shear rate

$$\pm\gamma = \left.\frac{\partial v_r}{\partial z}\right|_{z=\pm\frac{h}{2}} = \pm\frac{h}{2\eta}p'(r), \tag{5.4}$$

thus, $c = -\left(b+\frac{h}{4}\right)\gamma$ (b, h and γ are function of r, b is the shear rate dependent slip length $b(\gamma(r))$).

Finally, $v_r(r,z) = \frac{p'(r)}{2\eta}z^2 - \left[b(\gamma(r)) + h(r)/4\right]\gamma(r)$ (5.5)

Following Bikerman,[27] at a rate of change of separation $\dot{h}$, mass conservation of the fluid implies that the rate of change of volume of a cylinder of radius r must equal the rate of fluid flow across the side walls of the cylinder:

$$\begin{aligned}\pi r^2\dot{h} &= -\int_{-h(r)/2}^{h(r)/2} dz\, 2\pi r v_r(r,z) \\ &= -2\pi r\left\{\frac{-p'(r)}{12\eta}h(r)^3 - b(\gamma(r))\gamma(r)h(r)\right\}.\end{aligned} \tag{5.6}$$

5.2.2 No-Slip Boundary Condition

Setting the slip length to zero, $b(\gamma(r))=0$, Eq. 5.6 gives the pressure gradient for the no-slip boundary condition,

$$p'(r) = \frac{6\eta r\dot{h}}{h^3(r)}. \tag{5.7}$$

Substituting Eq. 5.7 into Eq. 5.4 gives the no-slip local shear rate,

$$\gamma(r) = \frac{3r\dot{h}}{h(r)^2} = \frac{3r\dot{h}}{\left(h_0 + r^2/2R\right)^2}. \tag{5.8}$$

The second equality uses the local separation for a spherical particle of radius R interacting with a flat substrate, valid for $r<<R$. The shear rate is zero at $r = 0$ and for large

r, and it reaches a maximum at $r^* = \sqrt{2h_0R/3}$, where the derivative of Eq. 5.8 vanishes. This gives the maximum shear rate as

$$\gamma^{\max} = \frac{27\dot{h}}{16h_0^{\,2}}\sqrt{2h_0R/3} \tag{5.9}$$

It can be seen that the maximum local shear rate increases with decreasing separation. It also scales with the rate of change of separation, which means in practice it also varies with piezo velocity, depending upon the experimental conditions.

In the following we introduce two alternative models for shear dependent slip, the saturation model and the scaling model, and compare their characteristics.

5.2.3 Saturation Model for Slip

For the case of a constant slip length b_0, Vinogradova[2] solved the above creeping flow equations and obtained an expression for the drainage force. In the present case of a slip length that varies with r due to the variation in the local shear rate, the analysis up to Eq. 5.6 is exact for arbitrary shear rate dependence of the slip length (and for arbitrary geometry $h(r)$). The simplest model for a slip length that decreases with increasing shear rate and that allows the slip velocity to reach a maximum value (saturate, hence the name of the model) at high shear rates is:

$$b(\gamma) = b_0 / \left(1 + |\gamma|/\gamma_c\right) \tag{5.10}$$

Here b_0 is the low shear rate slip length, and is the limiting constant slip length at large separations (previously called *b,* the Navier/Vinogradova slip length). The cross-over shear rate γ_c demarks the low and high shear rate regimes. For shear rates much smaller than γ_c, the slip length is constant and the slip velocity goes to zero with decreasing shear rates. For shear rates very much greater than γ_c, the slip length goes to zero as the shear rate goes to infinity and the slip velocity is constant. γ_c also gives the saturation value of the slip velocity as $v_s^{sat} = b_0\gamma_c$, which occurs at high shear rates ($\gamma >> \gamma_c$).

The motivation for the choice of this model is not only that it allows the slip velocity to saturate to a maximum value, but also that it allows easy comparison with the values of b_0 commonly used in the literature to quantify slip. Another advantage of this model is that it enables Eq. 5.6 to be solved explicitly for the pressure gradient, because in this model the local slip length, Eq. 5.4, gives

$$b(\gamma(r)) = \frac{b_0}{1+|\gamma(r)|/\gamma_c} = \frac{b_0}{1-h(r)p'(r)/(2\eta\gamma_c)}. \tag{5.11}$$

This formula is written for approach, where $\dot{h}<0$ and $p'(r)<0$. For retraction, the minus sign in the denominator should be changed to a plus sign. With this expression for the local slip length, Eq. 5.6 may be written as a quadratic equation for the pressure gradient, which has solution

$$p'(r) = \frac{-B \pm \sqrt{B^2 - 4AC}}{2A}, \tag{5.12}$$

here

$$A(r) \equiv \frac{h(r)^4}{24\eta^2\gamma_c},$$

$$B(r) \equiv -\left[\frac{rh(r)\dot{h}}{4\eta\gamma_c} + \frac{h(r)^3}{12\eta} + \frac{b_0 h(r)^2}{2\eta}\right],$$

$$C(r) \equiv \frac{r\dot{h}}{2}. \tag{5.13}$$

In Eq. 5.12, the negative sign before the square root applies to approach, and the positive sign for retraction. This result is exact for arbitrary $h(r)$. Using Eq. 5.12 and Eq. 5.4, the local shear rate in the case of this model of shear-rate-dependent slip is

$$\gamma(r) = \frac{\left(-B \pm \sqrt{B^2 - 4AC}\right)h(r)}{4\eta A}. \tag{5.14}$$

The net drainage force is the integral over the contact region of the pressure inside the gap minus the external pressure, and it can be written in terms of the pressure gradient as

$$F^{\text{drain}}(\dot{h},h_0)=\int_0^R \mathrm{d}r\, 2\pi r\left[p(r)-p_{\text{out}}\right] = -\pi\int_0^R r^2\, p'(r)\, dr \qquad (5.15)$$

This is readily evaluated numerically using the exact formula for the local separation for sphere–flat geometry, $h(r)=h_0+R-\sqrt{R^2-r^2}$.

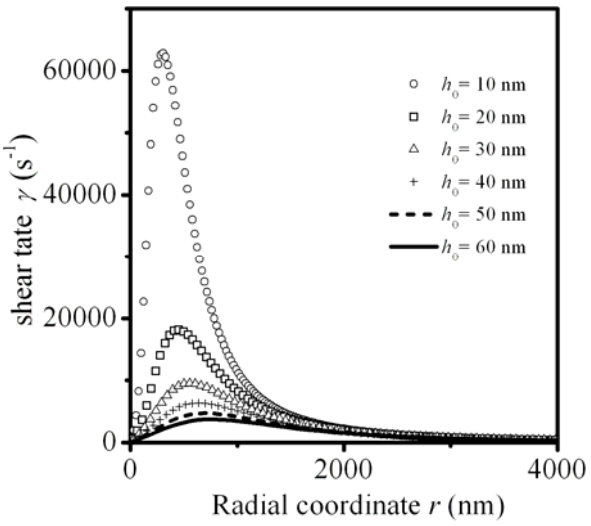

Figure 5.2 Calculated variation of the shear rate with the radial coordinate r at fixed separations h_0 for shear-rate-dependent slip boundary conditions. Values used in the calculation: η = 48.58 mPa s, R = 9.26 μm, b_0 = 32 nm, and γ_c^{eff} =5000 s^{-1}. The rate of change separation is fixed at $\dot{h}$ = 30.1 μm/s.

Figure 5.2 illustrates how the shear rate varies in a colloid probe experiment with the radial coordinate r at several distances of closest separation h_0 (calculation using Eq. 5.14). The shear rate is zero at large separations, reaches a maximum value at intermediate separations (500–800 nm), and then decreases to zero again at the zero separation.

The exact drainage force calculation as shown in Eq. 5.15 requires an integration at each time step and is not suitable for spreadsheet use. Therefore we have also explored a

convenient approximation that does allow the shear-rate-dependent slip length (Eq. 5.10) to be used in conjunction with the Vinogradova expression for the drainage force. The largest contribution to the drainage force comes from the region of maximum shear rate, which, in the case of no-slip, is expressed by Eq. 5.9. Using this expression one can replace the local slip length by an effective slip length that is independent of the radial coordinate,

$$b^{\text{eff}} = b_0 \Big/ \left(1 + \left|\gamma^{\max}\right| \Big/ \gamma_c^{\text{eff}}\right) \tag{5.16}$$

We call this expression the saturation model for slip. This effective slip length can be simply inserted into the Vinogradova expression for the constant slip length (Eq. 5.2).[2] Here $\gamma^{\max}$ can be calculated using Eq. 5.9 under no-slip boundary conditions and γ_c^{eff} is the effective crossover shear rate, below which b^{eff} is constant, and above which b^{eff} decreases with increasing shear rate. Although b^{eff} changes as $\dot{h}$ and h_0 change during a drainage force calculation, these have to be updated at each time step anyway so that it is no more difficult to calculate drainage forces using a shear-dependent b^{eff} than it is to use a constant b.

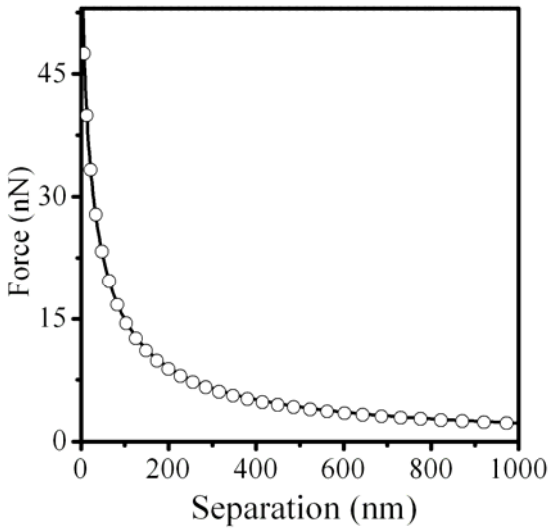

Figure 5.3 Calculated shear-rate-dependent saturation model for slip, with the black solid line being effective, Eq. 5.16, with γ_c^{eff} = 5000 s^{-1}, and the empty circles being exact, Eq. 5.10, with γ_c = 1250 s^{-1}. The parameters used in the calculation are: the radius of the microsphere R = 9.26 μm, the spring constant is 0.53 N/m, the viscosity is 48.58 mPa s, the driving velocity is 30.1 μm/s. Both models were fitted with b_0 = 32 nm.

A comparison between the approximate and the exact drainage force is shown in

Figure 5.3. The exact model (open circles), Eq. 5.10, overlaps the approximate model (solid line), Eq. 5.16, for all separations, and both give a slip length b_0 = 32 nm at low shear rate, but the fitting term is $\dot{\gamma}_c^{eff}$ = 5000 s^{-1} in the approximate case (i.e., when the maximum shear rate $\dot{\gamma}^{max}$ is used in the calculation), and $\dot{\gamma}_c$ = 1250 s^{-1} in the exact case (i.e., when the exact local shear rate $\dot{\gamma}$ is used in the calculation). This excellent agreement justifies using the simple spreadsheet calculation of the maximum shear rate $\dot{\gamma}^{max}$ instead of the full integrative calculation. Performing extensive numerical calculations for a range of realistic experimental parameters, shown in Figure 5.4, we found that the best fit of the exact crossover shear rate $\dot{\gamma}_c$ = 1250 s^{-1}. In Figure 5.4, the experimental hydrodynamic drainage force is fitted by the saturation model; the theoretical hydrodynamic slip forces were calculated at different exact crossover shear rate $\dot{\gamma}_c$. It can be seen that the experimental hydrodynamic drainage force (triangles) is fitted well by the exact shear rate dependent theoretical slip force $\dot{\gamma}_c$ = 1250 s^{-1} (black solid line) with a fitted slip length b_0 = 32 nm, up to contact. This slip length b_0 remains the same value as the one fitted by the Vinogradova's constant slip length expression.[2] The theoretical hydrodynamic forces at the exact crossover shear rates $\dot{\gamma}_c$ of 5000 s^{-1} (dots), 2500 s^{-1}(gray dashed line), 500 s^{-1} (crosses), and 200 s^{-1} (gray solid line) are also investigated, shown in Figure 5.4. The best fit of the effective crossover shear rate $\dot{\gamma}_c^{eff}$ was experimentally demonstrated to be about 4 times the magnitude of the exact crossover shear rates $\dot{\gamma}_c$, i.e. $\dot{\gamma}_c^{eff} \approx 4\dot{\gamma}_c$ = 5000 s^{-1}, shown in Figure 5.7.

A typical simulation of how the effective slip length b^{eff} varies with separation is shown in Figure 5.5. At large separations b^{eff} approximates the result with a constant b_0. As the separation is decreased, the maximum shear rate increases and the term $\left|\dot{\gamma}^{max}\right|/\dot{\gamma}_c^{eff}$ in Eq. 5.16 becomes increasingly important, so that the effective slip length markedly decreases. This implies that the shear-dependent slip length is particularly useful in the high-shear-rate regime at small separations. As we will discuss again later, this could explain why plotting the inverse of the hydrodynamic force versus separation and

extrapolating a line from the large separation data (as, for example, in reference 4, the inverse force plotting method) results in a constant slip length.

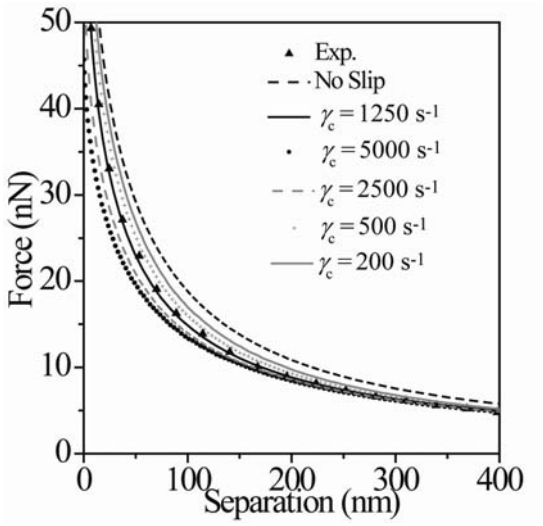

Figure 5.4 Theoretical hydrodynamic forces versus separations at different exact crossover shear rates γ_c. The theoretical hydrodynamic force with $\gamma_c = 1250 s^{-1}$ (solid black line) is the best for fitting the experimental hydrodynamic force (triangles) at small separations and obtains a fitted slip length of fitted b_0 = 32 nm; the no-slip theoretical hydrodynamic force (black dashed line) is also shown. Theoretical hydrodynamic slip forces at the crossover shear rates γ_c of 5000 s^{-1} (dots), 2500 s^{-1}(gray dashed line), 500 s^{-1} (crosses), and 200 s^{-1} (gray solid line) are also shown with the same slip length b_0 = 32 nm and the same parameters. An OTS silicon wafer was used as a substrate, the radius of the microsphere R = 9.26 μm, the spring constant is 0.53 N/m, the viscosity is 48.58 mPa s, the driving velocity is 30.1 μm/s. (experimental details in Chapters 2 and 4)

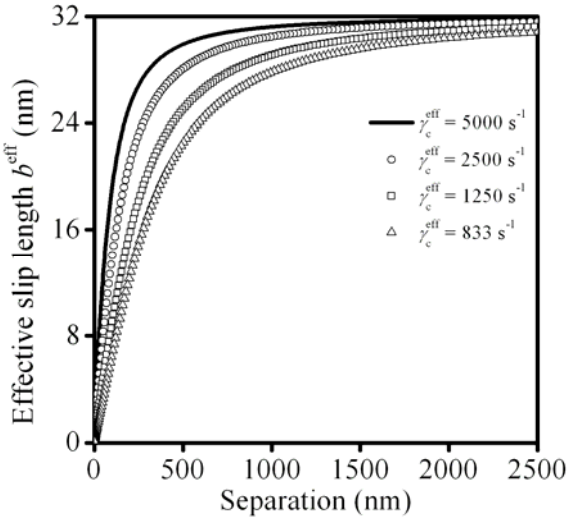

Figure 5.5 Simulation of a typical experiment generated by the saturation model for slip showing the variation of the effective slip length with separation for different crossover shear rates γ_c^{eff}. Here the values used in the calculation are the same as in Figure 5.2.

5.2.4 Scaling Model for Slip

We also investigated alternative shear-dependent models for slip, which are physically plausible. We propose a second shear-rate-dependent model based on a simple scaling argument for tangential momentum transfer between the liquid and the solid. The physical reasoning for this choice is presented here. According to Newton's second law of motion, the force exerted by the liquid on the solid (F_{ls}) is the rate of change of momentum (momentum P, $F_{ls} = dP/dt$). The force exerted by the liquid on the solid is the product of the number of liquid–solid atom collisions per unit time (n_c), which scales with the slip velocity v_s, and of the momentum transferred in each atom collision (ΔP_c), which also scales with v_s. As a result, the force scales with the slip velocity squared ($F_{ls} \propto v_s^2$). The shear force in the liquid is linear in the shear rate ($F_{shear} \propto \eta\gamma$). In quasi-static shear, if there is a shear force of the liquid on a solid (F_{ls}), there must be an equal and opposite shear force within a liquid (F_{shear}). So the slip velocity must scale as $v_s \propto \gamma^{1/2}$. According to Eq. 5.1, this implies that $b \propto \gamma^{-1/2}$.

In the most general case, one can introduce a scaling constant α, and a scaling slip model for the shear-rate-dependent slip length can be expressed as,

$$b(\gamma) = b_0 (\gamma/\gamma_c)^{-\alpha}, \tag{5.17}$$

where α is expected to be positive and less than 1 (see below).

Inserting this into Eq. 5.6 and using Eq. 5.4, one has

$$c = a\, p'(r) + d\, p'(r)^{1-\alpha}. \tag{5.18}$$

where $a = h(r)^3/(6\eta)$,

$d = (b_0/\eta)(2\eta\gamma_c)^{\alpha} h(r)^{2-\alpha}$,

$$c = r\dot{h}_0 \tag{5.19}$$

Eq. 5.18 needs to be solved for $p'(r)$ at each r and $h(r)$ for a fixed α. One way to solve Eq. 5.18 is by iteration,

$$p'_{n+1}(r) = c/\left(a + p'_n(r)^{-\alpha} d\right), \text{ n=0, 1, 2,…} \tag{5.20}$$

$$p'_0(r) = 0\,. \tag{5.21}$$

Inserting the converged $p'(r)$ into Eq. 5.15 gives the drainage force.

In practice, the maximum shear rate can replace the local shear rate and give an effective approximation of the slip length

$$b^{eff} = b_0 \left(|\gamma_{\max}| / \gamma_c^{eff}\right)^{-\alpha} \tag{5.22}$$

We call this expression with α = ½ the scaling model for slip. This effective slip length b^{eff} replaces b_0 in Vinogradova's constant slip expression (Eq. 5.2) for fitting hydrodynamic forces.

Figure 5.6 shows how the effective slip length b^{eff}, calculated from Eq. 5.22 with α = ½ and with a constant slip length b_0 = 32 nm, increases with increasing separations at different crossover shear rates γ_c^{eff}. According to this scaling model for slip, the slip length diverges at low shear rates, $b(\gamma) \to \infty$ as $\gamma \to 0$. This divergence is counterintuitive and needs an explanation, provided below. Even so, the scaling model fits well the experimental force data, as shown in the inset of Figure 5.6, which proves the value of this model even at large separations (low shear rates).

There could be two possible reasons for the divergence of the slip length at low shear rates. First, the physical quantity that needs to be finite is the slip velocity, not the slip length. According to Eq. 5.1 and Eq. 5.17, the slip velocity v_s scales like $v_s = b\gamma \sim \gamma^{1-\alpha}$**.** So as the shear rate $\gamma \to 0$, the slip velocity vanishes provided that $\alpha < 1$. Second, in this scaling model for slip, the drainage force coincides with the no-slip force at large separations, notwithstanding the infinite b. This may be seen from the fact that the

maximum shear rate, Eq. 5.9, for large separations goes like $\gamma^{max} \sim h_0^{-3/2} \rightarrow 0$ as $h_0 \rightarrow \infty$. Hence $b(\gamma) \sim h_0^{3\alpha/2} \rightarrow \infty$ as $h_0 \rightarrow \infty$. Although the slip length goes to infinity at large separations, the drainage force is well fitted at large separations. The reason is that the Vinogradova factor for slip is a function of the slip length divided by the separation, $f^*(b/h_0)$, with $f^*(0) = 1$. This yields the no-slip theory at large separations when the slip length is fixed. For the present scaling model, $b/h_0 \sim h_0^{(3\alpha-2)/2} \rightarrow 0$ as $h_0 \rightarrow \infty$, and this goes to zero when $\alpha < 2/3$. This means that if α is not too large (such as in the present fit of α = 1/2), then the slip theory will coincide with the no-slip theory at large separations. This last result is illustrated in the inset of Figure 5.6.

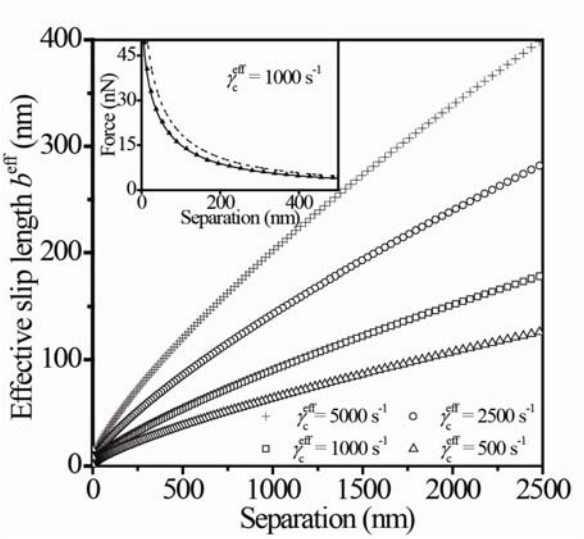

Figure 5.6 Simulation of a typical experiment generated by the scaling model for slip with α = ½, showing the variation of the effective slip length with separation for different crossover shear rate $\dot{\gamma}_c^{eff}$. Inset: result of a typical colloid probe experiment measuring the hydrodynamic drainage force in di-*n*-octylphthalate, fitted by the scaling model for slip. The experimental data (filled triangles) are presented together with the no-slip force (dashed line), and the shear dependent scaling model for slip (solid line). An OTS silicon wafer was used as a substrate, the radius of the microsphere R = 9.26 μm, the spring constant is 0.53 N/m, the viscosity is 48.58 mPa s, the driving velocity is 30.1 μm/s, fitted b_0 = 32 nm, and fitted $\dot{\gamma}_c^{eff}$ = 1000 s^{-1}.

It is important to notice that in this scaling model there is only one fitting parameter, namely, $b_0 (\dot{\gamma}_c^{eff})^{1/2}$. In this product, we fix the slip length b_0 at 32 nm on the basis of our fits with the constant slip length model, and vary $\dot{\gamma}_c^{eff}$, which gives a well fitted drainage

force over the whole separation regime with a fitted γ_c^{eff} = 1000 s^{-1}, as shown in the inset of Figure 5.6.

5.3 Experimental Results and Discussion

In this paper we compare our experimentally measured drainage forces to the no-slip model, b = 0, the constant slip model (Eq. 5.2),[2] and our saturation model for slip (Eq. 5.16). Figure 5.7a shows that the measured drainage forces in a partially wetting system (di-*n*-octylphthalate on OTS-coated silicon, θ = 45º) can be fitted by the constant slip model (grey line)[2] using a constant slip length of b_0 = 32 nm from large separations down to about 150 nm. At separations closer to zero, the experimental data depart from the constant slip theory, with the experimental force increasing more steeply in this region and approaching the no-slip force (dashed line).

Using our shear-dependent saturation model, the fitted value of b_0 is the same value as that obtained by the Vinogradova constant slip length model, fitted from large separations up to small separation (150 nm). The crossover shear rate γ_c^{eff} = 5000 s^{-1} is fitted so that the theoretical drainage force coincides with the experimental force along the whole approach, down to contact. The agreement shown in Figure 5.7a is typical of seven separate experiments, each performed in three positions of the flat substrate and each with at least nine approach rates. All the data could be fitted with the same value of b_0 and γ_c^{eff}. Drainage force measurements in a more wetting situation (di-*n*-octylphthalate on silicon, θ = 21º) were also fitted well by our saturation model for slip, only with a lower value of the constant slip length b_0 of 12 nm, shown in Figure 5.7c. The corresponding full scale fitted force curves in Figure 5.7a and c are shown in Figure 5.7 b and d, respectively. As can been seen, the shear dependent model fits the experimental data well along the whole separation range, down to contact between the surfaces.

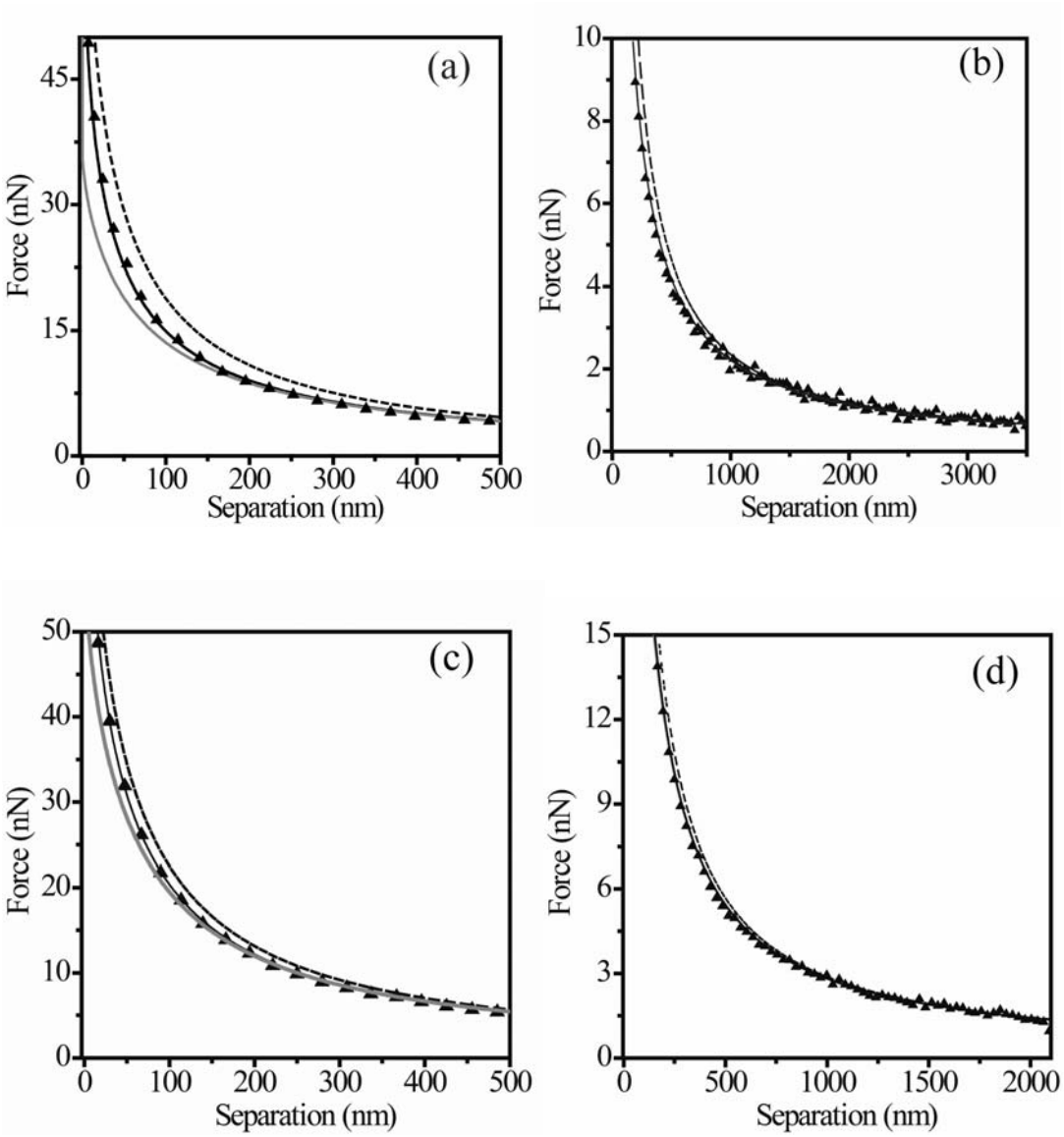

Figure 5.7 Measurement of the hydrodynamic drainage force in di-*n*-octylphthalate in a colloid probe experiment. The experimental data (filled triangles) are presented together with the no-slip force (dashed line), the constant slip force (grey line),[2] and the shear dependent slip force (saturation model, Eq. 5.16, solid black line). (a) An OTS silicon wafer was used as a substrate, the radius of the microsphere R = 9.26 μm, the spring constant is 0.53 N/m, the viscosity is 48.58 mPa s, the driving velocity is 30.1 μm/s, fitted b_0 = 32 nm, and fitted γ_c^{eff} = 5000 s^{-1}. (b) The full scale of the same hydrodynamic in figure (a) fitted by the no slip model and the saturation model. (c) A plain silicon wafer was used as a substrate, R = 9.18 μm; the spring constant is 0.55 N/; the viscosity of the liquid is 59.8 mPas, the velocity of the piezo is 30.5 μm/s, fitted b_0 = 12 nm, and fitted γ_c^{eff} = 5000 s^{-1}. (d) The full scale of the same hydrodynamic in figure (c) fitted by the no slip model and the saturation model.

Typical force curves captured at different driving velocities v in a colloid probe AFM experiment are shown in Figure 5.8. Here again b_0 = 32 (± 2) nm, and the γ_c^{eff} = 5000 s^{-1} for all approach rates. Again the shear-rate-dependent slip model fits the experimental force very well almost down to contact between probe and surface. The fact that we can employ one single fitting value of b_0 and γ_c^{eff} for any approach rate and in the same experiment with the same system indicates that this shear-rate dependent effect is not an experimental artefact, but a genuine experimental measurement of the physics of flow. At low piezo driving velocities (< 5 μm/s), the shear dependent slip length expression does not fit the experimental data obviously better than the Vinogradova constant slip length expression (Eq. 5.2). The reason is that the local shear rate γ in this case is much smaller than the crossover shear rate γ_c^{eff}, and the local slip length $b(\gamma)$ is approximately equal to the constant slip length b_0 in such a low shear rate regime (see Eq. 5.16). In addition, at low shear rates the signal/noise ratio is lower. Therefore the shear model for slip becomes more useful and necessary for a good fit at the higher shear rates of the liquid. Note that in Figure 5.7 and Figure 5.8, the exact calculation for the drag force on the cantilever (as presented in Chapter 3) was not employed, as the cantilevers were relatively stiff here.

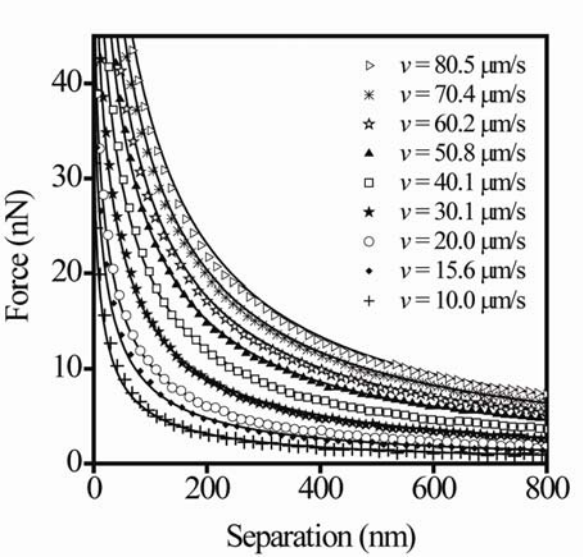

Figure 5.8 Measurement of the hydrodynamic drainage force in di-*n*-octylphthalate in a colloid probe experiment at different driving rates v. The experimental data (symbols) overlaps the shear rate dependent slip force (saturation model, Eq. 5.16, lines). Here R = 9.26 μm, the spring constant is 0.53 N/m, η = 48.9 mPa s, fitted b_0 = 31 ± 3 nm, and fitted γ_c^{eff} = 5000 s^{-1}.

Both the saturation model and the scaling model allow us to specifically investigate the slip length as a function of shear rate, and in the following we illustrate a new way of plotting both experimental and theoretical data, so that the shear dependence becomes obvious. Instead of the common force versus separation plot, Figure 5.9 shows the effective slip length versus the maximum shear rate. This figure shows two different force measurements performed at a solvophilic surface (circles) and a partially solvophilic surface (filled triangles) and their corresponding theoretical data generated from the saturation model (solid line) and scaling model (dashed line). The procedure to obtain this plot consists of five steps:

(1) Values of the experimental hydrodynamic drainage force are recorded versus their corresponding values of separation h and rate of change of separation $\dot{h}$.

(2) The corresponding no-slip force is calculated using Eq. 5.2 with $f^* = 1$ using the same parameters as in the experiment and at the same values of separation.

(3) Values of the effective slip length b^{eff} are calculated, by equating $f^*(b^{\text{eff}}/h)$ to the ratio of the values of the experimental drainage force to the values of the no-slip drainage force at the same separations.

(4) Values of the experimental maximum shear rate $\gamma_{\max}$ are determined using Eq. 5.9 at the same separations and rates as in step 1–3.

(5) The theoretical effective slip lengths from the saturation and scaling models are calculated directly from Eq. 5.16 and Eq. 5.22, using values of γ_c previously obtained by fitting the force curve, and plotted versus shear rates arbitrarily chosen in the range of 10 s^{-1} to 100 s^{-1}.

Figure 5.9 shows clearly that the effective slip length decreases as the shear rate increases within one colloid probe experiment. Both the saturation model (solid curve) and the scaling model (dashed line) fit well the experimental data (filled triangles and circles). The noise in the experimental data is due to the use of the experimental velocity in the shear rate calculation. In the inset of Figure 5.9 we show the values obtained in computer

simulations by Pahlavan and Freund[22] at the much higher shear rate values of $\gamma \sim 10^{11}$ s^{-1}, which are typically used in simulations. Due to the different liquid molecules (Lennard-Jones argon liquid in the simulation, and di-*n*-octylphthalate liquid in our experiments) and the extremely high shear rate in the simulation (which cannot be achieved experimentally), a noticeable gap exists between the regime investigated in the simulation and the experiment. However, both simulation and experimental results show that the slip length decreases with increasing shear rates and finally reaches a small value. This finding might explain why the slip lengths obtained in nearly all simulations are significantly smaller than those obtained from the experiments. This new way of plotting the data illustrates the large range of shear rates accessible by AFM (close to four orders of magnitude, up to 10^5 s^{-1}) compared with other techniques. This new plotting method also allows a clear illustration of slip lengths decreasing with shear rates and a direct comparison of experiments with simulations.

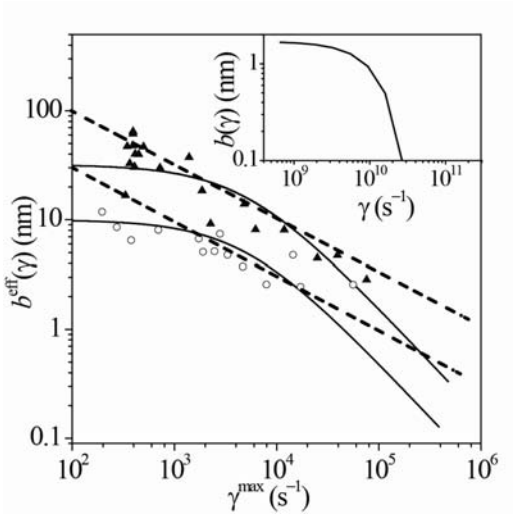

Figure 5.9 Shear-rate-dependent effective slip length versus maximum shear rate. The slip length fitted in experiments performed in a silica–silica system (circles), and in a silica–OTS system (filled triangles) are plotted together with the scaling model $b^{eff}(\gamma) = b_0(\gamma^{max}/\gamma_c^{eff})^{-0.5}$ (dashed line) and the saturation model $b^{eff}(\gamma) = b_0/(1+\gamma^{max}/\gamma_c^{eff})$ (solid curve). In the silica–silica system the fitted b_0 = 10 nm, γ_c^{eff} = 1000 s^{-1} for the scaling model, and γ_c^{eff} = 5000 s^{-1} for the saturation model. In the silica–OTS system the fitted b_0 = 32 nm, γ_c^{eff} = 1000 s^{-1} for the scaling model, and γ_c^{eff} = 5000 s^{-1} for the saturation model. A comparison with results of molecular dynamic simulations for argon atoms by Pahlavan *et al.*[22] is shown in the inset.

In the following we discuss our model in relation to previous findings on the shear dependence (or lack thereof) of slip. Firstly, our shear-rate-dependent model does not support previous findings of slip increasing with piezo driving velocity.[13, 16, 17] We can explain these previous observations as a consequence of imprecisely estimating the effect of drag force on the cantilever. As described in Chapter 4, for soft cantilevers (spring constant < 0.2 N/m) an exact calculation of the variable drag force on the cantilever must be taken into account in order to extract a correct slip length from AFM force measurements. If a constant drag force on the cantilever is assumed, the slip length is overestimated, and the error is larger, the larger the shear rate.

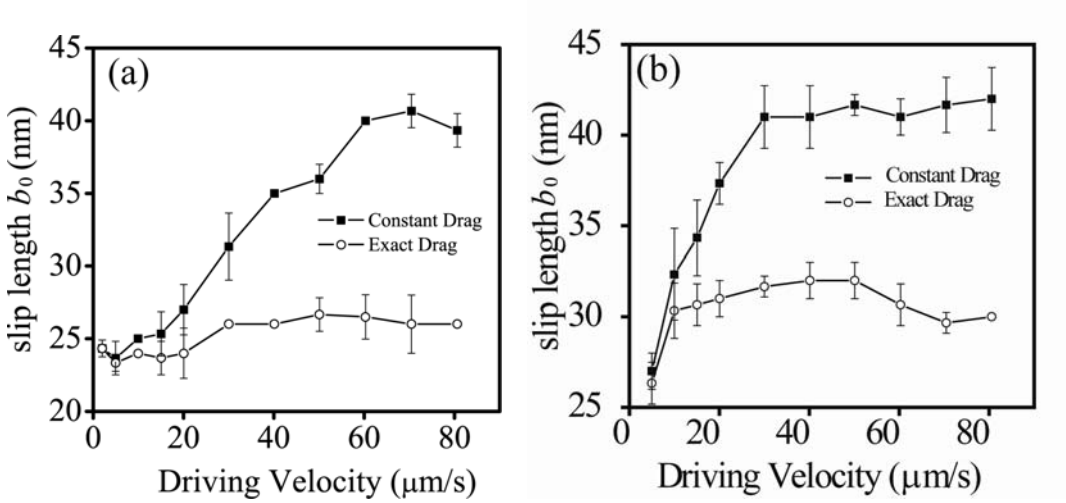

Figure 5.10 Two fitted slip length b_0 in two colloid probe experiments performed with silica spheres and hydrophobised (DCDMS) silicon wafers with two different cantilever of spring constant (a) k = 0.092N/m and (b) k = 0.115N/m. The fits are obtained using a constant drag force (filled square), and using the exact variable drag force (empty circles).[25] Using the constant drag approximation results in the spurious effect of slip length increasing with driving velocity, i.e. shear rate.

Figure 5.10 shows two experimental results of fitting at large separations experiments performed with two different weak cantilever with both the exact (variable) drag model, and the approximate (constant) drag model. Figure 5.10 clearly shows that the observed increase in the large separation fitted constant slip length b_0 with increasing driving rate is an artefact of using the constant drag force approximation. Conversely, the

fact that in the exact drag calculation the fitted b_0 is constant for all driving velocities provides further confirmation of the validity of the present shear rate dependent slip length.

Secondly, we believe that many studies conclude that the slip length is independent of shear rate due to the particular fit they employ, namely the inverse of the force versus separation. The inverse force plot does not highlight the shear rate dependence because it is dominated by the large separation, low-shear-rate regime. We simulated this inverse force plot in Figure 5.11. Here it is shown that the shear dependent slip force generated by the saturation model (dots), and the constant slip force generated by the Vinogradova slip model, Eq. 5.2 (plus signs), both turn down towards the no-slip force (solid line) near zero separation. The only difference between the two models is that the shear dependent slip force goes over the no-slip force near zero faster than the constant slip force. In the usual way of analysing the experimental data with the inverse force plot, the slip length is obtained from a linear extrapolation of the hydrodynamic drainage force at large separations, as in the dashed line in Figure 5.11. This fit almost gives the same value of b_0 as the saturation model but this plot masks completely the shear rate dependence.

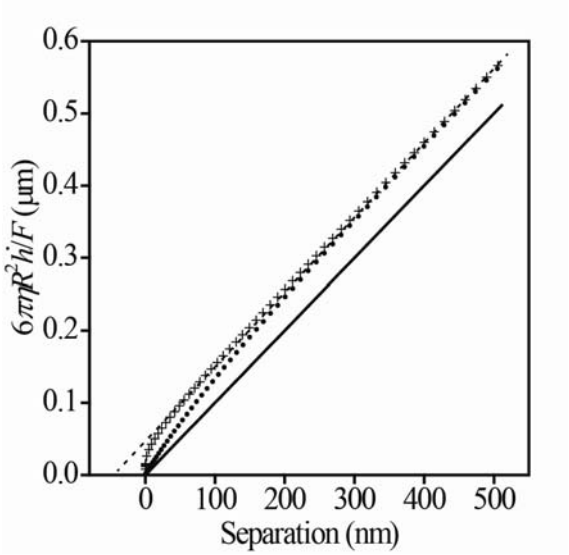

Figure 5.11 Conventional inverse force plot used for fitting slip models to drainage forces. Drainage forces calculated from the saturation model (dots), the constant Vinogradova slip force (Eq. 5.2) (plus signs) and no-slip force (f^* = 1 in Eq. 5.2) (solid line) are compared. The dashed line indicates the extrapolation procedure at large separations from which b_0 is commonly found. The parameters used in the calculation: η = 48.58 mPa s, R = 9.26 μm, the driving velocity is 30.1 μm/s, fitted b_0 = 32 nm, and γ_c^{eff} =5000 s^{-1}.

To our knowledge, no physical explanation for slip decreasing with shear rate has previously been offered. Here, we propose two possible physical explanations of it. One has been discussed in Section 5.2.4 on the scaling model for slip on the basis of a simple scaling law for tangential momentum transferred between the liquid and the solid. The second physical explanation can be argued from a molecular level. In the present experimental system, the shape of the rigid di-*n*-octylphthalate molecule is ellipsoidal,[28] and under low shear flows these molecules are likely to align near the smooth walls, forming layers with a lower viscosity than the bulk disordered liquid.[29] At higher shear rates, the extensional component of the shear flow disrupts the layered structure, and the molecular tumbling induced by the shear flow increases the momentum transfer between liquid molecules and leads to a higher viscosity. Therefore, the decrease in slip length with increasing shear rate may be due to the disordering of surface-induced structure due to extensional distortion and tumbling in shear flow, as sketched in Figure 5.12. We suggest that our fitted value γ_c identifies the point where the two regimes cross over. Formally, the second law of thermodynamics implies the continuity of the transverse momentum field, which means that the slip length can be written as $b = L\,(\eta-\eta_s)/\eta_s$,[2] where L is the depth of the surface region (typically less than about a nanometre), η is the viscosity in the bulk fluid, and η_s is the viscosity near the surface. At low shear rates, $\eta_s << \eta$ and the slip length is large. At high shear rates, η_s is close to η and the slip length goes to zero. It is the competition between surface-induced order and alignment on the one hand, and the shear-induced tumbling and disorder on the other, that leads to the slip length decreasing with increasing shear rate and saturating at low shear rates.

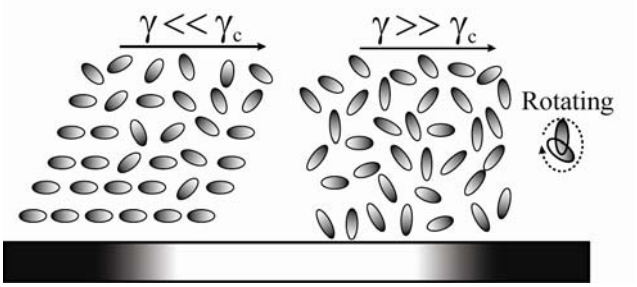

Figure 5.12 Schematic of the molecular structure in the liquid near the surface at low and high shear rates. The disruption of the layered structure in the liquid at high shear rates might explain the decrease in slip length at $\gamma >> \gamma_c$.

5.4 Conclusions

We have shown that current slip theories do not adequately describe drainage force measurements, and we have developed two models (the saturation model and the scaling model for slip) for the shear dependent slip length that are justified by the need to prevent the slip velocity becoming infinite at large shear rates. The experiments were performed at a wetting system and a partially system. Both models enable the experimental data to be well fitted down to very small separations, and to produce reliable and reproducible measurements of slip. Of the two models, we recommend employing the saturation model for fitting hydrodynamic drainage forces, because it provides a fitted slip length b_0 to easily compare with previous measurements of the Vinogradova constant slip length. We also developed a new way of plotting the experimental data (slip length versus shear rate). This new plotting easily illustrates the dependence of the slip length on the shear rate, especially useful in the large range of shear rates obtained in AFM experiments. We explained previous findings of slip increasing with driving velocity as spurious, due to an imprecise prediction of the variable drag force on the cantilever. We explained how the inverse force plot does not highlight the shear rate dependence because it focuses on fits at large separations and low shear rates, where the slip length is not sensitive to the shear rate.

We envisage that our shear-dependent model could be further tested in experiments where one uniform shear rate can be maintained throughout the experiment and higher shear rates than can be achieved in AFM, for example with quartz crystal microbalance. The present finding that the slip length decreases with increasing shear rate, and that the slip velocity saturates at shear rates higher than γ_c, provides some insight into the fundamental physical mechanism of slip and into the molecular nature of fluid flow at solid surfaces. The results suggest that slip is intimately connected with the rate of tangential momentum transfer between the solid and the adjacent fluid, and that this rate increases super-linearly with shear rate, at least at the shear rates accessible in the present experiments.

References

1. Navier, C. L. M. H. Mémoire sur les lois du mouvement des fluids. *Mem. Acad. Sci. Inst. Fr.* **1823**, *6*, 389-416, 432-436.

2. Vinogradova, O. I. Drainage of a thin liquid-film confined between hydrophobic surfaces. *Langmuir* **1995**, *11*, 2213-2220.

3. Cottin-Bizonne, C.; Steinberger, A.; Cross, B.; Raccurt, O.; Charlaix, E. Nanohydrodynamics: The intrinsic flow boundary condition on smooth surfaces. *Langmuir* **2008**, *24*, 1165-1172.

4. Cottin-Bizonne, C.; Cross, B.; Steinberger, A.; Charlaix, E. Boundary slip on smooth hydrophobic surfaces: Intrinsic effects and possible artifacts. *Phys. Rev. Lett.* **2005**, *94*, 056102.

5. Bonaccurso, E.; Kappl, M.; Butt, H. J. Hydrodynamic force measurements: boundary slip of water on hydrophilic surfaces and electrokinetic effects. *Phys. Rev. Lett.* **2002**, *88*, 076103.

6. Guriyanova, S.; Semin, B.; Rodrigues, T. S.; Butt, H. J.; Bonaccurso, E. Hydrodynamic drainage force in a highly confined geometry: role of surface roughness on different length scales. *Microfluid. Nanofluid.* **2010**, *8*, 653-663.

7. McBride, S. P.; Law, B. M. Improved in situ spring constant calibration for colloidal probe atomic force microscopy. *Rev. Sci. Instrum.* **2010**, *81*, 113703.

8. Zhu, L. W.; Attard, P.; Neto, C. Reliable measurements of interfacial slip by colloid probe atomic force microscopy. II. Hydrodynamic force measurements. *Langmuir* **2011**, *27*, 6712-6719.

9. Honig, C. D. F.; Ducker, W. A. Squeeze film lubrication in silicone oil: experimental test of the no-slip boundary condition at solid-liquid interfaces. *J. Phys. Chem. C* **2008**, *112*, 17324-17330.

10. Yordanov, S.; Best, A.; Butt, H.-J.; Koynov, K. Direct studies of liquid flows near solid surfaces by total internal reflection fluorescence cross-correlation spectroscopy. *Optics Express* **2009**, *17*, 21149-21158.

11. Lasne, D.; Maali, A.; Amarouchene, Y.; Cognet, L.; Lounis, B.; Kellay, H. Velocity profiles of water flowing past solid glass surfaces using fluorescent nanoparticles and molecules as velocity probes. *Phys. Rev. Lett.* **2008**, *100*, 214502.

12. Vinogradova, O. I.; Koynov, K.; Best, A.; Feuillebois, F. Direct measurements of hydrophobic slippage using double-focus fluorescence cross-correlation. *Phys. Rev. Lett.* **2009**, *102*, 118302.

13. Craig, V. S. J.; Neto, C.; Williams, D. R. M. Shear-dependent boundary slip in an aqueous Newtonian liquid. *Phys. Rev. Lett.* **2001**, *87*, 054504

14. Horn, R. G.; Vinogradova, O. I.; Mackay, M. E.; Phan-Thien, N. Hydrodynamic slippage inferred from thin film drainage measurements in a solution of nonadsorbing polymer. *J. Chem. Phys.* **2000**, *112*, 6424-6433.

15. Zhu, Y. X.; Granick, S. Rate-dependent slip of Newtonian liquid at smooth surfaces. *Phys. Rev. Lett.* **2001**, *87*, 096105.

16. Bonaccurso, E.; Butt, H. J.; Craig, V. S. J. Surface roughness and hydrodynamic boundary slip of a Newtonian fluid in a completely wetting system. *Phys. Rev. Lett.* **2003**, *90*, 144501.

17. Neto, C.; Craig, V. S. J.; Williams, D. R. M. Evidence of shear-dependent boundary slip in Newtonian liquids. *Eur. Phys. J. E* **2003**, *12*, S71-S74.

18. Churaev, N. V.; Sobolev, V. D.; Somov, A. N. Slippage of Liquids over Lyophobic solid Surfaces. *J. Colloid Interface Sci.* **1984**, *97*, 574-581.

19. Choi, C. H.; Westin, K. J. A.; Breuer, K. S. Apparent slip flows in hydrophilic and hydrophobic microchannels. *Phys. Fluids* **2003**, *15*, 2897-2902.

20. Lauga, E.; Brenner, M. P.; Stone, H. A., Microfluidics: The No-slip Boundary Condition. In *Handbook of Experimental Fluid Dynamics*, Foss, J.; Tropea, C.; Yarin, A., Eds. Springer: New York, 2005; Chapter 15.

21. Ho, T. A.; Papavassiliou, D. V.; Lee, L. L.; Striolo, A. Liquid water can slip on a hydrophilic surface. *Proc. Natl. Acad. Sci. U. S. A.* **2011**, *108*, 16170-16175.

22. Pahlavan, A. A.; Freund, J. B. Effect of solid properties on slip at a fluid-solid interface. *Phys. Rev. E* **2011**, *83*, 021602.

23. Thompson, P. A.; Troian, S. M. A general boundary condition for liquid flow at solid surfaces. *Nature* **1997**, *389*, 360-362.

24. Heinbuch, U.; Fischer, J. Liquid flow in pores-slip, no-slip, or multilayer sticking. *Phys. Rev. A* **1989**, *40*, 1144-1146.

25. Zhu, L. W.; Attard, P.; Neto, C. Reliable measurements of interfacial slip by colloid probe atomic force microscopy. I. Mathematical modeling. *Langmuir* **2011**, *27*, 6701-6711.

26. Reynolds, O. On the theory of lubrication and its application to Mr. Beauchamp Tower's experiments including an experimental determination of the viscosity of olive oil. *Philos. Trans. R. Soc. London* **1886**, *177*, 157-234.

27. Bikerman, J. J. The fundamentals of tackiness and adhesion. *J. Colloid Sci.* **1947**, *2*, 163-175.

28. Coughlin, C. S.; Mauritz, K. A.; Storey, R. F. A general free-volume based theory for the diffusion of large molecules in amorphous polymers above Tg .3. theoretical conformational-analysis of molecular shape. *Macromolecules* **1990**, *23*, 3187-3192.

29. Teixeira, R. E.; Babcock, H. P.; Shaqfeh, E. S. G.; Chu, S. Shear thinning and tumbling dynamics of single polymers in the flow-gradient plane. *Macromolecules* **2005**, *38*, 581-592.

Chapter 6 Reconciling Slip Measurements in Symmetric and Asymmetric Systems

6.1 Introduction

On the basis of molecular interactions, liquids flowing over solvophobic surfaces are expected to be less coupled to the surface and therefore show more slip than on solvophilic surfaces. This conclusion has been supported by many experimental and simulation papers that have measured no slip on solvophilic surfaces (Table 6.1). However, there is no theoretical reason why the slip length should be exactly zero on solvophilic surfaces. Contradictory findings from both experiments and simulations have measured a finite slip length on solvophilic surfaces. In Table 6.1, a selection of slip measurements done on solid surfaces with different wettabilities by different techniques is presented. On superhydrophobic surfaces (water contact angle >150°), Joseph *et al*.,[1] Choi *et al*.,[2] and Bhushan *et al.* [3] demonstrated large slip lengths on the order of micrometres or submicrometres. At solvophobic surfaces (liquid contact angle >90°, typically formed by applying a self-assembled monolayer, SAM), several groups[4-9] showed slip lengths varying from 20–100 nm by different techniques. At solvophilic surfaces, some research showed no-slip boundary conditions;[3, 4, 7, 9-14] however, other studies,[15-20] including a recent molecular dynamics simulation (MD)[21] and a nanofluidic experiment,[22] provided evidence of small values of the slip length on wetting or partially wetting surfaces.

Table 6.1 Summary of experimentally measured values of the slip length published in the literature, as ordered by the wettability (equilibrium liquid contact angle θ, advancing contact angle θ_A, receding contact angle θ_R) of the solid surface [a]

Author	Substrate (θ)	Sphere (θ)	Liquid	Techs.	Slip length (nm)
Ho *et al.*[21]	MgO (30°)		Water	MD	6.7
Lee *et al.*[22]	Anodized alumina membranes (12 ± 2º)		Water	Nanofluidics	Slip
Bonaccurso *et al.*[16]	Mica (θ_R = 0º)	Silica (θ_R = 0º)	water	AFM	8-9
Sun *et al* [19]	Mica	Silica	n-propanol	AFM	10-14
McBride and Law [17]	Silane SAM (5 ~ 40º)	Silane SAM (5 ~ 40º)	n-alkanes	AFM	10-14
Guriyanova *et al.*[23]	Silica (θ_A <5º)	Silica (θ_A <5º)	KCl or KNO_3 solution	AFM	6
Bowles *et al.*[20]	Silane SAM (θ_A = 11º)	Silane SAM (θ_A = 11º)	*n*-pentane / *n*-hexane	AFM	5-20
			n- hexadecane		0
Craig *et al.*[15]	Thiol SAM *[b] (55º)	Thiol SAM *[b] (55º)	sucrose solution	AFM	0-20
Cottin-Bizonne *et al.*[6]	OTS SAM	Pyrex	*n*-dodecane	SFA	20
Honig *et al.*[10]	Hydroxyl-glass (<5º), methyl-glass (78º), and graphite (30º)*[b]	Silica	Sucrose solution	AFM	< 2 (below resolution)
Honig *et al.*[11]	Hydroxyl-glass (<11º), methyl-glass (<12º), and graphite (<11º)*[b]	Silica	Silicon oil	AFM	0- 30
Lasne *et al.*[8]	OTS SAM(90º)		water	TIRF-PIV	45 ± 15
	OTS SAM (90º)	Silica (0º)	NaCl solution	AFM	50 ± 10
Cottin-Bizonne *et al.*[7]	Phospholipid SAM (θ_A = 95º) and OTS SAM (θ_A = 105º)	Pyrex (θ_A < 3º)	Water	SFA	8-20
	Pyrex(θ_A <3º)	Pyrex (θ_A <3º)			<2 (below resolution)
	OTS SAM (θ_A = 28º)	Pyrex (< 3º)	*n*-dodecane		<2 (below resolution)

Author	Substrate (θ)	Sphere (θ)	Liquid	Techs.	Slip length (nm)
Vinogradova *et al.*[9]	Silica (θ_A < 5º)		Electrolyte solution	DF-FCCS	0
	Silane SAM (θ_A = 95º)				80-100
Choi *et al.*[5]	Silica		Deionized water	flow metering system	uncertain
	OTS SAM				0-30
Schmitz *et al.*[12]	Silica (θ_A < 5 º)		Phosphate buffer	TIRF-FCS	<10 (below resolution)
Bouzigues *et al.*[4]	Silica (< 20º)		water	TIRF-PIV	0 ± 10
	OTS SAM (95º)				38 ± 6
Chinappi *et al.*[13]	OTS SAM (>105º)		water	MD	0.3-0.6
Bhushan *et al.*[3]	Soda lime glass	Mica(~0°)	water	Dynamic AFM	0
		n-hexatriacontane SAM (91±2.0°)			43±10
		Lotus wax (nonacosane-10,12-diol and nonocosane-10-ol) (167±0.7°)			236±18
Joseph *et al.*[1]	carbon nanotube forest (>165º)		water	μ-PIV	0-1500
Choi *et al.*[2]	Super-hydrophobic nanoturf (> 175º)		Deionized water	rheometer system	~ 20000
			30wt% glycerine		~ 50000

[a] SAM stands for self-assembled monolayer. OTS stands for octadecyltrichlorosilane.

*[b] Advancing and receding contact angles were reported in the cited papers; the values listed here are the average of the two.

AFM is one of the most sensitive techniques for measuring hydrodynamic drainage forces. It has been widely used to investigate liquid/solid boundary conditions on the microscale and nanoscale. The hydrodynamic drainage force on a sphere surface approaching a flat surface is given by the Taylor equation[24] and Vinogradova's f^* factor[24] in Eq. 6.1,

$$F_h = \frac{-6\pi\eta R^2 \dot{h}}{h} f^* \quad (h << R). \tag{6.1}$$

The f^* factor expresses the occurrence of slip. Under a no-slip boundary condition, $f^* = 1$. A general expression for the f^* factor was introduced by Vinogradova:[24, 25]

$$f^* = -\frac{2Ah}{BC} - \frac{2h}{C-B}\left[\frac{(B+h)(B-A)}{B^2}\ln\left(1+\frac{B}{h}\right) - \frac{(C+h)(C-A)}{C^2}\ln\left(1+\frac{C}{h}\right)\right] \tag{6.2}$$

$$A = b(2+k) \tag{6.3}$$

$$B = 2b(2+k+\sqrt{1+k+k^2}) \tag{6.4}$$

$$C = 2b(2+k-\sqrt{1+k+k^2}) \tag{6.5}$$

If the surfaces are different in their slip behaviour, then two different slip lengths must be defined. Vinogradova defined the slip length on one surface to be $b_2 = b$, whereas for the other surface, it is $b_1 = b_2\ (1+k) = b\ (1+k)$. Here, the slip length on the flat surface is b_2, while on the microsphere it is b_1 (Figure 6.1). The parameter k is a constant that is specific to the particular sphere and flat surface under study.

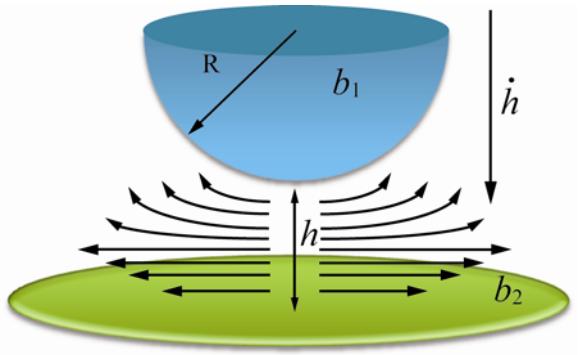

Figure 6.1 Schematic representation of the drainage of a thin liquid film between a microsphere with radius R approaching a stationary flat surface. The distance of closest approach between the two surfaces is h, and the rate of change of the separation of the sphere perpendicular to the flat surface is $\dot{h}$. The slip length on the microsphere surface is defined as b_1, whereas for the flat surface it is b_2, with $b_1 = b_2\ (1+k)$.

For a symmetric system in which the sphere surface and the flat substrate surface have identical surface properties in chemical nature, $k = 0$, $b_1 = b_2 = b$, and Eq. 6.2 can be written as[24]

$$f_{sym}^{*} = \frac{h}{3b}\left[\left(1+\frac{h}{6b}\right)\ln\left(1+\frac{6b}{h}\right)-1\right] \tag{6.6}$$

For an asymmetric system in which the sphere surface is not identical to the flat substrate surface (i.e. $k \neq 0, b_1 \neq b_2$), Eq. 6.2 is a function of separation h, slip length b on the flat surface, and constant k, (i.e., $f^* = (h, b, k)$).

In slip force measurements performed on asymmetric systems, typically a solvophilic colloid probe (a hydrophilic silica sphere) and a solvophobic flat surface (often self-assembled monolayer-coated silicon), it is common to assume that the slip length on the sphere is zero because the liquid wets the sphere surface.[6, 7, 10, 11] In these cases, the expression for the asymmetric f^* factor is used (Eqs. 6.2–6.5) assuming $k = -1$. However, as shown in Table 6.1, many experimental studies have demonstrated that small but finite values of the slip length can be measured on solvophilic (hydrophilic) surfaces.[16-19] Thus, previous studies that have employed the asymmetric f^* to fit asymmetric systems assuming $b_1 = 0$ have not measured the actual slip length on the investigated flat surface. In reality, what these studies have measured is an "effective slip length" over two surfaces with different slip behaviour. This also means that these slip lengths cannot be directly compared to those obtained from the other methods for estimating slip.

One way to solve this problem is to make a symmetric system (with both sphere and flat surface identical in chemical nature) and fit the experimental hydrodynamic drainage force using f_{sym}^* (Eq. 6.6). However, symmetric systems are not easy to obtain in practice because it is technically challenging to prepare a smooth, uniform coating on the colloid probe because of its fragility and small dimensions. For example, silica colloid probes are often coated with a silane SAM from the vapour phase, but great caution must be exercised to prepare uniform coatings reproducibly.[26, 27] Gold-coated colloid probes (for thiol SAMs) have the disadvantage of having a higher surface roughness, which could affect slip.

In this Chapter, slip in two symmetric systems and one asymmetric system was studied. It is demonstrated that the measured slip lengths in the three systems are in agreement with each other. An alternative way to easily fit the slip length on both the flat surface and the colloid probe in an asymmetric system is shown, so that a bare sphere can be directly used in a force measurement. Vinogradova's asymmetric model containing two different slip lengths has been used before by Bonaccurso *et al.*[28] and Vinogradova and Yakubov,[29] but in both of these studies the two slip lengths were fitted at the same time by a least-square fit, which could lead to substantial uncertainties in the independent variable. In this Chapter, one important improvement over previous approaches is made in that one of the two slip lengths in the asymmetric system is independently measured in a separate symmetric system. Therefore, only one variable needs to be fitted in the asymmetric system, which greatly improves the reliability of the results. Importantly, a method can be used to self-assess the accuracy and reproducibility of the slip force measurements. It also provides a convenient way by which other groups can reliably measure slip on any asymmetric system in a single experiment using published slip length values on the known surface. However, a simple prediction method allows one to re-derive the actual slip length on the asymmetric systems in the published literature, only calculating f^* without refitting all of the force curves. In addition, our recently published experimental advances, improvements in data analysis, and new modeling approach presented in Chapters 3–5 [30-32] are combined into one fit in this Chapter.

6.2 Materials and Methods

In this Chapter, the flat substrate surfaces were either a bare silicon wafer with a native silicon oxide layer or hydrophobised silicon wafers. The hydrophobic coating on the silicon wafer was either an octadecyltrichlorosilane (OTS) self-assembled monolayer prepared from the liquid phase[27, 33] or a dichlorodimethylsilane (DCDMS) self-assembled monolayer prepared from the vapour phase (see Chapter 2 Section 2.4.2 for details).[26] The microsphere was either bare silica, or DCDMS-coated silica attached to a tipless cantilever and silanised from the vapour phase in the same way as for the DCDMS-coated silicon wafer. The RMS roughness of the OTS-coated silicon substrates is about 0.271 nm, and

that of the DCDMS-coated silicon substrate is 0.388 nm as measured by AFM over a 5 × 5 μm^2 area. The coated microsphere surfaces are assumed to have the same rms roughness as the coated substrates.

6.3 Results and Discussion

6.3.1 Combining Best Practice Experimental Protocol, New Algorithm and Modeling into One Fit

In previous three Chapters, we described a new best practice experimental protocol, a new theoretical model for slip that includes a shear-dependent term, a correction term to account for the drag force on the cantilever, and a new mathematical fitting algorithm, which together form the most accurate and reproducible way to obtain a fitted slip length from AFM force measurements. Briefly, the new algorithm and theoretical model include the following effects:

1) The new mathematical algorithm, independent of actual experimental data, reduces noise in the theoretical force compared to that from previous treatments, which instead used experimentally derived data (e.g. colloid probe velocity) (see Chapter 3).[30]

2) The virtual deflection due to elastic stress and the artificial effect on compliance due to friction are eliminated in the analysis protocol of force curves (see Chapter 4).[31]

3) An exact drag calculation well describes the variable drag force on cantilevers with a low spring constant, replacing the often used constant drag estimation (see Chapters 3 and 5).[30, 32] This correction eliminates the spurious dependence of slip on the driving rate and cantilever spring constant. However, too stiff cantilevers have been shown to have too low sensitivity to be able to measure accurate slip lengths.[34]

4) A shear-rate-dependent model provides a new understanding of the connection between the slip length and the shear rate and also provides an accurate fit of hydrodynamic forces at all separations down to a few nanometres (see Chapter 5).[32] In our model, the slip length decreases with increasing shear rate in order to avoid an unphysical

divergence in the velocity of the liquid adjacent to the surface at small separations.[32] Our saturation model restricts the slip velocity to reach a maximum value at high shear rates (see Eq. 5.16 $b(\gamma)^{\text{eff}} = b_0 \Big/ \left(1 + \left|\gamma^{\max}\right| \Big/ \gamma_c^{\text{eff}}\right)$). This slip length $b(\gamma)^{\text{eff}}$ can simply be inserted into the Vinogradova *f**expression, replacing the constant slip length *b* in Eqs 6.2 and 6.6. The constant *k* in the *f** factor then becomes a function of the two low shear rate slip lengths b_{01} and b_{02} on the two surfaces.

6.3.2 Fitting the Slip Length in Symmetric and Asymmetric Systems

In this Chapter, we demonstrate a new way by which the reliability and accuracy of the fitted slip length can be independently tested by comparing measured slip lengths in related symmetric and asymmetric systems. Force measurements were performed in the following three systems:

- Symmetric systems:

- a solvophilic/solvophilic system (silica colloid probe – silica flat surface, see Experiments IA and IB in Table 6.2)

- a partially solvophilic/partially solvophilic system (DCDMS-coated colloid probe – DCDMS-coated flat surface, or OTS-coated flat surface, see Experiments IIA and IIB in Table 6.2. It was assumed that the OTS-and DCDMS-coated surfaces have similar properties for slip, given that their wettabilities are similar. This initial assumption was then confirmed by our results.)

- Asymmetric system:

- a solvophilic/partially solvophilic system (silica colloid probe – DCDMS-coated flat surface, see experiments IIIA, IIIB and IIIC in Table 6.2).

Force measurements were performed at three different positions on the flat surface and at each position with at least nine approach rates. In the following, wherever a fitted slip length per experiment is presented, it is implied that the reported value is an average over (at least) 27 (3 × 9) force measurements. Cantilevers with different spring constant

values were used to confirm our previous finding that slip is independent of cantilever type as long as the effect of cantilever drag is taken into account.[30]

Table 6.2 Fitted slip lengths b_0 for symmetric and asymmetric systems in di-*n*-octylphthalate.[a]

Expt.	Sphere	Substrate	Slip length b_0 (nm)	Spring constant (N/m)	γ_c^{eff}(s^{-1})
IA (Sym.)	Silica	Silica	10.1 ± 2.5	1.500	5000
IB (Sym.)	Silica	Silica	11.8 ± 2.2	0.550	5000
IIA (Sym.)	DCDMS	OTS	46.2 ± 3.6	0.270	5000
IIB (Sym.)	DCDMS	DCDMS	45.8 ± 4.3	1.700	5000
IIIA (Asym.)	Silica	DCDMS	25.1 ± 1.5	0.092	12500
IIIB (Asym.)	Silica	DCDMS	29.6 ± 3.1	0.115	12500
IIIC (Asym.)	Silica	DCDMS	24.0 ± 6.2	2.200	5000

[a]All slip lengths were fitted using the symmetric formula f^*_{sym} (Eq. 6.6). The b_0 values for IIIA, IIIB, and IIIC are the effective slip lengths over both silica and DCDMS-coated surfaces. The other b_0 listed are the fitted slip lengths on each individual surface.

In the first instance, data from both the symmetric and the asymmetric systems were fitted using the Vinogradova symmetric f^*_{sym} factor (Eq. 6.6) and our shear-dependent saturation slip model.[32] The slip lengths in these three systems are shown in Table 6.2. Using the symmetric f^*_{sym} factor, the fitted slip length was found to be 11 ± 2 nm on each of the two surfaces in the symmetric solvophilic system and 46 ± 4 nm on each of the two surfaces in the symmetric partially solvophilic system. The effective slip length in the

asymmetric solvophilic/partially solvophilic system was fitted to be 26 ± 4 nm, which is close to the average of the slip length values in the solvophilic symmetric system and the partially solvophilic symmetric system. Table 6.2 shows that repeat experiments in the same system produced consistent results and that the fitted slip lengths in OTS and DCDMS systems were very similar to each other.

For all experiments in Table 6.2, the fitted crossover shear rate γ_c^{eff} = 5000 s^{-1} produced a good fit. However, experiments IIIA and IIIB could be well fitted with γ_c^{eff} = 5000 s^{-1} for the separations greater than about 50 nm, but a more optimal fit could be achieved at γ_c^{eff} = 12500 s^{-1} for separations less than 50 nm. We do not believe this to affect the precision of the slip length fit, as the slip length b_0 is fitted at large separations (150–500 nm) and is independent of the value of γ_c^{eff} which instead affects the fit at small separations (0–150 nm). An excellent fit of the theory to the experiments was obtained in all cases.

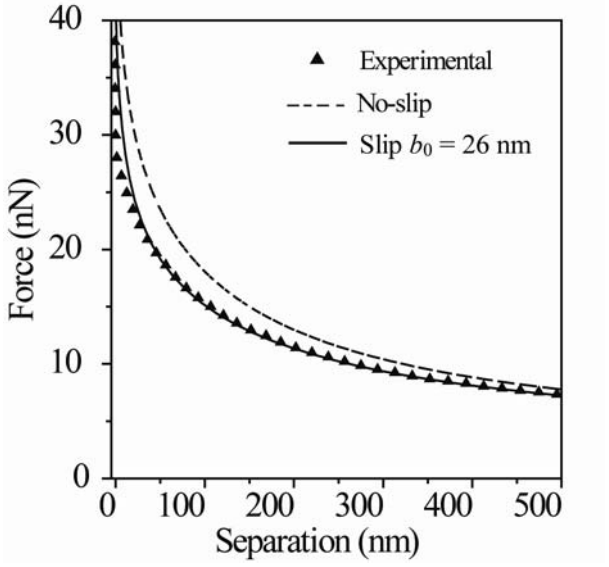

Figure 6.2 Experimental hydrodynamic force (▲) measured in di-*n*-octyphthlate between a silica colloid probe and a hydrophobised (DCDMS) flat surface. The theoretical shear-rate-dependent slip force combined with the exact drag force calculation (—) is compared to the no-slip theoretical hydrodynamic drainage force with the constant drag force (---). The parameters in the experiment are R = 9.67 μm, k = is 0.092 N/m and η = 53.87 mPas; the piezo driving velocity is 30.0 μm/s; γ_c^{eff} in the shear-dependent saturation model for slip is 12500 s^{-1}; and b_0 = 26 nm as fitted by the symmetric equation for this system.

The fit of theory to experiments is demonstrated in Figure 6.2, which presents an example of a hydrodynamic force fit from asymmetric experiment IIIB. Here, the exact drag calculation and the shear-dependent saturation model for slip were combined in one fit. The fitted effective slip length in this curve in the asymmetric system is about 26 nm as calculated by the symmetric equation (Eq. 6.6), which agrees with our previously measured slip results in the same system, presented in Chapter 4.

The procedure of using the symmetric factor f^*_{sym} to fit the asymmetric systems in Table 6.2 is not ideal because the fitted effective slip length is a combination of the individual slip lengths at each surface and it is impossible to decouple the slip length on each of the surfaces. Now the asymmetric f^* factor (Eq. 6.2 and $k \neq 0$) can be used to obtain the actual slip length in an asymmetric system, both on the flat surface and on the colloid probe.

From symmetric experiments IA and IB in Table 6.2, the slip length on the silica surface is about 11 nm, thus the experimental hydrodynamic drainage forces in asymmetric experiments IIIA and IIIB (solvophilic (silica)/partially solvophilic (DCDMS) system) can be refitted using Eq. 6.1 and Eq. 6.2 with $k = (11/b_{02} - 1)$. Figure 6.3 shows an experimental hydrodynamic drainage force obtained with an asymmetric system (experiment IIIC) fitted with a symmetric f^*_{sym} factor (part a) and with an asymmetric f^* factor (part b). In Figure 6.3a, using the symmetric factor f^*_{sym} gives an effective apparent slip length of 25 nm over both the silica colloid probe and the DCDMS-coated flat surface. In Figure 6.3b, using the asymmetric factor f^* of Eq. 6.2 with $k = (11/b_{02} - 1)$, gives a slip length of 44 nm on the DCDMS-coated flat surface. In this fit, the slip length of 11 nm on the silica sphere surface measured in advance in the symmetric solvophilic (silica–silica) system was used. Both the symmetric and asymmetric slip models in Figure 6.3 fit the experimental forces very well up to the contact region, but the first provides an effective slip length of 25 nm over both the surfaces (Figure 6.3a), and the latter provides the actual slip length of 44 nm on the DCDMS-coated flat surface (Figure 6.3b). Crucially, the value of b_{02} = 44 nm for the DCDMS-coated surface fitted with the asymmetric equation is

identical within error to that obtained for the DCDMS-coated surfaces in the symmetric systems (experiments IIA and IIB in Table 6.2).

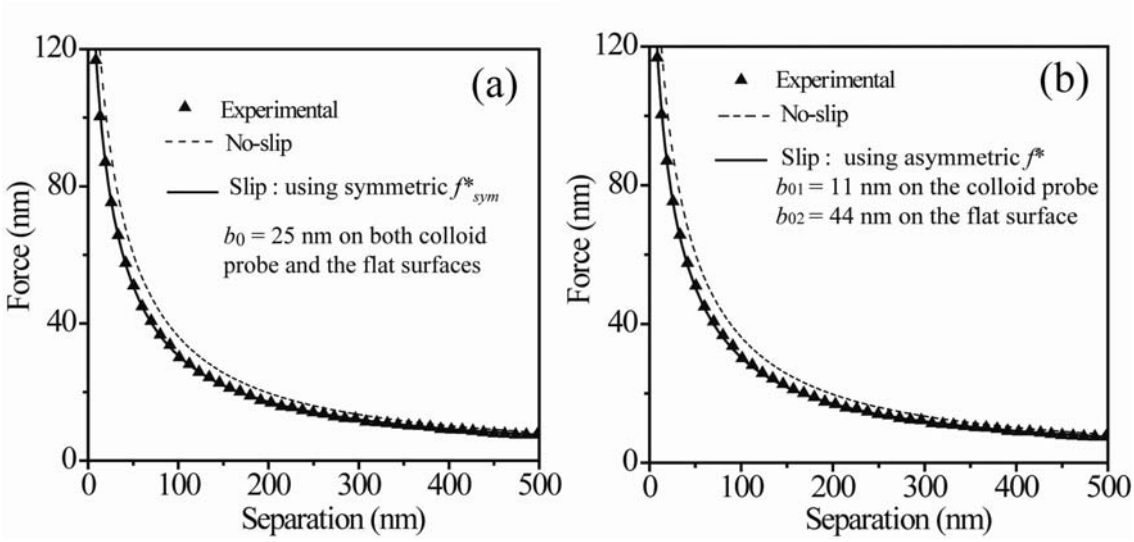

Figure 6.3 Experimental hydrodynamic force performed in di-*n*-octyphthlate between a silica sphere and a hydrophobised (DCDMS) flat surface. R = 9.29 μm, k = 2.2 N/m, η = 50.38 mPas, the piezo driving velocity is 50.1 μm/s, and the fitted γ_c^{eff} is 5000 s^{-1}. (a) The experimental force (▲) is fitted by the symmetric slip force equation (Eq. 6.1 with f^*_{sym} in Eq. 6.6, —), yielding b_0 = 25 nm over both colloid probe and flat surface. (b) The same experimental force (▲) is fitted by the asymmetric slip equation (Eq. 6.1 with f^* in Eq. 6.2 and $k = (11/b_{02} - 1)$, —). In this equation, b_{01} = 11 nm on the colloid probe was measured in a separate symmetric experiment and used in k. Therefore, b_{02} = 44 nm is the actual value for the DCDMS-coated flat surface. The dashed lines (---) in both figures represent the no-slip forces.

6.3.3 Procedure to Predict the Actual Slip Length on the Flat Surface from the Literature by Calculating only f^*

In Chapter 4, the effective slip length of di-*n*-octylphthalate in an asymmetric system (silica/OTS) was measured to be 24 – 31 nm, values that are in agreement with those for the asymmetric systems presented here. The actual slip length on the OTS-coated flat surface can now be predicted by using a simple procedure consisting of the following three steps without refitting all of the force curves:

1) The asymmetric factor f^* is calculated by Eq. 6.2 at different separations. The value of b_{01} from an independently symmetric experiment is used in this expression. In our case, the slip length of di-*n*-octylphthalate on the silica surface b_{01} was measured to be 11 nm, and that on the hydrophobised surface b_{02} is the one that needs to be predicted, and they are related by the constant $k = b_{01}/b_{02} - 1 = 11/b_{02} - 1$. Arbitrary separation values are chosen in the experimental separation regime (0–5000 nm).

2) The symmetric factor f^*_{sym} (Eq. 6.6) is calculated at the same separations as those in step 1 using the effective slip length $b_0 = 26$ nm.

3) The actual slip length b_{02} on the hydrophobised flat surface is fitted by equating the two factors (f^* and f^*_{sym}) derived from steps 1 and 2 at each separation, as shown in Figure 6.4. With the correct fitted value of b_{02}, the two f^* factors agree with each other from 5000 nm down to zero separation.

With these three steps, a fitted slip length b_{02} of 47 nm is obtained, which falls within the range of slip lengths (46 ± 4 nm) fitted in the symmetric system in experiments IIA and IIB in Table 6.2. This confirms experimentally that the actual slip length on the OTS-coated surface studied in our previous asymmetric experiments in Chapter 4 should be around 47 nm. Thus, it can be concluded that this prediction method allows us and others to derive the actual slip on the investigated flat surface in the literature by calculating only f^* without refitting all of the force curves.

Our approach is conceptually simple but has three important consequences. First, cross-testing results from different independent systems effectively assess the reproducibility and accuracy of the slip measurements. This should aid in developing a consistent physical understanding of slip. Second, this approach simplifies the experimental procedure needed to perform AFM slip measurements on coated surfaces, eliminating the need to prepare uniformly coated symmetric systems. If the slip length on the bare colloid probe surface is obtained from separate symmetric experiments or the literature, then one can simply perform a single experiment to investigate slip lengths on any flat surface. Third, for already published slip measurements that produced only an

effective slip length, a simple method is provided to reinterpret the data and deduce the actual slip length on the investigated coated surface.

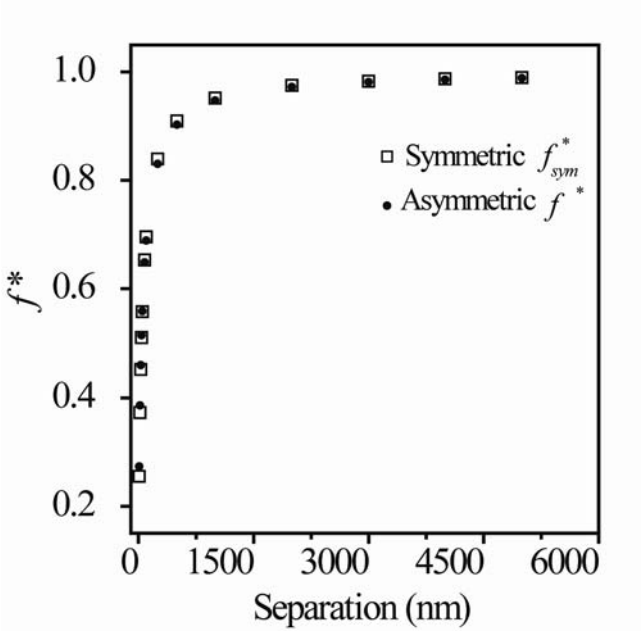

Figure 6.4 Comparison between the symmetric f^*_{sym} factor calculated using the average b_0 in the asymmetric system and the asymmetric f^* factor, calculated using the experimentally fitted b_{01} on the silica colloid probe (= 11 nm) with a fitting slip length of b_{02} on the hydrophobised silica surface. The two f^* factors are calculated at the same separation values and can be made to coincide by fitting a value for b_{02}. The two f^* factors coincide for a fitted effective slip length of b_{02} = 47 nm, which is close to the experimentally measured values in Table 6.2 (experiments IIA and IIB).

6.4 Conclusions

In this Chapter, hydrodynamic forces were measured by AFM in a one-component liquid (di-*n*-octylphthalate) on two symmetric systems and on one asymmetric system. The slip length in the symmetric solvophilic system was found to be 11 ± 2 nm over each surface, and the slip length over two identical partially solvophilic surfaces was fitted to be 46 ± 4 nm. In the asymmetric system, the hydrodynamic force was fitted using the Vinogradova asymmetric f^* factor based on the fixed slip length of 11 nm on the solvophilic surface; consequently, the actual slip length on the partially solvophilic surface was found to be 44 nm in this system, which is close to the experimentally measured average slip length of 46 ± 4 nm measured in the symmetric, partially solvophilic system.

This provides a new method to self-assess the accuracy and reproducibility of measured hydrodynamic forces and fitted slip lengths. It also demonstrates a convenient method for investigating the slip length on the flat surface simply using a bare colloid probe. This method avoids the procedure of preparing an identical coating on the sphere surface such as that on the investigated flat surface, which greatly improves the efficiency of force measurements for slip. Furthermore, only a single experiment can be performed to investigate slip on any different flat surface by using the slip length on the bare colloid probe from either our own experiments or the literature. In addition, we also provide a simple way to derive the actual slip length on the investigated flat surface from literature values by calculating only f^* without refitting all of the force curves

References

1. Joseph, P.; Cottin-Bizonne, C.; Benoit, J. M.; Ybert, C.; Journet, C.; Tabeling, P.; Bocquet, L. Slippage of water past superhydrophobic carbon nanotube forests in microchannels. *Phys. Rev. Lett.* **2006**, *97*, 156104.

2. Choi, C.-H.; Kim, C.-J. Large slip of aqueous liquid flow over a nanoengineered superhydrophobic surface. *Phys. Rev. Lett.* **2006**, *96*, 066001.

3. Bhushan, B.; Wang, Y.; Maali, A. Boundary slip study on hydrophilic, hydrophobic, and superhydrophobic surfaces with dynamic atomic force microscopy. *Langmuir* **2009**, *25*, 8117-8121.

4. Bouzigues, C. I.; Tabeling, P.; Bocquet, L. Nanofluidics in the debye layer at hydrophilic and hydrophobic surfaces. *Phys. Rev. Lett.* **2008**, *101*, 114503.

5. Choi, C. H.; Westin, K. J. A.; Breuer, K. S. Apparent slip flows in hydrophilic and hydrophobic microchannels. *Phys. Fluids* **2003**, *15*, 2897-2902.

6. Cottin-Bizonne, C.; Cross, B.; Steinberger, A.; Charlaix, E. Boundary slip on smooth hydrophobic surfaces: Intrinsic effects and possible artifacts. *Phys. Rev. Lett.* **2005**, *94*, 056102.

7. Cottin-Bizonne, C.; Steinberger, A.; Cross, B.; Raccurt, O.; Charlaix, E. Nanohydrodynamics: The intrinsic flow boundary condition on smooth surfaces. *Langmuir* **2008**, *24*, 1165-1172.

8. Lasne, D.; Maali, A.; Amarouchene, Y.; Cognet, L.; Lounis, B.; Kellay, H. Velocity profiles of water flowing past solid glass surfaces using fluorescent nanoparticles and molecules as velocity probes. *Phys. Rev. Lett.* **2008**, *100*, 214502.

9. Vinogradova, O. I.; Koynov, K.; Best, A.; Feuillebois, F. Direct measurements of hydrophobic slippage using double-focus fluorescence cross-correlation. *Phys. Rev. Lett.* **2009**, *102*, 118302.

10. Honig, C. D. F.; Ducker, W. A. Thin film lubrication for large colloidal particles: experimental test of the no-slip boundary condition. *J. Phys. Chem. C* **2007**, *111*, 16300-16312.

11. Honig, C. D. F.; Ducker, W. A. Squeeze film lubrication in silicone oil: experimental test of the no-slip boundary condition at solid-liquid interfaces. *J. Phys. Chem. C* **2008**, *112*, 17324-17330.

12. Schmitz, R.; Yordanov, S.; Butt, H. J.; Koynov, K.; Dünweg, B. Studying flow close to an interface by total internal reflection fluorescence cross-correlation spectroscopy: Quantitative data analysis. *Phys. Rev. E* **2011**, *84*, 066306.

13. Chinappi, M.; Casciola, C. M. Intrinsic slip on hydrophobic self-assembled monolayer coatings. *Phys. Fluids* **2010**, *22*, 042003.

14. Huang, D. M.; Sendner, C.; Horinek, D.; Netz, R. R.; Bocquet, L. Water slippage versus contact angle: a quasiuniversal relationship. *Phys. Rev. Lett.* **2008**, *101*, 226101.

15. Craig, V. S. J.; Neto, C.; Williams, D. R. M. Shear-dependent boundary slip in an aqueous Newtonian liquid. *Phys. Rev. Lett.* **2001**, *87*, 054504

16. Bonaccurso, E.; Kappl, M.; Butt, H. J. Hydrodynamic force measurements: boundary slip of water on hydrophilic surfaces and electrokinetic effects. *Phys. Rev. Lett.* **2002**, *88*, 076103.

17. McBride, S. P.; Law, B. M. Viscosity-dependent liquid slip at molecularly smooth hydrophobic surfaces. *Phys. Rev. E* **2009**, *80*, 060601.

18. Guriyanova, S.; Bonaccurso, E. Influence of wettability and surface charge on the interaction between an aqueous electrolyte solution and a solid surface. *Phys. Chem. Chem. Phys.* **2008**, *10*, 4871-4878.

19. Sun, G. X.; Bonaccurso, E.; Franz, V.; Butt, H. J. Confined liquid: simultaneous observation of a molecularly layered structure and hydrodynamic slip. *J. Chem. Phys.* **2002**, *117*, 10311-10314.

20. Bowles, A. P.; Honig, C. D. F.; Ducker, W. A. No-slip boundary condition for weak solid-liquid interactions. *J. Phys. Chem. C* **2011**, *115*, 8613-8621.

21. Ho, T. A.; Papavassiliou, D. V.; Lee, L. L.; Striolo, A. Liquid water can slip on a hydrophilic surface. *Proc. Natl. Acad. Sci. U. S. A.* **2011**, *108*, 16170-16175.

22. Lee, K. P.; Leese, H.; Mattia, D. Water flow enhancement in hydrophilic nanochannels. *Nanoscale* **2012**, *4*, 2621-2627.

23. Guriyanova, S.; Semin, B.; Rodrigues, T. S.; Butt, H. J.; Bonaccurso, E. Hydrodynamic drainage force in a highly confined geometry: role of surface roughness on different length scales. *Microfluid. Nanofluid.* **2010**, *8*, 653-663.

24. Vinogradova, O. I. Drainage of a thin liquid-film confined between hydrophobic surfaces. *Langmuir* **1995**, *11*, 2213-2220.

25. In Vinogradova's published paper (*Langmuir* **1995**,*11*, ref 33), there is a misprint in Eq. 3.19. This equation was corrected in Vinogradova's later paper (*J. Colloid Interface Sci.* **2000** *221*,1). The correct equation for general *f**should be written as Eq. 6.2 in our paper.

26. Fadeev, A. Y.; McCarthy, T. J. Self-assembly is not the only reaction possible between alkyltrichlorosilanes and surfaces: monomolecular and oligomeric covalently attached layers of dichloro- and trichloroalkylsilanes on silicon. *Langmuir* **2000**, *16*, 7268-7274.

27. Wasserman, S. R.; Tao, Y.-T.; Whitesides, G. M. Structure and reactivity of alkylsiloxane monolayers formed by reaction of alkyltrichlorosilanes on silicon substrates. *Langmuir* **1989**, *5*, 1074-1087.

28. Bonaccurso, E.; Butt, H. J.; Craig, V. S. J. Surface roughness and hydrodynamic boundary slip of a Newtonian fluid in a completely wetting system. *Phys. Rev. Lett.* **2003**, *90*, 144501.

29. Vinogradova, O. I.; Yakubov, G. E. Dynamic effects on force measurements. 2. Lubrication and the atomic force microscope. *Langmuir* **2003**, *19*, 1227-1234.

30. Zhu, L. W.; Attard, P.; Neto, C. Reliable measurements of interfacial slip by colloid probe atomic force microscopy. I. Mathematical modeling. *Langmuir* **2011**, *27*, 6701-6711.

31. Zhu, L. W.; Attard, P.; Neto, C. Reliable measurements of interfacial slip by colloid probe atomic force microscopy. II. Hydrodynamic force measurements. *Langmuir* **2011**, *27*, 6712-6719.

32. Zhu, L. W.; Attard, P.; Neto, C. Reliable measurements of interfacial slip by colloid probe atomic force microscopy. III. Shear rate dependent slip *Langmuir* **2012**, *28*, 3465-3473.

33. Brzoska, J. B.; Ben Azouz, I.; Rondelez, F. Silanization of solid substrates: a step towards reproducibility. *Langmuir* **1994**, *10*, 4367-4373.

34. Rodrigues, T. S.; Butt, H. J.; Bonaccurso, E. Influence of the spring constant of cantilevers on hydrodynamic force measurements by the colloidal probe technique. *Colloids & Surfaces A: Physicochem. Eng. Aspects* **2010**, *354*, 72-80.

Chapter 7 Conclusions and Outlook

This Thesis investigates liquid boundary conditions on solid surfaces using colloid probe atomic force microscopy. Boundary conditions are fundamental in fluid dynamics, but also have been a puzzle in interface science for two centuries. With the developments of nanotechniques, boundary conditions have become very important to understand liquid flow in confined geometries. The slip boundary condition is not necessarily observable on the macroscale but acquires more importance on the micro-and nano-scales. Colloid probe atomic force microscopy is the most accurate technique to study liquid boundary conditions on solid surfaces in confined geometries, compared to other current techniques. However, due to experimental artifacts and the issue of interpreting data, slip results in the current literature have large discrepancies.

To enhance the reliability and accuracy of slip results, the existing theoretical calculations and experimental protocols were improved. In view of problems in earlier theoretical models, a new mathematical algorithm to calculate the hydrodynamic drainage force independent of experimental data was generated, which significantly reduces noise in the theoretical force curves and improves the accuracy of force fitting procedure. This mathematical algorithm, which uses the Vinogradova slip model, is easy and convenient for fitting experimental data compared to other methods which require mathematical software and multistep processes, as it is suitable for use in a spreadsheet. This mathematical algorithm can also be simply modified to simulate effects of common experimental artifacts on hydrodynamic drainage forces, such as the effect of flattened microspheres and nanoparticle contamination. The results show that a large flat contact area on a microsphere could underestimate the fitted slip length, and the presence of nanoparticles in the system could cause a particularly large slip length.

In our experiments, Newtonian liquid slip was studied at silica surfaces and hydrophobised OTS-coated or DCDMS-coated solid surfaces using a very viscous liquid (di-*n*-octyphthalate). An improved experimental protocol was strictly implemented in each

experiment, such as following our critical cleaning procedure, repeating measurements at different positions on each substrate, examining the colloid probe before experiments and monitoring the solution temperature through an experiment. The virtual deflection and the friction effects on the compliance region were eliminated in our data analysis. Using our improved experimental protocol and analysing data with our precise theoretical model, our measurements showed that there is a finite and small slip length on the order of 10 nm on the solvophilic silica surface. This is in contrast with the finding of no-slip boundary condition at solvophilic surfaces indicated in some literature. Slip lengths on the order of 45 nm were measured on partially solvophilic OTS and DCDMS self-assembly monolayer surfaces, which agrees with the magnitude of the slip length determined by atomic force microscopy in most of the literature for similar systems. A simple method, which measures liquid slip in one asymmetric and two symmetric systems was produced to assess the reliability and accuracy of measured slip results. The assessed result indicated a good correlation in our measured slip lengths in different systems, and demonstrated the accuracy of our slip measurements. Our experiments showed that the slip length for partially solvophilic surfaces was about 4 times greater than that for solvophilic surfaces. Therefore, the slip results in systems of different surface chemistry confirmed that the wettability of solid surfaces is an important factor in liquid slip, as previously observed.

One of the most important findings in our work is the effect of the drag force on soft cantilevers on the measured slip length. The commonly used model of approximately constant drag force cannot fully describe the cantilever behaviour due to the drag force acting on it. In fact, the drag force is a force that varies along the cantilever at each position during a force measurement.We calculated exactly this variable drag force during a colloid probe force measurement. Comparison of the exact and constant drag models illustrated that the slip lengths could be overestimated if the constant drag force is assumed in all cases. This drag effect is much more significant when using relatively soft cantilevers ($k < 0.2$ N/m) compared to relatively stiff cantilevers. Importantly, the drag effect on soft cantilevers could lead to a spurious result of a slip length dependent on the driving velocity. Similarly, the argument of slip length being dependent on the cantilever type

could also be due to the drag effect on cantilevers. It has been shown that these spurious effects can be eliminated using our exact drag model.

Another important finding in our work is that the slip length depends on the shear rate. Contrary to the common assumption that the slip length is independent of the shear rate or increases with increasing shear rates, our experiments showed that the measured slip length is almost saturated to a constant value at low shear rates, and then decreases as the shear rate increases above a critical shear rate value. Two models were developed and shown to fit the experimental forces down to contact. These models can be combined with the Vinogradova hydrodynamic drainage force model. Our shear dependent saturation slip model allows the liquid slip velocity at the solid surface to become saturated when the shear rate goes to an infinite value, rather than reaching an unphysically infinite value as occurs in the previous shear rate independent models. The measured data and the fitted models show that the slip length could vanish or become extremely small when the shear rate becomes very large, which may explain the discrepancy between the large slip lengths measured experimentally compared to the small slip lengths found in computer simulations, since the shear rates used in simulations are many orders of magnitude greater than those that occur in the experiments.

In conclusion, in this Thesis some important problems have been solved in the study of Newtonian liquid slip on simple solid surfaces using colloid probe AFM in order to get reliable slip measurements. Our work provides a good platform for further studying the mechanism of liquid slip fundamentally in different systems. In the future the investigation of liquid slip on different surfaces, such as soft surfaces, would be an interesting expansion. The boundary conditions on soft surfaces are important to the understanding of flows in biological microfluidic systems, such as flows in blood vessels and propulsion of microorganisms. Suggested soft surfaces could be polymer brushes and nanobubble-covered surfaces. Different methods can be employed to chemically and physically attach polymer brushes on solid surfaces. The solvent exchange method has been demonstrated to generate reproducible nanobubbles on hydrophobic surfaces. Much research now also focuses on patterned superhydrophobic surfaces. These surfaces could not only greatly reduce the pressure needed to drive fluids in capillaries, but also enhance the mixing of

fluids in microfluidic channels. However, the problem with using these more interesting surfaces is to determine the actual zero separation and the optical sensitivity. Meanwhile, different liquids should be explored as well. In contrast with the ellipsoidal molecule, di-*n*-octylphthalate, which was used in our experiments and assumed to contribute to the shear rate dependence of the slip length, some spherical molecules could be tested. Low viscosity liquids, like pure water, might be used to get good results instead of the concentrated sucrose solution with the improved resolution and reliability of our fitting techniques and data analysis.

As mentioned, the effect of shear rate remains a puzzle in the current liquid slip field. Three different models, shear-independent slip, slip increasing and decreasing with increasing shear rates, have all been proposed. The present results, although arguably the most reliable to date because the exact drag force has been used, nevertheless could be extended and refined. Shear rate could be the reason that causes the observed discrepancy in slip lengths between experimental and simulation results. In the future, the effect of shear rate should be further explored using different methods. Velocimetry could be a suitable technique for investigating liquid phenomena with different shear rates if the resolution of this method can be improved. Quartz crystal balance is also a good choice in studying of liquid slip at extremely high shear rates which could approach the magnitude of shear rates used in computer simulations. Finally, supercomputers could be employed to simulate liquid slip phenomena at lower shear rates.

Appendix 1 CO_2 Snow cleaning procedure

CO_2 snow-jet cleaning uses the output stream from a CO_2 gun, which produces a high velocity solid and gas mixture, focused on a surface for cleaning. It can remove particles of all sizes ranging from those visible to the eye (e.g. dust) through to submicron, as well as hydrocarbon-based deposits and films.[1,2]

A successful CO_2 snow-jet cleaning procedure requires attention to the setup and details. A proper CO_2 snow-jet cleaning setup needs to:

1) Avoid recontamination of the sample once cleaned.

2) Avoid recontamination from the cleaning system itself: the fixtures and materials used to hold the sample, especially the hot plate surface, and the laminar flow cabinet.

3) Prevent moisture condensation.

4) Avoid static charge build-up: this is not a problem for metal samples, but is usually a problem for glass samples or electrically isolated parts on complex structures. In this case, devices to control static charge can be recommended in critical cleaning applications.

5) Follow methods and procedures scrupulously.

A1.1 Cleaning Procedure

Prior to commencing cleaning, the CO_2 gun filter was checked for cleanliness, and the CO_2 cylinder was checked for sufficient pressure. All tweezers were cleaned with fresh distilled ethanol in a sonication bath and blow dried using high purity nitrogen. A hot plate was placed inside the laminar flow cabinet, after wiping both the cabinet surface and the hot plate surface with ethanol using Kimwipes. The hot plate surface was further purged by the CO2 snow-jet before placing any samples.

The hot plate is used because during the cleaning procedure, the surface temperature is lowered by the cold CO_2 snow stream, and moisture would condense on the sample surface, which in itself leads to surface contamination. Therefore, in our procedure, the sample was placed on a hot plate inside the laminar flow cabinet and a vacuum suction applied in order to avoid blowing away the sample by the high force of the CO_2 stream. The temperature of the hot plate was usually set between 50 – 80ºC.

The CO_2 gun cleaning procedure should be systematic, moving from a clean region to a region which is to be cleaned as shown in Figure A1.1.

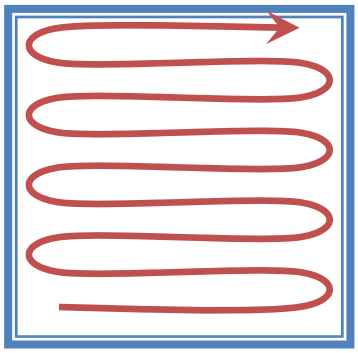

Figure A1.1 The cleaning direction should be constant, moving from the clean area to a dirty area.

During the CO_2 gun procedure, the gun nozzle was kept approximately 5 – 10 cm from the surface at an angle of about 45°. Lower angles can cause the sample to be blown away by the snow-jet (the strength of the vacuum in our hot plate was quite low). Wearing safety goggles is particularly important when doing this operation to avoid potential risks due to flying fragments.

After CO_2 snow-jet cleaning the sample surface was blow dried using pure N_2 to remove any deposits. Once cleaned, the sample was kept in a clean Petri dish that was kept inside the laminar flow cabinet.

A1.3 the Effect of CO_2 Snow Cleaning

The effect of CO_2 snow-jet cleaning on OTS-coated silicon wafers was examined in three different cases by AFM imaging, as shown in Figure A1.2 to Figure A1.4. An OTS-

coated silicon wafer that was not subjected to CO_2 snow cleaning is shown in Figure A1.2. The wafer was cleaned by sonication for 1 minute in fresh distilled ethanol and acetone, and blow dried. This image shows that there are many nanoparticles on the sample surface. Two representative nanoparticles sizes are highlighted in Figure A1.2: the first was 1.2 nm high and 156.6nm wide, the second was 0.8 nm high and 195.7 nm wide. The RMS roughness value is 101 pm (5 μm×5 μm).

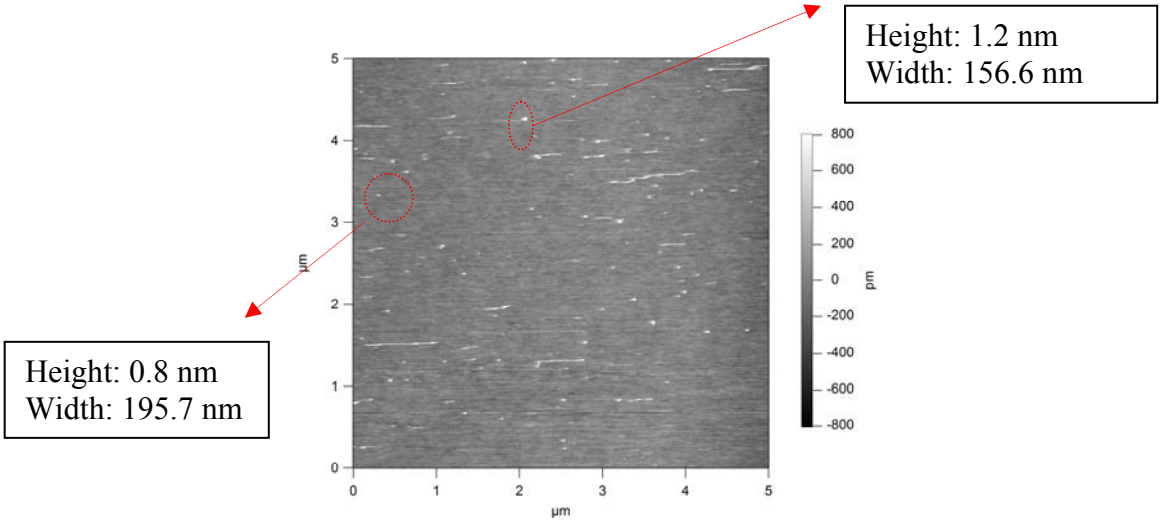

Figure A1.2 Effect of cleaning on an OTS-coated silicon wafer by simple sonication in clean solvents. The OTS-coated silicon wafer was sonicated in ethanol and acetone before imaging. The particle sizes are highlighted.

An OTS-coated silicon wafer subjected to CO_2 snow-jet cleaning but without sufficient precautious is presented in Figure A1.3. Before CO_2 snow-jet cleaning, 1 minute ethanol and acetone sonication for the silicon wafer was performed as same in the previous case. The image presents a large number of larger nanoparticles clearly due to recontamination. Two different size particles are marked as typical representatives in this figure, one is 13.6 nm high and 303.4 nm wide, and the other is 4.0 nm high and 166.4 nm wide. It is believed that these particles originated from a dirty area of the hot plate surface surrounding the silicon wafer during CO_2 snow-jet blowing the surface, as the hot plate surface on which the wafer was placed was not cleaned in advance.

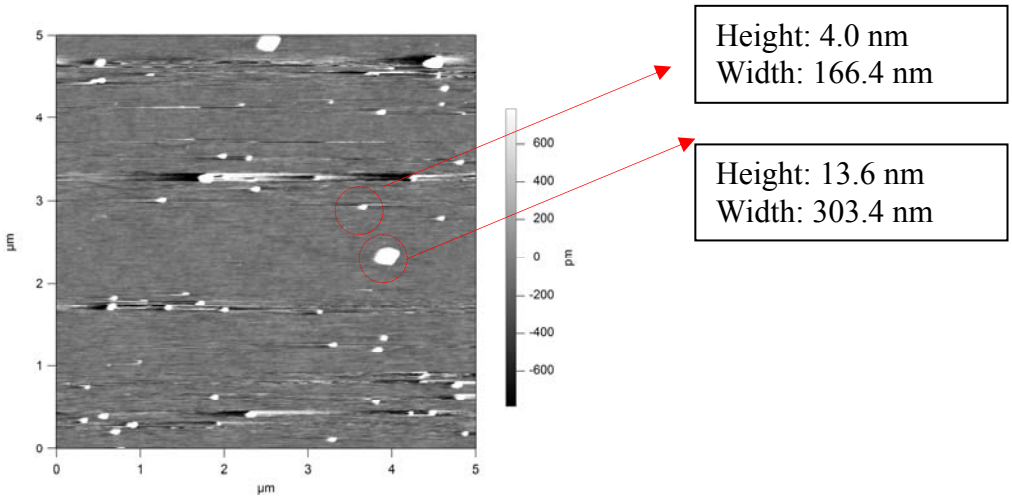

Figure A1.3 Result of recontamination on the OTS-coated silicon wafer. The OTS-coated silicon wafer was sonicated by ethanol and acetone and then cleaned by the CO_2 snow-jet before imaging, but the surface of the hot plate was not cleaned in advance. Two representative particle sizes are highlighted.

In the third case, prior to placing the sample on the hot plate, the hot plate surface was wiped using ethanol, and cleaned by the CO_2 snow-jet. The OTS-coated silicon wafer was cleaned by ethanol and acetone sonication as usual, and then by CO_2 snow-jet cleaning. As shown in Figure A1.4, compared with no CO_2 snow-jet treatment in the first case, the small nanoparticles were almost completely removed and no additional larger nanoparticles were introduced. The RMS roughness value in Figure A1.4 is 83 pm over the 5 µm×5 µm scan area.

The measured advancing contact angle of water on the OTS-coated silicon wafer was approximately 112º and the receding contact angle of water was 105º, both before and after CO_2 snow cleaning. It can be concluded that the OTS monolayer was not destroyed by the high velocity CO_2 snow-jet. The CO_2 snow-jet treatment is an effective way to clean OTS-coated silicon wafers, without damaging the self-assembly monolayers.

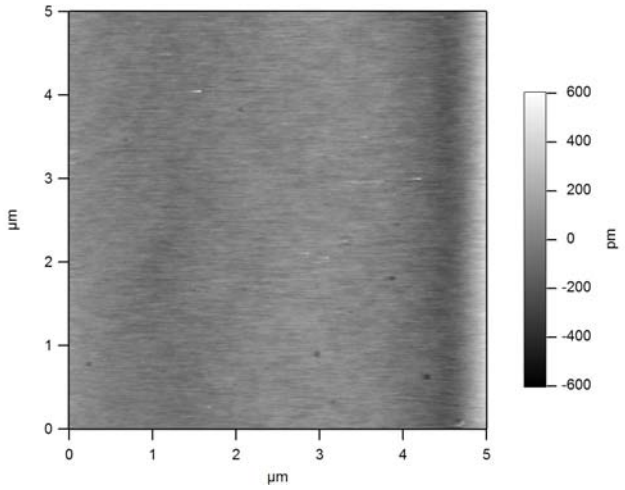

Figure A1.4 Properly cleaned OTS-coated silicon wafer surface after an effective CO_2 snow-jet treatment. The OTS-coated silicon wafer was sonicated by ethanol and acetone and then cleaned by the CO_2 snow-jet. The hot plate surface was cleaned by ethanol and CO_2 snow-jet prior to placing holding the silicon wafer on the hot plate. The RMS roughness value is 83 pm (5 µm×5 µm).

References

1. Sherman, R.; Hirt, D.; Vane, R. Surface cleaning with the carbon dioxide snow Jet. *J. Vac. Sci. Technol. A* **1994**, *12*, 1876-1881.

2. Applied Surface Technologies 1996, Applied Surface Technologies, New, Providence, New Jersey, USA, viewed 2 August 2012, <http://www.co2clean.com/issues.html>.

Appendix 2 Hydrodynamic Drainage Force Conversion

In a typical colloid probe hydrodynamic drainage force measurement, the colloid probe is made to approach and retracted from a substrate surface by applying a voltage to the piezo-crystal in the perpendicular direction Z. The deflection of the cantilever is measured in response to the force acting on the colloid probe. A light beam from a laser diode is focused onto the tip of the cantilever and reflected to a segmented photodiode. The bending of the cantilever due to the acting force is determined by the reflected laser beam moving up or down on the photodiode due to the change in angle of the deflected cantilever.

A2.1 Raw Data Obtained From a Force Measurement

The direct result of a force measurement obtained by atomic force microscopy (AFM) is a measurement of photodiode voltage (V) versus displacement of the piezo-crystal Z (nm), which is shown in Figure A2.1. The purple curve represents the extension force and the blue curve corresponds to the retraction force. Both curves consist of two parts, the non-contact and contact parts. In the non-contact regime, the microsphere is at a non-zero distance from the substrate surface. In this region, the change in the deflection is due to the hydrodynamic forces acting on the colloid probe, such as hydrodynamic drainage force. After the microsphere and the substrate surface come into ‘contact’, the microsphere starts to push against the substrate surface. If the substrate surface is much stiffer than the cantilever, ideally the change in the deflection of the cantilever is equal to the change in the position of the Z piezo. This region is known as the contact regime or the constant compliance regime. The slope of the curve in this regime can be used as a conversion factor to convert the photodiode signal in Volts into the cantilever deflection in nanometres. This slope is defined as the optical lever sensitivity (*OLS*) (also sometime

called “compliance”). In some instruments such as the Asylum MFP-3D AFM, the inverse of this slope is used, which is referred to the inverse optical lever sensitivity (*Invols*, nm/V). In the inset of Figure A2.1, two linear ranges in the extension and retraction contact parts are selected to calculate the compliance value of each curve, which are highlighted by the yellow and green lines respectively.

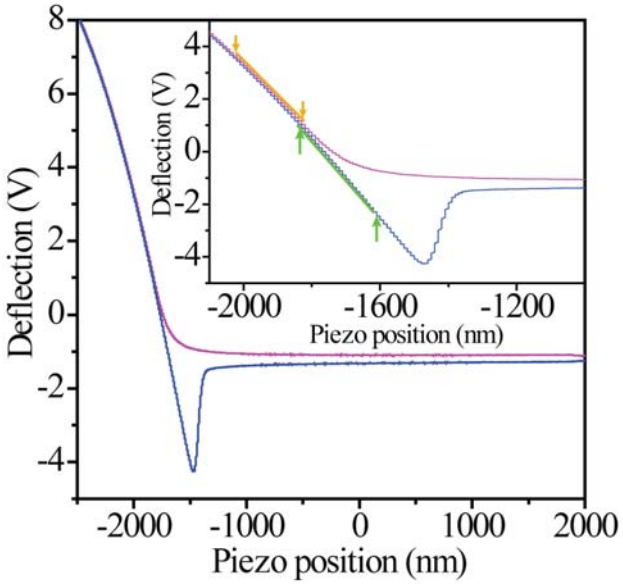

Figure A2.1 Raw data plot obtained from a typical AFM force measurement. The purple curve represents the extension curve and the blue curve represents the retraction curve. The inset is an enlargement of the contact region. The yellow line and the green line highlight the two ranges in the linear contact parts of the curves in extension and retraction respectively, which are chosen to calculate the compliance value. The viscosity in this experiment is 48.58 mPa s, and the driving velocity is 30.1 μm/s.

A2.2 Cantilever Deflection Conversion

The photodiode Volts signal can be converted into the cantilever deflection in nanometres by dividing by the optical lever sensitivity (*OLS*). The *OLS* is obtained from the slope of the linear contact part of the raw data curve shown in the inset of Figure A2.1, *OLS* (compliance) = ΔV / ΔZ at contact. Therefore, cantilever deflection (nm) = photodiode voltage signal (V) / compliance (V/nm).

Due to the friction force as the probe slides over the substrate surface, as discussed in Chapter 4, different values of the compliance are obtained during extension and retraction. In our analysis protocol, the individual value of the compliance is used to find the region of zero separation. This transformation produces a vertical portion of the force curve in correspondence with the contact region. However, the force curve starts to bend when the piezo extends far beyond the point of contact, as shown in the inset of Figure A2.2. The curvature in the contact regime is believed to be due to non-linear terms in the dependence of the cantilever deflection on the change in angle (i.e. the failure of the assumption that the change in the angle of the cantilever is small). This is most noticeable for large deflections, and for this reason the compliance region is chosen at relatively lower deflection values, i.e. at the beginning of the contact regime.

In experiments performed since this Thesis was first drafted, it was found that the two compliance values obtained from the extension and retraction curves become similar to each other, if the range of data chosen for the compliance, as highlighted in Figure A2.1 by the cursors, is selected in the same range of separations for both extension and retraction curves. This might mean that the friction force in this chosen linear contact regime is indeed quite small.

The average compliance value is used to calibrate the whole force curve. Figure A2.2 shows the converted cantilever deflection in nanometres using the individual compliances calculated using the extension curve and the retraction curve. In practice, the average compliance value is found by averaging several compliance values at different velocities in one experiment (usually low velocity compliance values are chosen, in the velocity range of 10 – 50 μm/s). The relative separation between the tip and the substrate surface is defined as the current Z piezo displacement plus the corresponding cantilever deflection in Figure A2.1. Due to the initially arbitrary piezo displacements, the zero separation is also initially arbitrarily assigned as shown in Figure A2.2. Subsequently the true zero separation is established.

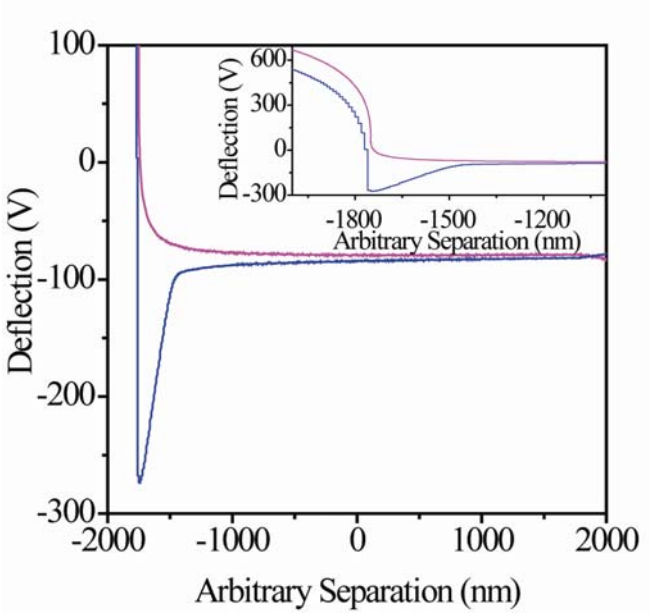

Figure A2.2 Cantilever deflection in nanometres versus relative separation in nanometres. The photodiode signal (V) is converted into the deflection (nm) using the individual compliance value.

A2.3 Setting the Zero of Separation

To shift the whole curve to its true zero separation, two steps have to be taken. The first step is to determine the current zero separation position in Figure A2.2 which is an average value of the sum of the cantilever deflection and the piezo position in the linear contact regime shown in the inset of Figure A2.1. The chosen range for calibrating this average value is the same as the one used for the compliance calibration. The second step is to shift the whole curve by this value, which moves the vertical contact regime to zero separation. However, because the average compliance value is used to calibrate the whole force at the end, the force curve slightly shifts from the true zero separation. Therefore, it is necessary preliminary work to find the first contact point at the contact regime by using the two individual compliance values for the extension and the retraction, and then move the pre-determined first contact point to zero by shifting the whole force.

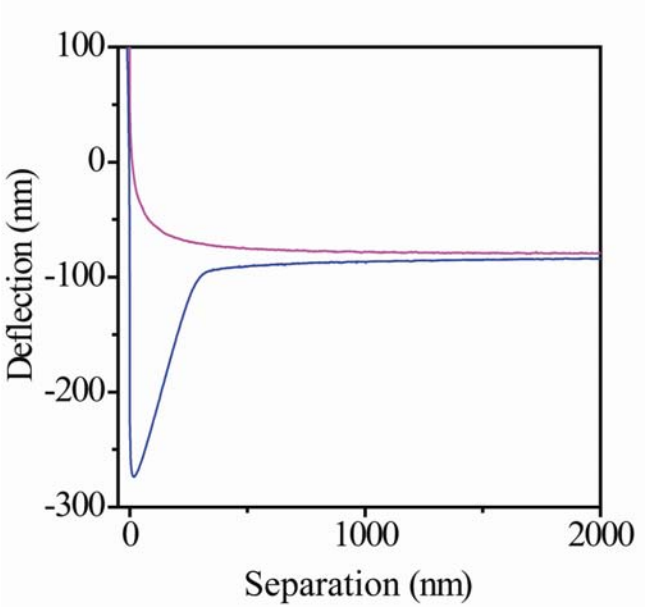

Figure A2.3 Deflection in nanometres versus true separation in nanometres of experimental hydrodynamic force data

A2.4 True Deflection

For most surface interactions, small deflections are expected at large separations (> 2000 nm). In a hydrodynamic force measurement, the deflection in the extension curve at large separations has the same magnitude, but opposite sign with respect to that in the retraction, and corresponds to the residual hydrodynamic drainage force and the drag force acting on the cantilever. Therefore, the extension and retraction curves in Figure A2.3 have to be shifted so that the two curves are symmetrical with respect to the zero deflection at large separations, as shown in Figure A2.4. The steep regions at the beginning of the extension curve and the end of the retraction curve are due to the piezo drive speeding up and slowing down to a stop respectively.

Due to the relative motion between the laser, the photodiode, and the cantilever during piezo movements in top scanning AFMs such as the Asylum MFP-3D AFM, an elastic stress effect normally occurs, which causes a virtual deflection: the magnitude of the deflection increases linearly with the piezo extension, and has a negative sign (see the inset in Figure A2.4, this effect has been described in Chapter 4). This virtual deflection can be corrected by subtracting a straight line. This slope of the line is calculated in the

separation interval D of around 1000 nm, shown in Figure A2.4, after the piezo velocity becomes stabilized, which should be the same range in the extension and the retraction curves. The magnitude of the slope is typically at 10^{-5} to 10^{-6} (V/nm). The slope seems to increase slightly with driving velocity, and the increase is more obvious for soft cantilevers than stiff cantilevers.

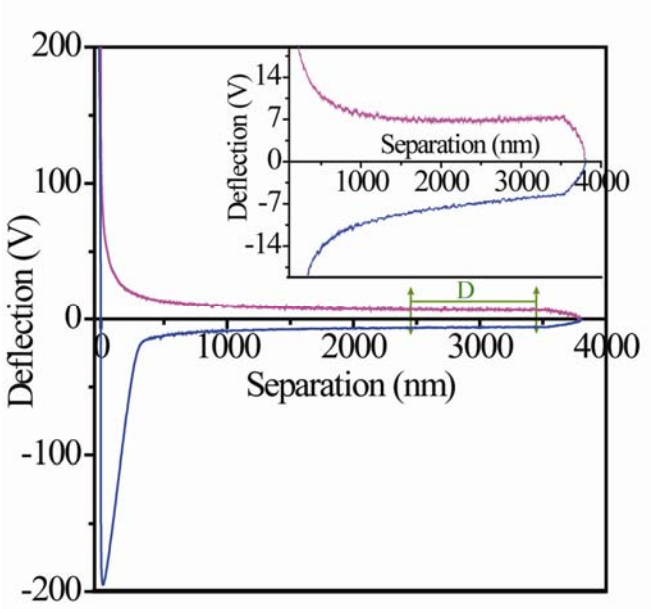

Figure A2.4 Extension and retraction curves are symmetrical about the zero deflection at large separations. For the extension, the initial deflection is positive. For the retraction, the final deflection is negative. Inset: small virtual deflection in the raw curves at large separations. This virtual deflection can be eliminated by subtracting a straight line with the average slope from the extension and retraction curves.

A2.5 Correction for the Constant Drag Forces on Stiff Cantilevers

At large separations, the drag force and the hydrodynamic drainage force are dominant, and the van der Waals force can be neglected. The hydrodynamic drainage force is the one required, so the drag force had to be removed.

The drag deflection in the experimental curve is the difference between the theoretical hydrodynamic drainage deflection and the experimental deflection, which is the sum of the drag deflection and the drainage deflection. If the cantilever is stiff enough ($k >$

0.2N/m), the drag force can be treated as a constant force during the measurement. Since the drag force is dominant at large separations, the separation interval D, as shown in Figure A2.4, is selected to determine the constant drag deflection. The constant drag deflection values obtained from the extension and retraction curves are assumed equal and opposite, so either the individual or the average drag deflection can be used. The experimental hydrodynamic drainage deflection is achieved by removing the constant drag deflection value, as shown in Figure A2.5. The average constant drag deflection value and the fitted spring constant k can be used later to calculate the effective drag length L_e. For softer cantilevers (k < 0.2 N/m), this approximation is not justified and lead to errors in the fitted slip length, as described in Chapter 5.

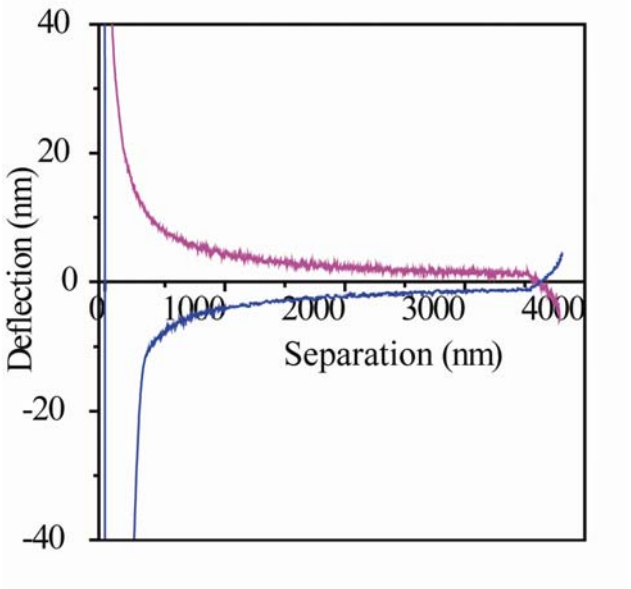

Figure A2.5 Hydrodynamic drainage deflections at all separations obtained after subtracting the drag deflections.

A2.6 Calibration of the Spring Constant Using the Hydrodynamic Method

The hydrodynamic drainage deflection is converted into a force by estimating the spring constant. The spring constant can be calculated from the Sader method,[1, 2] the thermal method[3] or by the hydrodynamic method.[4] Here, we use the hydrodynamic method to determine spring constant. For this method to work, the radius of the colloid probe and the

viscosity of the liquid need to be known independently. From the Vinogradova *f** equation, it can be shown explicitly that the influence of the slip length is negligible at large separations ($h >> b$), so that the Taylor equation can be used. Therefore the spring constant is obtained by fitting the experimental hydrodynamic drainage force (from Figure A2.5) with the theoretical hydrodynamic drainage force calculated using the no-slip boundary condition from the Taylor equation as shown by the green line in Figure A2.6. The best fit value of k is the one which offers an agreement between the two force curves from large separations down to the smallest separation at which a good fit is still possible. If the experimental hydrodynamic force is a no slip force, the experimental force should agree with the theoretical no-slip force up to the contact regime. However, if a slip exists in the experimental force, the fit should be incomplete at relatively small separations, such as below 1000 nm, as shown in Figure A2.6.

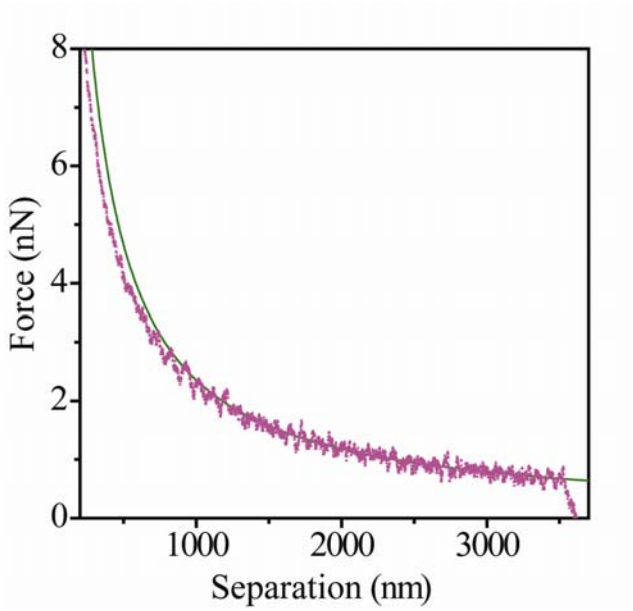

Figure A2.6 The no-slip force (green solid curve) fits well the experimental hydrodynamic drainage force (purple filled triangles) from the separation of 3500 nm down to the minimum separation of 1000 nm, using a fitted spring constant of 0.53 N/m.

A2.7 Fitting of the Slip Length

The experimental hydrodynamic drainage force is obtained from the measured hydrodynamic drainage deflection by multiplying by the fitted spring constant described in

Section A2.6. By varying the slip length, the experimental hydrodynamic force can be fitted by the theoretical hydrodynamic drainage force in the slip boundary condition. The best slip length value is fitted so that the experimental hydrodynamic drainage force is in agreement with the theoretical slip force at the whole separations, as shown in Figure A2. 7. The main source of error in the fitted slip length comes from the error in the fitted the spring constant *k* and the fitting procedure itself. However, changing the value of the fitted spring constant *k* cannot change the shape of the experimental hydrodynamic force. Because of the difference in the shape of the curve between the slip force the no-slip force, in our experiments the experimental force could not be made to agree with the no-slip theoretical force, regardless of the choice of the spring constant. Therefore, some slip was always necessary to achieve a good fit.

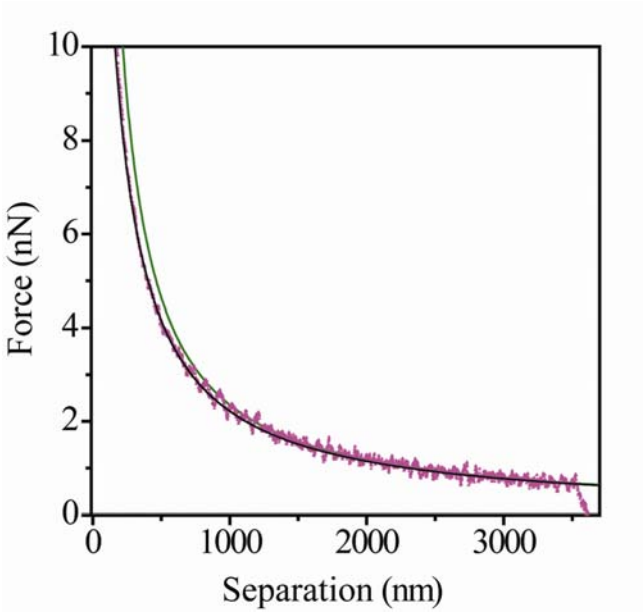

Figure A2. 7 The theoretical hydrodynamic drainage force (black solid line) under the slip boundary condition fits by the experimental hydrodynamic drainage force (purple filled triangles) at all separations using the slip length of 32 nm. The green line is the theoretical hydrodynamic drainage force under the no-slip boundary condition.

References

1. Sader, J. E.; Larson, I.; Mulvaney, P.; White, L. R. Method for the calibration of atomic force microscope cantilevers. *Rev. Sci. Instrum.* **1995**, *66*, 3789-3798.

2. Sader, J. E.; Chon, J. W. M.; Mulvaney, P. Calibration of rectangular atomic force microscope cantilevers. *Rev. Sci. Instrum.* **1999**, *70*, 3967-3969.

3. Hutter, J. L.; Bechhoefer, J. Calibration of atomic-force microscope tips. *Rev. Sci. Instrum.* **1993**, *64*, 1868-1873.

4. Craig, V. S. J.; Neto, C. In situ calibration of colloid probe cantilevers in force microscopy: hydrodynamic drag on a sphere approaching a wall. *Langmuir* **2001**, *17*, 6018-6022.

Appendix 3 FORTRAN Source Code for the Exact Drag Force Calculation

A3.1 FORTRAN CODE

This FORTRAN source code was created by A/Prof. Phil Attard, with some modification and testing by Ms Liwen Zhu. This code was used to perform the calculations of the hydrodynamic drainage force under the slip boundary condition, with non-uniform and non-constant drag force on the cantilever, as presented in Chapter 3 and applied in Chapter 5 and Chapter 6.

```
************************************************************************
***   File Name: slipdrag.for
***   outputs voltage versus drive distance
***   SI units throughout the whole program
***   The input data read from the "dragin.dat" file, and the output data
in the "dragout.dat" file


      IMPLICIT NONE
      INTEGER npts,nmax
      PARAMETER(npts=5000,nmax=100)          ! The number of data point is 5000
      REAL*8 rr,rr0,visc,visc0,kk,kk0,bb,bb0
      REAL*8  zdot,zdot0,ham,zz0,zz00,zstart,zstart0,zend,zend0,timefac
      REAL*8 length,length0,leff,leff0,alpha,alpha0
      REAL*8 cdrag,dy,bei
      REAL*8 xy(nmax),xdoty(nmax)    ! xy (namx) is x(y), which is the shape of the
cantilever as a function of the distance y from the base of the cantilever in Eq. 3.40;
xdoty(namx) is a derivative of dx(y) with respect to time t; y_i = i*dy
      REAL*8 xyp(nmax),xdotyp(nmax)                              ! x(t+dt)
```

```
      REAL*8 zin(npts),hin(npts),xin(npts),thetain(npts),
     &       fdrag(npts),fdrain(npts),fvdw(npts)
      REAL*8 pi,xxl,fl,hh,dragf,zzdot,t1,t2,t3,fac1,vino
      INTEGER i
      INTEGER tad(8)    ! 1=yyyy, 2=mm, 3=dd, 4=UTC, 5=hr, 6=min, 7=secs,
8=millisec
      CHARACTER*20 filename


      OPEN(unit=4,file='dragin.dat',status='old')
      OPEN(unit=2,file='dragout.dat',status='old')
      OPEN(unit=12,file='temp.dat',status='old')


      CALL date_and_time(values=tad) ! 1=yyyy, 2=mm, 3=dd, 5=hr, 6=min,
7=secs, 8=msecs
      pi = 4.d0*ATAN(1.d0)


      READ(4,*) filename
      WRITE(2,60) filename,tad(1),tad(2),tad(3),tad(5),tad(6),tad(7)
      WRITE(6,60) filename,tad(1),tad(2),tad(3),tad(5),tad(6),tad(7)
      FORMAT(5x,'Drainage force, slipdrag.for',/,' File=',a20,
     &           5x,i4,'.',i2,'.',i2,2x,i2,':',i2,':',i2)


      READ(4,*) rr0            ! rr0 is the input microsphere radius in micrometres
      rr = rr0*1.E-6                    ! rr is the Microsphere radius in metres
      READ(4,*) kk0                     ! kk0 is the input spring constant, N/m
      kk = kk0
      READ(4,*) visc0                   ! visc0 is the input viscosity, mPa s
      visc = visc0*1.E-3                ! visc is the viscosity in Pa s
      t1 = visc*rr**2/kk
      READ(4,*) bb0                ! bb0 is the input slip length in nanometres
      bb = bb0*1.E-9                    ! bb is the slip length in metres
      WRITE(2,61) rr0,kk0,visc0,bb0,t1
      WRITE(6,61) rr0,kk0,visc0,bb0,t1
 61   FORMAT(' Input values: R=',f5.2,' um, k=',f6.3,' N/m, eta=',f6.2,
     &       ' mPa s, slip length=',f5.1,' nm',/,' eta R^2/k=',e10.4)
```

```
READ(4,*) zdot0
```
! zdot0 is the input drive velocity, micrometre/sec

```
zdot = ABS(zdot0)*1.E-6
```
! make drive velocity positive in metre /sec

```
READ(4,*) ham
```
! Ham is the Hamaker constant, it is set at 4.0×10^{-22} J/m^2 in the input file

```
READ(4,*) zz00
```
! zz00 is the input L-J length scale, it is set at 0.5 nm in the input file

```
zz0 = zz00*1.E-9
WRITE(2,62) zdot0,ham,zz00
WRITE(6,62) zdot0,ham,zz00
FORMAT(' zdot=',f5.1,' um/s, Ham=',e8.2,' J/m^2, z0=',f4.2,' nm')
```

```
READ(4,*) zstart0
```
! zstart0 is the input piezo starting position in nanometres, we normally make this value corresponding to our experimental separation, around 5000 to 4000 nm.

```
zstart = zstart0*1.E-9
READ(4,*) zend0
```
! zend0 is the input piezo ending position in nm, we normally put a negative value, between -500 to -5000 nm, in the input file

```
zend = zend0*1.E-9
```
! zend is the piezo ending position in metres

```
READ(4,*) timefac
```
! timefac is the time step reduction factor, it is set at 0.0005 in the input file

```
WRITE(2,63) zstart0,zend0,timefac
WRITE(6,63) zstart0,zend0,timefac
FORMAT(' zstart=',f6.0,' nm, zend=',f5.0,' nm, timefac=',e8.2)
IF( zend .GT. zstart ) STOP ' zstart must be greater than zend'
```

```
READ(4,*) length0
```
! Length0 is the actual cantilever length in micrometres obtained from the SEM measurement

```
length = length0*1.d-6
```
! Length is the actual cantilever length in metres

```
READ(4,*) leff0
```
! leff0 is the apparent effective drag length in micrometres obtained from the experimentally measured force at large separations, which is defined in Eq.3.6

```
leff = leff0*1.d-6*9.d0/8.d0
```
! leff is the effective drag length as defined in page 86 of Chapter 3 ($L_e = 9\tilde{L}_e/8$)

```
      READ(4,*) alpha0                    ! alpha0 is the calibration Factor which is
the constant compliance slope obtained in contact, V/nm, see Eq. 3.48 in Chapter 3
      alpha = alpha0*1.d9                 ! alpha is constant compliance slope in V/m
      WRITE(2,64) nmax,length0,leff0,leff*1.d6,alpha0
      WRITE(6,64) nmax,length0,leff0,leff*1.d6,alpha0
      FORMAT(' N=',i4,' length=',f6.1,' um, Leff0=',f6.2,
     &       ' (',f6.2,') um, alpha=',e10.4,' V/nm')


      cdrag = 16*pi*visc*leff/length    ! cdrag is the drag coefficient, defined as
c in Eq. 3.43 in Chapter 3
      dy = length/nmax                   ! the node spacing dy, y_i = i*dy, x_i =
x(y_i)
      bei = length**3*kk/3               ! bei is the elastic parameter B in Eq. 3.33



**********************************************************************
***   This section calculates the initial deflection xx1 before the time stepping
      zzdot = -ABS(zdot)                      ! zzdot < 0 on approach, zdot is the
positive drive velocity in metres /sec
      pi = 4.d0*ATAN(1.d0)
      fac1 = 6*pi*visc*rr**2                  ! fac1 is defined as the hydrodynamic
drainage force factor
      vino = 1.d0                                          ! Vinogradova No-slip force,1
      hh = zstart                  ! The separation before the cantilever starts to bend
      IF( bb .GT. 0.d0 )
     &  vino = hh/3/bb * ( (1.+hh/6/bb)* LOG(1.+6*bb/hh) - 1. )          !
Vinogradova symmetric slip f* factor, see Eq. 3.3 in Chapter 3
      xxl = ( -6*pi*visc*leff*zzdot
     &    - fac1*zzdot/hh*vino
     &    + ham*rr/6/hh**2*( -1.+0.25*(zz0/hh)**6 ) ) /kk          ! xxl is
the tip deflection of the cantilever, see Eq. 3.12 in chapter 3
```

```
      hh = zstart + xxl                ! Separation after the cantilever starts to
bend
      IF( bb .GT. 0.d0 )
     &  vino = hh/3/bb * ( (1.+hh/6/bb)* LOG(1.+6*bb/hh) - 1. )          !
Vinogradova symmetric slip f* factor, see Eq. 3.3 in Chapter 3
      xxl = ( -6*pi*visc*leff*zzdot
     &    - fac1*zzdot/hh*vino
     &    + ham*rr/6/hh**2*( -1.+0.25*(zz0/hh)**6 ) ) /kk


      hh = zstart + xxl
      IF( bb .GT. 0.d0 )
     &  vino = hh/3/bb * ( (1.+hh/6/bb)* LOG(1.+6*bb/hh) - 1. )          !
Vinogradova symmetric slip f* factor
      xxl = ( -6*pi*visc*leff*zzdot
     &    - fac1*zzdot/hh*vino
     &    + ham*rr/6/hh**2*( -1.+0.25*(zz0/hh)**6 ) ) /kk


      hh = zstart + xxl                ! Better separation
      IF( bb .GT. 0.d0 )
     &  vino = hh/3/bb * ( (1.+hh/6/bb)* LOG(1.+6*bb/hh) - 1. )          !
The Vinogradova symmetric slip f* factor
      fl = -fac1*zzdot/hh*vino
     &   + ham*rr/6/hh**2*( -1.+0.25*(zz0/hh)**6 )          ! fl is the sum
of the hydrodynamic drainage force and the van der waals force acting on the microsphere
      DO i=1,nmax
         xdoty(i)  = 0.d0    ! initial deflection velocity
      END DO
      CALL make_xy(nmax,bei,cdrag,zzdot,dy,fl,xdoty,dragf,xy)          ! call
SUBROUTINE make_xy to calculate the initial drag force

      WRITE(6,*) 'Init defln (nm)=',xxl*1.d9,xy(nmax)*1.d9
```

```
************************************************************************
```

**** The subroutine calculates the hydrodynamic drainage force, the drag force and van der waals force for current parameters*

```
      CALL calc_fdr(npts,nmax,rr,visc,kk,bb,
     &            zdot,ham,zz0,zstart,zend,timefac,
     &            cdrag,bei,dy,xy,xdoty,dragf,
     &            zin,hin,xin,thetain,fdrag,fdrain,fvdw)


      WRITE(2,73) CHAR(9),CHAR(9),CHAR(9),CHAR(9),
     &             CHAR(9),CHAR(9),CHAR(9),CHAR(9)
 73   FORMAT('z (nm)',a,'V (V)',a,'h (nm)',a,'x (nm)',
     &       a,'happ (nm)',a,'xapp (nm)',
     &       a,'Fdrain (nN)',a,'FvdW (nN)',a,'Fdrag (nN)')


      DO i=1,npts,10
         t1 = -thetain(i)*alpha*2*length/3    ! t1 is the photodiode voltage V, thetain is the angle of the cantilever θ, alpha is the defined constant compliance, see α in Eq.3.48
         t3 = -t1/alpha                       ! t3 is the apparent deflection in metres
         t2 = zin(i) + t3                     ! t2 is the apparent separation in metres


         WRITE(2,74) zin(i)*1.d9,CHAR(9),t1,CHAR(9),hin(i)*1.d9,
     &       CHAR(9),xin(i)*1.d9,CHAR(9),t2*1.d9,CHAR(9),t3*1.d9,
     &       CHAR(9),fdrain(i)*1.d9,CHAR(9),fvdW(i)*1.d9,
     &       CHAR(9),fdrag(i)*1.d9
 74      FORMAT(9(e12.6,a))
      END DO


      STOP
      END
```

```
**********************************************************************
```

**** The subroutine calculates the hydrodynamic drainage force, the exact drag force and van der waals force.*

```
      SUBROUTINE calc_fdr(npts,nmax,rr,visc,kk,bb,
     &           zdot,ham,zz0,zstart,zend,timefac,
     &           cdrag,bei,dy,xy,xdoty,dragf,
     &           zin,hin,xin,thetain,fdrag,fdrain,fvdw)
***   calculate trajectory of the colloid probe
      IMPLICIT NONE
      INTEGER npts,nmax,i,iy,j
      REAL*8 rr,visc,kk,bb,zdot,ham,zz0,zstart,zend,timefac,
     &       cdrag,bei,dy,dragf
      REAL*8 xy(nmax),xdoty(nmax),xyp(nmax),xdotyp(nmax)
      REAL*8 zin(npts),hin(npts),xin(npts),thetain(npts),
     &       fdrag(npts),fdrain(npts),fvdw(npts)
      REAL*8 pi,fac1,dt,zz,zzdot,hh,vino,fl,t1,xfl,xldot

      pi = 4.d0*ATAN(1.d0)
      fac1 = 6*pi*visc*rr**2            ! The hydrodynamic drainage force factor
      vino = 1.d0                                  ! No-slip force unless bb > 0

      dt = ( zstart - zend ) /zdot
     &   * timefac /(1.d0 - (1.d0-timefac)**npts )       ! Setting the initial
time step, see Eq. 3.19

      zin(1) = zstart - xy(nmax)              ! Setting the initial piezo position
      xin(1) = xy(nmax)                        ! Setting the initial deflection
      hh = zin(1) + xy(nmax)                   ! Setting the initial separation
      hin(1) = hh
      thetain(1) = ( xy(nmax) - xy(nmax-1) )/dy          ! Setting tThe initial
cantilever deflection angle
***   Initially xdot = 0:
      zzdot = -ABS(zdot)                       ! Define the sign of the Extension
      fdrag(1) = dragf                                    ! Total drag force
      IF( bb .GT. 0.d0 )
     &  vino = hh/3/bb * ( (1.+hh/6/bb)* LOG(1.+6*bb/hh) - 1. )          !
Vinogradova symmetric slip f* factor
```

```
      fdrain(1) = -fac1*zzdot/hh*vino    ! The hydrodynamic drainage force
      fvdw(1) = ham*rr/6/hh**2*( -1.+0.25*(zz0/hh)**6 )        ! The van der
Waals force

      zz = zin(1)                                              ! Start piezo position
      DO i=2,npts
         dt = dt*(1.d0-timefac)                    ! Reduce time step, see Eq.3.17
         zz = zz + dt*zzdot                                    ! Next piezo position


         DO iy=1,nmax                    ! initially xdot(t+dt) = xdot(t)
            xdotyp(iy) = xdoty(iy)
         END DO
         DO j=1,5
            fl = 0.d0
            CALL make_xy(nmax,bei,cdrag,zzdot,dy,fl,xdotyp,dragf,xyp)
            xfl = xyp(nmax)      ! The cantilever deflection due to drag force alone
            hh = zz + xy(nmax) + dt*(xdoty(nmax)+xdotyp(nmax))/2      ! The
estimation of the separation
            IF( bb .GT. 0.d0 )
     &          vino = hh/3/bb * ( (1.+hh/6/bb)* LOG(1.+6*bb/hh) - 1. )
! The Vinogradova slip f* factor

           xldot = ( -xin(i-1) - dt*xdoty(nmax)/2 + xfl
     &     - fac1*zzdot/kk/hh*vino
     &     + ham*rr/6/kk/hh**2*( -1.+0.25*(zz0/hh)**6 ) )
     &     /( dt/2 + fac1/kk/hh*vino )          ! New tip velocity, see Eq. 3.14
           hh = zz + xy(nmax) + dt*( xdoty(nmax) + xldot ) /2          !
Improved separation

            IF( bb .GT. 0.d0 )
     &          vino = hh/3/bb * ( (1.+hh/6/bb)* LOG(1.+6*bb/hh) - 1. )
! The Vinogradova symmetric slip f* factor

            xldot = ( -xin(i-1) - dt*xdoty(nmax)/2 + xfl
     &            - fac1*zzdot/kk/hh*vino
     &            + ham*rr/6/kk/hh**2*( -1.+0.25*(zz0/hh)**6 ) )
```

```
     &            /( dt/2 + fac1/kk/hh*vino )        ! The new tip velocity, see
Eq. 3.14
            hh = zz + xy(nmax) + dt*( xdoty(nmax) + xldot ) /2
            IF( bb .GT. 0.d0 )
     &         vino = hh/3/bb * ( (1.+hh/6/bb)* LOG(1.+6*bb/hh) - 1. )  !
The Vinogradova symmetric slip f* factor
            fl  =  -fac1*(zzdot+xldot)/hh*vino          ! The hydrodynamic
drainage force acting on the microsphere
     &           + ham*rr/6/hh**2*( -1.+0.25*(zz0/hh)**6 )    ! The van der
waals force
            xdotyp(nmax) = xldot
            CALL make_xy(nmax,bei,cdrag,zzdot,dy,fl,xdotyp,dragf,xyp)
            DO iy=1,nmax-1
               xdotyp(iy) = ( xyp(iy) - xy(iy) )/dt
            END DO

         END DO    ! j=1,5


***      Shape and deflection velocity are updated in this section.
         DO iy=1,nmax
            xdoty(iy) = xdotyp(iy)
            xy(iy) = xyp(iy)
         END DO
         zin(i) = zz
         xin(i) = xy(nmax)                              ! deflection
         hh = zz + xy(nmax)
         hin(i) = hh
         thetain(i) = ( xy(nmax) - xy(nmax-1) )/dy      ! Deflection angle θ
         fdrag(i) = dragf                               ! Total drag force
         fvdw(i) = ham*rr/6/hh**2*( -1.+0.25*(zz0/hh)**6 )
         vino = 1.d0                          ! The no-slip Vinogradova f* factor = 1
         IF( bb .GT. 0.d0 )
     &     vino = hh/3/bb * ( (1.+hh/6/bb)* LOG(1.+6*bb/hh) - 1. )  ! The
Vinogradova symmetric slip f* factor
         fdrain(i) =  -fac1*(zzdot+xdoty(nmax))/hh*vino

         IF( (i/100)*100 .EQ. i ) WRITE(6,60) zz*1.d9,hh*1.d9
```

```
      END DO
  60  FORMAT(2x,f7.2,2x,f8.3)

      RETURN
      END
```

```
**********************************************************************
******* This section calculates the exact drag force
      SUBROUTINE make_xy(nmax,bei,cdrag,zdot,dy,fl,xdoty,dragf,xy)
***   Calculates moment of force and then cantilever shape
      IMPLICIT NONE
      INTEGER nmax,i
      REAL*8 bei,cdrag,zdot,dy,fl,fy,fym1
      REAL*8 xy(nmax),xdoty(nmax),dragf
      REAL*8 im0(nmax),im1(nmax),mm(nmax)    ! imn(y) = int_0^y dy' m(y')
y'^n

***   Obtain moment of force, M(y)
***   im0 and im1 are running integrals along the cantilever of the force moments
      fym1 = -cdrag * zdot                   ! xdot(0) = 0 the initial uniform
force per unit length when deflection is zero, see Eq.3.43
      fy = -cdrag * ( xdoty(1) + zdot )      ! The uniform force per unit
length when deflection is non-zero, see Eq.3.43
      im0(1) = dy*( fy + fym1 )/2
      im1(1) = dy*( dy*fy + 0.d0 ) /2
      fym1 = fy
      DO i=2,nmax   ! y = i*dy
         fy = -cdrag * ( xdoty(i) + zdot )
         im0(i) = im0(i-1) + dy*( fy + fym1 )/2
         im1(i) = im1(i-1) + dy*( fy*i*dy + fym1*(i-1)*dy )/2
         fym1 = fy
      END DO
      DO i=1,nmax
      mm(i) = ( nmax*dy - i*dy )*fl          ! The cantilever length =nmax*dy
     &        + i*dy*( im0(i) - im0(nmax) )
```

```
     &          -       ( im1(i) - im1(nmax) )          ! mm(i) is the force moment M(y) in Eq.3.38.
      END DO
      dragf = im0(nmax)                                  ! Total drag force

***   Integrate moment to obtain shape x(y)
      fym1 = nmax*dy*fl + im1(nmax)    ! M(0)
      fy = mm(1)
      im0(1) = dy*( fy + fym1 )/2
      im1(1) = dy*( dy*fy + 0.d0 ) /2
      fym1 = fy
      DO i=2,nmax    ! y = i*dy
         fy = mm(i)
         im0(i) = im0(i-1) + dy*( fy + fym1 )/2
         im1(i) = im1(i-1) + dy*( fy*i*dy + fym1*(i-1)*dy )/2
         fym1 = fy
      END DO
      DO i=1,nmax
      xy(i) = ( i*dy*im0(i) - im1(i) ) /bei      ! The shape, see x(y) defined in Eq.3.40
      END DO

      RETURN   ! Check that xy(nmax) = xxl
      END
```

A3.2 The List of Definitions of the Parameters used in the Exact Drag Force FORTRAN Program

npts: the number of data point used in the simulated force curve, here it is set at 5000.

nmax: the cantilever is divided into 100 nodes (nmax) and its deflection at each node is stored. The integral is the sum of the values of the various functions at each node, multiplied by the node spacing dy.

rr0: the input microsphere radius in micrometres.

rr: the Microsphere radius in metres.

kk0: the input spring constant in N/m.

kk = kk0

visc0: the input viscosity in mPa s.

visc: the viscosity in Pa s.

bb0: the input slip length in nanometres.

bb: the slip length in metres.

zdot0: the input drive velocity in microns/sec.

zdot: the positive drive velocity in metres /sec.

Ham: the Hamaker constant, it is set at 4.0e-22 J/m^2 in the input file.

zz00: the input L-J length scale, it is set at 0.5 nm in the input file.

zstart0: the input piezo starting position in nanometres; we normally make this value corresponding to our experimental separation, around 5000 to 4000 nm.

zend0: the input piezo ending position in nanometres; we normally put a negative value around -500 to-5000 nm in the input file

zend: the piezo ending position in metres.

timefac: the time step reduction factor, it is set at 0.0005 in the input file.

Length0: the actual cantilever length in micrometres obtained from the SEM measurement.

Length: the actual cantilever length in metres.

leff0: the apparent effective drag length in micrometres obtained from the experimentally measured force at large separations, which is defined in Eq.3.6 in Chapter 3.

leff: the effective slip length after correcting for wrong AFM fit, see Eq.3.42 in Chapter 3.

alpha0: the calibration factor that is the constant compliance value obtained in contact, V/nm, see Eq. 3.48 in Chapter 3.

alpha: the constant compliance value in V/m

cdrag: the drag coefficient for force density, cdrag =16πηLe/L, see Eq. 3.43 in Chapter 3.

bei: the elastic parameter B in Eq. 3.33.

mm(i): the force moment M(y) in Eq.3.38.

fac1: the hydrodynamic drainage force factor, fac1=$6\pi\eta R^2$

hh: the separation between the microsphere and the flat surface.

Vino: the Vinogradova f^*. Under the no slip boundary condition, Vino = 1. Under the slip boundary condition, vino is the Vinogradova slip f^* factor, see Eq. 3.3 in Chapter 3.

Fdrain: the hydrodynamic drainage force.

Fvdw: the van der Waals force.

xldot: the tip deflection velocity, including drag force, drainage force, and van der waals force = $\dot{x}'$ in Eq.3.14.

xfl: the tip deflection due to drag force alone.

fym1: the initial uniform force per unit length when deflection is zero, see Eq.3.43

fy: the uniform force per unit length when deflection is non-zero, see Eq.3.43

f1: The forces acting on the tip (microsphere) of the cantilever, including the hydrodynamic drainage force and the van der waals force.

A3.3 Example of “dragin.dat” File

The following list parameters have to be filled in before running the exact FORTRAN program.

```
Drag_test
8.61, radius, um
0.095, spring constant, N/m
52.57, viscosity, mPa s
12, slip length, nm
30.01, drive velocity, um/s
4.0e-22, Hamaker constant, J/m^2
0.5, LJ length scale, nm
4000, Start piezo, nm
-5000, End piezo, nm
0.0005, time step factor
283, Length Cantilever, um
86.53 Effective Drag Length, um
-0.0204, CC Calibration factor, V/nm
```

A3.4 Example of “dragout.dat” file

The following list is the output parameters obtained from the exact FORTRAN program.

The drag force given in this output file, Fdrag, is the distributed drag force along the cantilever. Fdrain and Fvdw are the actual drainage force and the van der Waals force acting on the tip. *h* and *x* are the actual separation and deflection of the tip. *happ* and *xapp* are the apparent separation and deflection that would be deduced from an AFM measurement using the photodiode voltage. It is *happ* and *xapp* that should be compared with AFM measurements.

```
Drainage force, slipdrag.for
File=Drag_test              2012. 3. 1  12:58:17
Input values:
R= 8.61 um,  k= 0.095 N/m,
eta= 52.57 mPa s,  slip length= 12.0 nm
eta R^2/k=0.4102E-10,  zdot= 30.0 um/s,
Ham=0.40E-21 J/m^2,  z0=0.50 nm
zstart= 4000. nm,  zend=***** nm,
timefac=0.50E-03, N= 100 length= 283.0 um,
Leff0= 86.53 ( 97.35) um,  alpha=-.2040E-01 V/nm
z(nm)        V(V)     h(nm)        x(nm)      happ(nm)     xapp(nm)    Fdrain(nN)     FvdW(nN)     Fdrag(nN)
3963.81    0.669181    4000         36.1908     3996.61     32.803       0.54784    -3.5875E-08     7.71957
.....................................................................................................
.....................................................................................................
.....................................................................................................
-266.78      5.48193    4.09091    270.871    1.94184    268.722     24.3129     -0.0342982      5.37978
```